System Simulation of Combustion in Direct-Injection Spark-Ignition Engines

Federico Pellegrino

NNT : 2019SACLC075

Thèse de doctorat

System Simulation of Combustion in Direct-Injection Spark-Ignition Engines

Thèse de doctorat de l'Université Paris-Saclay
préparée à CentraleSupélec

Ecole doctorale n°597 Sciences mécaniques et énergétiques, matériaux et géosciences (SMEMAG)
Spécialité de doctorat : Combustion

Thèse présentée et soutenue à Rueil-Malmaison, le 17 octobre 2019, par

FEDERICO PELLEGRINO

Composition du Jury :

Nasser Darabiha Professeur des Universités, CNRS & CentraleSupélec (EM2C)	Président
Luis Le Moyne Professeur des Universités, Université de Bourgogne (ISAT)	Rapporteur
Raul Payri Professeur, Universitat Politécnica de Valéncia (CMT)	Examinateur
Alain Maiboom Maître de conférences HDR, École Centrale Nantes (LHEEA)	Rapporteur
Denis Veynante Directeur de Recherche, CNRS & CentraleSupélec (EM2C)	Directeur de thèse
Alessio Dulbecco Ingénieur de Recherche, IFP Energies nouvelles	Co-directeur de thèse

université PARIS-SACLAY
ÉCOLE DOCTORALE
Sciences mécaniques et énergétiques, matériaux et géosciences (SMEMAG)

Titre : Simulation système de la combustion dans les moteurs à allumage commandé à injection directe.

Mots clés : Simulation Systeme, Combustion, Injection Directe Essence

Résumé : La présence de contraintes de plus en plus strictes sur les émissions de polluants on poussé les contruteurs vers l'injection directe essence (IDE), afin d'améliorer les performances et réduire la consommation de carburant et les émissions des moteurs à combustion interne. Par conséquent, de nouveaux défis sont introduits en termes d'optimisation de la combustion, en raison d'une plus complexe phénomenologie tandis que les modéles système demande des paramètres de calibration supplémentaires.
Cette thèse présente le développement et la validation d'un modèle zéro-dimensionnel (0D) de combustion en IDE pour application en simulation système. Le modèle proposé détaille la physique de l'atomisation, et évaporation des gouttes, de la préparation du mélange air/carburant, de la propagation de flamme dans un mélange non-homogène ainsi que l'intéraction entre ces phénomènes.
La phase liquide est discretisés en paquets groupant des gouttes de la même taille. Un modèle d'atomisation empirique basé sur la vitesse d'injection, les propriétés du carburant et les conditions thermodynamiques fournit les diamètres initiaux. Un modèle Lagrangien détaillant une dynamique de trainée/inértie, échange thermique et convection forcée décrit la pénétration liquide et l'evaporation des paquets. La formation du mélange air/carburant est décrite avec une PDF qui discretise la charge en un mécanisme de classes intéragissant les unes avec les autres et avec les paquets de gouttes. La propagation de flamme prend en compte les effets de ł'hétérogéneité du mélange sur la vitesse de flamme et la formation des polluants.
Le modèle proposé a été implémenté dans la plateforme Simcenter Amesim, dédiée á la modélisation de systémes multi-physiques, et intégrée dans le modèle de combustion essence CFM1D, de la librairie IFP-Engine.
Des approche de modélisation de l'evaporation de carburant, de la dynamique de spray et de la formation du mélange, inspirés de la literature sur les moteurs Diesel, ont été adaptés aux conditions IDE. Le modèle a initialement été validé sur des mesures et des simulations RANS 3D réalisées avec le code IFP-C3D, d'une bombe d'injection à volume constant. Un vortex de tumble, dans un premier temps, et des variations rapides du voulume de la chambre ensuite, ont été ajoutés aux expériments numériques afin d'évaluer la réponse du modèle à l'aérodynamique dans la chambre de combustion et à des conditions thermodynamiques variables, en termes d'évaporation, développement du spray et distribution de la richesse. Des simulations d'injections dans un moteur entraîné, dont les résultats ont été comparés avec des mesures et des calculs CDF, complètent la validation du modèle avec à la fois des conditions thermodynamiques variable et de l'aérodynamique.

Title : System Simulation of Combustion in Direct-Injection Spark-Ignition Engines.

Keywords : System Simulation, Combustion, Gasoline Direct Injection

Abstract : Future constraints on pollutant emissions pushed car manufacturers towards gasoline direct injection (GDI) technologies to improve engine performances and reduce fuel consumption and emissions. New challenges are then introduced in terms of combustion optimization due to a more complex phenomenology while system models require additional calibration parameters.
This PhD work presents the development and validation of a Zero-Dimensional (0D) model of GDI combustion for system simulation. The proposed model focuses on physics of atomization and drop evaporation, fuel/air mixing, flame propagation in heterogeneous charge and mutual interaction between these phenomena.
The liquid phase is discretized in parcels grouping drops of the same size. An empirical atomization model based on injection velocity, fuel characteristics and thermodynamic conditions provides initial diameters. A Lagrangian model including drag-inertia dynamics, heat-up and forced convection describes drop parcel penetration and evaporation. Fuel / air mixing is described using a discrete Probability Density Function (PDF) approach, based on constant-mixture-fraction classes interacting with each other and with the drop parcels. Flame propagation takes into account mixture heterogeneity effects on flame speed and pollutant production is modelled.
The model was implemented in the Simcenter Amesim platform for multi-physical modelling and integrated in a generic Spark Ignition (SI) combustion chamber submodel, CFM1D, from the IFP-Engine library.
Fuel evaporation, spray dynamics and mixture formation modelling approaches, inspired by literature on Diesel engines, were adapted to GDI operating conditions. The model was first validated on a constant-volume vessel with quiescent gas in different thermodynamic conditions by means of experiments and 3D RANS CFD simulations performed with IFP-C3D. A tumble vortex in a constant volume vessel, in a first time, and rapid variations of the vessel volume, in a second time, were then added to the numerical experiment in order to test the model response to in-cylinder flow aerodynamics and variable thermodynamic conditions, respectively, in terms of fuel evaporation, spray development and fuel/air mixing and equivalence ratio distribution. Computations of fuel injections in a motored engine complete the model validation campaign in variable thermodynamic conditions and with realistic aerodynamics and the results were compared to both experiments and CFD computations.

Université Paris-Saclay
Espace Technologique / Immeuble Discovery
Route de l'Orme aux Merisiers RD 128 / 91190 Saint-Aubin, France

Remerciements

I would like to thank all members of the jury, especially the reviewers Luis Le Moyne and Alain Maiboom, for accepting to participate in my PhD defense, for your questions and remarks.

Un remerciment spécial à mon directeur de thèse, Denis Veynante, qui a su orienter mon travail dans les moments difficiles et enrichir mon manuscrit.

Grazie ad Alessio Dulbecco, che ha seguito il mio lavoro da vicino a IFPEN in questi tre lunghi anni. Tre anni di discussioni tecniche accompagnate — senza soluzione di continuità — da chiacchierate molto meno tecniche sulla nostra terra e non solo.

Mes trois ans à IFPEN n'auraient pas été les mêmes sans mes copains de voyage, que je remercie du fond de mon cœur. Je commence par mes collègues de bureau: Haïfa qui, avec son accueil chaleureux, m'a fait sentir chez moi dès le premier jour et pendant l'année qui a suivi et Lama *Drama*, dont la folie a souvent éclairé mes journées : tu sais répandre la bonne humeur même quand tout va mal, merci d'avoir été là. Valerio, con cui ho condiviso due uffici qualche imprecazione e non so più quanta birra e quanto vino, e Michele, ambasciatore del Grana Padano e del Culatello.

Je n'oublie pas la sagesse de *maman* Betty, point de repère des doctorants motoristes à IFPEN, Elias l'expert *zeperfs*, ni le humour génial de mes chimistes préférés : Mickaël, Karl & Tiphaine (bien plus qu'un plus un, tu mérites une place ici), ni le maître des geeks : Benji le grimpeur marseillais.

Un peu plus loin : les folles rigolades avec Sophie, les remarques tranchantes de Damien. And Jan, funny and discreet, who had to cope with the two crazy Italians for more than one year.

Merci à Nicolas I. de m'avoir appris le français qui compte, tous les mots et les expressions qu'on ne trouve pas dans le Robert. J'évite de les citer ici.

Contents

Remerciements iii

Contents iv

List of Symbols vii

1 Introduction 1
- 1.1 Context . . . 1
- 1.2 Gasoline Direct Injection . . . 4
- 1.3 The role of system simulation in Internal Combustion Engine development . . . 5
- 1.4 Plan of the Manuscript . . . 6

2 Direct Injection Spark-Ignition Engines 7
- 2.1 Direct injection and spray . . . 7
  - 2.1.1 Atomization . . . 7
  - 2.1.2 Evaporation of fuel drops . . . 10
  - 2.1.3 Spray gaseous penetration and air entrainement . . . 15
  - 2.1.4 Liquid length . . . 16
- 2.2 Combustion . . . 19
  - 2.2.1 Basic Concepts . . . 19
  - 2.2.2 Stratified combustion . . . 20

3 Numerical tools for ICE Combustion Process Analysis and Understanding 30
- 3.1 Computational Fluid Dynamics (CFD) . . . 30
  - 3.1.1 The governing equations of reactive flows . . . 30
  - 3.1.2 Approaches to turbulence . . . 31
  - 3.1.3 Description of multiphase flows . . . 35
  - 3.1.4 Description of chemical kinetics . . . 35
  - 3.1.5 CFD codes . . . 36
- 3.2 System simulation . . . 36
  - 3.2.1 Commercial system simulation platforms . . . 37
- 3.3 Overview of 0D/1D predictive models of ICE combustion chambers in literature 38
  - 3.3.1 Spark-ignition engine models . . . 38
  - 3.3.2 Diesel engine models . . . 41

4 Model development 43
- 4.1 The base model: CFM1D . . . 43
  - 4.1.1 The CFM approach . . . 43
  - 4.1.2 Turbulence model . . . 45
  - 4.1.3 Burning rate . . . 46

4.1.4 Balance equations for the gas zones . . . 49
4.2 Overview of the new developments . . . 51
4.3 Three-zone thermodynamic model . . . 52
4.3.1 Balance equations for the primary gas zones . . . 54
4.4 Liquid Phase Description . . . 58
4.4.1 Coupling atomization and evaporation models . . . 58
4.4.2 Atomization model . . . 63
4.4.3 Evaporation and liquid/gas interaction model . . . 65
4.5 Gas phase description . . . 69
4.5.1 Tip penetration and spreading rate . . . 69
4.5.2 Air entrainment . . . 70
4.6 Mixture formation and stratification . . . 71
4.7 Stratified combustion . . . 79
4.7.1 Flame front reaction . . . 79
4.7.2 Interaction of the flame front with the class mechanism . . . 81
4.8 Summary of the model equations . . . 83
4.8.1 3-zone thermodynamic model . . . 83
4.8.2 Liquid Phase . . . 83
4.8.3 Gas Phase . . . 84
4.8.4 Small-scale mixing: Y_F PDF . . . 84
4.8.5 Combustion . . . 85

5 Validation of the Spray Model 87
5.1 Constant-volume vessel: the MAGIE experiment . . . 87
5.1.1 Test case . . . 87
5.1.2 Experimental data . . . 88
5.1.3 3D numerical simulations . . . 91
5.1.4 0D numerical simulations . . . 94
5.1.5 PDF convergence and computational cost . . . 109
5.2 Constant-volume vessel with tumble flow . . . 112
5.2.1 3D numerical simulations . . . 112
5.2.2 0D numerical simulations and validation . . . 114
5.3 Variable-volume vessel . . . 123
5.3.1 3D numerical simulations . . . 124
5.3.2 0D numerical simulations and validation . . . 124
5.4 Conclusion . . . 131

6 Validation of the Complete Combustion Model: the ICAMDAC Engine 132
6.1 Description of the test case . . . 132
6.2 Mixture formation in different operating conditions . . . 133
6.2.1 3D numerical simulations . . . 133
6.2.2 0D numerical simulations . . . 135
6.3 Combustion and emissions on the whole operating map . . . 153
6.3.1 Computation time . . . 160

Conclusions and Perspectives 162

A SAE Paper 2015-24-2471: Development of a Quasi-Dimensional Spray Evaporation and Mixture Formation Model for Direct-Injection Spark-Ignition Engines 164

B THIESEL 2018: Development and Validation of a Quasi-Dimensional Spray Model for DI-SI engines **178**

C Résumé du manuscrit (en français) **183**
C.1 Introduction . . . 183
C.2 Description du modèle . . . 183
C.2.1 Modélisation de la phase liquide . . . 183
C.2.2 Modélisation de la phase gas . . . 184
C.2.3 Modélisation de la combustion . . . 185
C.3 Validation et résultats . . . 186
C.3.1 Bombe à volume constant . . . 186
C.3.2 Bombe à volume variable . . . 187
C.3.3 Moteur entraîné . . . 187
C.4 Conclusion et Perspectives . . . 188

Bibliography **189**

List of Symbols

Physical dimensions

L	length
T	time
M	mass
Θ	temperature

Dimensionless quantities

Y_F	fuel mass concentration
Re	Reynolds number
Nu	Nusselt number
Le	Lewis number
Pr	Prandtl number
Sc	Schmidt number
Ξ	flame wrinkling
P	probability

Dimensional quantities

ρ	density
c_p	constant pressure specific heat
c_v	constant volume specific heat
λ	thermal conductivity
S_L	laminar flame speed
$\mathcal{A}_T$	turbulent flame surface
$\mathcal{A}_M$	mean flame surface
K	mean kinetic energy
k	turbulent kinetic energy
$\mathcal{M}$	mass
$\mathcal{P}$	momentum
$\mathcal{H}$	enthalpy
$\mathcal{Q}$	heat
$\mathcal{S}$	surface
V	volume
T	temperature
D	diameter

Subscripts and superscripts

g	gas
l	liquid
F	fuel
rc	reactive charge
fg	fresh gas
bg	burned gas
ag	ambient gas
ent	entrainment
ev	evaporation
ff	flame front
po	post-oxidation
pdf	propability density function

Chapter 1

Introduction

This chapter presents a brief introduction of the Direct-Injection Spark-Ignition (DI-SI) concept in the framework of the current European regulations on emissions.

1.1 Context

Major objectives of today's automotive industry are the reduction of pollutant emissions and the increase of the overall powertrain efficiency of new vehicles.

These objectives follow regulation constrains that fix increasingly strict limits on tailpipe emissions of pollutants and greenhouse gases. In particular, fuel economy is required to make vehicle use more affordable and to comply with regulations on CO_2 emission.

Internal Combustion Engine emissions

Considering the complete combustion reaction of iso-octane, as an example, it can be observed that carbon dioxide, CO_2, and water, H_2O, are the main products:

$$C_8H_{18} + 12.5\,O_2 \longrightarrow 8\,CO_2 + 9\,H_2O \tag{1.1}$$

Though for a generic hydrocarbon, C_xH_y, the proportions between CO_2 and H_2O may change, their production depends only on the composition and quantity of the considered hydrocarbon.

In real engines, different phenomena affect combustion, complicating the ideal case presented by Eq. (1.1) and leading to the production of pollutant species:

$$\begin{aligned} C_8H_{18} + 12.5\,O_2 \longrightarrow\ & N_{CO2}CO_2 + N_{H2O}H_2O + N_{CO}CO + N_{O2}O_2 + \\ & + N_{NOx}NO_x + N_{H2}H_2 + N_{HC}C_mH_nO_n + N_{soot}\text{soot} \end{aligned} \tag{1.2}$$

The formation of these species is due to several mechanisms such as, for example:

- the lack of oxygen due to incomplete mixing or globally rich conditions leads to the production of carbon monoxide, CO, and unburned hydrocarbon, $C_mH_nO_n$;
- the high temperature inside the combustion chamber can promote the oxidation of nitrogen, N_2, into NO_x;
- local flame extinctions in the combustion chamber and, especially, in the crevices leaves some of the fuel unburned, that is found in the exhaust gas in the form of a variety of $C_mH_nO_n$ molecules summarized with the generic denomination of HC;

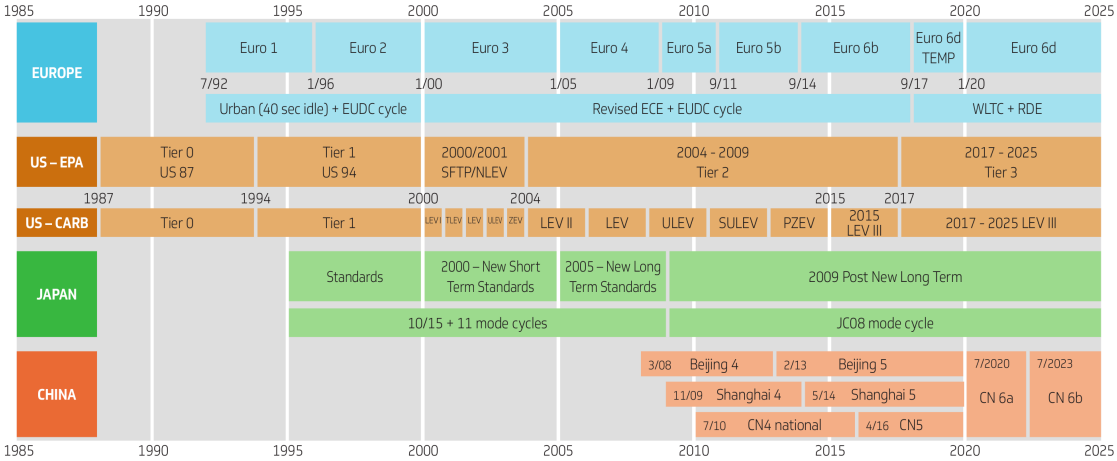

Figure 1.1: Timeline of the emission standards for passenger cars. Image from Delphi Technologies (2018).

- the presence of rich pockets due to direct injections generates soot.

Important differences exist between these compounds (CO, NO_x, HC and soot) and CO_2:

quantity: pollutants are generally produced in small quantities ($< 1000\,\text{ppm}$) while CO_2 is one of the main products of hydrocarbon combustion ($> 10\,\%$)[1];

health and environment effects: pollutants are poisonous substances that directly affect human (and animal) health (Kampa and Castanas, 2008), especially in big cities where concentrations are high; CO_2, on the other hand, presents no direct health risk but it is a greenhouse gas held responsible of climate change on a global scale (Le Treut et al., 2007);

methods of reduction: while improvements in combustion and aftertreatment systems can considerably reduce pollutant emissions, the only way to cut down CO_2 production is to reduce fuel consumption or burning fuels that contain less C.

Governments throughout the world are issuing increasingly restrictive standards on pollutant and CO_2 since almost two decades. As shown in Fig. 1.1, regulations in the USA start in 1988 while the first EU standard appeared in 1993.

CO_2 emission standards are rapidly evolving and the Euro6d standard targets $95\,\text{g/km}$ by 2020 (Delphi Technologies, 2018).

New Concepts

The need to reduce consumption and pollutant emissions leads to:

- the development and improvement **aftertreatment systems** such as Three-Way Catalysts (TWC), Gasoline Particle Filters (GPF), Selective Catalytic Reduction (SCR), to reduce pollutant concentration in the exhaust gas;

[1] considering approximately $3.7\,\text{mole}$ of N_2 per mol of O_2, Eq. (1.1) leads to the following composition of the exhaust gas resulting from burning a mol of C_8H_{18}:

$$46\,N_2 + 8\,CO_2 + 9\,H_2O$$

which corresponds approximately to $13\,\%$ of CO_2 (molar concentration).

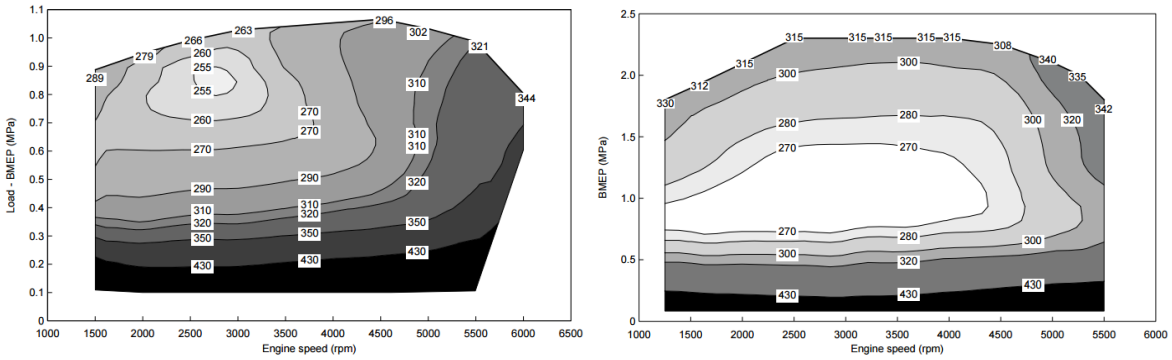

(a) Naturally aspirated engine. **(b)** Turbocharged downsized engine.

Figure 1.2: Example of spark ignition engine fuel consumption (BSFC) maps: Downsizing allows to extend the optimal BSFC zone. Image from Leduc et al. (2003).

- the conception of **innovative powertrain solutions** that pollute less at the source.

Concerning fuel economy and CO_2 emissions, a particular drawback of Spark Ignition (SI) engines is the poor efficiency at partial load due to throttling. As such engines are required to burn close stoichiometric ratio, power modulation implies a simultaneous reduction of fuel and air flow in order to conserve the optimal ratio between the two. A throttle is used to control the air flow towards the cylinders, causing significant pressure losses that affect the overall efficiency at partial load.

Figure 1.2:(a) shows a typical fuel consumption map of a naturally aspirated gasoline engine. The values of the Brake Specific Fuel Consumption (BSFC), defined as the fuel mass burned to obtain the unit brake energy and measured in g/kWh, are shown on a 2D map, as a function of the engine speed and load.

Engine load, expressed in terms of the Break Mean Effective Pressure (BMEP), is defined as:

$$\mathrm{BMEP[bar]} = \frac{P[\mathrm{kW}]\ n_R}{6\ V_d[\mathrm{l}]\ N[\mathrm{rpm}]} \tag{1.3}$$

with P the brake power, N the crank speed, $V_d[\mathrm{l}]$ the engine displacement, and n_R the number of revolutions per engine cycle ($n_R = 2$ for four stroke engines). The brake torque, M, is related to the BMEP by the following relation:

$$M[\mathrm{Nm}] = \frac{10\ \mathrm{BMEP[bar]}\ V_d[\mathrm{l}]}{2\pi\ n_R} \tag{1.4}$$

The BSFC shown in Figure 1.2:(a) presents a minimum at $2500-3000$ rpm and $0.8-0.9$ bar BMEP. Efficiency drops at lower loads or higher speeds as a result of throttling an friction, respectively.

Since passenger car engines are dimensioned to satisfy a required peak output power – only needed in particular situations like accelerations – they end up operating most of the time at part load, where efficiency is lower.

One of the possible strategies to reduce fuel consumption in SI engine is to make them work at higher loads, closer to the optimal operating conditions. Powertrain hybridization and downsizing are two ways to achieve this goal.

Hybridization. Hybrid vehicles combine a conventional ICE (SI or Diesel) to an electric machine and a battery. This solution allows to dissociate the torque and speed requested by the driver from the ICE operating conditions.

This allows to implement control strategies that maximize the ICE fuel economy by making it work closer to the minimum BSFC zone in Fig. 1.2:(a). When the driver requires a lower power, depending on the State Of Charge (SOC) of the batteries, the control chooses between:

- turning off the ICE and switching to a full electrical traction, thus discharging the batteries;
- using the ICE at full load and sending the excess power to the electrical machine working as a generator thus recharging the batteries.

Furthermore, having an electrical machine coupled to the transmission allows a certain degree of regenerative braking: part of the kinetic energy lost by the vehicle during deceleration is converted into electric energy and stored in the battery for later use.

Downsizing and turbocharging. The fact that naturally aspirated engines present an efficiency optimum at high load (Fig. 1.2:(a)) and that they are mostly used at part load motivate downsizing, which consists of a reduction of the engine size. Using an engine with a smaller displacement, V_d, for the same application ensures that it will operate more often close to the minimum BSFC, in Fig. 1.2:(a).

The power reduction caused by the smaller displacement is compensated with the addition of a turbocharger.

In the resulting downsized engine, throttling is used for power control up to mid load, while mid to full load regulation is achieved with turbocharger actuation. Its minimum BSFC zone is both wider and centred at part load, as shown in Fig. 1.2:(b).

As an example, the EB Puretech from PSA Peugeot Citroën – a 1.2 L, 96 kW turbocharged engine – presents a fuel economy of about 17% with respect to a naturally aspirated 1.6 L engine from the same manufacturer (Souhaite and Mokhtari, 2014).

1.2 Gasoline Direct Injection

Direct Injection in Spark-Ignition (DI-SI) engines appears as early as 1916 in a Junkers Airplane two-stroke engine. An injection system for automotive application was first designed by Bosch in 1952, with a mechanically driven injection pump. Appearance on the automotive market dates back to 1955 with the launch of Mercedes-Benz 300SL, that used direct fuel injection.

Gasoline Direct Injection (GDI) consists of injecting the liquid fuel directly in the combustion chamber. Injection timing varies depending on engine operation:

- in *homogeneous* charge engines, injection takes place during the intake stroke or at the beginning of compression, so that the charge has enough time to mix;
- in *stratified* charge engines, fuel is injected during the end of the compression stroke, so that the mixture is kept confined in a portion of the chamber: shape of the piston, tumble and swirl flows all help containing the charge.

GDI offers many advantages with respect to traditional homogeneous charge spark ignition engines. In particular in highly stratified DI-SI engines, the fact that the charge is confined in a portion of the combustion chamber leads to:

- moderately rich mixtures near the spark plug, reducing the risk of misfire and producing higher flame speeds;

- lean mixtures far from the spark plug which lowers the risk of knock, thus allowing higher compression ratios;
- decreased pumping losses since power regulation can be achieved acting on the injected fuel mass instead of throttling the intake air flow;
- lower thermal losses since an air layer separates the flame from cylinder walls.

The advantages of stratified direct injection promoted the spread of this technology on the automotive market during the last two decades with introduction of stratified engines by the major constructors such as Volkswagen FSI, Renault IDE or Toyota D4.

Downsizing makes the engine work at higher Indicated Mean Effective Pressures (IMEP) with an increase in the global efficiency. Adopting direct injection in such engines allows to

- benefit from the latent heat of vaporization to cool the fresh gases and increase the volumetric efficiency of the engine;
- reduce the residence time of the reactive mixture at high temperature and pressure before ignition, with consequent benefits on the knock limit and the possibility of achieving higher compression ratios.

Furthermore, as fuel is injected after Exhaust Valve Closing (EVC) valve overlap can be prolonged thus producing a better scavenging. This leads to an internal cooling of the combustion chamber with, once more, benefits on the knock limit (Turner et al., 2014).

GDI challenges simulation with the description of new phenomena with respect to traditional spark-ignition engines. Injecting liquid fuel in the combustion chamber introduces the necessity to evaluate the occurrence of unwanted phenomena such as cylinder wall or piston wetting or incomplete evaporation during flame propagation since both cause soot production.

1.3 The role of system simulation in Internal Combustion Engine development

Internal Combustion Engines (ICE) are very complex systems including a large number of components and their operation involves many branches of physics.

System simulation responds to different needs of the engineering process spanning a wide range of time and space scales, such as:

- investigation of engine performances and of the interaction with other complex system such as vehicle and environment;
- testing for different possible architectures to optimize the choice of components;
- development, testing and optimization of control strategies;
- evaluation of the effects of engine calibration on combustion performance.

The evolution of experimental techniques together with the progress of CFD modelling in the last decades improved the knowledge and understanding of physic phenomena taking place in combustion chambers as well as in other engine components. All this provides the expertise necessary to the development and validation of phenomenological models of components for system simulation, which is increasingly replacing test bench in most applications due to the short time needed to run a simulation and the reduced cost to perform tests of exploitation, integrating as much physics as possible in order to get accurate numerical predictions of the real system.

1.4 Plan of the Manuscript

The objective of this work is to develop a phenomenological 0D combustion model for system simulation of DI-SI engines and to evaluate its predictions. The thesis is organized as follows.

- Chapter 2 presents a literature review of the main physical phenomena that characterize DI-SI engine operation and of the corresponding relevant modelling approaches presented in the past. The developments realized in this PhD work focus on these phenomena.
- Chapter 3 presents an overview of the numerical tools available to study ICE, focusing on 3D RANS CFD, used to provide reference data in this work, and 0D/1D models like the one developed during this PhD.
- Chapter 4 details the new 0D model developed during this PhD, focusing on the description of the main phenomena accounted for that characterize direct injection, i.e. atomization, evaporation, fuel/air mixing and stratified mixture description.
- Chapter 5 presents the validation cases studied throughout the development of the 0D model. Three cases were retained to focus on free spray development in constant and variable thermodynamic conditions and on the interaction between spray and aerodynamics.
- Chapter 6 presents the validation of the model in a real engine configuration.

Chapter 2

Direct Injection Spark-Ignition Engines

This chapter presents a literature review on the physical phenomena described above, that characterize DI-SI engine operation.

In DI-SI engines, gasoline is injected directly in the combustion chamber. In particular, the injector introduces a liquid stream into the cylinder, that subsequently interacts both thermally and mechanically with the in-cylinder gas.

Turbulence and shear forces between the liquid and gas break the continuity of the liquid fuel stream, generating large drops that subsequently break into smaller ones: these phenomena are known as primary and secondary break-up, respectively.

The liquid drops that form as a result of break-up, are then heated by the surrounding gas and evaporate.

The injected fuel creates therefore a jet of air and fuel vapor, loaded with liquid drops, known as spray, that spreads in the cylinder. Injection provides the initial kinetic energy to ensure break-up and mixing between fuel and air.

Depending on the level of atomization, drop velocity and in-cylinder aerodynamics, the resulting charge will be more or less uniform when it is ignited: at this point, the spark plug generates a flame kernel that subsequently propagates in the mixture. Flame propagation is affected by the thermodynamic conditions of the mixture, as by its global and local composition and by turbulence.

Section 2.1 describes the elementary phenomena that lead to the preparation of a stratified reactive charge through direct injection. Possible approaches to the description of the generation of a disperse liquid phase through atomization, its evaporation and mixing with air are detailed.

Section 2.2 presents a basic description of laminar and turbulent combustion and focuses on flames propagating mixtures with composition gradients, followed by a literature review of both experimental and numerical studies of such flames.

2.1 Direct injection and spray

2.1.1 Atomization

Atomization is the process that breaks the liquid jet flowing out of the injector nozzle into small drops and ligaments. Two different phases can be identified (Lefebvre, 1989):

- in **primary atomization** the continuity of the jet is first broken into drops of different sizes;

- some of these drops are too big to be stable from a fluid dynamic point of view and undergo further breakups, **secondary atomization**, until their diameter is small enough to ensure stability in the gas flow.

The atomized spray injected into the combustion chamber is a collection of fuel drops of different sizes. The Sauter Mean Diameter, SMD, defined as (Sauter, 1926; Lefebvre, 1989):

$$\mathrm{SMD} = \frac{\sum_{i=1}^{N} D_i^3}{\sum_{i=1}^{N} D_i^2} \tag{2.1}$$

with D_i the diameter of the i-th drop and N the drop number is often used as a macroscopic parameter to classify the drop size distribution. It represents the diameter of a single drop having the same volume-to-surface ratio of the whole spray.

Other definitions of a distribution representative mean diameter can be obtained generalizing the exponents in Eq. (2.1) with a and b as follows (Lefebvre, 1989):

$$D_{ab} = \left(\frac{\sum_{i=1}^{N} D_i^a}{\sum_{i=1}^{N} D_i^b} \right)^{\frac{1}{a-b}} \tag{2.2}$$

With this notation the SMD can be expressed as D_{32}.

Possible approaches to atomization range from simple empirical correlations providing an average diameter (SMD) to more complex models that differentiate the two phases mentioned above:

- primary atomization is accounted for providing an initial drop size which can be related to the parameters of the nozzle flow (Khan et al., 2012);
- secondary atomization can be detailed in a phenomenological model that takes into account the drop size, density and surface tension and the relative velocity between the two phases to predict further breakup of the original drop (Khan et al., 2012; Lefebvre, 1989).

Modelling secondary atomization explicitly has the advantage of providing a realistic drop size distribution: the large number of drops injected in the computational domain will find themselves in different conditions in terms of gas and liquid velocity, pressure and temperature so that secondary break-up will affect each one differently.

Models for secondary atomization are often adopted in 3D simulations, where the important variations in the flow characteristics near the injector nozzle are resolved and can be used to provide a realistic size distribution.

In 0D simulations, on the other hand, this level of information is not available. It is therefore preferred to determine the average diameter with an empirical correlation and use an analytical expression to describe the final size distribution, thus describing the two break-up phases with a single model. Several suitable distributions are available in literature.

The Rosin-Rammler distribution – originally developed for solid disperse phase (Lefebvre, 1989) – is widely used in 3D calculations to provide the initial conditions for the Lagrangian liquid phase. The analytical definition expresses – as a function of the drop diameter D – the ratio of the volume of liquid particles having a diameter lower than D to the total liquid volume:

$$\frac{V(D)}{V_{\mathrm{tot}}} = 1 - e^{\left(\frac{D}{D_{\mathrm{ref}}}\right)^q} \tag{2.3}$$

where D_{ref} and q define the mean and deviation of the distribution (Fig. 2.1). The former is related to the SMD and is computed as follows

$$D_{\mathrm{ref}} = \Gamma\left(1 - \frac{1}{q}\right) \mathrm{SMD} \tag{2.4}$$

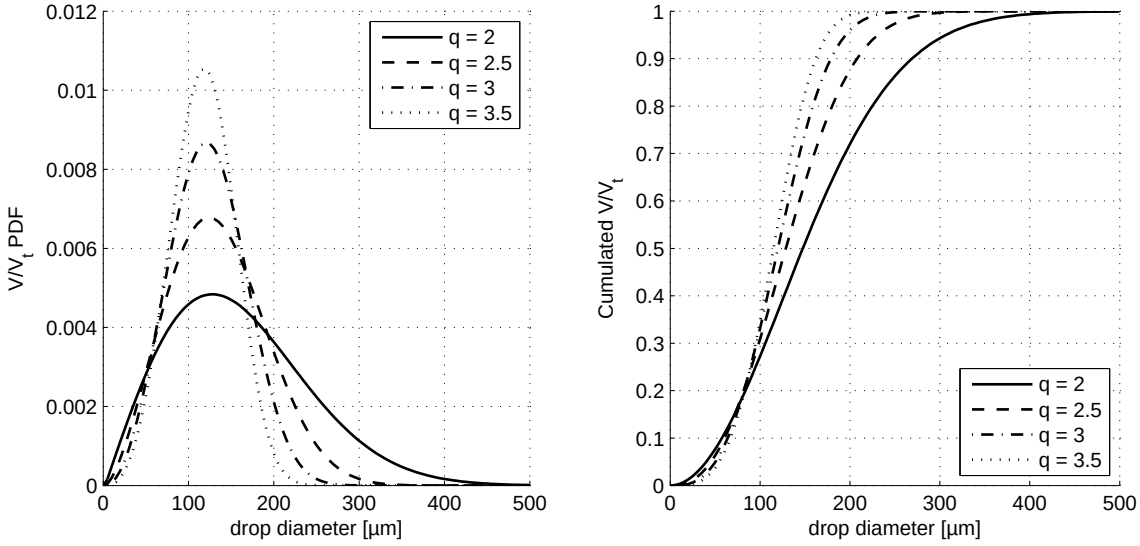

(a) Volume probability density $\frac{d}{dD}\left(\frac{V(D)}{V_{tot}}\right)$. **(b)** Cumulative volume $\frac{V(D)}{V_{tot}}$.

Figure 2.1: Rosin-Rammler distribution for SMD $= 100\,\mu m$ and different values of the exponent q.

where Γ denotes the Gamma function.

For computational reasons it is not feasible to follow the evolution of every single drop in describing evaporation. The use of a reference drop, of averaged diameter, is preferred for 0D applications since it provides sufficient detail at an affordable computational cost.

A complete characterization of the distribution, like the one given by Eq. 2.4, is therefore not necessary: an empirical correlation can be used to provide a single value for the initial drop size. Several of these correlations for the drop size are available in the literature, most of which are derived from phenomenological considerations and fitted on experimental data in engine operating conditions. A detailed review of these correlations is given by Dos Santos and Le Moyne (2011); Stiesch (2003); Steimle et al. (2013). Some of the most widely used are recalled here.

An empirical correlation for SMD after drop breakup process has been presented by Elkotb (1982)

$$\mathrm{SMD} = 6156\,10^{-6}\,\nu_l^{0.385}\,\rho_l^{0.737}\,\rho_g^{0.06}\,\Delta p^{-0.54} \quad [\mu m] \tag{2.5}$$

The validity of Eq. (2.5) is supported by experimental data on kerosene, gasoline, Diesel fuel (DF) and light Diesel fuel (LDF) (Elkotb, 1982). The symbols at the rhs are

- Δp [bar], pressure drop across the injector nozzle;
- ρ $\left[\mathrm{kg/m^3}\right]$, density of fuel ($\rho_l$) and chamber gas ($\rho_g$);
- ν_l $\left[\mathrm{m^2/s}\right]$, liquid fuel kinematic viscosity.

Varde et al. (1984) provided a correlation for the ratio of the SMD to the injector hole diameter, D_{noz}:

$$\frac{\mathrm{SMD}}{D_{\mathrm{noz}}} = 8.7\,\left(Re\,We\right)^{-0.28} \tag{2.6}$$

where the Reynolds and Weber numbers are calculated on the liquid fuel and nozzle properties

$$Re = \frac{u_{\mathrm{inj}}\,D_{\mathrm{noz}}}{\nu_l} \qquad We = \frac{\rho_g\,u_{\mathrm{inj}}^2\,D_{\mathrm{noz}}}{\sigma_l} \tag{2.7}$$

with u_{inj} the injection velocity and σ_l the fuel surface tension. Eq. (2.6) has the advantage of taking into account the injector hole diameter, D_{noz}, and liquid fuel surface tension. The pressure drop across the injector hole does not appear explicitly in Eq. (2.6) but it is directly related to the injection velocity once the orifice geometry and fuel characteristics are fixed.

Hiroyasu et al. (1989) performed a dimensionless analysis and fitting of experimental observations of sprays obtained using Rayleigh scattering. Two different cases were studied depending on whether the injection velocity is high enough to fully atomize the spray (complete spray) or not (incomplete spray). Different fluids were used in order to investigate the effect of viscosity and surface tension on atomization. The analysis leaded to the two following correlations valid for complete and incomplete sprays respectively

$$\begin{aligned} \frac{\text{SMD}}{D_{\text{noz}}} &= 0.14\, Re^{0.25}\, We^{-0.32} \left(\frac{\mu_l}{\mu_g}\right)^{0.37} \left(\frac{\rho_l}{\rho_g}\right)^{0.17} \\ \frac{\text{SMD}}{D_{\text{noz}}} &= 4.12\, Re^{0.12}\, We^{-0.75} \left(\frac{\mu_l}{\mu_g}\right)^{0.54} \left(\frac{\rho_l}{\rho_g}\right)^{0.18} \end{aligned} \tag{2.8}$$

where μ_l and μ_g represent the dynamic viscosity, $\mu = \rho\nu$, of the liquid fuel and ambient gas, respectively. The breakup model proposed by Hiroyasu et al. (1989) consists in taking the maximum of the two values obtained with Eq. (2.8).

2.1.2 Evaporation of fuel drops

The liquid fuel delivered into the combustion chamber through the injector and atomized into small drops has to evaporate in order to be mixed with the surrounding air and burn. A detailed study of the evaporation process is therefore essential to predict the behavior of the combustion process: different phenomena such as the mixing with air and the formation of liquid films on chamber walls are strongly dependent on the evaporation rate.

A liquid drop injected into the combustion chamber exchanges both heat and mass with the surrounding gas. The following non-dimensional parameters that are widely used in the literature to characterize heat and mass transfer phenomena in the gas phase surrounding liquid drops:

the Nusselt number is the ratio of the convective heat transfer to the conductive heat transfer. It is defined as:

$$Nu = \frac{hL}{\lambda} \tag{2.9}$$

where h is the convective heat transfer coefficient ($MT^{-3}\Theta^{-1}$), L is a characteristic length and λ is the thermal conductivity ($LMT^{-3}\Theta^{-1}$);

the Sherwood number expresses the ratio of the convective mass transfer coefficient to the diffusive mass transfer coefficient. It is defined as:

$$Sh = \frac{KL}{\mathcal{D}} \tag{2.10}$$

where K is the mass transfer coefficient (LT^{-1}), L is a characteristic length and $\mathcal{D}$ is the mass diffusivity (L^2T^{-1}). It is often regarded as the equivalent of Nu for mass transfer;

the Lewis number is the ratio of the thermal diffusivity to the mass diffusivity:

$$Le = \frac{\lambda}{\rho c_p \mathcal{D}} \tag{2.11}$$

where ρ and c_p are the density (ML^{-3}) and the constant pressure specific heat ($L^2T^{-2}\Theta^{-1}$);

the Prandtl number is the ratio of the thermal diffusion rate to the viscous diffusion rate:

$$Pr = \frac{\rho c_p \nu}{\lambda} \tag{2.12}$$

with ν being the kinematic viscosity (L^2T^{-1});

the Schmidt number is the ratio of the viscous diffusion rate to the molecular diffusion rate, expressed as:

$$Sc = \frac{\nu}{\mathcal{D}} \tag{2.13}$$

Equations (2.11 – 2.13) imply therefore:

$$Le\, Pr = Sc \tag{2.14}$$

Steady state evaporation

The evaporation of a monocomponent fuel drop under steady conditions is discussed in this section. The temperature is assumed to be uniform within the drop and constant in time[1], and the surrounding gas is at rest. Under these assumptions the heat flux from the surrounding gas towards the liquid/gas interface of the drop is completely absorbed as latent heat of the evaporating mass.

A differential equation for the fuel mass fraction, Y_F, field around an evaporating spherical drop can be derived based on the species conservation equation (Poinsot and Veynante, 2011):

$$\frac{\partial \rho_g Y_F}{\partial t} + \frac{\partial}{\partial x_i}\left[\rho_g \left(u_i + V_F\right)\right] = 0 \tag{2.15}$$

where:

- the diffusion velocity, V_F, of fuel in air is substituted with the expression given by the Fick law (Poinsot and Veynante, 2011):

$$V_F\, Y_F = -\mathcal{D}\, \nabla Y_F \tag{2.16}$$

with $\mathcal{D}$ the mass diffusivity of fuel in air;

- ρ_g is the density of the gas mixture which includes the fuel vapour.

Eq. (2.15) is then integrated on a control volume consisting of a sphere concentric with the drop of generic radius r, which leads to the differential equation (Lefebvre, 1989; Abarham and Wichman, 2011)

$$\frac{dY_F}{1 - Y_F} = \frac{1}{\rho_g \mathcal{D}} \frac{\dot{\mathcal{M}}_F}{4\pi} \frac{dr}{r} \tag{2.17}$$

where $\dot{\mathcal{M}}_F$ is the mass flow rate of fuel through the surface of the control volume which – under steady-state conditions – is independent of r and equals the evaporation rate $\dot{\mathcal{M}}_{ev}$ (Lefebvre, 1989; Abarham and Wichman, 2011).

Eq. (2.17) is then integrated between the drop surface and a r_∞ where the gas temperature and fuel mass fraction, respectively T_∞ and $Y_{F\infty}$, are not affected by the evaporating drop, yielding to the following expression for the evaporation rate (Spalding, 1953):

$$\dot{\mathcal{M}}_{\text{ev}} = 2\pi D \frac{\lambda_g}{c_{p\,g}} \log\left(1 + B_M\right) \tag{2.18}$$

[1] Its value being the saturation temperature that corresponds to the fuel vapour partial pressure at liquid/gas interface.

with D the drop diameter. The fuel vapour is supposed to be saturated at the drop surface, i.e. the fuel mass fraction $Y_{F\,s}$ and the Spalding (1953) mass transfer number, B_M,

$$B_M = \frac{Y_{F\,s} - Y_{F\,\infty}}{1 - Y_{F\,s}} \tag{2.19}$$

are a function of the drop temperature only. Lefebvre (1989) recommends that the mean thermal conductivity λ_g and constant-pressure specific heat $c_{p\,g}$ of the gas phase are evaluated using the reference conditions given by the *one third rule*:

$$T_r = \frac{2\,T_s + T_\infty}{3} \qquad Y_r = \frac{2\,Y_F^s + Y_F^\infty}{3} \tag{2.20}$$

with T_s and Y_F^s, respectively, the temperature and fuel mass fraction on the drop surface.

Under steady-state condition the state variables of the liquid and gas phases do not vary in time. In particular the temperatures and fuel mass fractions are constant so that the only variables in Eq. (2.18) are the drop diameter D and the evaporation rate which are related by mass conservation:

$$\dot{\mathcal{M}}_{ev} = -\dot{\mathcal{M}}_d = -\frac{\pi}{3}\rho_l\, D^2\, \dot{D} \tag{2.21}$$

with $\mathcal{M}_d$ the drop mass and ρ_l the density of the liquid phase. The D^2-law (Lefebvre, 1989; Law, 1982):

$$D_0^2 - D^2 = \tau_{\mathrm{ev}} t \tag{2.22}$$

with D_0 the initial drop diameter, is derived combining Eq. (2.18) and Eq. (2.21). The evaporation constant τ_{ev} is given by:

$$\tau_{ev} = \frac{8}{\rho_l}\frac{\lambda_g}{c_{p\,g}} \log\left(1 + B_M\right) \tag{2.23}$$

(Spalding, 1953; Lefebvre, 1989).

With similar considerations, another expression for the evaporation rate can be derived based on the conservation of total enthalpy:

$$\dot{\mathcal{M}}_d = 2\pi D\, \frac{\lambda_g}{c_{p\,g}} \log\left(1 + B_T\right) \tag{2.24}$$

where the Spalding (1953) heat transfer number, B_T, is defined as:

$$B_T = \frac{c_{p\,g}\left(T_\infty - T_s\right)}{H_L} \tag{2.25}$$

with H_L the specific latent heat of the liquid fuel. The equality between Eq. (2.18) and Eq. (2.24) implies that the two transfer number must be equal under steady-state conditions. The solution of the equation

$$\frac{Y_{F\,s} - Y_{F\,\infty}}{1 - Y_{F\,s}} = \frac{c_{p\,g}\left(T_\infty - T_s\right)}{H_L} \tag{2.26}$$

can be used to calculate the temperature at the drop surface T_s. The hypothesis that the gaseous mixture at the drop surface is saturated with fuel vapour provides an $Y_{F\,s} = f\left(T_s\right)$ relation[2] so that T_s is the only unknown quantity in Eq. (2.26).

[2]The partial pressure of fuel can be deduced from the saturation curve once the temperature T_s is known. For a perfect gas the ratio of the partial pressures equals the ratio of the mole numbers which provides the mass ratio once the molar weights are known.

Transient evaporation

The heat up period is the phase in which a droplet is evaporating under unsteady conditions, meaning that its temperature varies with time. In this regime the equality between the heat flow from the gas to the drop and the latent heat absorbed by the evaporating mass is not valid anymore since a portion, $\dot{\mathcal{H}}_d$, of the heat flux, $\dot{\mathcal{Q}}$, coming from the gas phase:

$$\dot{\mathcal{Q}} = -\frac{\dot{\mathcal{M}}_d \, c_{p\,g} \, (T_\infty - T_s)}{B_M} \tag{2.27}$$

penetrates into the liquid phase and increases its enthalpy, $\mathcal{H}_d$, (Lefebvre, 1989; Law, 1982):

$$\dot{\mathcal{H}}_d - H_L \dot{\mathcal{M}}_d = \dot{\mathcal{Q}} \tag{2.28}$$

accordingly:

$$B_T \neq B_M \tag{2.29}$$

as long as $\dot{\mathcal{H}}_d \neq 0$.

The evaporation rate is still given by Eq. (2.18) (Lefebvre, 1989) but the Spalding transfer numbers need to be calculated explicitly from the drop surface temperature which evolves since the liquid phase receives the heat flux:

$$\dot{\mathcal{H}}_d = -\dot{\mathcal{M}}_d \, H_L \left(\frac{B_T}{B_M} - 1 \right) \tag{2.30}$$

In order to express this evolution an assumption must be made regarding the temperature field within the liquid drop. For a uniform temperature distribution, $T = \text{const.}$, it holds:

$$c_{p\,l} \mathcal{M}_d \frac{dT}{dt} = \dot{\mathcal{H}}_d \tag{2.31}$$

with $c_{p\,l}$ the constant pressure specific heat of the liquid phase.

Figure 2.2 shows the evolution square diameter, D^2, of an isolated iso-octane drop in a quiescent gas. The initial drop temperature is $T^0_{\text{drop}} = 50\,^\circ\text{C}$ and the gas is at 2 bar and variable temperature, T_{gas}. The square diameter decreases linearly in time when the gas temperature equals the drop temperature. For higher gas temperatures, the linear segment appears after an initial heat-up phase, characterized by an increasingly negative slope and therefore an increasing evaporation rate.

Transient evaporation with forced convection

The model proposed by Abramzon and Sirignano (1989) is a generalization of the one presented above and it reproduces the evaporation of a single drop of liquid injected in a gas with a non null velocity field. Forced convection is therefore taken into account for the evaluation of the heat and mass transfer; since the droplet moves into the quiescent gas, a relative velocity between the two phases is present.

Spalding mass and heat transfer numbers are here defined as:

$$B_M = \frac{Y_{F\,s} - Y_{F\,\infty}}{1 - Y_{F\,s}} \qquad B_T = \frac{c_{p\,l} \, (T_\infty - T_d)}{H_L - \dot{\mathcal{Q}}/\dot{\mathcal{M}}_d} \tag{2.32}$$

The authors use the Frossling correlations to evaluate the Nusselt, Eq. (2.9), and Sherwood, Eq. (2.13), numbers in the non-evaporating case:

$$\begin{aligned} Nu_0 &= 2 + 0.552 \, Re^{1/2} \, Pr^{1/3} \\ Sh_0 &= 2 + 0.552 \, Re^{1/2} \, Sc^{1/3} \end{aligned} \tag{2.33}$$

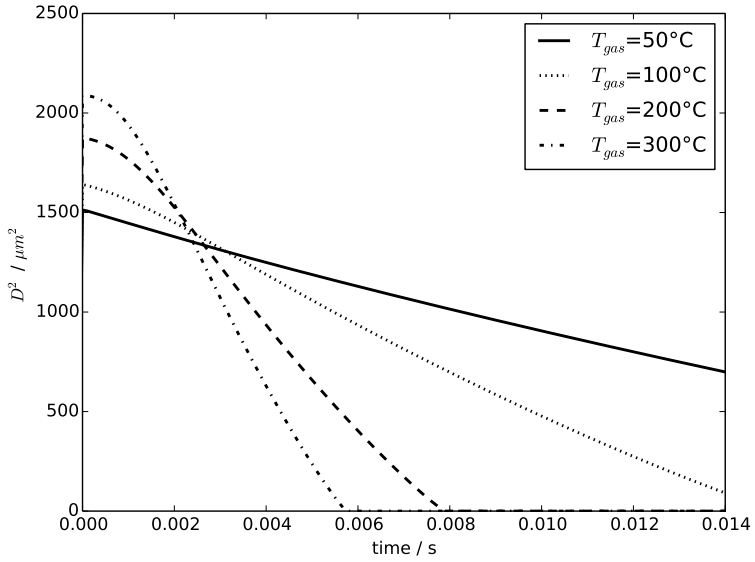

Figure 2.2: Transient evaporation of an isolated iso-octane drop in a quiescent gas at 2 bar for different values of the gas temperature, T_{gas}. The initial liquid temperature is 50 °C. The drop square diameter, D^2, is linear with time when $T_{\text{gas}} = 50\,°\text{C}$. At higher gas temperatures the initial heat-up phase generates the slope variation in D^2.

as a function of the Prandtl, Eq. (2.12), and Schmidt, Eq. (2.13), numbers. These are then corrected with Spalding (1953) transfer numbers using the function:

$$f(B) = (B+1)^{0.7}\,\frac{\log(B)}{B} \tag{2.34}$$

as follows:

$$Nu = 2 + \frac{Nu_0 - 2}{f(B_T)} \qquad Sh = 2 + \frac{Sh_0 - 2}{f(B_M)} \tag{2.35}$$

to account for the transfer phenomena due to evaporation. The Reynolds number is here defined for the gas flow around the droplet:

$$Re = \frac{(u_g - u_d)\,D}{\nu_g} \tag{2.36}$$

with $(u_g - u_d)$ being the relative velocity between the gas and the drop, D the drop diameter and ν_g the kinematic viscosity of the gas. Without forced convection Nu and Sh are both equal to 2 and the evaporation rate ;

$$\dot{\mathcal{M}}_d = -\pi\,D\,\frac{\lambda_g}{c_{p\,g}}\,\frac{Sh}{Le}\,\log(1+B_M) \tag{2.37}$$

falls back to the value given by Eq. (2.18) for the non convective case.

The evolution of drop mass and enthalpy (or temperature) is described by differential equations that integrate evaporation rate and heat flux. For a given temperature the mass transfer number is known since the fuel mass fraction in the far field, $Y_{F\infty}$, is an external condition and its saturation value at the drop surface, Y_{Fs}, is related to the drop surface temperature through the saturation pressure. The heat transfer number, B_T is calculated

solving the system:

$$\begin{aligned} 1 + B_T &= (1 + B_M)^{\phi} \\ \phi &= \frac{c_{p\,g}}{c_{p\,l}} \frac{Sh}{Nu\,Le} \\ Nu &= 2 + \frac{Nu_0 - 2}{f\,(B_T)} \end{aligned} \tag{2.38}$$

iteratively. The drop enthalpy $\mathcal{H}_d$ varies according to:

$$\dot{\mathcal{H}}_d = \dot{\mathcal{M}}_d \left[\frac{c_{p\,l}\ (T_\infty - T_d)}{B_T} - H_L \right] \tag{2.39}$$

and can be calculated once the required accuracy on B_T is attained.

2.1.3 Spray gaseous penetration and air entrainement

The correlation for spray tip penetration derived by Naber and Siebers (1996) is widely used in Diesel injection calculation. The experimental data used to develop and validate correlations are extracted from Schlieren imaging in a constant volume combustion vessel with variable:

- cell gas density;
- fuel type;
- injection pressure;
- fuel temperature;

over a wide range of conditions, representative of Diesel operation.

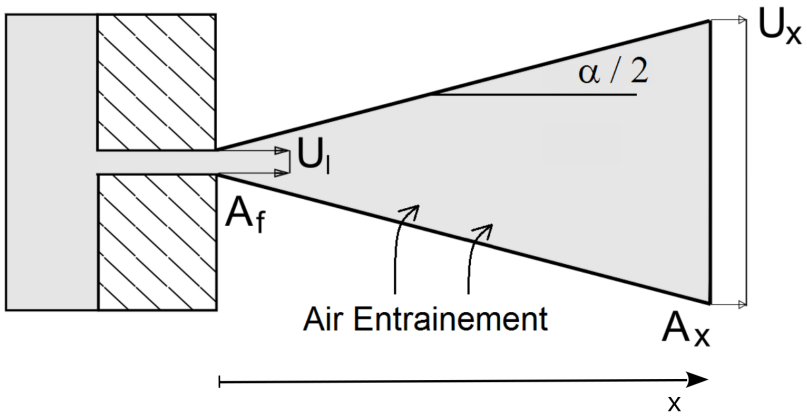

Figure 2.3: Schematic representation of the spray model developed by Naber and Siebers (1996).

The evolution of the modelled spray (Fig. 2.3) is described in terms of the non-dimensional tip penetration and time after Start of Injection (SOI), respectively:

$$\tilde{x} = \frac{x}{x^+} \qquad \tilde{t} = \frac{t}{t^+} \tag{2.40}$$

where the two quantities are normalized with respect to the characteristic length and time scales:

$$x^+ = \frac{D_l \sqrt{\frac{\rho_l}{\rho_g}}}{\tan \frac{\alpha}{2}} \qquad t^+ = \frac{x^+}{u_l} = \frac{D_l \sqrt{\frac{\rho_l}{\rho_g}}}{\tan \frac{\alpha}{2}\, u_l} \tag{2.41}$$

where u_l and D_l are – respectively – the effective velocity and diameter of the injected liquid fuel stream and α is the spreading angle (Fig. 2.3). The following expression gives a correlation between the non-dimensional spray penetration, $\tilde{x}$, and time, $\tilde{t}$:

$$\tilde{t} = \frac{\tilde{x}}{2} + \frac{\tilde{x}}{4}\sqrt{1+16\tilde{x}^2} + \frac{1}{16}\log\left(4\tilde{x} + \sqrt{1+16\tilde{x}^2}\right) \tag{2.42}$$

It was derived for non-vaporizing sprays using mass and momentum conservation and assuming that the model spray has a conical shape, Fig. 2.3, i.e. that the spreading rate is constant.

A delicate point of this model is the determination of the spreading rate α of the model spray, since it is crucial for the correct computation of spray penetration and air entrainment. The authors used experimental values obtained from Schlieren images of injections in a constant-volume vessel and defined the measured spray angle ϑ as:

$$\tan\vartheta = \frac{\mathcal{A}_s(x/2)}{(x/2)^2} \tag{2.43}$$

where x is the spray tip penetration. The area $\mathcal{A}_s(x/2)$ is that of the projected surface of the upstream half of the spray on a plane containing the injection axis, for a given tip penetration x. The value of the measured spray angle, ϑ, is in principle a function of x: it presents a negative slope at the beginning of injection and converges to a stable value ϑ when the spray is fully developed.

Supposing a linear dependance of the model angle α on the measured angle ϑ:

$$\tan\alpha = a\,\tan\vartheta \tag{2.44}$$

the authors recommend a value of 0.66 for the tuning parameter a.

While Naber and Siebers (1996) used experimental values for the spreading angle ϑ measured from Schlieren images, Siebers (1999) provided the following correlation between ϑ and the test operating conditions:

$$\tan\frac{\vartheta}{2} = c\left[\left(\frac{\rho_g}{\rho_l}\right)^{0.19} - 0.0043\sqrt{\frac{\rho_l}{\rho_g}}\right] \tag{2.45}$$

with c a calibration parameter, for which the author suggests the value 0.26 for Diesel sprays, to express the measured angle as a function of fuel and gas densities. Equation (2.45) combines the behaviors described by Naber and Siebers (1996) – who observed a linear dependecy of the spray angle with $(\rho_l/\rho_g)^{0.19}$ at high values of the density ratio – and by Reitz and Bracco (1979) – who observed a linear dependecy of the spray angle with $(\rho_l/\rho_g)^{0.5}$ for low values of the density ratio.

2.1.4 Liquid length

Liquid fuel requires energy to evaporate in subcritical conditions due to the absorption of latent heat. Equation (2.28) expresses the energy balance of an evaporating drop under unsteady conditions, showing that, unless heat is provided by the surrounding gas phase, the liquid drop will necessarily cool down during evaporation increasing the latent heat required to evaporate more mass. Furthermore, fuel vapour saturation around the liquid phase limits the evaporation rate.

Air entrainment plays therefore an essential role in evaporation, as it provides heat[3] to the evaporating liquid and mass to dilute the fuel vapor at the liquid-gas interface.

[3] In most of engine applications, in-cylinder gas has a higher temperature than the injected liquid fuel.

Looking at the spray as a whole, two main phenomena take a part in the above-mentioned heat and mass transfer, one being the *turbulent mixing* of the two phases, and the other being the *diffusive* transfer at the *inter-phase* (Siebers, 1998). Depending on which of the two phenomena is slower, the evaporation rate can be either:

mixing controlled, when the entrained air mass flow limits the evaporation rate by fixing the amount of turbulent kinetic energy, heat and mass entrained in the spray, or

local inter-phase transport controlled, when diffusion at the liquid/gas interface limits the heat and mass transfer.

This distinction is very useful in phenomenological modelling as it points out which phenomena have to be reproduced in order to get an accurate prediction of the evaporation rate.

Siebers (1998) shows that in Diesel operating conditions evaporation is always mixing controlled and proposes a method to predict the evaporation rate based on the concept of *liquid length*. Since the mechanism that limits the evaporation rate is air entrainment the former can be related to the latter without describing the state (size and temperature) of the liquid drops.

MIE scattering visualizations (Siebers, 1998) show that there is a maximum axial distance (the liquid length) above which no liquid phase is detected in steady state conditions.

On the assumption that evaporation is mixing-controlled the fuel drops undergo steady state evaporation so that the liquid phase temperature satisfies Eq. (2.26), that can be solved iteratively to obtain a value for the transfer number[4] B.

The scaling law proposed by Siebers (1999) for the non-dimensional liquid length $\tilde{l}$ is

$$\tilde{l} = b\sqrt{\left(\frac{2}{B}+1\right)^2+1} \tag{2.46}$$

with b a calibration parameter. The liquid length is here normalized with respect to the length scale x^+, defined in Eq. (2.40).

Higgins et al. (1999) measured the liquid length for different fuels such as:

- reference Diesel fuel;
- Fischer-Trop Diesel;
- Biodiesel;

– used in Diesel engines – and:

- standard, non-oxygenated, gasoline (Fig. 2.4:a);
- reformulated, oxygenated, gasoline (Fig. 2.4:b);
- methanol;
- a 85% methanol–15% gasoline blend;

[4]No distinction between B_T and B_M is made here since the two have the same value in steady-state conditions.

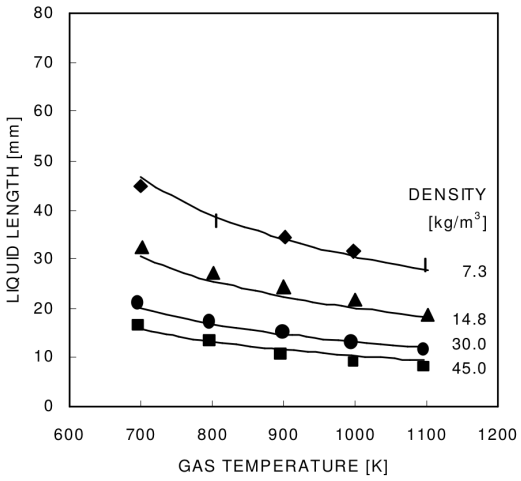

(a) Standard non-oxygenated gasoline, injected fuel initial temperature 138 °C.

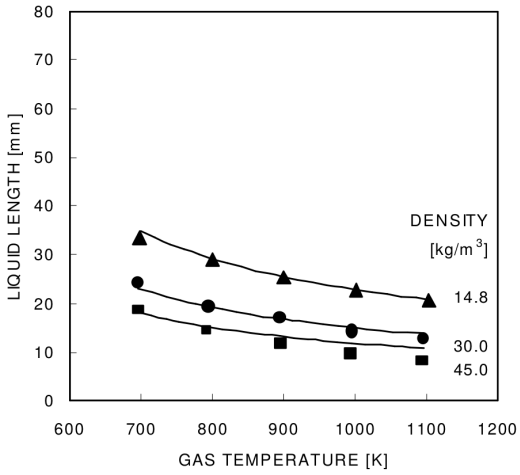

(b) Reformulated oxygenated gasoline, injected fuel initial temperature 94 °C

Figure 2.4: Liquid length against cylinder gas temperature for different gas densities: predictions given by Eq.(2.47) (solid lines) are compared to measurements (markers). (a): standard gasoline. (b): oxygenated gasoline. Figures from Higgins et al. (1999).

– typical of spark-ignition engines– in variable gas thermodynamic conditions. The following empirical relation, proposed and tested by Higgins et al. (1999), expresses the liquid length l normalized against the nozzle diameter D_{noz}:

$$\frac{l}{D_{\text{noz}}} = k \left(\frac{\rho_l}{\rho_a}\right)^{\alpha} \left(\frac{1}{B_T}\right)^{\beta} \tag{2.47}$$

with $k = 10.5$, $\alpha = 0.58$ and $\beta = 0.59$ three modelling constants, B_T the Spalding heat transfer number defined by Eq. (2.32). Predictions given by Eq. (2.47) are compared to measurements in Fig. 2.4.

Applicability in DI-SI conditions

Experimental observations on different Diesel fuels and thermodynamic conditions (Siebers, 1998, 1999) show that the dependence of the liquid length on liquid fuel temperature (Fig. 2.5) becomes more important for gas temperatures lower than $850 - 900\,K$. The same trend is observed concerning the dependence of the liquid length on the orifice pressure drop.

The validity of Eq. (2.47) is well established at high temperatures (standard deviation 6% for $800\,\text{K} < T < 1000\,\text{K}$), showing that the concept of liquid length is well adapted to describe the evaporation of gasoline as well as Diesel fuel, but only at high temperatures. Homogeneous GDI sprays, generally injected during the intake stroke, evaporate at much lower temperatures and densities.

This suggests that the hypothesis of mixing-controlled evaporation is not well sustained for gasoline direct injection applications because of the different operating conditions of such engines with respect to compression-ignition engines. Accordingly, it was chosen to adopt a local inter-phase transport controlled approach, like the ones detailed in Section 2.1.2, rather than an approach based on the liquid length, in this work.

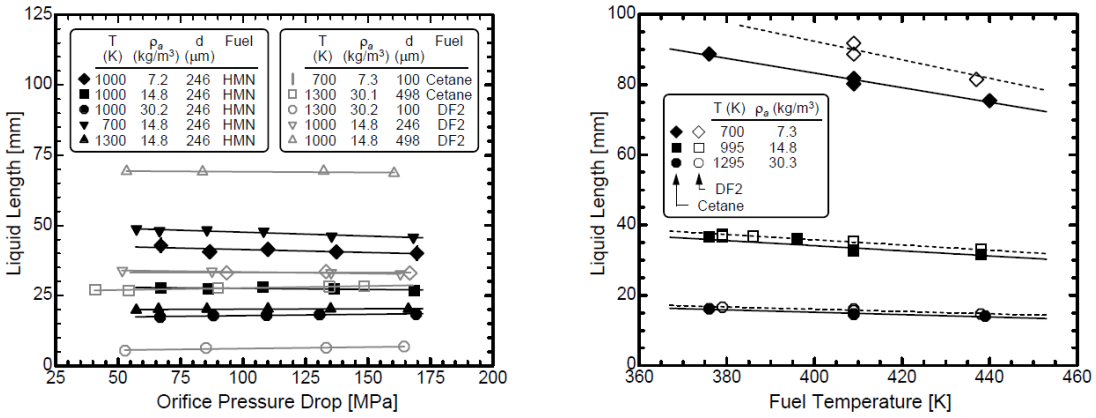

Figure 2.5: Liquid length against orifice pressure drop (left) and injected fuel temperature (right), at different ambient gas temperatures and densities (from Siebers (1998)). Small variations of the liquid length against these two parameters characterizes mixing-controlled evaporation.

2.2 Combustion

2.2.1 Basic Concepts

Combustion is a high-temperature exothermic chemical reaction involving a fuel (usually a hydrocarbon) and an oxidizer (usually oxygen). The complete reaction between a generic oxygenated hydrocarbon, $C_xH_yO_z$, and singlet oxygen, O_2, is:

$$C_xH_yO_z + \left(x + \frac{y}{4} - \frac{z}{2}\right) O_2 \longrightarrow x\,CO_2 + \frac{y}{2}\,H_2O \tag{2.48}$$

The exact mass of air needed to burn a unit mass of fuel completely according to Eq. (2.48) is called *theoretical air* (or stoichiometric air) and can be expressed as:

$$\mathrm{AFR}_{\mathrm{st}} = \left(\frac{\mathcal{M}_{\mathrm{Air}}}{\mathcal{M}_F}\right)^{\mathrm{st}} = \frac{M_{O_2} + 3,76 M_{N_2}}{M_{C_xH_yO_z}} \left(x + \frac{y}{4} - \frac{z}{2}\right) \tag{2.49}$$

with respect to the stoichiometric coefficients in Eq. (2.48) and the molar masses of oxygen, nitrogen and fuel (M_{O_2}, M_{N_2} and $M_{C_xH_yO_z}$). The actual air-to-fuel ratio of a mixture:

$$\mathrm{AFR} = \frac{\mathcal{M}_{\mathrm{Air}}}{\mathcal{M}_F} \tag{2.50}$$

can be greater, equal or lower than $\mathrm{AFR}_{\mathrm{st}}$ and the mixture is called *lean*, *stoichiometric* or *rich*.

The equivalence ratio, ϕ defined as:

$$\phi = \frac{\mathrm{AFR}_{\mathrm{st}}}{\mathrm{AFR}} \tag{2.51}$$

characterizes a homogeneous mixture with respect to its composition: values in the $[0, 1[$ interval indicate a lean mixture, those in the $]1, \infty[$ interval a rich one and $\phi = 1$ a stoichiometric mixture.

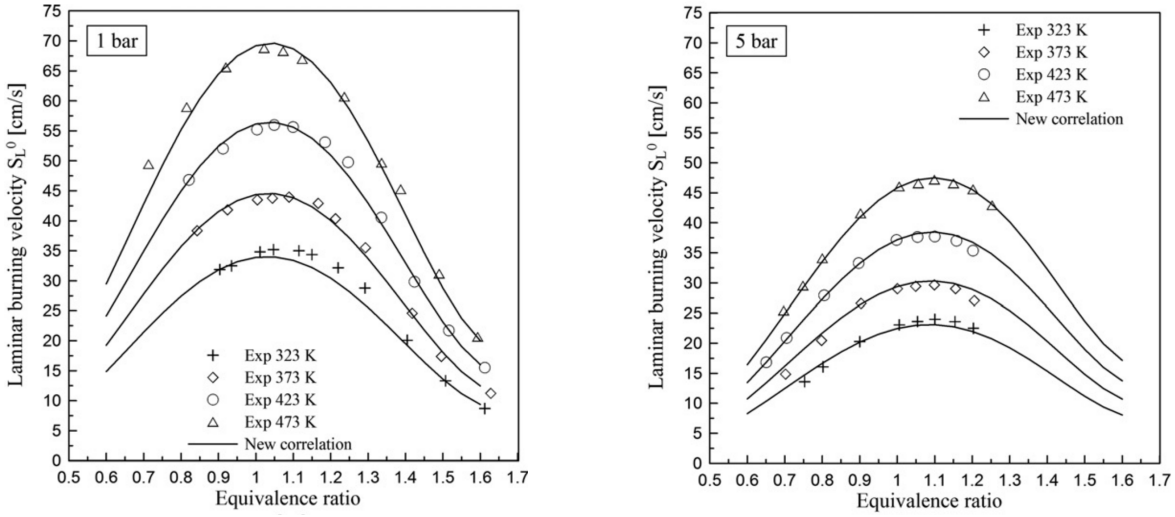

Figure 2.6: Experimental values of laminar flame speed, s_L, against equivalence ratio ϕ for iso-octane/air mixtures in different thermodynamic conditions. The results show that s_L has a maximum for slightly rich mixtures ($1,05 < \phi < 1,10$), increases with fresh gas temperature and decreases with pressure. Figures from Galmiche et al. (2012).

Laminar premixed flames. Laminar premixed flames are a basic problem in the study of combustion. The one dimensional configuration of a planar flame front propagating in a premixed gas is of special interest since laminar flames are viewed as the elementary building blocks of flamelet-based turbulent flame models (Poinsot and Veynante, 2011): the Coherent Flame Model (CFM) used in this work is an exemple.

The laminar flame speed s_L can be defined as the displacement speed of a planar flame front with respect to the fresh gases in a homogeneous mixture. Its values depend on the chemical composition and thermodynamic conditions of the mixture. Figure 2.6 shows experimental measurements of s_L for iso-octane/air mixtures as a function of the equivalence ratio and for different thermodynamic conditions.

Laminar diffusion flames In diffusion flames fuel and oxydizer meet at the flame front. There is no notion of propagation speed with diffusive flame, since the flame front is stabilized where the two streams interact and the burning rate is controlled by mixing, for sufficiently fast chemical reactions.

Stratified and partially premixed flames Between the two previous ideal cases are stratified and partially premixed flames, where fuel and oxydizer mix before burning but the charge is not homogeneous. Depending on the intensity of equivalence ratio fluctuations, flame propagation can be followed by a second – mixing controlled – stage where diffusion flames appear behind the main flame-front. Staged combustion is observed, for example, in Diesel engines.

2.2.2 Stratified combustion

Flame propagation in partially premixed charge

The presence of local heterogeneities in the fuel/air mixture affect several global characteristics of a combustion system and need therefore to be taken into account in a 0D model.

The local charge composition can be characterized by the mixture fraction Z, defined as:

$$Z = \frac{\nu Y_F - Y_{O_2} + Y_{O_2,2}}{\nu Y_{F,1} + Y_{O_2,2}} \tag{2.52}$$

where ν is the stochiometric oxigen-to-fuel mass ratio:

$$\nu = \left(\frac{\mathcal{M}_{O_2}}{\mathcal{M}_F}\right)_{st} \tag{2.53}$$

Y_F and Y_{O_2} are the mass concentrations of fuel and oxygen respectively and the numerical indexes – where indicated – indicate concentractions in the fuel (1) and air (2) streams before mixing. Assuming unity Lewis numbers and a simple chemistry, the so defined mixture fraction is not affected by chemical processes Poinsot and Veynante (2011) and can be used to characterize mixing in the fresh as well as in the burned gas. In particular, for a pure fuel stream mixing with air the fresh gas satisfies $Z = Y_F$.

The equivalence ratio ϕ, commonly used to characterize the mean engine charge, is defined as the fuel-to-air mass ratio normalized by its value for a stochiometric mixture. Its local value, in a non-uniform mixture is given by:

$$\phi = \nu \frac{Y_F}{Y_{O_2}} \tag{2.54}$$

and is only defined in the unburned mixture, where it can be related to the mixture fraction as:

$$\phi = \frac{Z}{1-Z}\frac{1-Z_{st}}{Z_{st}} \tag{2.55}$$

with Z_{st} the value of the mixture fraction in stoichiometric conditions.

Equivalence ratio fluctuations have an impact on the global heat release rate since they affect the turbulent flame propagation speed with two competing mechanisms:

- the reduced reaction rate in non-stoichiometric conditions slows flame propagation down;
- flame surface production due to a non-uniform propagation speed enhances the overall reaction rate.

The laminar flame speed s_L of a reactive mixture varies as a function of the equivalent ratio ϕ as well as the thermodynamic conditions: it has a maximum value for slightly rich mixtures, around $\phi \approx 1.1$ (Fig. 2.6). Since the $s_L(\phi)$ relation is strongly non-linear the average s_L of a non-homogeneous mixture is not – in general – equal to the s_L of a homogeneous mixture with the same mean composition. This effect is particularly strong for globally stoichiometric mixtures since the laminar flame speed is maximum in the homogeneous case and decreases when averaging with richer or leaner regions (Fig. 2.7). Globally-lean mixtures might show – on the other hand – no change in the s_L between the non homogeneous and non homogeneous case with a symmetrical mixture distribution or even an enhanced burning rate with a asymmetrical distribution involving rich pockets (Jiménez et al., 2002).

The second effect can be explained by referring to a planar laminar flame front advancing in a mixture with a uniform transverse equivalence ratio gradient, as shown in Fig. 2.8. The existence of a flame speed gradient ∇s_L on the flame surface causes different portions of the flame surface to advance with different velocities with consequent deformation of the flame front. The three flame fronts represented in Fig. 2.8 all have approximately the same burning rate per unit flame surface since they span the same equivalence ratio range. The global heat release is therefore expected to grow with time because of the increased flame surface.

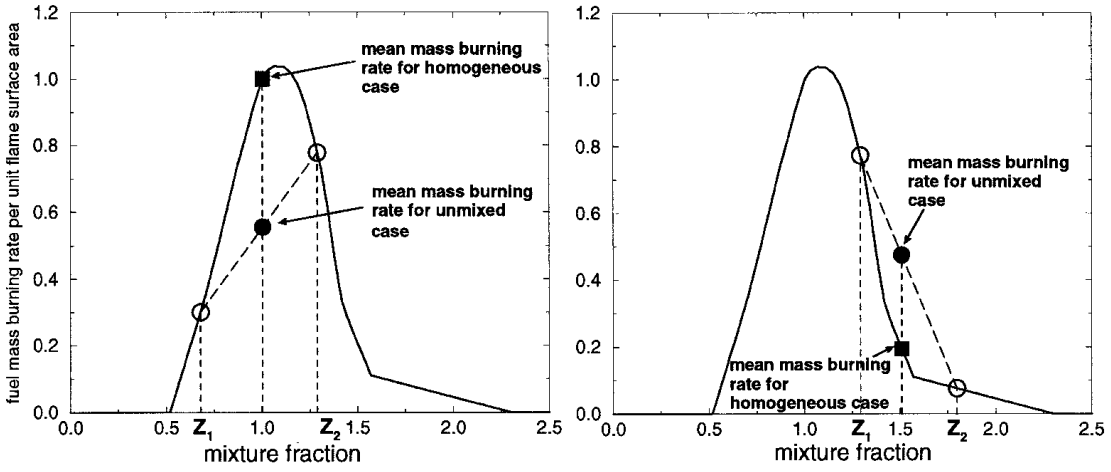

Figure 2.7: Plots of the laminar fuel mass burning rate $\dot{\mathcal{M}}_f = \rho Y_f \mathcal{S} s_L$ against the mixture fraction Z. Differences in laminar flame speed do not average out because of the non linearity of the $s_L(Z)$ relation: the mean burning rate of a stratified mixture can therefore differ from that of an iso-$\tilde{Z}$ homogeneous mixture. Figure from Hélie and Trouvé (2000).

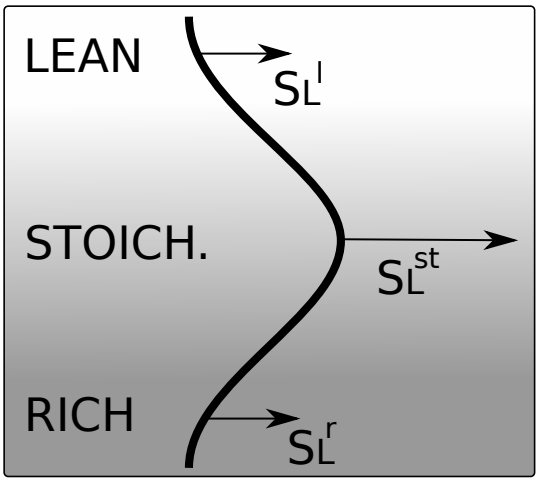

Figure 2.8: Laminar flame front stretch induced by a transverse mixture fraction gradient, from lean to rich: the propagation speed s_L is not uniform on the flame front. The difference in s_L wrinkles the front producing flame surface.

Literature review of partially premixed flames

This section discusses some of the numerical and experimental studies on partially premixed combustion published in the last two decades. The aim is to provide a satisfactory understanding of the significant phenomena outlined in the previous paragraphs and quantify them, in order to guide the modelling effort carried out in this work.

Poinsot et al. (1996) performed DNS of laminar and turbulent flame propagation in globally lean stratified mixtures.

2D laminar flames propagation in a globally lean mixture with sinusoidal equivalence ratio (period l_Z ranging between $2-6$ times the laminar flame thickness in stoichiometric conditions δ_L^0) show an increase in the global reaction rate due to the flame surface production mechanism. The authors define a Karlovitz number induced by partial premixing as:

$$Ka^{PP} = \frac{\delta_L^0/s_L}{l_Z/\Delta w} \tag{2.56}$$

with Δw the amplitude of the s_L variations across the mixture. Its values are small in all cases investigated ($Ka^{PP} < 0.2$), which suggests that the surface production effect will be negligible in highly turbulent flows (Poinsot et al., 1996).

3D turbulent flames propagating in a globally lean ($\bar{\phi} = 0.8$) are also investigated. The initial velocity and mixture fraction field length scales (l_t and l_Z) are both equal to $2\delta_L^0$. Two cases with different flow velocity scales $u'/S_L = 2.5$ and $u'/S_L = 7.5$ are discussed, both presenting strong local variations of the burning rate that tend to average out. The flame surface production from stratification is found to be small with respect to turbulent wrinkling (Poinsot et al., 1996).

Hélie and Trouvé (1998) present a numerical study of the influence of small-scale stratification on turbulent flame propagation. A DNS of a globally-stoichiometric partially premixed flame was performed. The flame was embedded in a three-dimensional domain with homogeneous isotropic decaying turbulence, with a large flow velocity scale ($u'/S_L = 7.5$).

The flame surface production due to partial premixing is found to be negligible with respect to turbulent wrinkling. On the other hand, stratification causes a reduction of the reaction rate per unit flame surface since the local composition is not stoichiometric. This leads to an overall reduction of the burning rate of globally-stoichiometric charge, as opposed to the observations of Poinsot et al. (1996) for globally-lean flames.

The authors also proposed a modelling approach to take into account mixture inhomogeneity effects in a modified Coherent Flame Model, CFM-Z (Hélie and Trouvé, 2000; Hélie et al., 2001). Combustion is here described as a staged process consisting of:

a primary stage where a premixed flame propagates through the mixture producing burned gas that contain excess reactants;

a secondary stage where the excess reactants burn in a mixing-controlled mode described by the local concentrations and turbulent time scale k/ε, where k its the specific turbulent kinetic energy (L^2T^{-2}) and ε its dissipation rate (L^2T^{-3}).

Large scale (resolved) variations of the equivalence ratio are accounted for through the introduction of a transport equation for the mixture fraction Z, while the small-scale effects are

modelled with a presumed β-PDF.[5] The local s_L rate is therefore obtained with an average over the β-pdf:

$$s_L(\mathbf{x},t) = \int_0^1 s_L(Z)\beta(Z;\mathbf{x},t)\,dZ \tag{2.57}$$

The same approach to the description of mixture inhomogeneities was adopted by Colin et al. (2003) in the development of the extended CFM model (*ECFM*) which adapts the original CFM approach to mixtures with multicomponent fuels and equivalence ratio fluctuations. The latter are described by a presumed truncated Gaussian PDF, with transport equations for mixture fraction mean, variance and scalar dissipation (Colin and Benkenida, 2003).

Haworth et al. (2000) compared the results of 2D DNS of globally stoichiometric turbulent ($u'/s_L = 4.67$) propane flames propagating in both homogeneous and stratified charge, using a detailed mechanism. In these conditions the authors drew the following conclusions for the stratified case:

- there is no leakage of the primary fuel behind the premixed heat release zone, meaning that the second stage identified by Hélie and Trouvé (1998) only involves the final oxydation of the chemical species generated by incomplete combustion in the flame front: this is a consequence of using a detailed chemical mechanism;
- the thin premixed heat release zone can be described with usual flamelet concepts;
- heat release in the secondary stage is controlled by turbulent mixing and CO kinetics;
- differences in the heat release and flame length are small (i.e. less than 10%) with respect to the homogeneus case.

Jiménez et al. (2002) presents 2D DNS simulations of a flame front propagating in globally lean ($\phi = 0.60$) propane-air mixture, with an initial turbulent field ($u'/s_L = 11.6$, representative of GDI combustion) and complex chemistry to predict NO formation (30 species, 76 reactions). The homogenous case is compared to non-homogeneous cases obtained initializing the ϕ field with a distribution along the normal to the direction of propagation. Different initial wavelengths (3mm and 0.75mm) and amplitudes ($\phi'^2 = 0.15$ symmetrical around the mean and $\phi'^2 = 0.45$ non symmetrical) were tested and the flame surface production due to stratification is always negligible except for the case with large scale and amplitude. Large scale non-symmetrical stratification is found to increase the heat release when the distribution is wider on the rich side, the mixture being globally lean.

Renou et al. (2004) performed an experimental analysis of the propagation of a spark-ignited propane/air flame with accurate control of the concentration and turbulence fields via Planar Laser-Induced Fluorescence (PLIF) and Laser Doppler Velocimetry (LDV). Test conditions include different equivalence ratio distributions, all with a small flow scale ratio ($u'/s_L = 0.6$) and with a scalar distribution lengthscale δ_ϕ smaller than the integral scale l_t ($0.5 < \delta_\phi/l_t < 0.7$).

Flame contours obtained via tomographic recordings are used to evaluate the flame front wrinkling: two characteristic radii are defined based on the surface of burned gases on the

[5] The β-PDF is identified with its Favre-average $\tilde{Z}$ and variance $\tilde{Z''^2}$ so that a transport equation for the latter is also necessary.

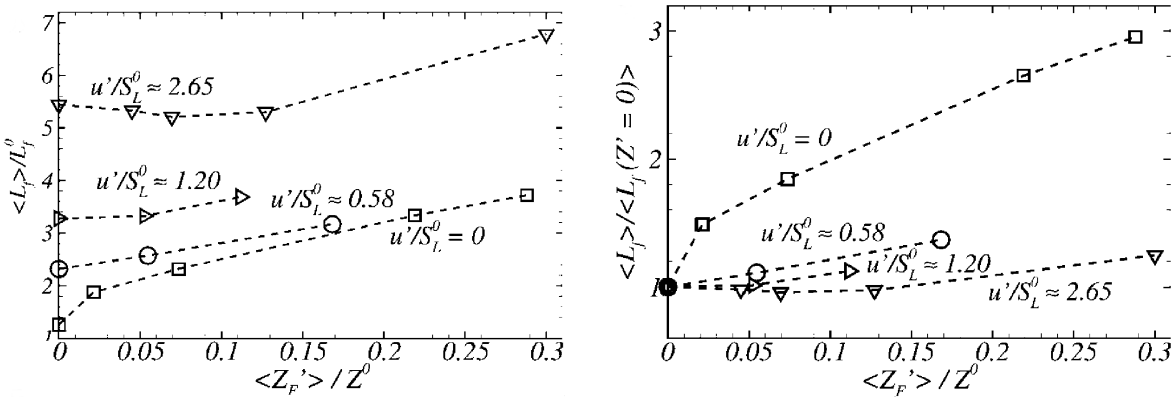

(a) Normalized by the length of the planar flame, L_f^0.

(b) Normalized by the mean flame length, $\langle L_f(Z'=0)\rangle$, of the corresponding (same u'/s_L) homogeneous case.

Figure 2.9: Variation of the mean flame length, $\langle L_f \rangle$, as a function of the mixture fraction fluctuation, $\langle Z_F' \rangle$, normalized with respect to the mean mixture fraction, Z^0. Values are plotted for different (u'/s_L). Flame surface production from stratification is noticeable in laminar flows and tends to be negligible with respect to turbulent wrinkling for high values of the u'/s_L ratio. Figure from Garrido-López and Sarkar (2005).

laser sheet, S, and its perimeter, P, leading to the following definitions:

$$r_S = (S/\pi)^{0.5} \quad r_P = P/(2\pi) \tag{2.58}$$

Results show a decrease of the wrinkling ratio r_P/r_S with stratification, showing that heterogeneities do not add large wrinkles and tend to smooth flames.

A further analysis of the mean radius of curvature of the flame front $\bar{r}$ against propagation time shows that:

- in the homogeneous case the mean radius converges to half the integral length scale $\bar{r} \to 0.5\, l_t$;
- in all the stratified cases $\bar{r}$ converges to values lower than $0.5\, l_t$.

Mixture fraction fluctuations generates therefore an additional – non negligible – small-scale wrinkling.

Garrido-López and Sarkar (2005) addressed the influence of stratification on flame length and burning rate and how it interacts with turbulence and hydrodynamic instabilities. The numerical study presents 2D DNS of a globally lean flame front interacting with imposed equivalence ratio and velocity gradients, parallel to the flame front. The characteristic length of these fluctuations are much larger that the flame thickness.

The effect of mixture fraction fluctuations is analyzed, showing that stratification:

- reduces the burning rate per unit surface of flame, with a negative effect on the global burning rate;
- contributes to flame surface production with a positive effect on the global burning rate.

Figure 2.9 shows two plots of the flame lengths obtained from 2D simulations, with different velocity and mmixture fraction gradients. The mean flame lengths, $\langle L_f \rangle$, normalized

against the length of a planar (laminar) flame, L_f^0, (panel a) and that of the corresponding (iso u'/S_L) homogeneous flame, $\langle L_f(Z'=0)\rangle$, (panel b), are plotted against the normalized mixture fraction fluctuation. The slope of the data lines representing the:

$$\frac{\langle L_f\rangle}{\langle L_f(Z'=0)\rangle} = f\left(\frac{\langle Z'\rangle}{Z^0}\right) \tag{2.59}$$

correlation tends to decrease as the u'/S_L ratio increases.

The ratio of the velocity fluctuation u' to the reference flame speed S_L can therefore be used as a criterion for assessing the relative impact of inhomogeneity and turbulence on flame wrinkling, showing that, unless:

$$\frac{u'}{s_L} < 1 \tag{2.60}$$

the flame surface production due to partial premixing is negligible with respect to the turbulent contribution. This conclusion is consistent with the observations of Hélie and Trouvé (1998) and has been confirmed in more recent DNS results as summarized in Table 2.1.

It is therefore concluded that the balance between the reduction of the burning rate per unit length and the flame surface production depends on the level of velocity fluctuations. For moderately turbulent and laminar flames, the surface production generated by inhomogeneity prevails and the global burning rate is increased with respect to a fully premixed flame in the same conditions. When the turbulent flame wrinkling is important, on the other hand, flame surface production from stratification has a negligible effect: in this case the overall burning rate decreases.

The observed flame surface production is explained by the hydrodynamic instability caused by gas thermal expansion that amplifies flame wrinkling: both velocity and composition fluctuations can trigger this effect, so that when the former is present the effect of the latter is negligible. Proof of thermal expansion instability is found by comparing DNS of standard and passive reaction simulations, the latter being performed without heat release (Garrido-López and Sarkar, 2005).

Anselmo-Filho et al. (2009) performed an experimental study of globally lean ($\bar{\phi} = 0.77$) methane/air stratified V-flames: a two-dimensional slot burner provides two parallel inlet flows of known equivalence ratios (ϕ_1 and ϕ_2) and a rod is used to stabilize the flame close to the inlet, thus burning with a large-scale mixture fraction gradient. Different inlet mixtures covering both homogeneous ($\phi_1 = \phi_2$) and stratified ($\phi_1 > \phi_2$) over a lean-lean ($\phi_1 < 1$), lean-stoichiometric ($\phi_1 = 1$) and lean-rich ($\phi_1 > 1$) range are investigated. Results show a growth of the flame surface with the stratification rate attributed to the differential rate of propagation in leaner and richer pockets.

Grout et al. (2009) investigated the behavior of a planar flame front propagating in a globally lean ($\bar{\phi} = 0.74$) mixture with low turbulence level ($u'/S_L = 0.7$) through 3D DNS in a cubic box with turbulent inflow-outflow conditions in the direction of the flow and periodic boundary conditions in the two normal directions. Results show that the increase in flame surface is around:

- 80% in the homogeneous mixture;
- 100% in the stratified mixture ($\phi = 0.4 - 1.2$);

with respect to a laminar front propagating in a homogeneous charge. As the authors point out, the effect of partial premixing on flame surface density is not negligible ($\approx 20\%$) here due to the small value of the u'/S_L ratio.

Table 2.1: Summary of DNS and experimental results on the effects of small-scale stratification on turbulent flame surface production in recent literature. Results show that when turbulence intensity is sufficiently high ($u'/s_L > 1$), flame surface production from stratification is negligible with respect to turbulent wrinkling, as pointed out by Garrido-López and Sarkar (2005).

ref.	u'/s_L	δ_l^0/δ_ϕ	Ka	Ka^{PP}	$+\Sigma$	
Poinsot et al. (1996)	2.50	0.50	2.7	0.2	✗	
	7.50	0.50	1.3	0.2	✗	
Hélie and Trouvé (1998)	7.50	0.13	1.40	0.05	✗	
	7.50	0.07	1.40	0.07	✗	
Haworth et al. (2000)	4.67	0.06	2.23	0.03	✗	
Jiménez et al. (2002)	11.60	0.10	4.00	0.23	✗	
	11.60	0.40	4.00	0.93	✗	
Renou et al. (2004)	0.36	0.0076	0.038	0.0038	✓	$\bar{r} \searrow$
	0.32	0.0079	0.034	0.0040	✓	$\bar{r} \searrow$
	0.27	0.0086	0.027	0.0043	✓	$\bar{r} \searrow$
Grout et al. (2009)	0.70	0.20	0.12	0.23	✓	(20%)

The effect of a transverse large-scale equivalence ratio gradient was also investigated in an experimental analysis of iso-octane/air turbulent V-flames with different concentration gradients (Vena et al., 2011). The experimental setup allows to isolate the effects of equivalence ratio gradients from those of local mixture fraction: the fuel stream is seeded with 3-pentatone and PLIF imaging is used to track the stoichiometric surface and define an interrogation window for the analysis of the flame surface, also tracked with PLIF with a threshold on the concentrations of OH and CH_2O. The size of this window varies so that the equivalence ratio range is the same for all cases, with different values of its gradient.

A strong effect of large-scale fuel concentration gradients on flame wrinkling is observed, leading to an enhanced corrugation of the flame front. The increase in flame surface density is, however, more modest, partly because of the increase of flame thickness.

Heat release rate measurements were also performed on the same experiment (Vena et al., 2015). The isolated effect of equivalent ratio gradient on the heat release rate of a locally stoichiometric flame (interrogation window with fixed ϕ range) are compared to the overall HRR reduction on the flame, due to the combined effects of ϕ fluctuations and turbulence. The former is found to be an order of magnitude smaller.

Summary

This analysis can be extended estimating the partial-premixing Karlowitz number, Ka^{PP}, introduced by Poinsot et al. (1996) and defined by Eq. (2.56) for the literature work considered, as:

$$Ka^{\mathrm{PP}} = \frac{\Delta S_L / S_L}{\delta_\phi / \delta_L^0} \tag{2.61}$$

with S_L the laminar flame speed of the mean mixture, ΔS_L its variation in the stratified mixture, δ_ϕ the characteristic size of mixture fraction fluctuations and δ_L^0 the laminar flame

thickness of the mean mixture.

Since the values of S_L and ΔS_L are not indicated in most of the literature works considered, the $\Delta S_L/S_L$ ratio was estimated using the polynomial correlation proposed by Galmiche et al. (2012) for iso-octane (C_8H_{18}) flames:

$$\frac{S_L(\phi)}{S_L(\phi_{S_L}^{\max})} = \sum_{i=0}^{4} A_i \phi^i \tag{2.62}$$

where $\phi_{S_L}^{\max}$ is the equivalence ratio that maximizes S_L and A_i are a set of tuning coefficients, whose values are summarized in Table 2.2.

Table 2.2: Values of the coefficients in Eq. (2.62) for iso-octane (C_8H_{18}), according to Galmiche et al. (2012).

$\phi_{S_L}^{\max}$	A_0	A_1	A_2	A_3	A_4
1.07	1.00	−0.26	−3.81	0.77	4.75

The values of the Karlowitz numbers, Ka and Ka^{PP}, are summarized in Table 2.1 and traced in Figure 2.10: red +s indicate literature works that found an increase in surface flame due to partial premixing (Renou et al., 2004; Grout et al., 2009), blue Os indicate works that found no influence of stratification on flame surface.

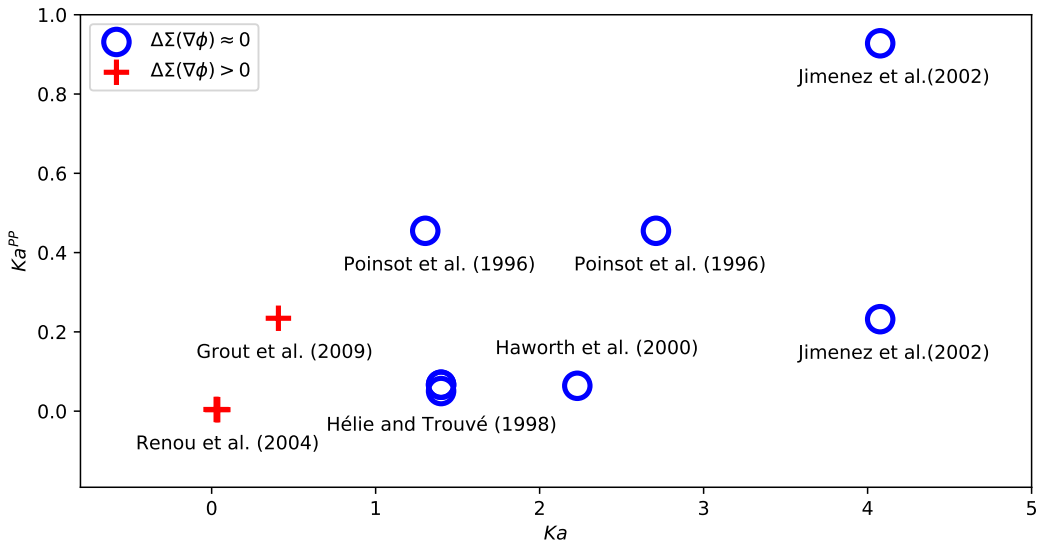

Figure 2.10: Values of Ka and Ka^{PP} in the studies summarized in Table 2.1.

An increase in surface flame due to partial premixing is observed in the works of Renou et al. (2004) and Grout et al. (2009), that study quasi-laminar flames ($Ka < 1$ and $u'/S_L < 1$). The turbulent flames ($Ka > 1$ and $u'/S_L > 1$) studied in the other works, on the other hand, show no flame surface production, regardless of Ka^{PP}.

The values of Ka^{PP} are always smaller than unity, as a consequence of the limited amplitude of S_L variations, which are always of the same order as the mean S_L or smaller.

Summarizing, literature shows that mixture stratification has the following effects on flame propagation:

- global burning rate is affected by the non linearity of the $s_L(\phi)$ relation, so that the effects of non-homogeneity of the local flame speeds do not average out: for globally stoichiometric mixtures in particular the average burning rate is reduced;
- the presence of intense turbulent wrinkling makes flame surface production by small-scale stratification – i.e. when the characteristic scale of equivalence ratio fluctuations is smaller than the integral lengthscale – negligible.

While it is necessary to take into account charge inhomogeneity in the calculation of the global burning rate, modelling an additional wrinkling source due to stratification can be avoided under the hypothesis that the characteristic length scale of charge inhomogeneities is small[6], since turbulence is always intense in an ICE combustion chamber ($u'/s_L > 1$).

Accordingly, the modelling approach proposed in this work neglects the effect of equivalence ratio fluctuations on flame wrinkling.

[6]This point is actually still open: recent LES computations show large-scale equivalence ratio gradients in downsized GDI engines with early injection (Iafrate, 2016).

Chapter 3

Numerical tools for ICE Combustion Process Analysis and Understanding

This chapter presents an overview of the numerical tools available to simulate ICE. Particular focus is given to the fundamentals of the 3D Computational Fluid Dynamics (CFD) approach, with a brief description of the governing equations and the problems associated to turbulence. 3D CFD is used in this work to provide reference data for the development and validation of the 0D model.

System simulation is also briefly introduced, providing an overview of the most important system simulation platforms. Because of the multitude of approaches available, a thorough description goes beyond the scope of this chapter. Since this work focuses on the development of a 0D system simulation model, the chosen approach is detailed in Chapter 4, together with the description of the new developments introduced.

Finally, a literature review of 0D/1D ICE combustion chamber models concludes the chapter.

3.1 Computational Fluid Dynamics (CFD)

3D models are useful to predict or reproduce the thermo-chemical behaviour of engines with great accuracy, since they solve the fluid mechanics equations in dedicated computational domains that take into account the detailed combustion chamber geometry.

This section gives a brief account of the different approaches available, underlining the main challenges associated to 3D CFD modelling.

3.1.1 The governing equations of reactive flows

Momentum and mass conservation. The second law of motion for a continuum fluid is expressed by (Kundu and Cohen, 2000):

$$\frac{\partial \rho u_i}{\partial t} + \frac{\partial \rho u_i u_j}{\partial x_j} = -\frac{\partial p}{\partial x_i} + \frac{\partial \rho \tau_{ij}}{\partial x_j} + \rho g_i \tag{3.1}$$

with ρ, u_i, p and g_i, respectively the density, velocity, pressure and body mass force fields in Eulerian coordinates, x_i. The stress tensor, τ_{ij}, is a function of the velocity gradient, $\partial u_i / \partial x_j$.

Likewise, mass conservation is expressed by (Kundu and Cohen, 2000):

$$\frac{\partial \rho}{\partial t} + \frac{\partial \rho u_i}{\partial x_i} = 0 \tag{3.2}$$

The expression of the stress tensor, τ_{ij}, called *constitutive equation*, is, in principle, specific to a material or substance:

$$\tau_{ij} = \lambda \frac{\partial u_k}{\partial x_k} \delta_{ij} + \mu \left(\frac{\partial u_i}{\partial x_j} + \frac{\partial u_j}{\partial x_i} \right) \tag{3.3}$$

with λ and μ, respectively, the bulk and dynamic viscosities and δ_{ij} the identity tensor.

Species conservation. The conservation of chemical species links the mass concentration of the generic k-th specie, Y_k, to the effects of transport by the velocity field, u_i, diffusion driven by its gradient, $\partial Y_k / \partial x_i$, and chemical reactions, $\dot{\omega}_k$:

$$\frac{\partial \rho Y_k}{\partial t} + \frac{\partial}{\partial x_i} \left[\rho \left(Y_k u_i - \mathcal{D} \frac{\partial Y_k}{\partial x_i} \right) \right] = \dot{\omega}_k \qquad \text{for } k = 1, \ldots, N_{\text{SP}} \tag{3.4}$$

with N_{SP} the number of chemical species, and $\mathcal{D}$ a diffusion coefficient, assumed equal for all species[1], under Fick's Law (Williams, 1985).

Eq. (3.4) is derived combining the generic species conservation equation (Poinsot and Veynante, 2011) with the expression for the diffusion velocity obtained from Fick's Law (Williams, 1985).

Energy conservation. The first law of thermodynamics can be written in terms of conservation of sensible enthalpy, h ($L^2 T^{-2}$), as:

$$\frac{\partial \rho h}{\partial t} + \frac{\partial \rho u_i h}{\partial x_i} = \dot{\omega}_T + \frac{\partial p}{\partial t} + u_i \frac{\partial p}{\partial x_i} + \lambda_T \frac{\partial^2 T}{\partial x_i \partial x_i} + \tau_{ij} \frac{\partial u_i}{\partial x_j} + \dot{\mathcal{Q}} \tag{3.5}$$

with $\dot{\omega}_T$ the source term due to chemical reactions, λ_T the thermal conductivity and $\dot{\mathcal{Q}}$ a source term due to radiation or other local heat sources (Poinsot and Veynante, 2011).

Challenges in reactive flow simulation

The solution of Eq.s (3.1 – 3.5) for DI-SI combustion problems implies three main challenges that have been objects of research for decades and still are nowadays. These challenges consist in providing modelling approaches for turbulence, multiphase flows and chemical kinetics.

3.1.2 Approaches to turbulence

Turbulence consists of a collection of random coherent structures that subtract energy from the mean flow and deliver it to molecular dissipation. The computational resolution achievable with actual computers does not allow to capture all the turbulent structures that participate in turbulent flame propagation in ICE: models have to be provided to account for what happens at unresolved scales.

For simplicity, the problem is described referring to the incompressible Navier-Stokes equations, obtained from Eq.s (3.1 – 3.3): (Kundu and Cohen, 2000):

$$\begin{cases} \dfrac{\partial u_i}{\partial t} + u_j \dfrac{\partial u_i}{\partial x_j} = -\dfrac{1}{\rho} \dfrac{\partial p}{\partial x_i} + g_i + \nu \dfrac{\partial^2 u_i}{\partial x_j \partial x_j} \\ \dfrac{\partial u_i}{\partial x_i} = 0 \end{cases} \tag{3.6}$$

with $\nu = \mu / \rho$ the kinematic viscosity.

[1] More accurate descriptions of species diffusion exist but their description is beyond the scope of this work.

Direct Numerical Simulation (DNS)

Direct Numerical Simulation (DNS) consists in solving the Navier-Stokes Eq.s 3.6 by meshing the computational domain with a resolution such as to allow a proper description of all the scales of motion involved: from the largest eddies, that start the energy cascade and depend strongly on the geometry of the flow, down to the dissipative eddies, whose scale is of the same order of the Kolmogorov length, η.

This technique allows to describe the behaviour of all the variables involved with such a great accuracy that its results are considered as valuable as experimental data: even more valuable considering that experiments often imply invasive techniques and rarely allow to achieve a great spatial resolution. On the other hand one might show that the computational cost of a DNS simulation makes this procedure too heavy for high Reynolds number flows of industrial interest, such as ICE combustion. Considering a grid spacing of the order of η[2]:

$$\Delta x \approx \eta \tag{3.7}$$

the number of grid points in each direction is:

$$N_x = \frac{L_x}{\Delta x} \propto \frac{L_x}{\eta} = \left(\frac{L^4 U^3}{L \nu^3} \right) = Re^{3/4} \tag{3.8}$$

with L_x the domain length and U the characteristic flow velocity. For three-dimensional simulations, this leads to:

$$N = N_x^3 \propto Re^{9/4} \tag{3.9}$$

With respect to the Kolmogorov time scale, τ_η, the number of needed time steps to describe accurately the dissipative eddies is:

$$N_t \propto \frac{T}{\tau_\eta} = \left(\frac{L^2/U^2}{\nu\, U^3/L} \right)^{1/2} = Re^{1/2} \tag{3.10}$$

with T the simulation time. In most applications it is also necessary to decrease the time-step, Δt, to grant the stability of numerical integration, leading to even greater values of N_t. The total computational cost is proportional to the number of grid points times the number of timesteps:

$$T_{\text{sim}} \propto Re^{11/4} \tag{3.11}$$

Reynolds-Averaged Navier-Stokes (RANS)

The goal of reducing the computational cost of a simulation can be achieved by solving the Reynolds-Averaged Navier-Stokes equations:

$$\begin{aligned} &\frac{\partial U_i}{\partial t} + U_j \frac{\partial U_i}{\partial x_j} = -\frac{1}{\rho} \frac{\partial P}{\partial x_i} + F_i + \frac{\partial}{\partial x_j} \left(2\,\nu\, E_{ij} + \left\langle u_i' u_j' \right\rangle \right) \\ &\frac{\partial U_i}{\partial x_i} = 0 \end{aligned} \tag{3.12}$$

instead of Eq. (3.6), where uppercase U_i and P represent the mean values of u_i and p, respectively, and E_{ij} is the symmetric part of the velocity gradient:

$$E_{ij} = \frac{1}{2} \left(\frac{\partial U_i}{\partial x_j} + \frac{\partial U_j}{\partial x_i} \right) \tag{3.13}$$

[2]It was demonstrated in Kim et al. (1987) that a spatial resolution of about $2\eta < \Delta x < 3\eta$ is enough to ensure a well resolved DNS.

This technique implies cutting out turbulent motions from the simulation and forces to renounce to their detailed description. The scales to be resolved being much larger, this kind of simulations can be run on coarse grids, with subsequent advantages on the computational cost as well as on data storage requirements. On the other hand, the appearance of the Reynolds stress tensor, τ^R, involves the nine additional unknowns:

$$\tau^R = \rho \left\langle u_i' u_j' \right\rangle = \rho \begin{bmatrix} u'^2 & u'v' & u'w' \\ v'u' & v'^2 & v'w' \\ w'u' & w'v' & w'^2 \end{bmatrix} \tag{3.14}$$

making the Eq. (3.12) unclosed.

An exact transport equation for $\left\langle u_i' u_j' \right\rangle$ can be derived multiplying the equation of the floating component of the velocity field along the i-th axis by u_j' and Reynolds averaging. It would, however, involve higher order moments to be modeled ($\left\langle u_i' u_j' u_k' \right\rangle$): the reiteration of this process generates an endless *hierarchy* of equations:

$$\frac{D \left\langle u_i' u_j' \right\rangle}{Dt} = -\frac{\partial}{\partial x_k} \left\langle u_i' u_j' u_k' \right\rangle + \dots \tag{3.15}$$

$$\frac{D \left\langle u_i' u_j' u_k' \right\rangle}{Dt} = -\frac{\partial}{\partial x_l} \left\langle u_i' u_j' u_k' u_l' \right\rangle + \dots \tag{3.16}$$

that, step by step, makes the problem more complex – for the appearance of supplemental variables – and yet not closed. The equation set needs therefore to be closed at some level by means of mathematical modelling, which means providing an expression of the unresolved statistics in terms of the other variables involved, i.e. lower order statistics.

Using higher moments complicates, in general, the solution. On the other hand, the higher is the level of closure, the lower the influence on the mean flow. The only two levels currently used in computations are:

- Eddy-viscosity models;
- Second-moment closure models.

Eddy-viscosity models: the k-ε model. Eddy-viscosity models deserve a brief overview because of their wide diffusion. The trace of the Reynolds stress tensor is, by definition, twice the turbulent kinetic energy:

$$\left\langle u_i' u_i' \right\rangle = 2\,k \tag{3.17}$$

Its spherical component being therefore $\frac{2}{3}\,k\,\delta_{ij}$, the eddy-viscosity hypothesis consists in modelling the deviatoric component as:

$$\left\langle u_i' u_j' \right\rangle - \frac{2}{3}\,k\,\delta_{ij} = -2\,\nu\,E_{ij} \tag{3.18}$$

in direct analogy with the relation for the viscous stresses: the idea behind all this is to describe the effects of turbulence on the mean flow as an enhancement of diffusivity, which might seem quite reasonable at first sight. Nevertheless, the eddy-viscosity model conceals the assumption that the Reynolds stress and the mean rate of strain tensors are parallel, which is not true in general.

To achieve the closure of the problems it remains to express the turbulent viscosity, ν_T, in terms of other variables, which differentiates the various models. The most used is the k-ε model that relates it to the turbulent kinetic energy and the dissipation rate, ε:

$$\nu_T = C_\mu \frac{k^2}{\varepsilon} \tag{3.19}$$

with C_μ a modelling constant. In addition to this, the model consists of the transport equations for k and ε (Jones and Launder, 1972).

The 3D simulations used as a reference to validate the 0D model developed in this PhD work are carried out with the k-ε model.

Second-moment closure models. Second-moment closure models use Eq. 3.15 to resolve the Reynolds stress field and provide empirical models for third-order moments.

Large Eddy Simulation (LES)

Under the point of view of accuracy as well as computational cost the Large Eddy Simulation is a compromise between DNS and RANS. It is based on the intuition that through the energy cascade the turbulent motions acquire universal features that make them suitable to be modelled, while their influence on the mean motion vanishes. In LES the largest three-dimensional unsteady turbulent motions are directly resolved, whereas the effects of the smaller ones are modelled. It implies four conceptual steps:

- The equations for the filtered fields are derived from (3.6) by the application of the normalized filter G_Δ:
$$\tilde{u}_i = \int_{\mathcal{D}} G_\Delta(\vec{x}, \vec{r})\, u_i(\vec{x} - \vec{r}, t) dV \tag{3.20}$$
where the definition of the filter G_Δ is crucial as it specifies what is meant by *large eddy*. Note that, unlike the Reynolds decomposition, in this case the filtered subgrid velocity:
$$\int_{\mathcal{D}} G_\Delta(\vec{x}, \vec{r})\, u_i'(\vec{x} - \vec{r}, t) dV \neq 0 \tag{3.21}$$
is not null in general and:
$$\tilde{\tilde{u}} \neq \tilde{u} \tag{3.22}$$
- The formulation of a closure model for the residual stresses (analogous to the Reynolds stresses in RANS).
- The numerical solution of the filtered equations, which provides an approximation of the mean field and of the large-scale motions in one realization.

Filtered equations. The LES equations are obtained applying the filter Eq. (3.20) to Eq. (3.6), under the hypothesis that the filter permutes with time and spatial derivatives.

The relative formulation for an incompressible flow is:

$$\frac{\partial \tilde{u}_i}{\partial t} + \tilde{u}_j \frac{\partial \tilde{u}_i}{\partial x_j} = \tilde{f}_i + \nu \frac{\partial^2 \tilde{u}_i}{\partial x_j \partial x_j} - \frac{1}{\rho} \frac{\partial \tilde{p}}{\partial x_i} - \frac{\partial \tau_{ij}^R}{\partial x_j} \tag{3.23}$$

$$\frac{\partial \tilde{u}_i}{\partial x_i} = 0 \tag{3.24}$$

The *residual stress tensor*, defined as:

$$\tau_{ij}^{R} = \widetilde{u_i\, u_j} - \tilde{u}_i\, \tilde{u}_j \tag{3.25}$$

takes into account the influence of the subgrid (unresolved) motions on the large (resolved) eddies: symmetric by definition, the residual stress tensor adds six more unknown variables in the governing equations, with the consequent rise of a closure problem. Hence it needs to be modelled just like the Reynolds stress tensor in RANS.

3.1.3 Description of multiphase flows

Combustion in DI-SI engines involves high-pressure injection of liquid fuel in the combustion chamber. A description of the liquid phase and its interaction with the gas phase is therefore necessary and can be achieved with two different approaches: the Eulerian approach or the Lagrangian approach.

The Eulerian formalism describes the spray as a continuum characteristic of the gas: a transport equation for the liquid fraction is coupled to Eq.s (3.1 – 3.5).

The Lagrangian formalism, on the other hand, treats the spray as a collection of liquid drops that move in the computational domain under the effect of shear forces caused by the interaction with the gas phase. Evaporation is described by multi-phase models like the one proposed by Abramzon and Sirignano (1989) and described in Section 2.1.2.

The Lagrangian formalism can be implemented directly, by representing each liquid drop with a discrete particle. A stochastic approach is also possible, where the discrete particles represent a collection of drops of the same size and thermodynamic condition. The former approach is more precise and computationally expensive than the latter. The stochastic approach is implemented in most RANS and LES codes and it is used in the CFD computation that serve as a reference for the development and validation of the 0D model presented in Chapter 4.

3.1.4 Description of chemical kinetics

Modelling chemical kinetics is essential to determine the reaction rate, $\dot{\omega}_k$, that constitutes a source term in Eq. (3.4). Its accuracy depends on the complexity of the reaction mechanism adopted.

The simplest scheme can be generated considering a single reaction and three species (fuel, F, oxidizer, O, and products, P)

$$\mathrm{F} + \mathrm{O} \longrightarrow \mathrm{P} \tag{3.26}$$

Considering, as an example, hydrogen combustion this can be written as:

$$\mathrm{H_2} + \tfrac{1}{2}\,\mathrm{O_2} \longrightarrow \mathrm{H_2O} \tag{3.27}$$

Equation (3.27) provides a simplified mechanism involving one reaction and three species (H_2, O_2 and H_2O).

A more accurate description can be obtained detailing the intermediate steps behind Eq. (3.27), that involve the formation of radicals such as H and OH and their subsequent oxidation. Furthermore, if O_2 is obtained from an air stream, the oxidation of N_2 into NO, NO_2 and N_2O must also be taken into account.

As a general rule, increasing the number of species, N_{SP}, and reactions, N_{RE}, considered leads to more accurate results and to a higher computational cost.

Chemical time scales can be very small and their resolution can sometimes requires a time step that is orders of magnitudes smaller than in a non-reactive simulation (Poinsot and Veynante, 2011). This translates in a constraint on the mesh size, to ensure stability (Courant condition), with a negative effect on computation time. A reduced reaction scheme is therefore necessary in most industrial applications.

3.1.5 CFD codes

The following paragraphs present the main characteristics of some of the available CFD codes. All the CFD solutions presented are adapted to High Performance Computing (HPC) and provide compressible flow solvers that are necessary for ICE combustion computations.

ANSYS Fluent. Fluent is a proprietary CFD code, originally conceived for RANS but also providing LES models. It provides models for reactive and multiphase flows, acoustics. Since 2006 it is distributed and integrated within ANSYS, a 3D solid mechanics FEM solver.

Website: https://www.ansys.com/products/fluids/ansys-fluent

OpenFOAM. OpenFOAM (for Open source Field Operation And Manipulation) is an open source software, freely distributed in the form of a C++ library for the development of customized numerical solvers. Initially developed at the Imperial College (London), it is now community maintained. It is adapted to different CFD problems like combustion and multiphase flow as well as other 3D applications like solid mechanics and electromagnetics.

Website: https://www.openfoam.com/

Converge. Converge is a commercial RANS code, developed and distributed by Convergent Science. Its main strength is the ease of use, since it can mesh complex geometries autonomously: the user doesn't need particular meshing skills or tools. Applications include ICE, gas turbines, fuel injectors and sprays, exhaust aftertreatment devices and turbomachines.

Website: https://convergecfd.com/

AVBP. AVBP is a CFD code, dedicated mainly to LES and DNS, developed by CERFACS and IFPEN. It is used in research works on related to ICE (Iafrate, 2016; Mouriaux et al., 2017; Vermorel et al., 2009), gas turbines (Rehayem et al., 2017) as well as other combustion and aerodynamics problems.

Website: http://www.cerfacs.fr/avbp7x/

IFP-C3D. C3D is a RANS code developed by IFPEN (Velghe et al., 2011) dedicated to ICE simulation. Due to the availability of the source code in IFPEN and the previous studies realized with this code, it was chosen for all the 3D RANS simulations performed within this PhD work. The results obtained with C3D were used as reference data for the development (model reduction) and validation of the 0D model.

3.2 System simulation

While 3D CFD simulations are involved in the design of single components such as a combustion chamber or an exhaust after-treatment system, the goal of system simulation is to investigate the interaction of different components in a complex system.

The need to contain the computational cost of system simulators requires a simplified description of the single components. For this reason 0D/1D modelling has become a synonym of system simulation and almost all commercial codes contain both types of component models.

Zero-dimensional (0D). Zero-dimensional (0D) or quasi-dimensional models represent the state of a physical object as a function of time only, that is governed by ordinary differential equations (ODE).

This is the preferred approach for mechanical components such as connecting rods or shafts whose state evolves according to dynamic or kinematic inputs.

Mono-dimensional (1D). The state of a component modelled with a mono-dimensional (1D) approach is a function of time, t, and a space coordinate, x and evolve according to partial differential equations (PDE) in t and x. This approach is preferred when there is an interest in reproducing physical effects related to the spatial dimension.

The air path of an ICE is an example of a system that benefits from a 1D description: a discretization of the intake and exhaust ducts allows to reproduce acoustic phenomena that are crucial to the description of air load, especially in non-turbocharged engines.

Mapped characteristic response. An even simpler modelling option is to provide the component response to its environment in the form of a table that relates input and output.

Components that have a fast response and whose present state is not strongly influenced by its past states are well represented by characteristic maps. This is often the case with turbines and compressors for turbo-boosting and turbomachines in general, for which manufacturers provide tables that relate rotational speed, pressure ratio and mass flow rate.

3.2.1 Commercial system simulation platforms

The following paragraphs present an overview of commercial system simulation platforms.

GT-Power GT-Power is a ICE simulation tool widely used in the automotive industry. Initially developed as a 1D tool, it is well adapted to describe acoustic phenomena in ICE. With the Fast Running Model (FRM) approach, it allows the creation of 0D models that offer interesting computational costs: such models can be integrated in Hardware in the Loop (HiL) simulations. GT-Power allows to develop user-defined models through a C/Fortran interface: for this reason it has been used in research works involving the development of new models (Demesoukas, 2015; Kaprielian, 2015).

Website: `https://www.gtisoft.com/`

Cruise/CruiseM. The AVL Advanced Simulation Tools suite provides two separate 0D simulation tools: Cruise and Cruise M. Derived from the same solver, the former is dedicated to vehicle and driveline simulation while the latter is a multi-disciplinary simulation platform. Cruise M has been successfully used to perform Model Based Calibration tasks and integrated into a virtual test-bed (Keuth et al., 2016).

Website: `https://www.avl.com/cruise`

Website: `https://www.avl.com/cruise-m`

Simcenter Amesim Software. Simcenter Amesim is a multi-physics system simulation platform developed and distributed by Siemens PLM Software. It provides both 0D and 1D components and has interesting ICE and powertrain simulation capabilities, thanks to the IFP-Engine, IFP-Drive and IFP-Exhaust libraries, developed by IFPEN. Like GT-Power, Amesim offers the possibility of developing customized models through Ameset: the models can be coded both in C or Fortran. Several research works involving the development of new models (Lafossas et al., 2005; Richard et al., 2009; Dulbecco et al., 2015; Rudloff et al., 2015) or the use of the existing ones in innovative contexts (Belhassein et al., 2014) have been carried out with Amesim.

Website: https://www.plm.automation.siemens.com/global/en/products/simcenter/simcenter-amesim.html

3.3 Overview of 0D/1D predictive models of ICE combustion chambers in literature

This section provides a brief review of the 0D models dedicated to ICE combustion chambers discussed in literature. Since direct injection for spark-ignition is a relatively new concept – at least from the point of view of numerical simulation – almost all the available literature discussing spray-related issues mainly covers Diesel direct injection.

3.3.1 Spark-ignition engine models

The following paragraphs present an overview of SI engine system simulation models available in literature, with particular focus on the CFM1D, used as a base for this PhD work.

The IFP-Engine CFM1D model

The first version of the CFM1D was developed by Lafossas et al. (2005) as a quasi-dimensional formulation of the Coherent Flame Model (CFM) for premixed combustion in the flamelet regime adapted to spark ignition engine combustion. Mass and energy balance equations describe the evolution of three gas species (fuel vapour, air and combustion products) in the two zones identified by the cylinder walls and flame front:

the cylinder gas identifies all the gas contained in the cylinder, its global mass varies because of valve flows and blow by;

the fresh gas that has not yet been reached by the propagating flame and whose global mass is affected by flame front reactions as well as valve flows and blow by;

the burned gas behind the flame front, whose masses and energy are obtained as the difference between the values for cylinder and fresh gas.

Furthermore, each one can in principle contain any of the three species since combustion products can be used to dilute the fresh gas (EGR or IGR) and air or unburned fuel can be found in the burned gas because of lean or rich operation, respectively.

The mass fuel burning rate, $\dot{\mathcal{M}}_F$, is obtained as the propagation of a turbulent (wrinkled) thin flame surface at the laminar flame speed s_L:

$$\dot{\mathcal{M}}_F = Y_{F\,fg}\,\dot{\mathcal{M}}_{fg} = \rho_{fg}\,Y_{F\,fg}\,s_L\,\mathcal{S}_T \tag{3.28}$$

with $\dot{\mathcal{M}}_{fg}$ the fresh gas mass rate of consumption, ρ_{fg} the fresh gas density and $Y_{F\,fg}$ the fuel mass concentration in the fresh gas;

- the laminar flame speed s_L is calculated with an empirical correlation (Metghalchi and Keck, 1982) from the composition and thermodynamic conditions of the unburned gas;
- the area of the turbulent flame surface

$$\mathcal{S}_T = \mathcal{S}_M \, \Xi \tag{3.29}$$

  is obtained as the mean flame surface $\mathcal{S}_M$ times the turbulent wrinkling Ξ, which is a function of the turbulent kinetic energy and its dissipation rate;
- the burned gas volume yields to the mean flame surface $\mathcal{S}_M$ under the hypothesis of an initially isotropic (spherical) propagation.

A phenomenological turbulence model based on the quasi-dimensional reduction of the RANS approach describes the evolution of turbulent kinetic energy, k, with a production-dissipation equation

$$\frac{\mathrm{d}k}{\mathrm{d}t} = \mathcal{K}_{turb} \frac{\dot{E}_{k\,tr}}{\mathcal{M}} - \mathcal{K}_{diss} \, k \tag{3.30}$$

where $\mathcal{K}_{turb} = 1$ and $\mathcal{K}_{diss} = 150$ are modelling constants and $\mathcal{M}$ the in-cylinder gas mass – which includes both fresh and burned gases. The source $\dot{E}_{k\,tr}$ in the production term represents the energy transfer from the tumble motion – representing the mean kinetic energy – towards the turbulent motion and it equals the variation in tumble kinetic energy

$$\dot{E}_{k\,tr} = \dot{E}_k = \frac{1}{8} \mathcal{M} \omega^2 \left[L^2 \, \dot{N}_t + 2 N_t \, L \, \dot{L} \right] \tag{3.31}$$

with L the height of the combustion chamber, ω the crankshaft rotation speed and N_t the tumble number, defined as the ratio of the tumble angular velocity to the crankshaft angular velocity.

The initial value of the tumble number, N_t, at IVC is an input parameters of the model that have to be provided at the beginning of each cycle and depend on the operating point.

Richard et al. (2009) and Bougrine (2012) describe the following evolutions of CFM1D and their validation on experimental results:

- the mixture composition of fresh and burned gas is detailed considering 15 species (fuel, N_2 , O_2 ,H_2 , H_2O, CO, CO_2 , NO, NO_2 , HC, NH_3 , soot, O, H, OH) whose partial densities evolve independently;
- the introduction of post-flame reactions using reduced chemistry to describe CO oxidation and NO_x formation (Zel'dovitch);
- the prediction of occurrence, timing and intensity of autoignition (knock) based on fuel characteristics, fresh gas composition and temperature;
- the introduction of a physical differential equation for the evolution of the turbulent flame wrinkling Ξ, derived by Richard and Veynante (2015):

$$\frac{1}{\Xi} \frac{\mathrm{d}\Xi}{\mathrm{d}t} = \Gamma \left(\frac{u'}{s_L}, \frac{l_t}{\delta_l} \right) \frac{u'}{l_t} \left(\frac{\Xi_{\mathrm{eq}} - \Xi}{\Xi_{\mathrm{eq}} - 1} \right) - \frac{2}{r_{\mathrm{bg}}} \, (1 + \tau) \, (\Xi - 1) \, s_L \tag{3.32}$$

  with:
  - l_t – the integral length scale characterizing the turbulent flow;
  - $\tau = \rho_{\mathrm{fg}} / \rho_{\mathrm{bg}}$ – the thermal expansion rate, which accounts for the density change due to combustion;

- δ_l – the laminar flame thickness;
- r_{bg} – the burned gas radius, which is related to the burned gas volume V_{bg} according to the following equation:

$$r_{\mathrm{bg}} = \sqrt[3]{\frac{3V_{\mathrm{bg}}}{4\pi}}$$

  under the spherical mean flame-front assumption – V_{bg} being evaluated knowing the burned gas mass, $\mathcal{M}_{bg}$, temperature and composition as well as the pressure in the cylinder, by means of the perfect gas state equation;
- Γ – the wrinkling efficiency function derived by Charlette et al. (2002) accounting for the effect of turbulence on flame stretch;
- $u' = \sqrt{2k/3}$ – the turbulent velocity fluctuation, where k is the specific turbulent kinetic energy (L^2T^{-2});
- Ξ_{eq} the equilibrium value of the flame wrinkling.

Bougrine et al. (2014) developed a new approach to describe pollutant formation in post-flame reaction based on tabulated chemistry.

NO and CO Relaxation Approaches, respectively NORA and CORA, assume an exponential relaxation for the mass concentrations of the two species in the burned gas (Y_{NO}^{bg} and Y_{CO}^{bg}) towards their equilibrium values (Y_{NO}^{eq} and Y_{CO}^{eq}), so that the respective source terms ($\dot{\omega}_{NO}$ and $\dot{\omega}_{CO}$, M^2T^{-1}) can be written as:

$$\dot{\omega}_{NO} = \frac{Y_{NO}^{eq} - Y_{NO}^{bg}}{\tau_{NO}}\mathcal{M}_{bg} \quad ; \quad \dot{\omega}_{CO} = \frac{Y_{CO}^{eq} - Y_{CO}^{bg}}{\tau_{CO}}\mathcal{M}_{bg} \tag{3.33}$$

with $\mathcal{M}_{bg}$ the burned gas mass, τ_{NO} and τ_{CO} the relaxation times of NO and CO. The values of the equilibrium concentrations and relaxation times are stored in specific look-up tables as a function of the composition and thermodynamic conditions of the burned gas mixture. Tables are generated numerically, based on the results of a a homogeneous complex chemistry (53 species and 325 reactions) reactor modelled with the CHEMKIN solver (Kee et al., 1989).

The CFM1D model was subsequently improved to account for cycle-to-cycle variations (CCV) caused by fluctuations of the flow characteristics both at global and local scale (Richard et al., 2015; Dulbecco et al., 2015). LES results were used to derive the parameters of the Gaussian PDF used to model the statistical behaviour of:

- the integral length scale l_t;
- the tumble number N_t;
- the flame convection velocity at the spark plug u_{SP}.

Random values for these quantities are generated according to the respective PDF. The two former parameters are input of the turbulence model and influence the global flow characteristics such as the evolution of turbulent kinetic energy. The latter is used by a detailed ignition model describing the arc length as a function of u_{SP}: this affects the volume of the spark kernel and therefore the critical ignition energy to form a stable flame kernel.

Dulbecco et al. (2016) included a physical turbulence model based on the (K-κ) approach that allows to reproduce 3D CFD results with a fixed set of calibration parameters for all operating points and takes into account the contribution of injection on both mean and turbulent kinetic energies The new model consists of two evolution equations for the mean and turbulent kinetic energy (K and κ), derived with an integration of RANS equations over the chamber volume.

The developments described in this work, aiming to take into account some of the issues related to direct injection, were implemented as an evolution of the existing CFM1D model detailed in Section 4.1.

Other SI engine models

The 0D model proposed by Bozza et al. (2002, 2005) is also based on the flamelet assumption writing the global burning rate as the one of a wrinkled surface propagating at the laminar flame speed (Eq. 3.28). The flame front is modelled as a fractal surface and the wrinkling ratio is expressed as a function of the integral length scale l_t and Kolmogorov scale η_k:

$$\frac{\mathcal{S}_T}{\mathcal{S}_L} = \left(\frac{l_t}{\eta_k}\right)^{D_3-2} \tag{3.34}$$

with D_3 a fractal dimension that depends on the u'/s_L ratio. Turbulence is modelled with a K-κ approach.

The same model was also adapted to twin-spark ignition with a three-zone approach (Bozza et al., 2004).

The PhD work carried out by Kaprielian (2015) proposes a 0D model for homogeneous spark-ignition combustion. The general approach is similar to the one adopted in CFM1D (Lafossas et al., 2005; Richard et al., 2009) in that:

- a two-zone approach (fresh gas and burned gas) is adopted;
- a correlation for the laminar flame speed and a turbulence model are used to calculate the global burning rate, hence the mass transfer from FG to BG.

The aim of this model is to account for the influence near-wall thermal loss on flame propagation. For this purpose, the flame surface is divided into a free propagation zone and a wall interacting zone. In the latter, the equilibrium temperature is reduced by the thermal loss to the wall. Furthermore, the flame is discretized along its thickness so that a temperature distribution is available in the reaction zone.

Demesoukas (2015) developed a complete SI combustion chamber model for the GT-POWER® simulation platform, using a two zone thermodynamic approach (fresh-burned gas). Combustion is described with a coherent flame model with a K-κ turbulence model providing information to characterize the flame wrinkling, Ξ. Flame front and post-oxidation reactions are modelled with simplified kinetic schemes. Near wall phenomena are taken into account damping the flame wrinkling close to the boundaries.

3.3.2 Diesel engine models

0-dimensional models of Diesel combustion chambers are particularly interesting in this study since they address the issues related to direct injection such as atomization, spray geometry, evaporation and mixing.

The 0D phenomenological combustion model for common rail Diesel engines presented by Barba et al. (2000) uses an empirical correlation for atomization that provides an initial drop diameter for the whole spray. Fuel evaporation is accounted for via a steady-state D^2 model, Eq. (2.22), where the evaporation constant τ_{ev} is used as a tuning parameter.

The Universal Diesel Engine Simulator (UniDES) proposed by Inagaki et al. (2008) uses the Hiroyasu model equations for the spray penetration and cone angle to predict the air entrainment in the spray. Droplet evaporation is reproduced with the Spalding D^2 model (Eq. (2.22)) and the initial drop size is provided with Kawamura's equation. Fuel/air mixing is described with a simplified PDF model based on the interaction of fixed-equivalence ratio classes.

The 0D combustion model developed at IFPEN (MC0D) (Mauviot et al., 2006) for Diesel and Diesel HCCI engines uses the spray penetration and spreading rate model proposed by Naber and Siebers (1996) to predict air entrainment. The evaporation rate calculation is based on the concept of liquid length (Siebers, 1998) which provides an estimation of the characteristic global evaporation time τ_{ev}: this approach leaves asides the isolated drop description and does not require an atomization model. Mixture evolution is described providing model equation for the mean and variance of a β-PDF function.

Dulbecco et al. (2009); Dulbecco (2010) developed an evolution of this model, the dual-CM model, that adapts the approach devised by Naber and Siebers (1996) to multi-injection strategies.

The Diesel combustion model developed by Bordet et al. (2010) uses the approach developed by Naber and Siebers (1996) to describe the geometrical evolution of the spray (penetration and air entrainment). Overall evaporation is controlled by a characteristic time τ_{ev} that depends on the thermodynamic conditions and nozzle diameter. A β-PDF describes the mixture fraction distribution with model equations for its first and second order momentum (mean and variance).

Chapter 4

Model development

The aim of this PhD work is to develop a 0-dimensional model of a GDI (Gasoline Direct Injection) combustion chamber for application in system simulations.

The Simcenter Amesim Software™ multi-physics simulation platform, distributed by Siemens PLM Software, is chosen as a framework for the implementation, testing and validation of this model. This choice is motivated by both technical and commercial reasons, such as:

- the possibility of integrating the combustion model in a complete system simulation platform, which increases its possible applications;
- the established partnership between IFPEN and Siemens PLM Software in developing and distributing the powertrain model libraries IFP-Engine, IFP-Exhaust and IFP-Drive;
- the existence, within the IFP-Engine library of a homogeneous SI (Spark Ignition) combustion model (CFM1D), used as a starting point for this work.

A GDI combustion model is necessary to follow the technical evolution of automotive engines, according to the orientation given by the industry to SI engines.

This chapter describes the final version of the model proposed in this work, detailing the most significant aspects leading to the results and conclusions shown in the following. In particular:

- Section 4.1 describes CFM1D, as it was at the beginning of this PhD;
- the following sections detail the developments realized within this PhD to introduce the different physical aspects that characterize direct injection.

4.1 The base model: CFM1D

The CFM1D submodel of the IFP-Engine library is a combustion chamber model for homogeneous charge spark-ignition engines (Richard et al., 2009).

4.1.1 The CFM approach

Combustion is described with a mono-dimensional Coherent Flame Model (CFM), Fig. 4.1, where the turbulent flame-front separating the fresh gases from the burned gases, propagates with a speed equal to the laminar flame speed s_L towards the fresh gases. Accordingly, two

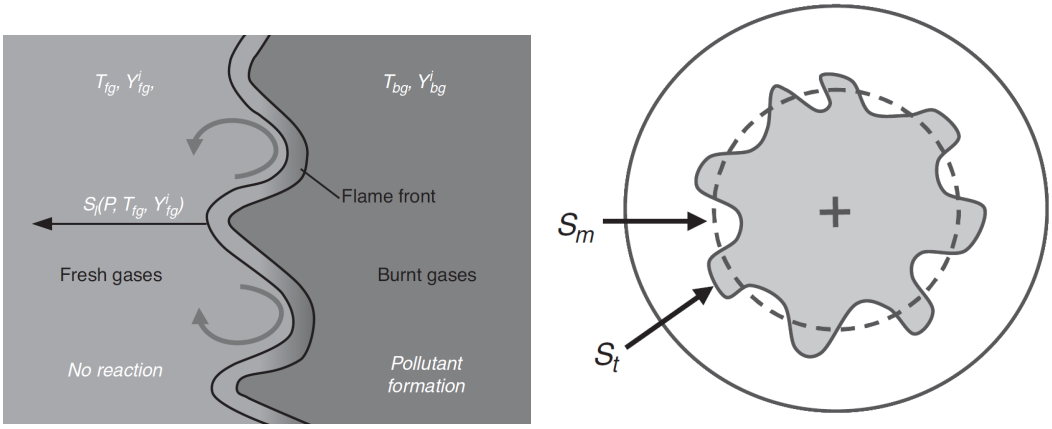

Figure 4.1: 1D Coherent Flame Model approach: the cylinder gas is divided into two zones (fresh and burned gas), separated by a wrinkled spherical flame surface. Figure from Richard et al. (2009).

zones can be distinguished, each characterized by its own thermochemical state, expressed in terms of temperature, pressure and composition. The turbulent flame surface $\mathcal{A}_T$ is given by the following equation:

$$\mathcal{A}_T = \mathcal{A}_M \, \Xi \tag{4.1}$$

with $\mathcal{A}_M$ the mean flame front surface, assumed spherical. The flame-front wrinkling, Ξ, evolves according to the 0D differential equation (Richard et al., 2009):

$$\frac{1}{\Xi}\frac{\mathrm{d}\Xi}{\mathrm{d}t} = \Gamma\left(\frac{u'}{s_L}, \frac{l_t}{\delta_l}\right)\frac{u'}{l_t}\left(\frac{\Xi_{\mathrm{eq}} - \Xi}{\Xi_{\mathrm{eq}} - 1}\right) - \frac{2}{r_{\mathrm{bg}}}\,(1+\tau)\,(\Xi - 1)\,s_L \tag{4.2}$$

with:

- S_L – the laminar flame speed;
- δ_l – the laminar flame thickness;
- $u' = \sqrt{2k/3}$ – the turbulent velocity fluctuation, where k is the specific turbulent kinetic energy (L^2T^{-2});
- l_t – the integral length scale of the turbulent flow;
- Γ – the wrinkling efficiency function derived by Charlette et al. (2002) accounting for the effect of turbulence on flame stretch;
- Ξ_{eq} – the equilibrium value of the flame-front wrinkling, determined via a KPP analysis for a planar mean flame propagating in steady turbulence;
- $\tau = \rho_{\mathrm{fg}}/\rho_{\mathrm{bg}}$ – the thermal expansion rate, which accounts for the density change due to combustion;
- r_{bg} – the burned gas radius, which is related to the burned gas volume V_{bg} according to the following equation:

  $$r_{\mathrm{bg}} = \sqrt[3]{\frac{3V_{\mathrm{bg}}}{4\pi}}$$

  under the spherical mean flame-front assumption – V_{bg} being evaluated knowing the burned gas mass, $\mathcal{M}_{\mathrm{bg}}$, temperature and composition as well as the pressure in the cylinder, by means of the perfect gas state equation.

4.1.2 Turbulence model

Cylinder gas aerodynamics are described by the turbulence model developed and implemented by Dulbecco et al. (2016).

The approach is based on the decomposition of the complex flow into two contributions:

- one related to the mean flow motions, constituted by coherent macroscopic structures, characterized by the mean kinetic energy K and strongly dependent on cylinder geometry and valve flows;
- one related to the turbulent flow, constituted by small structures supposed homogeneous and isotropic, characterized by the turbulent kinetic energy k.

Conservation equations for K and k are derived from RANS equations under the hypothesis that the mean flow is constituted by a tumble vortex coherent structure while turbulence groups all the other components.

Mean kinetic energy

The specific mean kinetic energy (L^2T^{-2}) evolves according to:

$$\frac{\mathrm{d}K}{\mathrm{d}t} = -T_{K\to\kappa} + \frac{1}{2}c_K\frac{\dot{\mathcal{M}}^{\mathrm{in}}}{\mathcal{M}}u_{\mathrm{in}}^2 + I_K + K\frac{\dot{\mathcal{M}}^{\mathrm{out}}}{\mathcal{M}} + c_{\mathrm{cmp}}\frac{\dot{\rho}}{\rho} - K\left(\frac{\dot{\rho}}{\rho} + \frac{\dot{V}}{V}\right) \tag{4.3}$$

with V, $\mathcal{M}$ and ρ the cylinder volume, the total gas mass it contains and the ratio of the latter to the former, respectively. The rhs terms represent:

energy transfer from mean to turbulent kinetic energy:

$$T_{K\to\kappa} = 2c_\beta\frac{\mu_t}{\mathcal{M}}\frac{K}{\Delta^2}$$

with μ_t the turbulent viscosity, Δ the characteristic tumble length scale and c_β a modelling constant;

valve inflow of mean kinetic energy, expressed as a fraction c_K of the kinetic energy of the gas stream entering the cylinder:

$$\frac{1}{2}c_K\frac{\dot{\mathcal{M}}^{\mathrm{in}}}{\mathcal{M}}u_{\mathrm{in}}^2$$

with u_{in} the velocity at the intake valve (or exhaust backflow), $\dot{\mathcal{M}}^{\mathrm{in}}$ the corresponding mass flow rate and c_K a modelling constant;

valve outflow of mean kinetic energy:

$$K\frac{\dot{\mathcal{M}}^{\mathrm{out}}}{\mathcal{M}}$$

injection contribution to mean energy I_K;

compressibility and closure terms:

$$c_{\mathrm{cmp}}\frac{\dot{\rho}}{\rho} - K\left(\frac{\dot{\rho}}{\rho} + \frac{\dot{V}}{V}\right)$$

with c_{cmp} a modelling constant.

Turbulent kinetic energy

The model equation for turbulent kinetic energy (L^2T^{-2}):

$$\frac{\mathrm{d}\kappa}{\mathrm{d}t} = T_{K\to\kappa} + \frac{1}{2}c_\kappa\frac{\dot{\mathcal{M}}^{\mathrm{in}}}{\mathcal{M}}u_{\mathrm{in}}^2 + I_\kappa + \kappa\frac{\dot{\mathcal{M}}^{\mathrm{out}}}{\mathcal{M}} + c_{\mathrm{cmp}}\frac{\dot{\rho}}{\rho} - \kappa\left(\frac{\dot{\rho}}{\rho} + \frac{\dot{V}}{V}\right) - \varepsilon \tag{4.4}$$

is formulated likewise with the addition of the dissipation rate ε, modelled as:

$$\varepsilon = \frac{\left(\frac{2}{3}\kappa\right)^{\frac{3}{2}}}{l_t} \tag{4.5}$$

with l_t the integral length scale.

Scales

Both the characteristic length scales involved in the turbulence model are computed as a function of the distance between head and cylinder, δ:

$$\Delta = c_\Delta\left[\delta\left(\alpha - \varphi_\Delta\right)\right]^{1/3} + c_\Delta^{\mathrm{offs}} \tag{4.6}$$

$$l_t = c_{l_t}\left[\delta\left(\alpha - \varphi_{l_t}\right)\right]^{1/3} + c_{l_t}^{\mathrm{offs}} \tag{4.7}$$

Tuning coefficients allow to adjust the amplitude (c_Δ and c_{l_t}), phase (φ_Δ and φ_{l_t}) and offset (c_Δ^{offs} and $c_{l_t}^{\mathrm{offs}}$). Their values are supposed to be exclusively dependent on the geometry and kept constant across the operating map of a given engine.

4.1.3 Burning rate

The combustion progress variable, c, in the 1D CFM model is defined as the ratio of the burned gases mass, $\mathcal{M}_{\mathrm{bg}}$, to the total mass in the chamber:

$$c = \frac{\mathcal{M}_{\mathrm{bg}}}{\mathcal{M}} = 1 - \frac{\mathcal{M}_{\mathrm{fg}}}{\mathcal{M}} \tag{4.8}$$

with $\mathcal{M}_{\mathrm{fg}}$ the mass of the fresh gases.

Once the wrinkled flame surface $\mathcal{S}_T$, Eq. (4.1), is known, the fuel burning rate is given by:

$$\dot{\mathcal{M}}_F = Y_{F\,\mathrm{fg}}\,\dot{\mathcal{M}}_{\mathrm{fg}}^{\mathrm{ff}} = \rho_{\mathrm{fg}}\,Y_{F\,\mathrm{fg}}\,s_L\,\mathcal{A}_T \tag{4.9}$$

where ρ_{fg} is the density of the fresh gas mixture and $Y_{F\,\mathrm{fg}}$ is the fuel mass fraction within the fresh gases (Richard et al., 2009; Lafossas et al., 2005). The variation $\dot{\mathcal{M}}_{\mathrm{fg}}^{\mathrm{ff}}$ of fresh gas mass represents the mass transfer from the fresh gases to the burnt gases due to the progress of the flame front. The laminar flame speed s_L is calculated with the empirical correlation proposed by Metghalchi and Keck (1982):

$$S_L = S_L^0\left(\frac{T_{\mathrm{fg}}}{T_0}\right)^\alpha\left(\frac{p}{p_0}\right)^\beta\left(1 - 2.1\,X_{\mathrm{GBR}}\right) \tag{4.10}$$

as a function of the reference laminar speed, S_L, measured at p_0 and T_0, of cylinder pressure, p, and fresh gas temperature T_{fg} and of the diluent mass fraction, X_{GBR}. The exponents α and β depend on the fuel/air equivalence ratio.

Flame front reaction

According to Eq. (4.9), the flame front consumes all the fuel encountered during its propagation. Concerning the rates of consumption and production of the other species involved (O_2, CO_2, CO and H_2), the following reaction scheme is considered for a generic $C_xH_yO_z$ hydrocarbon fuel:

$$\alpha_r \left[C_xH_yO_z + \left(x + \frac{y}{4} - \frac{z}{2}\right) O_2 \longrightarrow x\,CO_2 + \frac{y}{2}\,H_2O \right] \tag{4.11}$$

$$(1-\alpha_r) \left[C_xH_yO_z + \frac{x-z}{2}\,O_2 \longrightarrow x\,CO + \frac{y}{2}\,H_2 \right] \tag{4.12}$$

with the reaction parameter, α_r, that defines the fraction of fuel that burns according to the complete reaction in Eq. (4.11), expressed as:

$$\alpha_r = \frac{\max(0.98, \phi)\,\dfrac{4x+y-2z}{\phi} - 2x + 2z}{2x+y} \tag{4.13}$$

The value of parameter is $\alpha_r = 1$ for lean mixtures[1] ($\phi < 0.98$), i.e. when there is enough oxygen to burn all the available fuel completely. For stoichiometric and rich mixtures, on the other hand, the reaction parameter satisfies $\alpha_r < 1$ and a portion $(1-\alpha_r)$ of the available fuel burns according. the incomplete reaction, Eq. (4.12).

In both cases the flame front consumes all the available fuel and only combustion products(O_2, CO_2) or intermediate combustion species (CO, H_2) are transferred to the burnt gas zone.

The stoichiometric coefficients in Eq.s (4.11 – 4.12) are used to calculate the oxygen consumption $\dot{\mathcal{M}}^{\text{ff}}_{O_2}$ and the combustion products source terms $\dot{\mathcal{M}}^{\text{ff}}_{H_2O}$, $\dot{\mathcal{M}}^{\text{ff}}_{CO_2}$, $\dot{\mathcal{M}}^{\text{ff}}_{H_2}$ and $\dot{\mathcal{M}}^{\text{ff}}_{CO}$ resulting from flame front propagation (Richard et al., 2009).

Post flame reactions

Chemical reactions also take place in the burnt gas after the passage of the flame front favoured by the high temperature. These reactions produce additional pollutants such as nitrogen oxides and may increase or reduce the concentration of incomplete combustion products such as CO and H_2.

Carbon monoxide (CO) The following reduced kinetic scheme, describing the evolution of carbon monoxide in the burnt gas:

$$\begin{cases} N_2 \rightleftharpoons 2\,N \\ O_2 \rightleftharpoons 2\,O \\ O_2 + 2\,CO \rightleftharpoons 2\,CO_2 \\ H_2 \rightleftharpoons 2\,H \\ O_2 + H_2 \rightleftharpoons 2\,OH \\ O_2 + 2\,H_2O \rightleftharpoons 4\,OH \end{cases} \tag{4.14}$$

is used to calculate the equilibrium molar concentration, X_i^{eq}, of each of the species involved. A pseudo-kinetics is used to express the evolution of each molar concentration towards equi-

[1] The threshold value of 0.98, as boundary between the applicability of the complete reaction, Eq. (4.11), comes from the experimental observation that CO is produced even for $\phi \approx 1$.

Table 4.1: Summary of the reaction constants in Eq. (4.16).

forward reaction		reverse reaction	
$\mathcal{K}_{\mathrm{Ze}}^{1+}$	$7.6\,10^{13}\,\mathrm{e}^{\frac{-38000}{T_{\mathrm{bg}}}}$	$\mathcal{K}_{\mathrm{Ze}}^{1-}$	$1.6\,10^{13}$
$\mathcal{K}_{\mathrm{Ze}}^{2+}$	$6.4\,10^{9}\,T_{\mathrm{bg}}\,\mathrm{e}^{\frac{-3150}{T_{\mathrm{bg}}}}$	$\mathcal{K}_{\mathrm{Ze}}^{2-}$	$1.5\,10^{9}\,T_{\mathrm{bg}}\,\mathrm{e}^{\frac{-19500}{T_{\mathrm{bg}}}}$
$\mathcal{K}_{\mathrm{Ze}}^{3+}$	$4.1\,10^{13}$	$\mathcal{K}_{\mathrm{Ze}}^{3-}$	$2.0\,10^{14}\,\mathrm{e}^{\frac{-23650}{T_{\mathrm{bg}}}}$

librium:

$$\left.\frac{dX_i}{dt}\right|_{\mathrm{CO}} = \frac{X_i - X_i^{\mathrm{eq}}}{\tau_{\mathrm{chem}}} \quad \text{for} \quad i = \mathrm{N_2, N, O_2, O, CO, CO_2, H_2, H, OH, H_2O}. \tag{4.15}$$

with τ_{chem} a relaxation time, linearly dependent on T_{bg}. This mechanism is only considered for $T_{\mathrm{bg}} > 1700K$, while CO kinetics are neglected for lower temperatures.

Nitrogen monoxide (NO) An extended Zel'dovitch mechanism:

$$\begin{cases} \mathrm{N_2 + O} \rightleftharpoons \mathrm{NO + N} \\ \mathrm{O_2 + N} \rightleftharpoons \mathrm{NO + O} \\ \mathrm{OH + N} \rightleftharpoons \mathrm{H + NO} \end{cases} \tag{4.16}$$

is used to describe NO formation for $T_{\mathrm{bg}} > 2500K$, while for lower temperature NO formation is neglected. The rate of production of NO is expressed as:

$$\begin{aligned} \left.\frac{dX_{\mathrm{NO}}}{dt}\right|_{\mathrm{Ze}} = \; & +\mathcal{K}_{\mathrm{Ze}}^{1+} X_{\mathrm{O}} X_{\mathrm{N_2}} \quad +\mathcal{K}_{\mathrm{Ze}}^{2+} X_{\mathrm{N}} X_{\mathrm{O_2}} \quad +\mathcal{K}_{\mathrm{Ze}}^{3+} X_{\mathrm{N}} X_{\mathrm{OH}} + \\ & -\mathcal{K}_{\mathrm{Ze}}^{1-} X_{\mathrm{N}} X_{\mathrm{NO}} \quad -\mathcal{K}_{\mathrm{Ze}}^{2-} X_{\mathrm{O}} X_{\mathrm{NO}} \quad -\mathcal{K}_{\mathrm{Ze}}^{3-} X_{\mathrm{H}} X_{\mathrm{NO}} \end{aligned} \tag{4.17}$$

with X_i denoting the molar concentrations of the species involved in Eq. (4.16). The values of the reaction constants that appear in Eq. (4.16) are summarized in Table 4.1.

Unburned hydrocarbons (HC). CFM1D models the production of this pollutant by the fresh gas stored in the crevices. The amount of Unburned hydrocarbons released in the burnt gas during an engine cycle is estimated calculating the mixture mass trapped in the crevices during flame propagation.

In fact, these zones are not reached by the flame front and stock fresh mixture when pressure rises. During the expansion stroke, cylinder pressure drops and this fresh mixture is released from the crevices into the burnt gas, where it can find favourable conditions to oxidize.

The fuel released from the crevices to the burned gas, is subsequently oxidized according to the reaction scheme in Eq.s (4.11 – 4.12). The reaction rate is controlled by the following Arrhenius law:

$$\left.\frac{dX_{\mathrm{Fu}}}{dt}\right|_{\mathrm{HC}} = 7.7\,10^{15}\,\mathrm{e}^{\frac{-37230}{1.987\,T}}\,X_{\mathrm{Fu}}\,X_{\mathrm{O_2}} \tag{4.18}$$

The total mass rate of production/destruction of each species due to post-flame reactions in the burned gas is therefore:

$$\frac{d\mathcal{M}_i^{\mathrm{po}}}{dt} = M_i V_{\mathrm{bg}} \left(\left.\frac{dX_i}{dt}\right|_{\mathrm{CO}} + \left.\frac{dX_i}{dt}\right|_{\mathrm{Ze}} + \left.\frac{dX_i}{dt}\right|_{\mathrm{HC}} \right) \quad \text{for} \quad i = 1, \ldots, N_{\mathrm{SP}}. \tag{4.19}$$

with M_i the molar mass of the i-th species and V_{bg} the volume of the burned gas zone.

4.1.4 Balance equations for the gas zones

With the CFM approach, the flame front identifies two separate zones – the fresh gas and the burnt gas – in the cylinder. Their evolutions are described by differential equations for the species masses $\mathcal{M}_i$ (M) and enthalpies $\mathcal{H}$ (ML^2T^{-2}), for the cylinder gas as a whole and the fresh gas.

The mean pressure – assumed homogeneous in the cylinder – is computed from the cylinder volume, total enthalpy and species masses using a perfect gas state equation. The fresh gas volume V_{fg} is determined likewise, from the mean pressure and fresh gas composition and enthalpy.

The burnt gas extensive properties, on the other hand, are then obtained by subtracting the ones of fresh gas from those of the cylinder gas.

Mean cylinder gas state

The masses of each of the N_{SP} species evolve according to:

$$\dot{\mathcal{M}}_i = \dot{\mathcal{M}}_i^{\text{va}} + \dot{\mathcal{M}}_i^{\text{bb}} + \dot{\mathcal{M}}_i^{\text{ff}} + \dot{\mathcal{M}}_i^{\text{po}} \quad \text{with} \quad i = 1, \ldots, N_{SP} \tag{4.20}$$

where the following terms appear:

the flow through the intake and exhaust valves $\dot{\mathcal{M}}^{\text{va}}$ is an input to the model and is decomposed into a positive and a negative contribution:

$$\dot{\mathcal{M}}^{\text{va}} = \dot{\mathcal{M}}^{\text{va in}} + \dot{\mathcal{M}}^{\text{va out}} \tag{4.21}$$

As a general rule the exhaust flow has the same composition as the cylinder gas, while the intake flow composition is fixed by a boundary condition:

$$\dot{\mathcal{M}}_i^{\text{va}} = \dot{\mathcal{M}}_i^{\text{va in}} + \frac{\mathcal{M}_i}{\mathcal{M}} \dot{\mathcal{M}}^{\text{va out}} \quad \text{with} \quad i = 1, \ldots, N_{SP} \tag{4.22}$$

buffer volumes keep track of the gas composition in the admission/exhaust ducts to account for backflows;

blow-by flow $\dot{\mathcal{M}}^{\text{bb}}$ is also an input to the model and it's treated as the valve flow:

$$\dot{\mathcal{M}}_i^{\text{bb}} = \dot{\mathcal{M}}_i^{\text{bb in}} + \frac{\mathcal{M}_i}{\mathcal{M}} \dot{\mathcal{M}}^{\text{bb out}} \quad \text{with} \quad i = 1, \ldots, N_{SP} \tag{4.23}$$

In order to simplify the description, the blow-by and valve flow terms will be grouped together into general inflow, $\dot{\mathcal{M}}_i^{\text{in}}$, and outflow, $\dot{\mathcal{M}}_i^{\text{in}}$, as:

$$\dot{\mathcal{M}}^{\text{va}} + \dot{\mathcal{M}}^{\text{bb}} = \dot{\mathcal{M}}^{\text{in}} + \dot{\mathcal{M}}^{\text{out}} \tag{4.24}$$

flame front reaction introduce production and destruction terms for the species involved $\dot{\mathcal{M}}_i^{\text{ff}}$: their values follow from the burning rate, Eq. (4.9), and the chemical scheme described by Eq.s (4.11 – 4.12).

post-oxidation reactions $\dot{\mathcal{M}}_i^{\text{po}}$ summarize the production/destruction of the species involved as shown in Eq.s (4.14 – 4.16).

Equation (4.20) provides, once integrated, the total mass $\mathcal{M}$ and composition Y_i (for $i = 1, \ldots, N_{SP}$):

$$\begin{aligned} \mathcal{M} &= \textstyle\sum_{i=1}^{N_{SP}} \mathcal{M}_i \\ Y_i &= \frac{\mathcal{M}_i}{\mathcal{M}} \qquad \text{with} \quad i = 1, \ldots, N_{SP} \end{aligned} \tag{4.25}$$

Cylinder volume V and its derivative $\dot{V}$ are derived from piston position and velocity, both model inputs provided by connecting the combustion chamber model to an imposed angular velocity boundary condition with a slider-crank linkage.

The mean pressure p is used as an additional state variable to completely determine the average thermodynamic conditions in the cylinder. Its evolution is derived from the perfect gas equation as:

$$\dot{p} = R\rho\dot{T} + RT\dot{\rho} + T\rho\dot{R} \tag{4.26}$$

in terms of the:

gas constant R whose value only depends on the gas composition:

$$R = \sum_{i=1}^{N_{SP}} R_i Y_i = \sum_{i=1}^{N_{SP}} \frac{R^*}{M_i} Y_i \tag{4.27}$$

with M_i and R_i the molar mass and gas constant of the i-th species and $R^* = 8.314\,\mathrm{J\,K^{-1}\,mol^{-1}}$ the universal gas constant;

density ρ is a function of the mass flows and volume:

$$\dot{\rho} = \frac{\dot{\mathcal{M}}}{V} - \rho\frac{\dot{V}}{V} \tag{4.28}$$

temperature T whose evolution is derived substituting the energy conservation equation expressed as:

$$\dot{\mathcal{U}} = -p\,\dot{V} + \dot{\mathcal{H}}^{\mathrm{va}} + \dot{Q}^{\mathrm{ff}} + \dot{Q}^{\mathrm{po}} + Q_W \tag{4.29}$$

in terms of the internal energy of the gas $\mathcal{U}$ into:

$$\dot{T} = \frac{\dot{\mathcal{U}} - \dfrac{\mathcal{U}}{\mathcal{M}}\dot{\mathcal{M}} - \mathcal{M}\sum_{i=1}^{N_{SP}} u_i \dot{Y}_i}{c_V\,\mathcal{M}} \tag{4.30}$$

with u_i the internal energy per unit mass of the i-th species.

Eq. (4.29) includes source terms related to mass transfer and chemical reactions, that correspond to those of Eq. (4.20):

intake and exhaust valve flow the enthalpy transported by the mass flows entering and leaving the cylinder can be expressed as:

$$\dot{\mathcal{H}}^{\mathrm{va}} = h_0^{in}\dot{\mathcal{M}}^{\mathrm{in}} - \frac{\mathcal{H}}{\mathcal{M}}\dot{\mathcal{M}}^{\mathrm{out}}$$

where – similarly to the compositions in Eq. (4.20) – the specific enthalpy of the intake flow, h_0^{in}, is provided as a boundary condition while that of the exhaust flow is based on the average cylinder gas properties;

heat release $\dot{Q}_{\mathrm{ff}}$ and $\dot{Q}_{\mathrm{po}}$ indicate, respectively, the heat release by the chemical reactions in the flame front and during post oxidation; these terms are calculated based on the chemical reaction schemes described in Eq.s (4.11 – 4.12) and Eq.s (4.14 – 4.16), respectively, and the enthalpies of formation of the chemical species involved.

wall heath flux Q_W indicates the heat flux transferred to all the solid walls (cylinder head, piston and liner) and is calculated with the Woschni (1967) model;

as well as the piston work $-p\dot{V}$.

Fresh gas state

The equation for the fresh gas mass follows from Eq. (4.20) under the hypothesis that the valve flow:

- is directed to the fresh gas zone when it enters the cylinder;
- is taken from the fresh and burned gas zones – proportionally to their respective masses – when it exits the cylinder.

This is consistent with the approach adopted since the intake takes place before combustion and the fresh gas is reinitialized as:

$$\mathcal{M}_{i\,\mathrm{fg}} = \mathcal{M}_i \quad \text{with} \quad i = 1, \ldots, N_{SP} \tag{4.31}$$

at IVC. The balance equations for the mass of each species in the fresh gas is therefore:

$$\dot{\mathcal{M}}_{i\,\mathrm{fg}} = \dot{\mathcal{M}}_i^{\mathrm{in}} + \frac{\mathcal{M}_{i\,\mathrm{fg}}}{\mathcal{M}} \dot{\mathcal{M}}^{\mathrm{out}} - Y_{i\,\mathrm{fg}}\, \rho_{\mathrm{fg}}\, s_L\, \mathcal{A}_T \quad \text{with} \quad i = 1, \ldots, N_{SP} \tag{4.32}$$

where the sink term representing the propagation of the flame front only depends on the fresh gas composition ($Y_{i\,\mathrm{fg}}$) regardless of the kinetic scheme used.

The thermodynamic state of the fresh gas is defined by the values of two state functions: the thermodynamic pressure p is assumed to be uniform in the cylinder and have the same value for the fresh and burnt gas while the fresh gas enthalpy evolves according to

$$\dot{\mathcal{H}}_{\mathrm{fg}} = V_{\mathrm{fg}}\, \dot{p} - \frac{V_{\mathrm{fg}}}{V} Q_W + h_0^{\mathrm{in}}\, \dot{\mathcal{M}}^{\mathrm{in}} + \frac{\mathcal{H}_{\mathrm{fg}}}{\mathcal{M}_{\mathrm{fg}}} \dot{\mathcal{M}}^{\mathrm{out}} \tag{4.33}$$

which differs from Eq. (4.29) in the expression of:

the wall heath flux Q_W, which is split between the fresh and burnt gas proportionally to the respective volumes;

the pressure term $V_{\mathrm{fg}}\, \dot{p}$ represents the enthalpy variation due to the compression of the fresh gas as a result of piston displacement and burned gas expansion.

4.2 Overview of the new developments

The main goal of this work is to develop and integrate new features into the CFM-1D model – described in Section 4.1 – to make it suitable for gasoline direct injection combustion process computations. Particular attention was paid to the physics related to multi-phase flow, evaporation and mixing that directly impact combustion with a clear effect on performance and emissions. The new developments can be summarized by the following steps:

- a new zone was added to the original fresh/burned gas partitioning; this zone – that we call here *reactive charge* – identifies the region where air and vapour fuel mix;

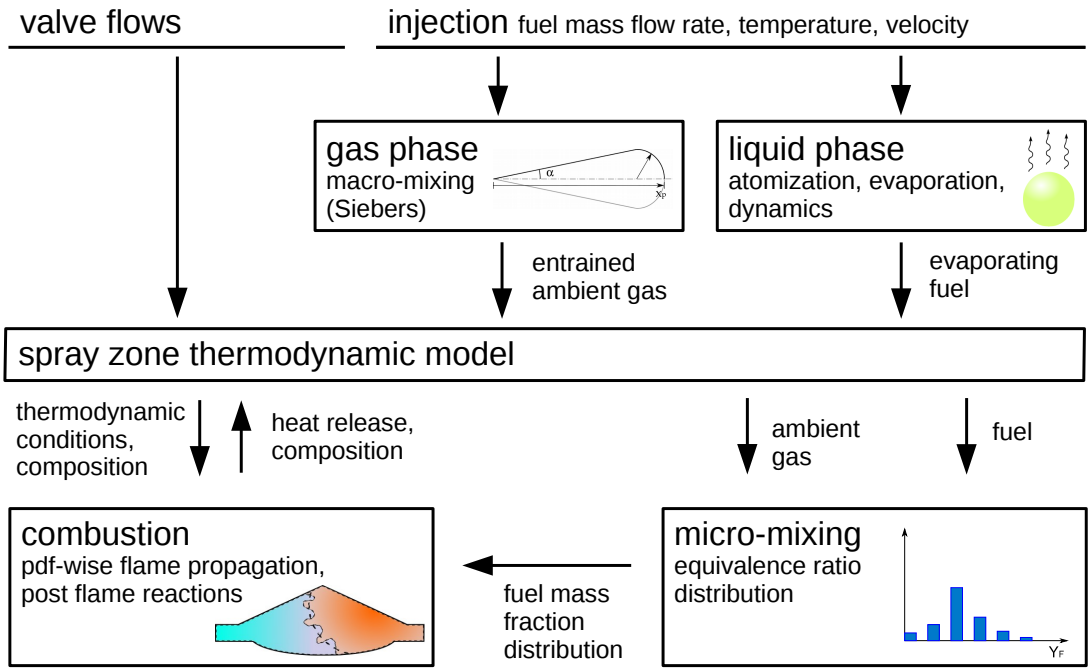

Figure 4.2: Schematic decomposition of the new model in elementary blocks: the arrows identify input and output of each block and indicate their interactions.

- a description of the liquid phase, discretized in drop parcels, that follows the evolution of drop size, velocity and temperature in time – for each parcel – allows to retrieve the value of the evaporation rate; this approach also provides additional information such as position and velocity of fuel drops, that can further be used to predict the impact on piston wall and film formation;
- a model for spray penetration and spreading rate allows to predict the entrainment of ambient gas in the reactive charge zone;
- a small scale mixing model based on a discrete probability density function (PDF) for the equivalence ratio is used to provide a description of the stratified charge to refine the characterization of combustion;
- the existing combustion model is modified to account for very rich mixtures and coupled with the PDF.

An overview of these elementary blocks of the new model – described in detail in the following sections – is given in Fig. 4.2.

4.3 Three-zone thermodynamic model

The introduction of direct injection complicates the zoning approach of the CFM-1D with the creation of a new *ambient gas zone* representing the portion of cylinder gas that has not been reached by the injection and where no reaction takes place. This distinction is necessary for stratified DI-SI engines, where high efficiency at partial load is achieved through globally lean operation: injection takes place late in the compression stroke in order to have a nearly stoichiometric charge in a portion of the combustion chamber, and in particular close to the spark plug at spark timing, and uncarburated air (and diluent) elsewhere.

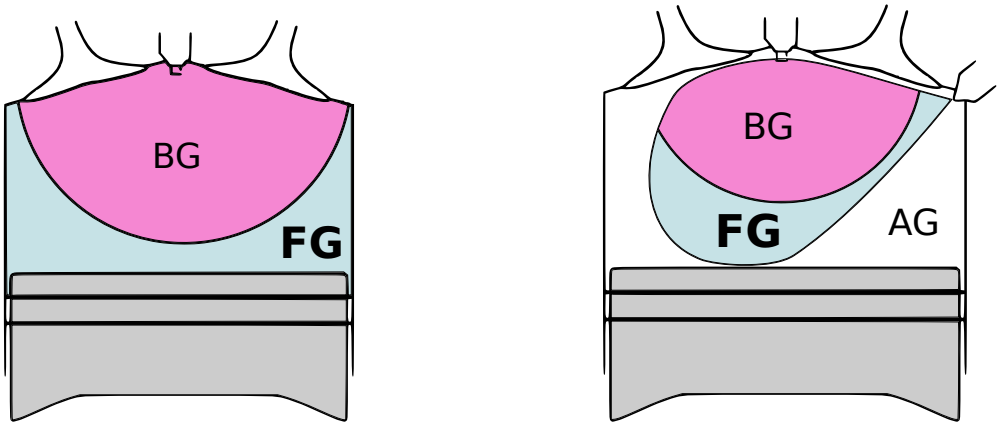

(a) Two zones approach (old model): the flame front separates the burnt (BG) from the fresh gas (FG). The whole chamber is occupied by a fuel/air mixture.

(b) Three zones approach (new model): the flame front develops inside the fuel/air mixing zone (RC), while the rest of the chamber is occupied by Ambient Gas, AG.

Figure 4.3: New zoning approach: with the introduction of direct injection a fuel/air mixing zone is created, fresh (FG) and burned (BG) mixtures only exist within a portion of the cylinder while the rest of the chamber is occupied by air and diluent that constitute the new *Ambient Gas* (AG) zone.

In homogeneous DI-SI engines, fuel is injected during intake or early in the compression stroke so that ignition takes place when the ambient gas zone is empty. In such engines – that are the main focus of this work – flame propagation sweeps the whole cylinder volume as happens in indirect injection (and carburated) engines (Fig. 4.3a), so that following the evolution of this additional zone during combustion is not relevant. Its development *before* combustion, on the other hand, is necessary to characterize the small-scale charge inhomogeneities with a model that takes into account the *history* of air/fuel mixing.

For these reasons, the zoning approach presented in Section 4.1.4, on which the conservation Eq.s (4.20 – 4.33) are based, was modified according to Fig. 4.3b, introducing the new *Ambient Gas* (AG) zone, that contains uncarburated air and diluent. The three zones shown in Fig. 4.3b may not all exist simultaneously depending on the engine concept and operating conditions: in homogeneous operation, for example, the mixture is generally ignited after the reactive charge has filled the combustion chamber, so that at least one of the the AG and BG zones is empty. Taking all the zones into account allows nevertheless to:

- build a more general model with a wider range of application (stratified and homogeneous);
- obtain the exact reactive charge composition and mixture fraction distribution, that depends on the history of reactive/ambient gas mixing.

In the original modelling approach presented in Section 4.1.4, the two gas zones (FG and BG) are modelled solving conservation equations for the total mass a and FG and determining the state of BG by difference. Likewise it was chosen here to solve mass and energy conservation equations for the following, *primary*, zones:

Cylinder gas (BG+FG+AG) includes the whole gas mass, as in the original CFM-1D model for indirect injection and is still described by Eq.s (4.20 – 4.30);

Reactive charge (RC = BG+FG) is created during injection and fed with the evaporating fuel and entrained air: combustion takes place in the reactive charge, whose

evolution is described by Eq.s (4.35 – 4.36);

Fresh gas (FG) includes only the unburned gas in the reactive charge zone and is described by Eq.s (4.39 – 4.40).

The state variables of the burned and ambient gas are determined by difference:

$$\begin{aligned} \mathcal{M}_{\mathrm{bg}} &= \mathcal{M}_{\mathrm{rc}} - \mathcal{M}_{\mathrm{fg}} \qquad & \mathcal{H}_{\mathrm{bg}} &= \mathcal{H}_{\mathrm{rc}} - \mathcal{H}_{\mathrm{fg}} \\ \mathcal{M}_{\mathrm{ag}} &= \mathcal{M} - \mathcal{M}_{\mathrm{rc}} & \mathcal{H}_{\mathrm{ag}} &= \mathcal{H} - \mathcal{H}_{\mathrm{rc}} \end{aligned} \tag{4.34}$$

This choice was made in order to highlight the physical phenomena that produce each flow:

- valve flow and blow-by affect the cylinder gas;
- air entrainment into the spray affects the reactive charge and ambient gas;
- flame-front reaction affects the fresh and burned gas.

Describing, for example, the reactive charge and ambient gas as primary zones, would lead to two equations containing the entrained mass as a source term (one for the reactive charge and one for the ambient gas) and no equation including the whole valve flow, making the model less readable.

4.3.1 Balance equations for the primary gas zones

This section presents the conservation equations for energy and mass used to describe the state of the three primary zones. Fig. 4.3b.

The first zone, containing all cylinder gas and defining its mean state, is unchanged in the new model: its evolution is described by Eq.s (4.20 – 4.30) introduced in Section 4.1.4.

The following paragraphs illustrate the conservation equations that define the state of the reactive charge (RC) gas zone, introduced with the new model, and the fresh (FG) gas zone, contained in the reactive charge according to its new definition.

Reactive charge state (RC=FG+BG)

The reactive charge zone is created at the beginning of injection, so that its initial masses $\mathcal{M}_{i\,\mathrm{rc}}$ are all null. The evolution of the mass of each species is described by:

$$\dot{\mathcal{M}}_{i\,\mathrm{rc}} = \frac{\mathcal{M}_{\mathrm{rc}}}{\mathcal{M}}\dot{\mathcal{M}}_i^{\mathrm{in}} + \frac{\mathcal{M}_{i\,\mathrm{rc}}}{\mathcal{M}}\dot{\mathcal{M}}^{\mathrm{out}} + \dot{\mathcal{M}}_i^{\mathrm{ent}} + \dot{\mathcal{M}}_i^{\mathrm{ev}} + \dot{\mathcal{M}}_i^{\mathrm{ff}} + \dot{\mathcal{M}}_i^{\mathrm{po}} \quad \text{with} \quad i = 1, \ldots, N_{\mathrm{SP}} \tag{4.35}$$

is at first dominated by ambient gas entrainment $\dot{\mathcal{M}}_i^{\mathrm{ent}}$ and evaporation $\dot{\mathcal{M}}_i^{\mathrm{ev}}$ that will be detailed in the description of the spray model, sections 4.4 – 4.5.

If injection occurs during the intake phase, the mass flows entering, $\dot{\mathcal{M}}_i^{\mathrm{in}}$, and exiting, $\dot{\mathcal{M}}^{\mathrm{out}}$, the cylinder through intake, exhaust and blow-by, are split between the reactive charge (RC) and ambient gas (AG), proportionally to the respective masses of the two zones.

During combustion, the terms related to flame front propagation $\dot{\mathcal{M}}_i^{\mathrm{ff}}$ and post-flame chemical reactions $\dot{\mathcal{M}}_i^{\mathrm{po}}$ affect the composition of the reactive charge with no impact on the global mass.

Table 4.2: Summary of the main variables in the evolution equations of the 3-zone thermodynamic model.

Subscripts		
$\mathcal{M}_i$	Mass the i-th chemical specie.	When omitted a sum over all the species is implied.
$\mathcal{M}_{\text{rc}}$ ($\mathcal{H}_{\text{rc}}$)	Mass (enthalpy) of the reactive charge (FG+BG).	When omitted the variables are referred to the cylinder gas (SP+AG = FG+BG+AG).
$\mathcal{M}_{\text{fg}}$ ($\mathcal{H}_{\text{fg}}$)	Mass of the fresh gas (FG).	
$\mathcal{M}_{\text{bg}}$ ($\mathcal{H}_{\text{bg}}$)	Mass of the burned gas (BG).	
$\mathcal{M}_{\text{ag}}$ ($\mathcal{H}_{\text{ag}}$)	Mass of the ambient gas (AG).	
Mass source and transfer terms		
$\dot{\mathcal{M}}^{\text{in}}$	Mass entering the cylinder through the intake and exhaust valves and blow-by.	
$\dot{\mathcal{M}}^{\text{out}}$	Mass leaving the cylinder through the intake and exhaust valves and blow-by.	
$\dot{\mathcal{M}}^{\text{ent}}$	Entrained ambient gas mass, provided by the model detailed in Section 4.5	
$\dot{\mathcal{M}}_i^{\text{ev}}$	Evaporating mass, provided by the model detailed in Section 4.4.	
$\dot{\mathcal{M}}_i^{\text{ff}}$	Front flame reactions : represents the chemical reactions that take place at the flame front (the total mass is conserved so that $\sum_i \dot{\mathcal{M}}_i^{\text{ff}} = 0$)	
$\dot{\mathcal{M}}_i^{\text{po}}$	Post-oxidation reactions : represents the chemical reaction that take place in the burned gas (the total mass is conserved so that $\sum_i \dot{\mathcal{M}}_i^{\text{po}} = 0$)	
Energy source and transfer terms		
$\dot{Q}_W$	Heat exchange at the combustion chamber boundary (piston, liner and cylinder head walls).	
$\dot{Q}_{\text{ff}}$	Heat released by flame-front reactions.	
$\dot{Q}_{\text{po}}$	Heat released by post-oxidation reactions.	
h_0^L	Initial specific enthalpy (L^2T^{-2}) of the liquid fuel.	
h_0^{in}	Initial specific enthalpy (L^2T^{-2}) of the gas entering the cylinder.	

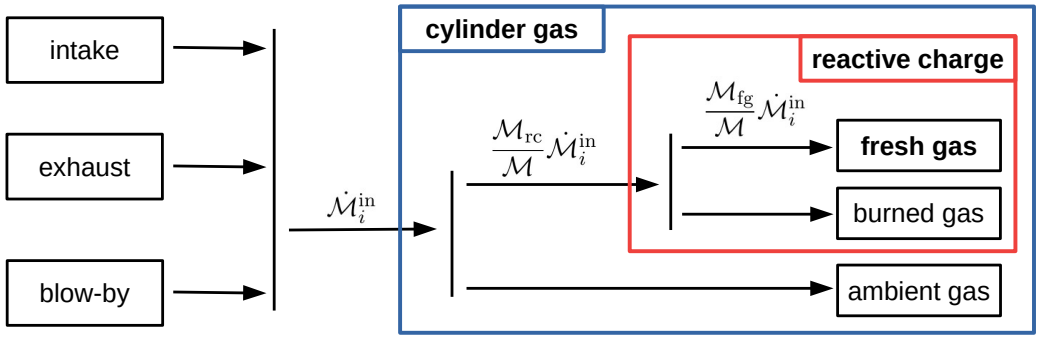

(a) Flows entering the cylinder.

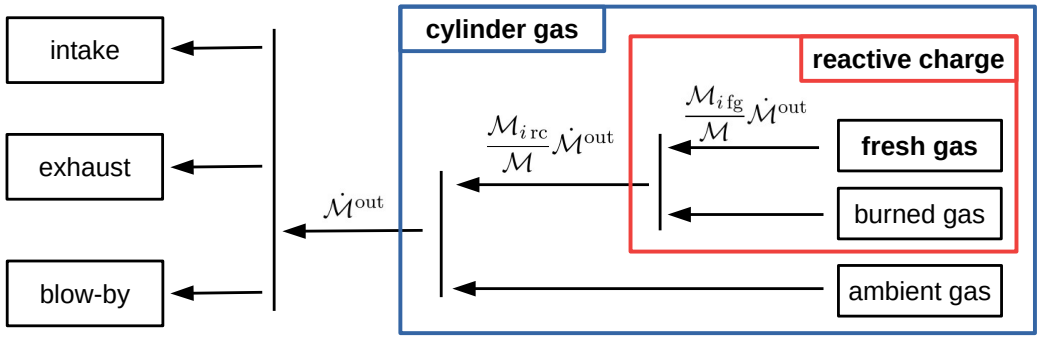

(b) Flows exiting the cylinder.

Figure 4.4: The 3-zone thermodynamic model: distribution of the external flows between the different gas zones of the thermodynamic model. Mass and energy conservation equations are solved to determine the state of the zones indicated in bold.

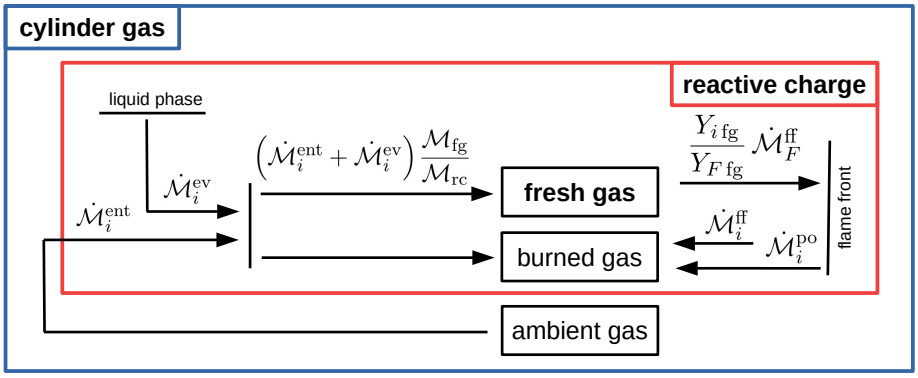

Figure 4.5: The 3-zone thermodynamic model: internal flows between the different gas zones of the thermodynamic model. Mass and energy conservation equations are solved to determine the state of the zones indicated in bold.

The thermodynamic state of the reactive charge is determined once its enthalpy and the cylinder pressure are known. Both are obtained from energy conservation: the former applying the first principle of thermodynamics to the reactive charge:

$$\dot{\mathcal{H}}_{\rm rc} = V_{\rm rc}\,\dot{p} - \frac{V_{\rm rc}}{V}\,Q_W + \dot{Q}_{\rm ff} + \dot{Q}_{\rm po} + h_0^L\,\dot{\mathcal{M}}^{\rm ev} + \left(h_0^{\rm in}\,\dot{\mathcal{M}}^{\rm in} + \frac{\mathcal{H}_{\rm rc}}{\mathcal{M}_{\rm rc}}\,\dot{\mathcal{M}}^{\rm out}\right)\frac{\mathcal{M}_{\rm rc}}{\mathcal{M}} \tag{4.36}$$

and the latter from Eq. (4.26), that applies the same principle to the mean cylinder gas, identified by the first zone (RC+AG).

The heat exchanged with solid walls Q_W is split between the reactive charge and ambient gas proportionally to the respective volumes, while the heat resulting from combustion,[2] $\dot{Q}_{\rm ff} + \dot{Q}_{\rm po}$, is entirely released in the reactive charge.

The evaporation term $h_0^L\,\dot{\mathcal{M}}^{\rm ev}$ introduces the evaporating mass with its specific enthalpy at injection conditions in Eq. (4.36), instead of using its value during evaporation and introducing a heat-up term. This approximation condensates the two effects in one, slightly delays the cooling effect of injection on the gas phase. However, since the energy absorbed for heat-up and vaporization is taken from the reactive charge gas, it does not alter the energy balance of this zone[3].

The pressure term, $V_{\rm rc}\,\dot{p}$, term includes the mechanical work exchanged with the outer gas region and solid walls.[4]

Mass flow through the inlet and exhaust valves and blow-by is split between the reactive charge (RC) and ambient gas (AG) proportionally to the respective masses with the usual convention that inflow carries the specific enthalpy of the inlet boundary condition, i.e. the enthalpy of the gas contained in the volume immediately upstream the intake valve:

$$\dot{\mathcal{H}}_{\rm rc}^{\rm in} = h_0^{\rm in}\,\frac{\mathcal{M}_{\rm rc}}{\mathcal{M}}\dot{\mathcal{M}}^{\rm in} \tag{4.37}$$

[2]The heat released during flame propagation, $\dot{Q}_{\rm ff}$, is calculated from the enthalpies of formation of the species involved, considering a fuel mass $\dot{\mathcal{M}}_F^{\rm ff}$ reacting according to the chemical scheme described in Section 4.7.1. The term $\dot{\mathcal{M}}_i^{\rm po}$ is computed likewise, considering the reaction of a mass of CO, $\dot{\mathcal{M}}_{\rm CO}^{\rm po}$, according to Eq. (4.14) and the reaction of a mass of NO, $\dot{\mathcal{M}}_{\rm NO}^{\rm po}$, according to Eq. (4.16).

[3] The evaporation model adopted in this work, and discussed in Section4.4, discretizes the liquid phase in N_P drop parcels. The energy balance of the reactive charge gas should be written taking into account the fact that each drop parcel evaporates at a different liquid temperature, thus the fuel it introduces in the gas zone has a different specific enthalpy, h_i. Likewise, the energy needed to heat-up a drop parcel, $\dot{\mathcal{H}}_L^i$, is taken from the surrounding gas. The approximation adopted in this work, consists of substituting the rhs of the following equation with it lhs:

$$h_0^L\,\dot{\mathcal{M}}^{\rm ev} \approx \sum_{i=1}^{N_P}\left(h_i\dot{\mathcal{M}}_{\rm ev}^i - \dot{\mathcal{H}}_L^i\right)$$

thus condensating the two effects in the moment of evaporation. Their equivalence is only verified for the integrals over the evaporation time of the two quantities:

$$\int_{\rm evap} h_0^L\,\dot{\mathcal{M}}^{\rm ev}dt = \int_{\rm evap}\sum_{i=1}^{N_P}\left(h_i\dot{\mathcal{M}}_{\rm ev}^i - \dot{\mathcal{H}}_L^i\right)dt$$

and derives from the energy balance of the liquid phase.

[4]The definition of enthalpy:

$$\mathcal{H}_{\rm rc} = \mathcal{U}_{\rm rc} + V_{\rm rc}\,p$$

leads to the following expression of the pressure term in Eq. (4.36):

$$V_{\rm rc}\,\dot{p} = \dot{\mathcal{H}}_{\rm rc} - \dot{\mathcal{U}}_{\rm rc} - \dot{V}_{\rm rc}\,p$$

Eq. (4.36) can therefore be rewritten replacing the enthalpy, $\mathcal{H}_{\rm rc}$, with the internal energy, $\mathcal{U}_{\rm rc}$, and the pressure term, $V_{\rm rc}\,\dot{p}$, with the thermodynamical work, $-\dot{V}_{\rm rc}\,p$.

while outflow advects mass from the reactive charge with its specific properties:

$$\dot{\mathcal{H}}_{\mathrm{rc}}^{\mathrm{out}} = \frac{\mathcal{H}_{\mathrm{rc}}}{\mathcal{M}_{\mathrm{rc}}} \frac{\mathcal{M}_{\mathrm{rc}}}{\mathcal{M}} \dot{\mathcal{M}}^{\mathrm{out}} = h_{\mathrm{rc}} \frac{\mathcal{M}_{\mathrm{rc}}}{\mathcal{M}} \dot{\mathcal{M}}^{\mathrm{out}} \tag{4.38}$$

Fresh gas (FG) state

The main difference in the definition of the fresh gas with respect to the two zone approach is that the former is considered here as a subset of the reactive charge, which is created when injection starts. This zone is therefore empty at IVO and its growth is an effect of air entrainment, evaporation and intake flow[5] while flame propagation and blow-by reduce it, the former transferring mass to the burned gas, the latter leaking it out of the cylinder.

The species masses in the fresh gas are given by:

$$\dot{\mathcal{M}}_{i\,\mathrm{fg}} = \frac{\mathcal{M}_{\mathrm{fg}}}{\mathcal{M}} \dot{\mathcal{M}}_i^{\mathrm{in}} + \frac{\mathcal{M}_{i\,\mathrm{fg}}}{\mathcal{M}} \dot{\mathcal{M}}^{\mathrm{out}} + \left(\dot{\mathcal{M}}_i^{\mathrm{ent}} + \dot{\mathcal{M}}_i^{\mathrm{ev}} \right) \frac{\mathcal{M}_{\mathrm{fg}}}{\mathcal{M}_{\mathrm{rc}}} - \frac{Y_{i\,\mathrm{fg}}}{Y_{F\,\mathrm{fg}}} \dot{\mathcal{M}}_F^{\mathrm{ff}} \quad \text{with} \quad i = 1, \ldots, N_{\mathrm{SP}} \tag{4.39}$$

where the entrained and evaporating mass flows are split between fresh and burnt gas proportionally to their masses.[6]. The combustion term only depends on the fresh gas composition, $Y_{i\,\mathrm{fg}}$ with $i = 1, \ldots, N_{\mathrm{SP}}$, and on the fuel mass burning rate $\dot{\mathcal{M}}_F^{\mathrm{ff}}$ provided by the stratified combustion model, detailed in Section 4.7

The energy balance of the fresh gas is affected by the mass flows that affect this zone and by the energy exchanged with the other zones in the form of expansion work ($V_{\mathrm{fg}}\,\dot{p}$) and with walls (Q_W).

The resulting equation for the fresh gas enthalpy is:

$$\dot{\mathcal{H}}_{\mathrm{fg}} = V_{\mathrm{fg}}\,\dot{p} - \frac{V_{\mathrm{fg}}}{V} Q_W + h_0^L\, \dot{\mathcal{M}}_i^{\mathrm{ev}} \frac{\mathcal{M}_{\mathrm{fg}}}{\mathcal{M}_{\mathrm{rc}}} + \left[(h_0^{\mathrm{in}}\, \dot{\mathcal{M}}^{\mathrm{in}} + \frac{\mathcal{H}_{\mathrm{fg}}}{\mathcal{M}_{\mathrm{fg}}} \left(\dot{\mathcal{M}}^{\mathrm{out}} - \dot{\mathcal{M}}^{\mathrm{ff}} \right) \right] \frac{\mathcal{M}_{\mathrm{fg}}}{\mathcal{M}} \tag{4.40}$$

4.4 Liquid Phase Description

This section details how the liquid phase is described in the model focusing on the discretization of the liquid mass in drop parcels and the models used to described atomization and evaporation.

4.4.1 Coupling atomization and evaporation models

An isolated-drop model, described in the previous chapter is used to predict the evaporation rate of the liquid phase. As seen in Section 2.1.2, the evaporation rate of an isolated drop in a gas stream depends strongly on its size as well as on the thermodynamic conditions of the two phases and their relative velocity. A real spray is a collection of liquid drops whose diameters, temperatures and velocities are randomly distributed around a mean value that is affected by:

[5] The intake flow is split between the reactive charge (RC) and ambient gas (AG) proportionally to their masses: the intake flow only feeds the reactive charge – and therefore the fresh gas – if this zone already exists, i.e. after the start of injection (SOI).

[6] If liquid drops are still present during combustion they are assumed to be equally distributed between fresh and burnt gas: their evaporation brings fuel vapour in the burned gas that participates in post-flame oxidation.

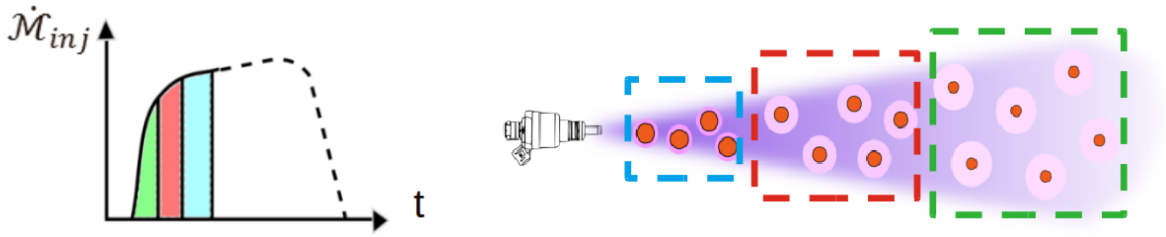

(a) Discretization of the injection profile.

(b) Homogeneous drop parcels.

Figure 4.6: Qualitative example of the homogeneous drop parcel approach: drops in the same parcel share similar atomization, evaporation and drag histories and are supposed to have the same characteristics (size, temperature and velocity).

atomization: the injection velocity and the mass flow rate, which varies throughout the injection, affect strongly the initial drop size and velocity;

evaporation: the size and temperature of a drop at a certain time t depends on the thermodynamic conditions and on the evaporation time $t - t_0$ (with t_0 the time when the drop was injected in the domain);

dynamic interaction with the gas phase: the drop slows down as it penetrates the gas phase so that the velocity of a particular drop at a certain time t is strongly dependent on the evaporation time, $t - t_0$.

A characterization of the evaporation of each drop of fuel in the combustion chamber would lead to an infeasible computational cost while modelling the whole spray with a unique reference drop would lack of precision. The compromise chosen in this work consists of a discretization of the injected mass, $\mathcal{M}_{\text{inj}}$, in a number, N_P, of drop parcels containing identical drops (same size, temperature, position and momentum). This identifies a non-uniform discretization of the injection time, since the injection rate is not necessarily constant, and the drop parcel have the same initial mass.

With the adopted definition, each parcel will contain drops that have been injected in the corresponding time interval (whose width depends on the fuel injection rate profile and on N_P). Each parcel models a collection of drops that have been created in similar break-up conditions (similar initial size) and that have been evaporating for comparable times (similar size evolution). For these two reasons, the drop parcels are modelled as collections of identical drops.

This simplification rules out the description of the intrinsic size variability that real injectors provide even in steady injection rate conditions but it provides a way of taking into account for the poor atomization during the injector transients and the effect of injection duration on drop size variance.

The coupling problem

The discretization of the liquid mass into parcels introduces a modelling issue related to the coupling of the atomization and evaporation models. A generic atomization model[7] provides

[7] This section discusses the coupling of an atomization and and evaporation model in general, the details of the models adopted to describe these two phenomena are given in the following sections.

the initial Sauter mean diameter, D_{32}^{inj}, as a function of the thermodynamic state of the liquid and gas phases $(T_{\mathrm{g}}, p_{\mathrm{g}}, T_{\mathrm{inj}})$, their compositions $(X_{\mathrm{g}}, X_{\mathrm{l}})$, the injection rate, $\dot{\mathcal{M}}_{\mathrm{inj}}(t)$, and nozzle geometry. All these parameters, except the latter are – in general – time-dependent so that D_{32}^{inj} also varies with time:

$$D_{32}^{\mathrm{inj}}(t) = f\left(T_{\mathrm{g}}(t), p_{\mathrm{g}}(t), T_{\mathrm{inj}}(t), X_{\mathrm{g}}(t), X_{\mathrm{l}}(t)\dot{\mathcal{M}}_{\mathrm{inj}}(t), \mathrm{geometry}\right) \tag{4.41}$$

Since the drop parcels take a finite time to be generated, the value of the Sauter mean diameter, D_{32}^{i}, provided by the atomization model for the generic i-th parcel, varies over the parcel injection time.

In order to provide a consistent initial condition for the isolated-drop evaporation model:

$$\left\{ \begin{array}{c} \dot{\mathcal{M}}_L \\ \dot{\mathcal{P}}_L \\ \dot{\mathcal{H}}_L \end{array} \right\} = f\left(T_{\mathrm{g}}(t), p_{\mathrm{g}}(t), \mathcal{M}_L(t), \mathcal{P}_L(t), \mathcal{H}_L(t), T_l(t), \dot{\mathcal{M}}_{\mathrm{inj}}(t)\right) \tag{4.42}$$

used to describe the evolution of the drop parcel, a mean drop – representative of the whole parcel – needs to be defined averaging, over the parcel injection time, Eq. (4.41), the injection velocity and temperature need to be averaged to obtain the initial drop mass, $\mathcal{M}_L(0)$, momentum, $\mathcal{P}_L(0)$, and enthalpy, $\mathcal{H}_L(0)$. The mean properties of a drop parcel will therefore only be available when it has completely been injected.

From the modelling point of view this means that the initial condition of the evaporation model of the i-th is only available when the $(i+1)$-th parcel is being injected. The evaporation model cannot run on the i-th parcel unless it has been completely injected.

The need to describe evaporation during the parcel injection time identifies the problem of coupling the evaporation and atomization models. Two approaches are presented in the following sections:

the two-step coupling the two-step coupling postpones the start of the evaporation of the i-th parcel after its complete injection; with respect to the parcel equations of state, the atomization model constitutes an initial condition while the evaporation model is a source term;

the continuous coupling initializes the evaporation model at the beginning of its injection: the initial condition provided is then continually updated during injection by means of an additional source term in its state equation; The atomization and evaporation model are then coupled and provide both source terms in the parcel equations of state.

Two-Step coupling

This method separates the injection from the evaporation of each parcel by splitting the two phenomena in time with a two step mechanism.

Step I - Injection: at first the parcel mass grows as a result of the injection and no evaporation takes place until the parcel is full. The overall mass $\mathcal{M}_L^i$, momentum $\mathcal{P}_L^i$ and

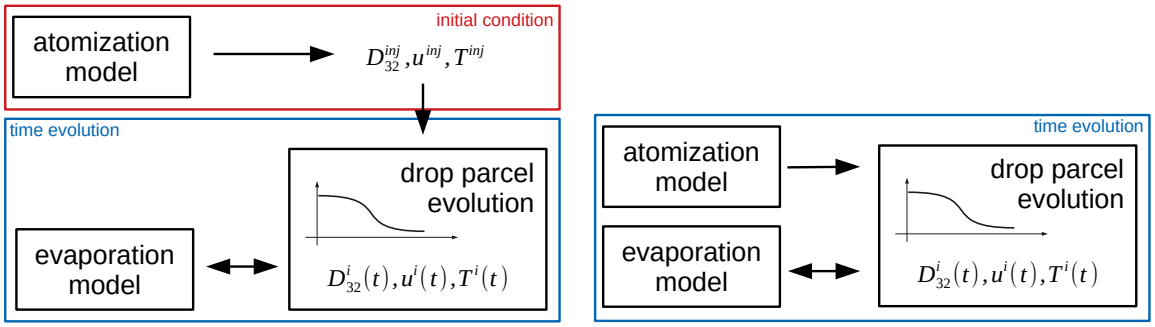

(a) 2-step coupling **(b)** Continuous coupling

Figure 4.7: Comparison of the two proposed coupling approaches to combine atomization and evaporation/drop dynamic models in the parcel-based liquid phase discretization.

enthalpy $\mathcal{H}_L^i$ of the liquid fuel are integrated as follows:

$$\mathcal{M}_L^i = \int_{t^i}^{t^{i+1}} \dot{\mathcal{M}}_{\text{inj}}(t)\, dt \tag{4.43}$$

$$\mathcal{P}_L^i = \int_{t^i}^{t^{i+1}} \dot{\mathcal{M}}_{\text{inj}}(t)\, u_{\text{inj}}(t)\, dt \tag{4.44}$$

$$\mathcal{H}_L^i = \int_{t^i}^{t^{i+1}} \dot{\mathcal{M}}_{\text{inj}}(t)\, h_0^L(t)\, dt \tag{4.45}$$

with t^i the time when the i-th parcel starts being filled, t^{i+1} the time when the i-th parcel reaches its final mass, $\mathcal{M}_{\text{inj}}/N_P$, and h_{inj} the specific enthalpy of the injected fuel.

Average atomization: the integral values of mass, momentum and enthalpy are used to calculate average injection velocity and temperature, representative of the parcel as a whole:

$$u^i = \frac{\mathcal{P}_L^i}{\mathcal{M}_L^i} \qquad h(T) = \frac{\mathcal{H}_L^i}{\mathcal{M}_L^i} \quad \rightarrow \quad T \tag{4.46}$$

These value are also used to characterize the mean injection conditions of the i-th drop parcel and lead to the evaluation of its Sauter Mean Diameter, D_{32}^i, using the model described in Section 4.4.2 which – together with the average temperature and velocity – provides the initial condition for the evaporation and dynamics models. The number of fuel drops in a parcel is derived from parcel mass and drop diameter:

$$n^i = \frac{6}{\rho_L\, \pi} \frac{\mathcal{M}_L^i}{{D_{32}^i}^3} \tag{4.47}$$

and is kept constant during the following step;

Step II - Evaporation: once the parcel has been initialized – the evaporation and dynamics models start in a second step, when the evolving variables are only affected by evaporation and liquid/gas dynamic interaction, according to the model described in Section 4.4.3

This approach is easier to implement and presents a lower computational cost since it separates positive and negative contributions to the package mass. It somehow mimics the real evolution of an isolated drop which is first created by atomization and subsequently evaporates, but it delays the evaporation, that starts when the parcel is completely injected.

Drop parcel description	
D_{32}^{inj}	Sauter mean diameter predicted by the atomization model.
D_{32}^{i}	Sauter mean diameter of the i-th drop parcel. It is a function of the atomization conditions and evolves due to evaporation.
$\mathcal{M}_L^i$	Mass of the i-th parcel.
n^i	Number of drops the i-th parcel.
$\mathcal{S}_L^i$	Surface of the i-th parcel (Continuous coupling only).
$\mathcal{H}_L^i$	Enthalpy of the i-th parcel.
$\mathcal{P}_L^i$	Momentum of the i-th parcel.
u^i	Velocity of the i-th parcel.
$\mathcal{X}_L^i$	Position of the i-th parcel.

Continuous coupling

Both weaknesses of the two-step method can be structurally overcome with the continuous coupling method devised here, that allows each parcel to evaporate while still being fed by the injected flow, assuring the continuity of the evaporation rate.

For each of the same state variables used by the previous method – i.e. mass $\mathcal{M}_L^i$, momentum $\mathcal{P}_L^i$ and enthalpy $\mathcal{H}_L^i$ – two contributions have to be considered, one for injection and the other for evaporation/dynamics.

In addition, a fourth state variable is needed to account for the supplementary degree of freedom associated to the variability of the drop number. It was chosen here to provide this additional information with the introduction of the total evaporating surface $\mathcal{S}_L^i$ as a state variable, since it is directly connected to the evaporation rate.

With this approach there is no need to wait until the parcel is completely injected to define its mean diameter (and therefore drop number): the Sauter mean diameter, D_{32}, of each parcel is determined, by definition, once $\mathcal{M}_L^i$ and $\mathcal{S}_L^i$ are known, as:

$$D_{32}^i = \frac{6\,\mathcal{M}_L^i}{\rho_L\,\mathcal{S}_L^i} \tag{4.48}$$

and the drop number n^i follows as:

$$n^i = \frac{6}{\rho_L\,\pi}\frac{\mathcal{M}_L^i}{{D_{32}^i}^3} = \frac{\rho_L^2}{36\,\pi}\frac{{\mathcal{S}_L^i}^3}{{\mathcal{M}_L^i}^2} \tag{4.49}$$

Both values are continuously updated according to the contributions of injection and evaporation at producing/consuming surface and mass.

The two contributions to the surface evolution, in particular, are derived based on the following observations:

- the injection of new mass into the fuel package adds new drops with known diameter D_{32}^{inj}, given by the atomization model – Eq. (4.53); this corresponds to the surface production term in Eq. (4.50);
- the evaporation of the existing drops reduces the average diameter, hence the total surface of the liquid parcel, according to the destruction term in Eq. (4.50);

The parcel evaporating surface $\mathcal{S}_L^i$ evolves therefore according to:

$$\dot{\mathcal{S}}_L^i = \underbrace{\frac{6}{\rho_L \, D_{32}^{\mathrm{inj}}(t)} \dot{\mathcal{M}}_{\mathrm{inj}}^i}_{\text{production (inj)}} - \underbrace{\frac{2}{3} \frac{\mathcal{S}_L^i}{\mathcal{M}_L^i} \dot{\mathcal{M}}_{\mathrm{ev}}^i}_{\text{destruction (ev)}} \tag{4.50}$$

where the underlined production and destruction terms describe the creation of new drops of known diameter D_{32}^{inj} and the evaporation of existing ones, respectively.

When the injection of a drop parcel is over ($\dot{\mathcal{M}}_{\mathrm{inj}}^i = 0$) only the second term at the rhs of Eq. (4.50) is active: in this condition the drop number is constant as can be verified by deriving Eq. (4.49) and substituting the following conditions:

$$\dot{\mathcal{S}}_L^i = -\frac{2}{3} \frac{\mathcal{S}_L^i}{\mathcal{M}_L^i} \dot{\mathcal{M}}_{\mathrm{ev}}^i \tag{4.51}$$

$$\dot{\mathcal{M}}_L^i = -\dot{\mathcal{M}}_{\mathrm{ev}}^i \tag{4.52}$$

Both the 2-step and continuous coupling models described above and summarized in Fig. 4.7 were developed and tested during this PhD work. Validations with the 2-step model are discussed in a previous paper (Pellegrino et al., 2015), available in Appendix A, while all the results presented in the following chapters are all obtained with the continuous coupling model, implemented afterwards.

Figure 4.8 compares the two coupling models, showing plots of the evaporation rate (a) and fuel vapour mass (b) against time with two values of the parcel number, N_P (10 and 50). The same quantities, traced over a short period of time after injection in panes (c) and (d), outline the main drawbacks of the two-step coupling method:

- the discontinuities on the evaporation rate – due to the sudden introduction of evaporating mass: once a parcel has been completely injected it begins evaporating, introducing a visible peak in the evaporation rate;
- a globally delayed evaporation, since during the time in which a parcel is created it does not yet evaporate;

Both these effects can be reduced by increasing the number of drop parcels N_P. As shown in Fig. 4.8, increasing N_P from 10 to 50 leads to:

- less pronounced evaporation rate discontinuities, since the evaporated mass introduced by the new parcel is smaller;
- a globally increased evaporation rate during injection, since the delay needed to create a parcel is shorter.

The latter effect leads to an increase in the fuel vapour mass (panes (b) and (d)), when the resolution is refined. All this drawbacks can be avoided using the continuous coupling approach.

4.4.2 Atomization model

The atomization model outputs a Sauter mean drop diameter that represents the injected drop distribution after primary and secondary breakup. It takes into account the evolution

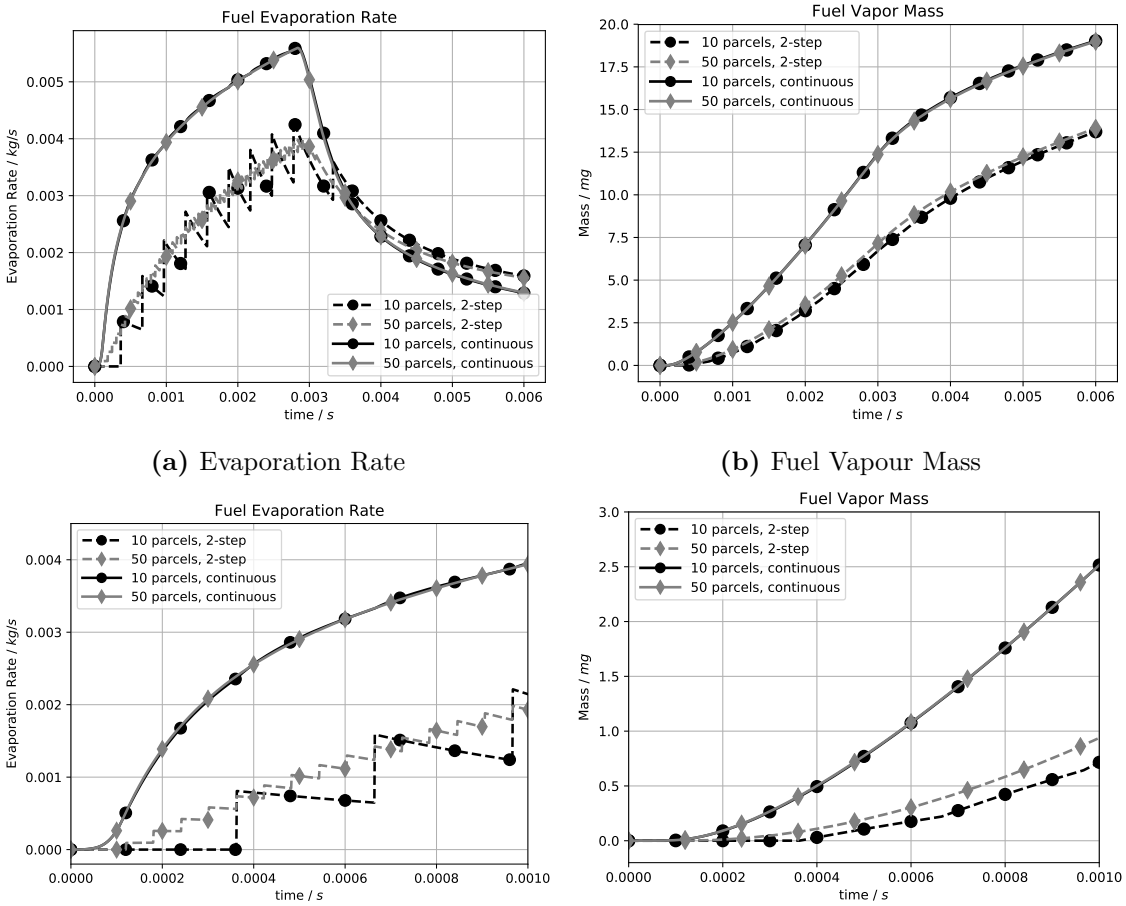

(a) Evaporation Rate

(b) Fuel Vapour Mass

(c) Evaporation Rate (detail)

(d) Fuel Vapour Mass (detail)

Figure 4.8: Evaporation rate and fuel vapour mass for the two-step coupling model with $N_P = 10$ and $N_P = 50$ drop parcels, with the two discussed coupling models. With the 2-step coupling, an increase in N_P accelerates the evaporation and reduces the amplitude of the evaporation rate discontinuities. With the continuous coupling, on the other hand, evaporation rate and liquid mass are independent on the discretization of the liquid phase. Results are obtained in a constant-volume vessel at 1.54 bar and 33 °C, boundary conditions are those of the MAGIE experiment (reference point), described in Section 5.1.

of the injection rate as well as the thermodynamic conditions and composition of cylinder gas and provides an instantaneous atomization diameter, according to the empirical correlation proposed by Varde et al. (1984):

$$\frac{D_{32}^{\text{inj}}}{D_{\text{noz}}} = \mathcal{K}_{\text{ato}} \left(Re_f \, We_f\right)^{-0.28} \tag{4.53}$$

retained here with the addition of the calibration parameter[8] $\mathcal{K}_{\text{ato}}$. The Reynolds and Weber numbers that appear in Eq. (4.53) are calculated based on the liquid fuel and air properties, according to Eq. (2.7), recalled here:

$$Re = \frac{u_{\text{inj}} \, D_{\text{noz}}}{\nu_l} \qquad We = \frac{\rho_g \, u_{\text{inj}}^2 \, D_{\text{noz}}}{\sigma_l} \tag{4.54}$$

with u_{inj} the injection velocity, σ_l the liquid fuel surface tension, ν_l its kinematic viscosity and ρ_g the cylinder gas density. The fact that Eq. (4.53) expresses the influence of the injection system in terms of injection velocity – instead of pressure drop through the nozzle orifice – constitutes an advantage of this atomization model, since:

- combustion chamber models in the IFP-Engine library take the injected mass flow rate as an input (injectors are modelled in separate elements);
- in most of the validation experiments the injection rate is measured and can be used as a reference in both 3D and 0D computations.

Moreover, the use of this breakup model allows to capture the influence of the operating conditions through its dependence on :

- injection pressure;
- injection temperature;
- injected fuel characteristics.

The applicability of Eq. (4.53) is however limited to plain orifice atomizers and this approach is not sensitive to detailed injector geometry features such as the aspect ratio of the injector nozzle holes. Accordingly, recalibration through the adjustment of the $\mathcal{K}_{\text{ato}}$ parameter is needed when a new injector is tested.

Depending on the coupling method used, the atomization model is either run once at the creation of each parcel (2-step) or included in the time integration loop (continuous) to provide an input diameter to the surface production term (fig. 4.7).

4.4.3 Evaporation and liquid/gas interaction model

The evolution of a liquid parcel is here described with respect to the previously discussed state variables: mass $\mathcal{M}_L^i$, momentum $\mathcal{P}_L^i$, enthalpy $\mathcal{H}_L^i$ (and surface $\mathcal{S}_L^i$ if the continuous coupling method is used) with the addition of the parcel penetration $\mathcal{X}_L^i$, obtained integrating the drop velocity:

$$\dot{\mathcal{X}}_L^i = u_d^i = \frac{\mathcal{P}_L^i}{\mathcal{M}_L^i} \tag{4.55}$$

that locates the drop parcel on the injection axis.

[8] Recommended values for this parameter, based on the applications studied in this work, are: $\mathcal{K}_{\text{ato}} \in [2; 4]$

Gas velocity field

The velocity field in the gas phase influences both dynamics and thermal equilibrium of the liquid phase through drag force and convection.

the turbulent velocity fluctuation is considered uniform in the combustion chamber and its value u' is given by the turbulence model discussed in Section 4.1.2.

the tumble flow is described by a rigid vortex whose width Δ and rotation velocity ω_t are time-dependent outputs of the turbulence model (Section 4.1.2). The rotation centre is assumed to be halfway between piston and cylinder head. The interaction between the tumble flow and the liquid phase is studied on a plane perpendicular to the tumble axis and containing the injection axis. Considering a Cartesian reference centred in the injector tip and whose x-axis corresponds to the injector axis, the centre of tumble is located at (x_t, y_t), that depend on the piston position and therefore vary in time. The tumble velocity field on the injector axis has, in general, a component perpendicular to the injection axis, $u_t^{\perp}$, given by:

$$u_t^{\perp}(x,t) = \begin{cases} -\omega_t\, y_t & \text{if} \quad (x-x_t)^2 + y_t^2 < \Delta^2 \\ 0 & \text{otherwise} \end{cases} \tag{4.56}$$

and a component parallel to the injection axis, $u_t^{\parallel}$, given by:

$$u_t^{\parallel}(x,t) = \begin{cases} \omega_t\,(x-x_t) & \text{if} \quad (x-x_t)^2 + y_t^2 < \Delta^2 \\ 0 & \text{otherwise} \end{cases} \tag{4.57}$$

the piston flow is the gas motion along the cylinder axis induced by piston displacement: the related velocity is assumed equal to that of the piston at $z = z_p$, zero at $z = 0$ and varies linearly in between:

$$u_p(z) = \dot{z}_p\, \frac{z}{z_p} \tag{4.58}$$

with z a coordinate along the piston axis with its origin on the cylinder head.

The gas velocity resulting from piston motion can also be decomposed in the two contributions $u_p^{\perp}(x)$ $u_p^{\parallel}(x)$, perpendicular and parallel, respectively, to the injection axis and as a function of the injection axis coordinate, x. The interaction between u_t and u_p is represented in Fig. 4.9.

Drop dynamics

The liquid drop parcels have a degree of freedom corresponding to their positions on the injection axis. Accordingly, an equation for their momentum is provided: neglecting the gravity effects, variations of momentum are solely due to the drag force of the surrounding gas, characterized by the velocity field described above. The local values of the gas velocities associated with tumble flow piston displacement around the i-th parcel and along the injection axis, $u_p^{\parallel}(\mathcal{X}_L^i)$ and $u_p^{\parallel}(\mathcal{X}_L^i)$ respectively (Fig. 4.9), affect its dynamic equilibrium, expressed as[9]:

$$\dot{\mathcal{P}}_L^i = \underbrace{\frac{1}{2}\, C_D\, \rho_g\, S_d^i \left(u_p^{\parallel}(\mathcal{X}_L^i) + u_t^{\parallel}(\mathcal{X}_L^i) - u_d^i\right)^2}_{\text{drag force}} + \underbrace{\mathcal{K}_v\, u_{\text{inj}}\, \dot{\mathcal{M}}_{\text{inj}}}_{\text{injection}} - \underbrace{u_d^i\, \dot{\mathcal{M}}_{\text{ev}}^i}_{\text{evaporation}} \tag{4.59}$$

[9] Eq. (4.59) with both source and sink terms refers to the continuous coupling approach discussed above. With the two-step approach the evolution of $\mathcal{P}_L^i$ is split into an injection phase:

$$\dot{\mathcal{P}}_L^i = \mathcal{K}_v\, u_{\text{inj}}\, \dot{\mathcal{M}}_{\text{inj}}$$

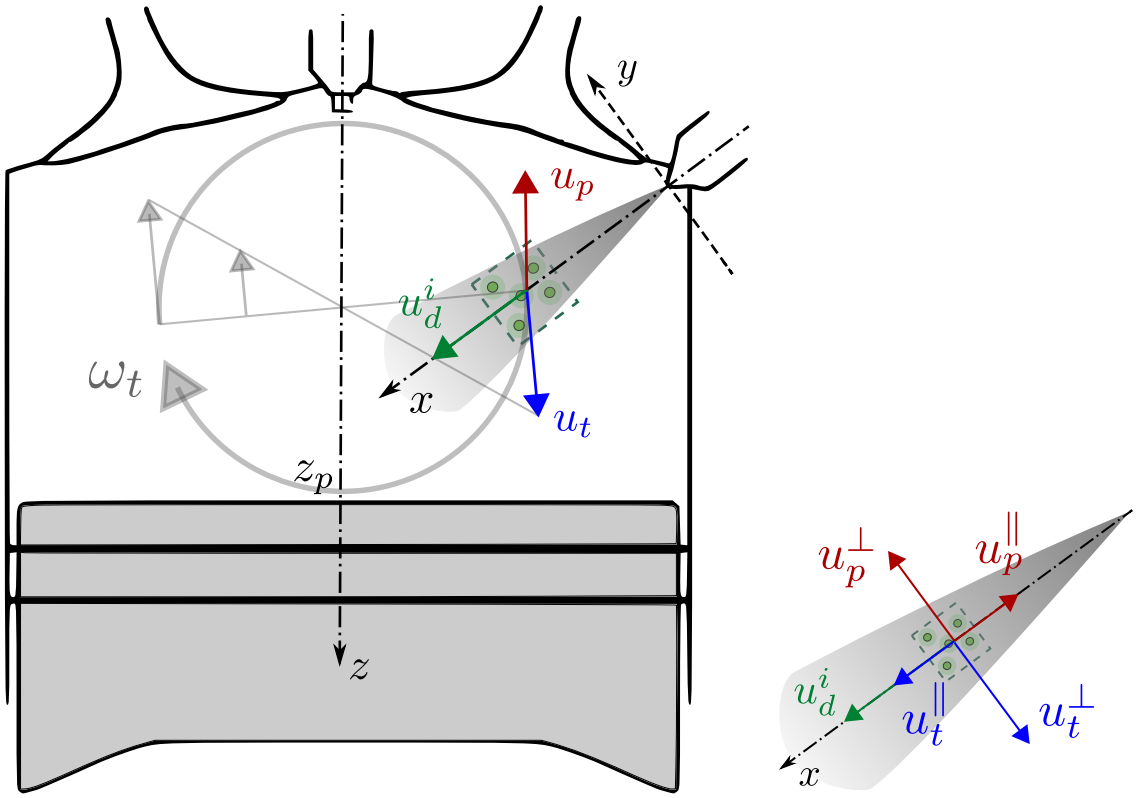

(a) Fuel drop interaction with cylinder gas aerodynamics.

(b) Decomposition of gas velocities with respect to the drop parcel.

Figure 4.9: Kinematic interaction between a generic, i-th, fuel drop parcel and the main cylinder flows. drop velocities are combined with the gas velocity field resulting from tumble and piston motion.

where the injected mass is introduced at the injection velocity u_{inj} adjusted by the calibration parameter $\mathcal{K}_v$, used to fit the liquid penetration, $\mathcal{X}_L^i$, and the evaporating mass conserves its velocity u_d^i. The surface S_d^i is the projection of the liquid body in the direction of the flow which – for a spherical drop – is a circle ($S_d^i = \pi(D_{32}^i)^2/4$) and the drag coefficient C_D is given by the expression:

$$C_D = \frac{24}{Re^i}\left[1 + \frac{\left(Re^i\right)^{2/3}}{6}\right] \tag{4.60}$$

that satisfies the viscous limit[10] $C_D \to 24/Re$ for $Re \to 0$.

A dynamic description of the drop parcel allows to estimate the positions of each parcel $\mathcal{X}_L^i$ which can be used to predict its impact on the wall[11] and the global liquid penetration:

$$X_L = \max_{i=1}^{N_P} \mathcal{X}_L^i \tag{4.61}$$

Evaporation and heat transfer

The description of heat and mass transfer between liquid and gas phases is based on the work of Abramzon and Sirignano (1989), detailed in Section 2.1.2, for the evaporation of an isolated drop in a gas stream.

The temperature field in each liquid drop is assumed to be uniform, and the parcel mass evolves according to

$$\dot{\mathcal{M}}_L^i = \underbrace{-\pi\, n^i\, D_{32}^i\, \frac{\lambda_g}{c_{p\,g}}\, \frac{Sh}{Le}\, \log\left(1 + B_M\right)}_{\dot{\mathcal{M}}_{\text{ev}}^i} + \dot{\mathcal{M}}_{\text{inj}}^i \tag{4.62}$$

where the evaporation rate, highlighted as $\dot{\mathcal{M}}_{\text{ev}}^i$, is calculated defined by Eq. (2.37), and $\dot{\mathcal{M}}_{\text{inj}}^i$ is the injected mass flow rate.

The energy balance of an isolated drop, expressed by Eq. (2.39), recalled here:

$$\dot{\mathcal{H}}_d = \dot{\mathcal{M}}_d \left[\frac{c_{p\,l}\ (T_\infty - T_d)}{B_T} - H_L\right] \tag{4.63}$$

---

and an evaporation phase:

$$\dot{\mathcal{P}}_L^i = \frac{1}{2}\, C_D\, \rho_g\, S_d^i \left[u_p^{\parallel}(\mathcal{X}_L^i) + u_t^{\parallel}(\mathcal{X}_L^i) - u_d^i\right]^2 - u_d^i\, \dot{\mathcal{M}}_{\text{evap}}$$

[10] The Reynolds number that appears in Eq. 4.60 is based on the drop diameter D^i, the liquid/gas relative velocity and the gas kinematic viscosity, ν_g:

$$Re^i = \frac{D_{32}^i \left[u_p^{\parallel}(\mathcal{X}_L^i) + u_t^{\parallel}(\mathcal{X}_L^i) - u_d^i\right]}{\nu_g}$$

[11] In the present version of the model, the dynamic description of a drop parcel is switched off when it reaches the combustion chamber wall and its drops are assumed to follow the wall kinematic law after the impact, i.e. the parcel position is assumed to be that of the piston.

An interesting evolution of the presented approach would be to implement a film model following the work of Iafrate (2016) to:

- predict the fraction of liquid that is captured on the wall forming a plane film;
- provide a dedicated evaporation model for the liquid film;
- predict the fraction of liquid that bounces back into the gas field in form of drops, which might undergo an additional breakup phase during the impact and have a reduced size.

is then applied to a drop parcel, leading to:

$$\dot{\mathcal{H}}_L^i = \dot{\mathcal{M}}_{\text{ev}}^i \left[\frac{c_{p\,L}\ (T_\infty - T_d^i)}{B_T} - H_L - \frac{\mathcal{H}_L^i}{\mathcal{M}_L^i} \right] + h_0^{\text{inj}} \dot{\mathcal{M}}_{\text{inj}}^i \tag{4.64}$$

where the first term is the heat transferred from the gas phase, H_L is the latent heat, $\mathcal{H}_L^i/\mathcal{M}_L^i$ is the enthalpy of the evaporating mass (that leaves the liquid parcel) and $h_0^{\text{inj}}\dot{\mathcal{M}}_{\text{inj}}^i$ is the enthalpy of the new drops injected in the liquid parcel.

The heat transfer number B_T and the Sherwood number, Sh, that appear in Eq. (4.62) and Eq. (4.64), are estimated using the Frossling correlations, Eq. (2.33), recalled here:

$$\begin{aligned} Nu_0 &= 2 + 0.552\, Re^{1/2}\, Pr^{1/3} \\ Sh_0 &= 2 + 0.552\, Re^{1/2}\, Sc^{1/3} \end{aligned} \tag{4.65}$$

with the following expression for the drop Reynolds number:

$$Re^i = \frac{D_{32}^i \sqrt{\left[(u_p^{\parallel}(\mathcal{X}_L^i) + u_t^{\parallel}(\mathcal{X}_L^i) - u_{d\,i}\right]^2 + \left[\mathcal{K}_{t\,\text{ev}}\, u_t^{\perp}(\mathcal{X}_L^i) + u_p^{\perp}(\mathcal{X}_L^i)\right]^2 + u'^2}}{\nu_g} \tag{4.66}$$

and assuming $Le = 1$ and $Sc = Pr = 0.669$.

For each parcel, the relative velocity between the liquid and gas phases used in Eq. (4.66) results from the composition of the drop velocity u_d^i with the local values at $\mathcal{X}_L^i$ gas velocities associated to piston motion ($u_p^{\parallel}(\mathcal{X}_L^i)$ and $u_p^{\perp}(\mathcal{X}_L^i)$), tumble ($u_t^{\parallel}(\mathcal{X}_L^i)$ and $u_t^{\perp}(\mathcal{X}_L^i)$), shown in Fig. 4.9, and the turbulent velocity fluctuation u'.

All the three components (tumble, piston and turbulent) of the gas velocity field are therefore taken into account in Eq. (4.66) and contribute to convective heat and mass transfer. The tuning parameter $\mathcal{K}_{t\,\text{ev}}$ is introduced to calibrate the effect of tumble on the evaporation rate.

4.5 Gas phase description

The following part of the spray model describes the evolution of the free spray that grows in a quiescent environment. Its volume grows following the evolution of the spreading rate $\tan\alpha/2$ and tip penetration x_p, and is calculated assuming a shape resulting from the union of a cone and a semisphere as shown in Fig. 4.10. An empirical approach – detailed in the following section – is used to compute the values of x_p and $\tan\alpha/2$, and their evolution in time. Based on experiments on free sprays, this model does not take into account the spray/wall interaction, which constitutes its biggest limitation. These informations are used to calculate the entrainment rate, i.e. the amount of gas that is transferred to the reactive charge (RC) zone

4.5.1 Tip penetration and spreading rate

The observations of Naber and Siebers (1996) concerning spray tip penetration and air entrainment were originally developed for Diesel sprays. Since this approach is based on momentum conservation it is retained here to describe the geometrical evolution of the spray in spite of the obvious differences in fuel characteristics and thermodynamic conditions.

The tip penetration is therefore calculated inverting Eq. (2.42) into:

$$x_p = \tilde{x}\, x^+ \tag{4.67}$$

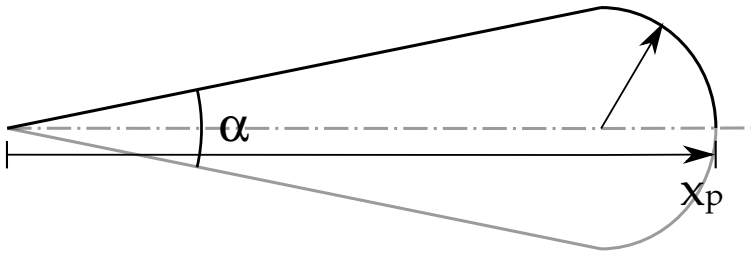

Figure 4.10: The reactive charge (RC) zone during the free evolution phase is represented by the union of a cone and a semisphere: the tip penetration x_p and the cone spreading angle α are given by Eq. 4.67 and Eq. 4.69, respectively.

$$\tilde{x} = \mathcal{K}_p \, \tilde{t} \left(1 + \tilde{t}^{\frac{n}{2}}\right)^{-\frac{1}{n}} \tag{4.68}$$

with $n = 2.2$ as recommended by Naber and Siebers (1996), with the introduction of the calibration parameter $\mathcal{K}_p$. The spreading rate of the model spray is likewise estimated according to Naber and Siebers (1996):

$$\tan\frac{\alpha}{2} = \mathcal{K}_a \left[\left(\frac{\rho_g}{\rho_f}\right) - 0.0043\sqrt{\frac{\rho_f}{\rho_g}}\right] \tag{4.69}$$

with the introduction of the calibration parameter $\mathcal{K}_a$.

4.5.2 Air entrainment

The values of the penetration x and spreading angle α define the region where fuel mixes with ambient gas, consisting of air and dilution gases, the most common being the EGR. The volume of the ideal spray, V_{sp}, grows as the spray penetrates, according to:

$$\dot{V}_{\text{rc}} = \frac{d}{dt}\left[\frac{\pi}{3}\, x^3 \, \tan^2\frac{\alpha}{2}\, \frac{1 + 2\,\tan\dfrac{\alpha}{2}}{\left(1 + \tan\dfrac{\alpha}{2}\right)^3}\right] \tag{4.70}$$

entraining gas from the ambient zone. The entrainment rate for each of the N_{SP} species in the gas mixture is given by

$$\dot{\mathcal{M}}_i^{\text{ent}} = \dot{V}_{\text{rc}}\, \rho_i \tag{4.71}$$

with ρ_i being the partial density of the i-th species in the external region.

Correction for tumble flow

The presence of a rotating flow inside the chamber affects the ambient gas/fuel mixing rate and enlarges the spray region. The tumble vortex shown in Fig. 4.9 provides an additional source of entrainment with respect to a reference case of a spray penetrating into a quiescent gas, since a transverse flow feeds the spray with ambient gas.

This effect can be measured by defining a *tumble entrainment factor* as:

$$\alpha_{t\,\text{ent}} = \frac{\mathcal{M}_{\text{rc}}\,(\omega, t)}{\mathcal{M}_{\text{rc}}\,(0, t)} - 1 \tag{4.72}$$

with $\mathcal{M}_{\mathrm{rc}}(\omega, t)$ and $\mathcal{M}_{\mathrm{rc}}(0, t)$ the reactive charge mass with a generic tumble angular velocity ω and in the quiescent case ($\omega = 0$), respectively. The average angular velocity of the gas phase around the tumble axis, y, is defined as:

$$\omega_y = \frac{\int_V \rho\,(r_x u_z + r_z u_x)\,dV}{\int_V \rho\,(r_x^2 + r_z^2)\,dV} \tag{4.73}$$

A linear correlation between the tumble angular velocity ω_y and the entrainment factor α:

$$\alpha_{t\,\mathrm{ent}} = \mathcal{K}_{t\,\mathrm{ent}}\,\omega_y \tag{4.74}$$

with $\mathcal{K}_{t\,\mathrm{ent}}$ a calibration parameter, is adopted to describe this phenomenon.

The corrected value of the mass flow rate for each of the N_{SP} species is therefore:

$$\dot{\mathcal{M}}_i^{\mathrm{ent}} = \dot{V}_{\mathrm{rc}}^{\mathrm{Sieb}}\,(1 + \alpha_{t\,\mathrm{ent}})\,\rho_i \quad \text{with} \quad i = 1, \ldots, N_{\mathrm{SP}} \tag{4.75}$$

and it is completed – where applicable – by the source terms expressing valve flows according to Eq. (4.35) and Eq. (4.32).

This correction was developed and subsequently validated based on the 3D numerical simulations that are presented in Section 5.2: iso-octane injections in a constant-volume vessel with an initial vortex were simulated to study the effects of tumble on fuel/air mixing and evaporation.

4.6 Mixture formation and stratification

This section presents a mixing model describing fuel mass fraction non-homogeneities within the spray by means of a discrete Probability Density Function (PDF). The model is based on the approach outlined by Inagaki et al. (2008) for a Diesel combustion simulator.

Inhomogeneities in the in-cylinder fuel mass fraction, Y_F, range in the $0 \leq Y_F \leq 1$ interval, the two limit conditions correspond to pure ambient gas ($Y_F = 0$) and pure fuel vapour ($Y_F = 1$). In the adopted modelling approach, the domain of variability of Y_F is discretized in N_{PDF} values:

$$Y_F^j = \frac{j-1}{N_{\mathrm{PDF}} - 1} \quad \text{with} \quad j = 1, 2, ..., N_{\mathrm{PDF}} \tag{4.76}$$

with N_{PDF} a model parameter to be chosen by the user. The air and fuel vapour masses contained in the spray region are organized into classes, each characterized by its mean Y_F^j. The air and fuel mass contained in the classes, identified by the Y_F^j values given by Eq. (4.76), forms a probability distribution.

Focusing on the PDF classes, the N_{PDF} values of Y_F^j do not change with time and are only calculated once at the beginning of the simulation when the model is initialized. On the other hand, the relative importance of each class on the global PDF depends on the mass, $\mathcal{M}_j$, it contains. Each class j is also characterized by a momentum $\mathcal{P}_j^{\mathrm{pdf}}$ and velocity u_j^{pdf} that evolve according to governing equations.

In this respect, the mass contained in each class varies as a result of:

external contributions such as the air and fuel vapour mass flows that enter the reactive charge (RC) zone, one as a result of entrainment, the other of evaporation (Fig. 4.12);

interaction mechanism that formalizes the effect of mixing on the Y_F distribution as shown in Fig. 4.11.

These two aspects will be described separately in the following. Each of the PDF classes is described by two state variables, its mass $\mathcal{M}_j^{\mathrm{pdf}}$ and momentum $\mathcal{P}_j^{\mathrm{pdf}}$, and every mass transfer that takes place within or towards the PDF produces a transport of momentum, too.

Table 4.3: Summary of the properties that characterize the PDF classes.

state variables		derived properties	
$\dot{\mathcal{M}}_j^{\mathrm{pdf}}$	Mass	$Y_F^j = \frac{j-1}{N_{\mathrm{PDF}}-1}$	Fuel mass fraction
$\dot{\mathcal{P}}_j^{\mathrm{pdf}}$	Momentum	$\phi_j = \frac{Y_F^j}{Y_F^{\mathrm{st.}}}$	Equivalence ratio
		$\rho_j = \left(\frac{Y_F^j}{\rho_F} + \frac{1-Y_F^j}{\rho_{\mathrm{ag}}}\right)^{-1}$	Density
		$V_j^{\mathrm{pdf}} = \frac{\mathcal{M}_j^{\mathrm{pdf}}}{\rho_j}$	Volume
		$\mathcal{R}_j^{\mathrm{pdf}} = \left(\frac{3\,V_j^{\mathrm{pdf}}}{4\,\pi}\right)^{1/3}$	Radius
		$u_j^{\mathrm{pdf}} = \frac{\mathcal{P}_j^{\mathrm{pdf}}}{\mathcal{M}_j^{\mathrm{pdf}}}$	Velocity

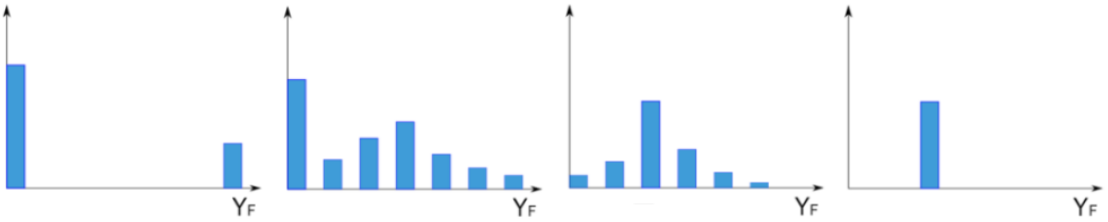

Figure 4.11: Qualitative example of the evolution of a discrete PDF of the fuel mass fraction Y_F. The various stages of mixing go from separate air and fuel vapour (represented by the double Dirac in the rightmost panel) to the final uniform charge (single Dirac centred in $\bar{Y}_F$) through intermediate steps.

External contributions

The input of the mixing model is organized in two mass flows, one representing the amount of ambient gas that enters the reative charge (RC) zone – through entrainment and valve flow – the other being the evaporating fuel.

This model block is therefore connected with those representing the evolution of the gas and liquid phases, as shown in Fig. 4.2. In particular it is assumed here that the vapour mass leaving a particular (i-th) liquid parcel (Section 4.4) enters the mixing mechanism in the class corresponding to fuel vapour saturation at cylinder pressure and liquid parcel temperature ($Y_F^{\mathrm{sat}}(T_i, p)$). This implies the assumption that the boundary condition for the vapour phase at the liquid interface is $Y_F = Y_F^{\mathrm{sat}}$.

The connection to the evaporation model has to be parcel-wise since each of the N_P liquid parcel has a different temperature and can, in principle, evaporate in a different class. The mass $\dot{\mathcal{M}}_F^{\mathrm{ev}}$ evaporating from the generic i-th parcel generates a mass flow:

$$\dot{\mathcal{M}}_i^{\mathrm{ev}} = \frac{\dot{\mathcal{M}}_{i\,F}^{\mathrm{ev}}}{Y_{i\,F}^{\mathrm{sat}}} = \underbrace{\dot{\mathcal{M}}_{i\,F}^{\mathrm{ev}}}_{\text{fuel}} + \underbrace{\dot{\mathcal{M}}_{i\,F}^{\mathrm{ev}} \frac{1 - Y_{i\,F}^{\mathrm{sat}}}{Y_{i\,F}^{\mathrm{sat}}}}_{\text{ambient gas}} \quad \text{with} \quad i = 1, \ldots, N_P \tag{4.77}$$

consisting of a mixture of fuel and ambient gas characterized by the mixture fraction $Y_{i\,F}^{\mathrm{sat}}$. The ambient gas mass needed to reach the saturation mass fraction in Eq. (4.77) is subtracted from the first class of the PDF, with $Y_F = 0$.

Because of the discretization of the Y_F axis no class corresponds, in general, to the exact

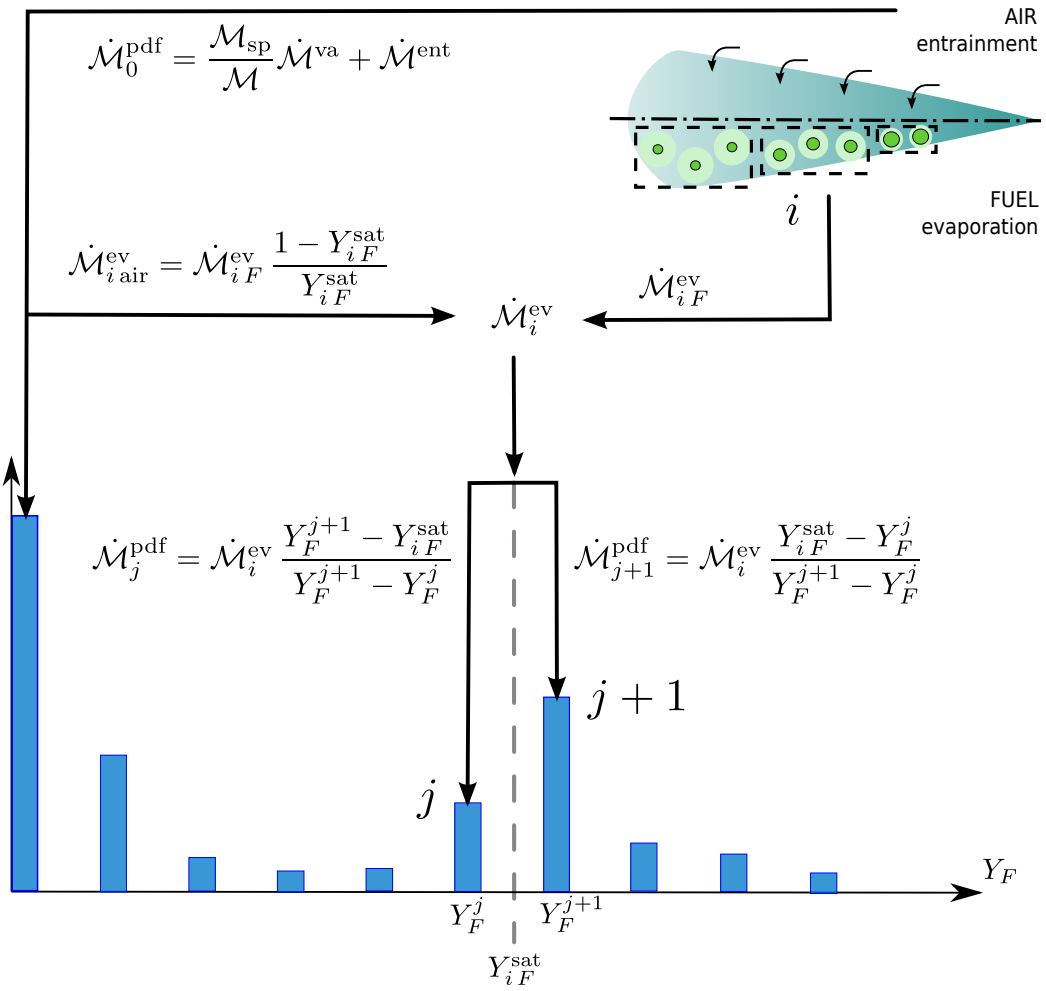

Figure 4.12: The **external contributions** to the discrete PDF: entrained air is attributed to the first PDF class ($Y_F = 0$) while the fuel evaporating from each liquid parcel feeds the class corresponding to its saturated mixture ($Y_F = Y_F^{\rm sat}$) taking the amount of air required from the first class. As a general rule, older parcels will have a higher $Y_F^{\rm sat}$ because of the longer heating times resulting in higher liquid temperatures.

mass fraction, $Y_{i\,F}^{\rm sat}$, of this mixture. Accordingly the model identifies the j-th class so that:

$$Y_F^j \leq Y_{i\,F}^{\rm sat} < Y_F^{j+1} \tag{4.78}$$

and the mass flow provided by Eq. (4.77) is split between classes j and $j+1$ according to the following lever rule:

$$\dot{\mathcal{M}}_j^{\rm pdf} = \dot{\mathcal{M}}_i^{\rm ev}\,\frac{Y_F^{j+1} - Y_{i\,F}^{\rm sat}}{Y_F^{j+1} - Y_F^j} \quad \text{and} \quad \dot{\mathcal{M}}_{j+1}^{\rm pdf} = \dot{\mathcal{M}}_i^{\rm ev}\,\frac{Y_{i\,F}^{\rm sat} - Y_F^j}{Y_F^{j+1} - Y_F^j} \tag{4.79}$$

which ensures mass conservation of air and fuel.

The ambient gas entering the reative charge (RC) zone due to entrainment and valve flow is attributed to the first class of the PDF, with $Y_F^1 = 0$

$$\dot{\mathcal{M}}_0^{\rm pdf} = \frac{\mathcal{M}_{\rm rc}}{\mathcal{M}}\dot{\mathcal{M}}^{\rm va} + \dot{\mathcal{M}}^{\rm ent} \tag{4.80}$$

The momentum transported by fuel and air flows into the PDF is calculated assuming that fuel vapour conserves the velocity of its liquid parcel while air enters with an entrainment velocity, proportional to the square root of the kinetic energy associated with tumble.

The terms that advect mass into the reative charge (RC) zone, schematized in Fig. 4.12 for a generic, i-th, parcel, consist therefore of:

fuel vapour coming from the evaporating drop parcels and feeding the PDF classes with the respective mixture fractions;

ambient gas entrained into the spray, most of which feeds the first (Y_F^1) class of the mechanism while the rest dilutes the evaporating fuel to obtain the saturation mixture fraction.

The former flow can be synthesized defining an interaction matrix C^{em} ($N_{\mathrm{PDF}} \times N_P$) to describe how all the N_P drop parcels and the N_{PDF} mixture classes are coupled, so that the net fuel mass entering the j-th class can be written as:

$$\sum_{i=0}^{N_P} C_{ij}^{\mathrm{em}} \dot{\mathcal{M}}_i^{\mathrm{ev}} \tag{4.81}$$

The evaporation-mixing interaction tensor C^{em} is therefore a sparse matrix with non-zero values where the mixture fraction of a class (Y_F^j) matches that of a parcel ($Y_{j\,F}^{\mathrm{sat}}$):

$$C_{ij}^{\mathrm{em}} = \begin{cases} \dfrac{Y_F^{j+1} - Y_{i\,F}^{\mathrm{sat}}}{Y_F^{j+1} - Y_F^j} & Y_F^j \le Y_{i\,F}^{\mathrm{sat}} < Y_F^{j+1} \\ \dfrac{Y_{i\,F}^{\mathrm{sat}} - Y_F^{j-1}}{Y_F^j - Y_F^{j-1}} & Y_F^{j-1} \le Y_{i\,F}^{\mathrm{sat}} < Y_F^j \\ 0 & \text{elsewhere} \end{cases} \tag{4.82}$$

with $j = 2, \ldots, N_{\mathrm{PDF}}$ and $i = 1, \ldots, N_P$.

The expression of the source terms $\dot{\mathcal{M}}_{\mathrm{so}\,i}^{\mathrm{pdf}}$ that feed the PDF mechanism is:

$$\dot{\mathcal{M}}_{\mathrm{so}\,j}^{\mathrm{pdf}} = \begin{cases} \overbrace{\dot{\mathcal{M}}^{\mathrm{ent}} + \dfrac{\mathcal{M}_{\mathrm{rc}}}{\mathcal{M}} \dot{\mathcal{M}}^{\mathrm{va}}}^{\text{entrained ambient gas}} - \overbrace{\sum_{k=2}^{N_{\mathrm{PDF}}} \dfrac{1 - Y_F^k}{Y_F^k} \sum_{i=1}^{N_P} C_{ik}^{\mathrm{em}} \dot{\mathcal{M}}_i^{\mathrm{ev}}}^{\text{ambient gas for fuel dilution}} & j = 1 \\ \underbrace{\dfrac{1}{Y_F^j} \sum_{i=1}^{N_P} C_{ij}^{\mathrm{em}} \dot{\mathcal{M}}_i^{\mathrm{ev}}}_{\text{ambient gas + fuel}} & j = 2, \ldots, N_{\mathrm{PDF}} \end{cases} \tag{4.83}$$

where the discussed terms are highlighted. Likewise, the class momentum source terms are:

$$\dot{\mathcal{P}}_{\mathrm{so}\,j}^{\mathrm{pdf}} = \begin{cases} \overbrace{u_a \left(\dot{\mathcal{M}}^{\mathrm{ent}} + \dfrac{\mathcal{M}_{\mathrm{rc}}}{\mathcal{M}} \dot{\mathcal{M}}^{\mathrm{va}} \right)}^{\text{entrained ambient gas}} - \overbrace{\dfrac{\mathcal{P}_0}{\mathcal{M}_0} \sum_{k=2}^{N_{\mathrm{PDF}}} \dfrac{1 - Y_F^k}{Y_F^k} \sum_{i=1}^{N_P} C_{ik}^{\mathrm{em}} \dot{\mathcal{M}}_i^{\mathrm{ev}}}^{\text{ambient gas for fuel dilution}} & j = 1 \\ \underbrace{\dfrac{\mathcal{P}_0}{\mathcal{M}_0} \dfrac{1 - Y_F^j}{Y_F^j} \sum_{i=1}^{N_P} C_{ij}^{\mathrm{em}} \dot{\mathcal{M}}_i^{\mathrm{ev}}}_{\text{ambient gas for fuel dilution}} + \underbrace{\sum_{i=1}^{N_P} u_{d\,i}\, C_{ij}^{\mathrm{em}} \dot{\mathcal{M}}_i^{\mathrm{ev}}}_{\text{fuel vapor}} & j = 2, \ldots, N_{\mathrm{PDF}} \end{cases} \tag{4.84}$$

where the entrainment velocity, u_a, is a function of the specific mean kinetic energy, K (L^2T^{-2}), defined in Section 4.1.2:

$$u_a = \frac{1}{2}\sqrt{K} \tag{4.85}$$

and represents the effect of aerodynamics on small scale mixing.

Interaction mechanism

The shape of the mixture fraction PDF – that fuel and air enter as described in the previous paragraph – evolves in time as a result of a mixing mechanism based on the mutual interaction of the existing classes and described below.

Sphere analogy. The rationale of the mixing mechanism is based on the model proposed by Inagaki et al. (2008), where each PDF class is associated to an imaginary sphere whose size is proportional to the class mass.

The spheres advance along the injection axis with different velocities – each proportional to the respective class momentum – and the relative velocity between each couple of spheres determines the mixing rate between the two.

Based on the mass $\mathcal{M}_j^{\mathrm{pdf}}$, momentum $\mathcal{P}_j^{\mathrm{pdf}}$ and mixture fraction Y_F^j of each class the following attributes characterize the mixing spheres:

density: the densities of the two boundary classes (ambient gas and pure fuel) are combined with a mass-weighted average

$$\rho_j = \left(\frac{Y_F^j}{\rho_F} + \frac{1 - Y_F^j}{\rho_{\mathrm{ag}}} \right)^{-1} \quad \text{with} \quad j = 1, \ldots, N_{\mathrm{PDF}} \tag{4.86}$$

and generate the values for all the intermediate classes; the values for fuel vapour and air are evaluated for a perfect gas at ambient conditions ($T_{\mathrm{a}} = 300\mathrm{K}$ and $p_{\mathrm{a}} = 10^5\mathrm{Pa}$).

$$\begin{aligned} \rho_F &= \frac{p_{\mathrm{a}}\, M_F}{R\, T_{\mathrm{a}}} \\ \rho_{\mathrm{ag}} &= \frac{p_{\mathrm{a}}\, M_{\mathrm{ag}}}{R\, T_{\mathrm{a}}} \end{aligned} \tag{4.87}$$

where M_{ag} and M_F are the molar masses of ambient gas and fuel and R the perfect gas constant;

size: the sphere volume V_j^{pdf} is derived from mass and density as:

$$V_j^{\mathrm{pdf}} = \frac{\mathcal{M}_j^{\mathrm{pdf}}}{\rho_j} \tag{4.88}$$

and its radius $\mathcal{R}_j^{\mathrm{pdf}}$ is:

$$\mathcal{R}_j^{\mathrm{pdf}} = \left(\frac{3\, V_j^{\mathrm{pdf}}}{4\, \pi} \right)^{1/3} \tag{4.89}$$

velocity: the sphere velocity is obtained as:

$$u_j^{\mathrm{pdf}} = \frac{\mathcal{P}_j^{\mathrm{pdf}}}{\mathcal{M}_j^{\mathrm{pdf}}} \tag{4.90}$$

once mass and momentum are known.

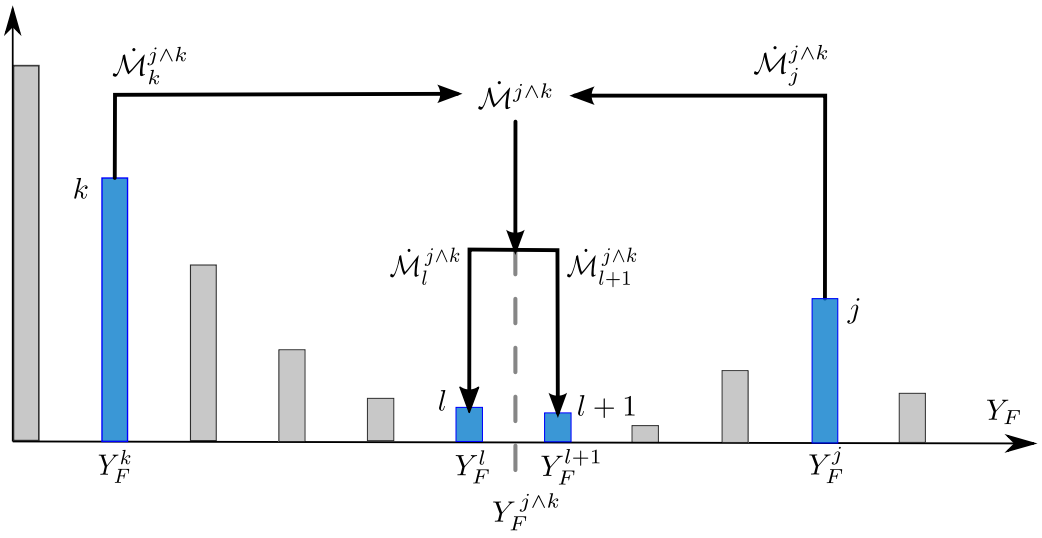

Figure 4.13: The **mixing mechanism** in the discrete PDF: the interaction between the j-th and k-th classes generates the mass flows $\dot{\mathcal{M}}_j^{j\wedge k}$ and $\dot{\mathcal{M}}_k^{j\wedge k}$ that mix to an intermediate fuel mass fraction, $Y_F^{j\wedge k}$, filling the corresponding classes l and $l+1$.

The idea behind the mixing mechanism is that the imaginary spheres progress in the same direction but with different velocities – given by Eq. (4.90) – and penetrate each other in doing so. This results in a loss of mass for two interacting spheres that is reallocated in a third class, according to the fuel mass concentration Y_F^{new} that results from blending the two original mixtures in the proportion given by the mixing mechanism. The following procedure is repeated to represent the interaction of each possible couple of classes[12]:

- the interference of the two spheres representing the j-th and k-th classes generates a volume, $\dot{V}_{\text{Sweep}}^{j\wedge k}$, where mass belonging to the two original classes is enclosed[13];
- the volume interference represented by $\dot{V}_{\text{Sweep}}^{j\wedge k}$ causes the two interacting classes j and k to loose the following amounts of mass:

$$\begin{aligned} \dot{\mathcal{M}}_j^{j\wedge k} &= -\rho_j \dot{V}_{\text{Sweep}}^{j\wedge k} \frac{V_j V_k}{V_{\text{tot}}^{5/3}} \sqrt{N_{\text{PDF}}} \\ \dot{\mathcal{M}}_k^{j\wedge k} &= -\rho_k \dot{V}_{\text{Sweep}}^{j\wedge k} \frac{V_j V_k}{V_{\text{tot}}^{5/3}} \sqrt{N_{\text{PDF}}} \end{aligned} \tag{4.91}$$

  and momentum:

$$\begin{aligned} \dot{\mathcal{P}}_j^{j\wedge k} &= -\frac{\mathcal{P}_j}{\mathcal{M}_j} \cdot \dot{\mathcal{M}}_j^{j\wedge k} \\ \dot{\mathcal{P}}_k^{j\wedge k} &= -\frac{\mathcal{P}_k}{\mathcal{M}_k} \cdot \dot{\mathcal{M}}_k^{j\wedge k} \end{aligned} \tag{4.92}$$

[12] Repetitions such as $j \wedge k$ and $k \wedge j$ are avoided as well as combinations of neighbouring classes such as $j \wedge j+1$, that would lead to a null flow.

[13] Since the description is given per unit time, $\dot{V}_{\text{Sweep}}^{j\wedge k}$ has the dimensions of a volumetric flow (L^3T^{-1}) while the masses cited in the following are in fact mass flows (MT^{-1}).

- these two flows mix generating the mass flow:

$$\dot{\mathcal{M}}^{j\wedge k} = \dot{\mathcal{M}}_j^{j\wedge k} + \dot{\mathcal{M}}_k^{j\wedge k} \tag{4.93}$$

characterized by the momentum:

$$\dot{\mathcal{P}}^{j\wedge k} = \dot{\mathcal{P}}_j^{j\wedge k} + \dot{\mathcal{P}}_k^{j\wedge k} \tag{4.94}$$

and fuel mass fraction:

$$Y_F^{j\wedge k} = \frac{\dot{\mathcal{M}}_j^{j\wedge k} Y_F^j + \dot{\mathcal{M}}_k^{j\wedge k} Y_F^k}{\dot{\mathcal{M}}_j^{j\wedge k} + \dot{\mathcal{M}}_k^{j\wedge k}} \tag{4.95}$$

- the mass and momentum, $\dot{\mathcal{M}}^{j\wedge k}$ and $\dot{\mathcal{P}}^{j\wedge k}$ are then split between the two contiguous classes l and $l+1$ that satisfy the relation $Y_l < Y_F^{\text{new}} < Y_{l+1}$, according to the following relations:

$$\begin{aligned} \dot{\mathcal{M}}_l^{j\wedge k} &= -\dot{\mathcal{M}}^{j\wedge k} \frac{Y_F^{l+1} - Y_F^{j\wedge k}}{Y_F^{l+1} - Y_F^l} \quad \text{and} \quad \dot{\mathcal{M}}_{l+1}^{j\wedge k} = -\dot{\mathcal{M}}^{j\wedge k} \frac{Y_F^{j\wedge k} - Y_F^l}{Y_F^{l+1} - Y_F^l} \\ \dot{\mathcal{P}}_l^{j\wedge k} &= -\dot{\mathcal{P}}^{j\wedge k} \frac{Y_F^{l+1} - Y_F^{j\wedge k}}{Y_F^{l+1} - Y_F^l} \quad \text{and} \quad \dot{\mathcal{P}}_{l+1}^{j\wedge k} = -\dot{\mathcal{P}}^{j\wedge k} \frac{Y_F^{j\wedge k} - Y_F^l}{Y_F^{l+1} - Y_F^l} \end{aligned} \tag{4.96}$$

The sweep volume, introduced in Eq. (4.91), results from the interaction of two classes and is defined by the displacement of a disc whose radius is the geometric average of the radii of the two corresponding spheres, moving with a speed computed as the difference between the two class velocities, increased by the turbulent fluctuation u':

$$\dot{V}_{\text{Sweep}}^{j\wedge k} = \pi \mathcal{R}_j \mathcal{R}_k \left[\mathcal{K}_\alpha^{\text{pdf}} \left| u_j^{\text{pdf}} - u_k^{\text{pdf}} \right| + \mathcal{K}_\beta^{\text{pdf}} u' \right] \tag{4.97}$$

with $\mathcal{K}_\alpha^{\text{pdf}}$ and $\mathcal{K}_\beta^{\text{pdf}}$ two calibration parameters used to tune the effects of injection pressure and turbulence on mixing, respectively.

The quantity:

$$\frac{V_j\, V_k}{V_{\text{tot}}^{5/3}} \sqrt{N_{\text{PDF}}} \tag{4.98}$$

that appears in Eq. (4.91) normalizes the mass flows ensuring convergence for $N_{\text{PDF}} \to \infty$.

Summing all the possible interactions described by Eq. (4.91) and Eq. (4.92) leads to the expression of the net mixing mass and momentum flows, $\dot{\mathcal{M}}_l^\wedge$ and $\dot{\mathcal{P}}_l^\wedge$, that involve a generic, l-th, class:

$$\dot{\mathcal{M}}_l^\wedge = \sum_{j=1}^{N_{\text{PDF}}} \sum_{k=1}^{j} \dot{\mathcal{M}}_l^{j\wedge k} \quad \text{and} \quad \dot{\mathcal{P}}_l^\wedge = \sum_{j=1}^{N_{\text{PDF}}} \sum_{k=1}^{j} \dot{\mathcal{P}}_l^{j\wedge k} \tag{4.99}$$

These quantities satisfy the following relations:

$$\sum_{l=1}^{N_{\text{PDF}}} \dot{\mathcal{M}}_l^\wedge = 0 \quad \text{and} \quad \sum_{l=1}^{N_{\text{PDF}}} \dot{\mathcal{P}}_l^\wedge = 0 \tag{4.100}$$

since they only redistribute mass and momentum over the classes.

This mechanism causes the distribution to shrink towards its equilibrium, represented by a Dirac function located at the distribution mean fuel concentration $\bar{Y}_F$, as shown in Fig. 4.11.

Momentum dissipation. The core of the mixing model consists of the interaction mechanism presented above: its effectiveness at smoothing the mixture fraction field towards homogeneity is directly proportional to the velocities of the evaporating drops with respect to the gas phase.

Shear generated by this motion and held responsible for mixing is expected to decrease with time as a consequence of viscous dissipation. This phenomenon is not taken into account by Eq. (4.92) that expresses a fully conservative momentum transfer. An exponential damping expressed as a function of the turbulent kinematic viscosity, ν_T, and the integral length scale, l_t, is therefore introduced to complete the evolution equations for $\mathcal{P}_j$:

$$\dot{\mathcal{P}}_j^{\text{diss}} = -\mathcal{K}_{\mathcal{P}}^{\text{pdf}} \frac{\nu_T}{l_t^2} \mathcal{P}_j \quad \text{with} \quad i = 1, \ldots, N_{\text{PDF}} \tag{4.101}$$

this effect causes the mixing velocity to decrease as a consequence of momentum dissipation. Its intensity can be calibrated via the parameter $\mathcal{K}_{\mathcal{P}}^{\text{pdf}}$.

Evolution equations for mass and momentum. The state variables that characterize the distribution of the equivalence ratio evolve therefore according to the following equations:

$$\begin{aligned} \dot{\mathcal{M}}_j^{\text{pdf}} &= \dot{\mathcal{M}}_{\text{so}\,i}^{\text{pdf}} + \dot{\mathcal{M}}_j^{\wedge} \\ \dot{\mathcal{P}}_j^{\text{pdf}} &= \dot{\mathcal{P}}_{\text{so}\,i}^{\text{pdf}} + \dot{\mathcal{P}}_j^{\wedge} + \dot{\mathcal{P}}_j^{\text{diss}} \end{aligned} \quad \text{with } j = 1, \ldots, N_{\text{PDF}} \tag{4.102}$$

with a source and a redistribution term for both quantities and a dissipation term for momentum only.

Probability density function

From a statistical point of view, if one imagines to randomly extract a small portion of the reative charge (RC) gas and measure the local fuel concentration Y_F, the latter is a random variable belonging to the domain identified by the N_{PDF} discrete values of Y_F^j defined in Eq. (4.76), with probability:

$$P(j) = P(Y_F^j) = \frac{\mathcal{M}_j^{\text{pdf}}}{\mathcal{M}_{\text{tot}}^{\text{pdf}}} \quad \text{with} \quad j = 1, \ldots, N_P \tag{4.103}$$

with $\mathcal{M}_{\text{tot}}^{\text{pdf}}$ the sum of the class masses, $\mathcal{M}_j^{\text{pdf}}$. Eq. (4.103) defines therefore the probability that a randomly extracted gas sample belongs to the j-th class.

A distribution for the fuel mass can be defined likewise:

$$P_F(j) = P_F(Y_F^j) = \frac{\mathcal{M}_{F\,j}^{\text{pdf}}}{\mathcal{M}_{F\,\text{tot}}^{\text{pdf}}} \quad \text{with} \quad j = 1, \ldots, N_P \tag{4.104}$$

with $\mathcal{M}_{F\,j}^{\text{pdf}}$ the fuel mass contained in the j-th class and $\mathcal{M}_{F\,\text{tot}}^{\text{pdf}}$ its sum over the distribution. It represents the probability that a randomly extracted fuel vapour sample belongs to the i-th class, i.e. that it is mixed with air according to Y_F. The two probability distributions satisfy the following conditions:

$$\begin{aligned} &\bar{Y}_F\, P_F(j) = Y_F^j\, P(j) \qquad \text{with} \quad j = 1, \ldots, N_{\text{PDF}} \\ &\sum_{j=1}^{N_{\text{PDF}}} P(j) = \sum_{j=1}^{N_{\text{PDF}}} P_F(j) = 1 \end{aligned} \tag{4.105}$$

4.7 Stratified combustion

The combustion model presented in Section 4.1.3 is adapted as follows to interact with stratified mixture characterization described in Section 4.6.

The new developments consist of the following modifications to the initial model:

- an incomplete combustion reaction scheme for very rich mixtures, required to describe the burning of the richest classes, described in Section 4.7.1;
- the introduction of:
  - an averaged flame propagation speed and burning rate, that take into account the different behaviour of each class;
  - a modified expression for the creation/consumption of each of the N_{SP} chemical species described, detailing the contribution of each class;

  described in Section 4.7.2.

4.7.1 Flame front reaction

The reaction scheme of the base CFM1D model, presented in Section 4.1.3, Eq.s (4.11 – 4.12), and recalled here:

$$\alpha_r \left[\mathrm{C}_x\mathrm{H}_y\mathrm{O}_z + \left(x + \frac{y}{4} - \frac{z}{2} \right) \mathrm{O}_2 \longrightarrow x\,\mathrm{CO}_2 + \frac{y}{2}\,\mathrm{H}_2\mathrm{O} \right] \tag{4.106}$$

$$(1-\alpha_r) \left[\mathrm{C}_x\mathrm{H}_y\mathrm{O}_z + \frac{x-z}{2}\,\mathrm{O}_2 \longrightarrow x\,\mathrm{CO} + \frac{y}{2}\,\mathrm{H}_2 \right] \tag{4.107}$$

results from the combination of a complete, Eq. (4.106), and an incomplete, Eq. (4.107), reaction, weighted according to the parameter:

$$\alpha_r = \frac{\max(0.98, \phi)\,\dfrac{4x+y-2z}{\phi} - 2x + 2z}{2x+y} \tag{4.108}$$

For lean mixtures ($\phi < 0.98$), the reaction parameter α_r has a unit value and all the $\mathrm{C}_x\mathrm{H}_y\mathrm{O}_z$ fuel burns according to the complete reaction, Eq. (4.106). For stoichiometric and rich mixtures, on the other hand, because of the lack of oxygen, a portion $(1-\alpha_r)$ of fuel burns incompletely according to Eq. (4.107).

The incomplete reaction in Eq. (4.107) assumes that all the carbon contained in the fuel burns partially producing CO while the hydrogen produces H_2. Increasing the value of the equivalence ratio, ϕ, will therefore lead to lower values of α_r and to a higher weight of the incomplete reaction, up to a limit where all the fuel burns according to Eq. (4.107). For common gasoline this happens with mixtures richer than $\phi \approx 3$ and corresponds to negative values of the rhs[14] of Eq. (4.108).

The reaction mechanism in Eq.s (4.106 – 4.107) is therefore not adapted to mixtures of higher equivalence ratio, since the available oxygen is not sufficient to ensure that all fuel

[14] The exact value of this threshold is obtained substituting Eq. (4.107) into $\alpha_r < 0$, leading to the expression:

$$\phi > 0.98 \frac{4x+y-2z}{2x-2z}$$

and varies with fuel composition. The value indicated here ($\phi > 3.06$) is obtained for iso-octane ($x = 8$, $y = 18$, $z = 0$).

Table 4.4: Summary of the reaction weights in Eq.s (4.110 – 4.112).

Equivalence Ratio	Reaction Weights	Solved Reactions
$0 < \phi \leq 0.98$	$\alpha_r = 1 \quad \beta_r = 1$	Eq. (4.110)
$0.98 < \phi < 0.98\frac{4x+y-2z}{2x-2z}$	$0 < \alpha_r < 1 \quad \beta_r = 1$	Eq.s (4.110 – 4.111)
$\phi \geq 0.98\frac{4x+y-2z}{2x-2z}$	$\alpha_r = 0 \quad 0 < \beta_r < 1$	Eq.s (4.111 – 4.112)

burns according to the incomplete reaction. As such rich mixtures are generally outside the flammability limit, this limitation is acceptable for homogeneous combustion.

When a flame front propagates through partially premixed charge, on the other hand, it may cross very rich (or very lean) pockets that, though outside the flammability limits, are not quenched because of the heat released in the surrounding gas. A modification to the reaction scheme in Eq.s (4.106 – 4.107) is therefore required to describe combustion in such rich pockets.

It is assumed here that, in this particular case, all the available oxygen is consumed in an incomplete combustion, producing CO and H_2 as described by Eq. (4.107), thus maximizing fuel consumption: the remaining fuel is transferred to the burnt gas as a generic unburned hydrocarbon, C_aH_b, according to the following reaction:

$$C_xH_yO_z \longrightarrow z\,CO + C_aH_b \tag{4.109}$$

with $a = x - z$ and $b = y$. The C_aH_b transferred to the burnt gas subsequently undergoes a post-oxidation reaction scheme.

The resulting combustion scheme for the flame front reaction can be summarized as follows: The following reaction scheme, resulting from the discussed hypotheses, is adopted to describe flame front chemical reactions:

$$\alpha_r\beta_r \left[C_xH_yO_z + \left(x + \frac{y}{4} - \frac{z}{2}\right) O_2 \longrightarrow x\,CO_2 + \frac{y}{2}\,H_2O\right] \tag{4.110}$$

$$(1-\alpha_r)\beta_r \left[C_xH_yO_z + \frac{x-z}{2}\,O_2 \longrightarrow x\,CO + \frac{y}{2}\,H_2\right] \tag{4.111}$$

$$(1-\beta_r)\left[C_xH_yO_z \longrightarrow z\,CO + C_aH_b\right] \tag{4.112}$$

It results from the combination of Eq.s (4.11 – 4.12) and Eq. (4.109), with the introduction of the reaction weight β_r:

$$\beta_r = \frac{0,98}{\phi}\frac{4x+y-2z}{2x-2z} \tag{4.113}$$

defined as the mass ratio of the partially oxidized fuel to the available fuel and a corrected definition of α_r, that excludes negative values:

$$\alpha_r = \max\left(0, \frac{\max(0.98,\phi)\,\dfrac{4x+y-2z}{\phi} - 2x + 2z}{2x+y}\right) \tag{4.114}$$

obtained under the same hypotheses as Equations (4.113 – 4.114) are both obtained imposing the conservation of O under the assumption that 98% of the available O_2 is consumed by flame-front reactions.

The values of two weights, α_r and β_r, as a function of the equivalence ratio are summarized in Table 4.4. For stoichiometric and moderately rich mixtures, β_r has a unit value and Eq. (4.112) is ruled out. For richer mixtures, β_r is lower than unity and α_r is necessarily zero, so that only Eq.s (4.111 – 4.112) are considered.

4.7.2 Interaction of the flame front with the class mechanism

The description of the equivalence ratio distribution given by the class PDF is 0-dimensional and provides no information on the spatial distribution of inhomogeneities. With this simplification it is assumed that fuel mass fraction, Y_F, varies randomly in all directions with no gradient of its mean and variance along the flame propagation direction. As a consequence, flame front reactions cannot influence the PDF shape as to do so would imply a sensitivity of the fuel distribution to the distance from the spark plug, requiring a dedicated model.

It was therefore chosen to represent the interaction between the PDF and the flame front as a one way relation: the PDF shape affects flame front propagation while flame propagation has no effect on the PDF. This hypothesis allows to simplify the interaction of the flame front with the mixture fraction PDF, that amounts to:

- the definition of an **average burning rate** that globally reduces the flame speed with respect to a homogeneous mixture with equal equivalence ratio[15];
- the application of the chemical mechanism in Eq.s (4.110 – 4.112) to each class of the PDF, to detail the local **pollutant formation**.

Average burning rate. The laminar flame speed in each class (s_L^i) is calculated using the empirical correlation proposed by Metghalchi and Keck (1982):

$$s_L^j = s_L^{MK}\left(\phi_j, p, T, Y_{\text{dilution}}\right) \quad \text{with} \quad j = 1, \ldots, N_{\text{PDF}} \tag{4.115}$$

with the mean fresh gas thermodynamic conditions (p and T_{fg}) and diluent mass fraction Y_{dilution}, and with the class equivalence ratio ϕ_j. The values of s_L^j obtained for each class are then weighted averaged with respect to the fuel mass PDF, leading to the following expression for the mean laminar flame speed:

$$\bar{s}_L = \sum_{j=1}^{N_{\text{PDF}}} s_L^j \, P_F(j) \tag{4.116}$$

The area of the turbulent flame surface $\mathcal{A}_T$ is given by the flame front wrinkling model, Eq.s (4.1-4.2) based on input received from the turbulence model detailed in Section 4.1.2.

The following expression give the total mass and fuel mass that the flame front consumes from each class:

$$\begin{aligned} \dot{\mathcal{M}}_j^{\text{ff}} &= \frac{\dot{\mathcal{M}}_{\text{F}}^{\text{ff}}}{\bar{Y}_F} \, \text{P}_F(j) \quad \text{with} \quad j = 1, \ldots, N_{\text{PDF}} \\ \dot{\mathcal{M}}_{\text{F}\,j}^{\text{ff}} &= \dot{\mathcal{M}}_{\text{F}}^{\text{ff}} \, \text{P}(j) \end{aligned} \tag{4.117}$$

Averaging the laminar flame velocities and assuming that each class is then consumed proportionally to its weight in the distribution ensures that the chemical reactions do not affect the shape of the mixture distribution.

This approach is consistent with the assumption that the characteristic length scale of stratification is small with respect to the integral length scale and that flame surface production from equivalence ratio gradients can be neglected.

[15] This is true for engines that operate in globally stoichiometric conditions. In the case of lean operation, stratification can increase the overall burning rate (Hélie and Trouvé, 2000).

Pollutant Formation. The source terms representing production (or consumption) of each species are obtained detailing the chemical reactions in each class.

The reaction scheme in Eq.s (4.110 – 4.112) is applied to each class:

- the class equivalence ratio ϕ_j is substituted in Eq. (4.114) and Eq. (4.113) to calculate the values of the reaction weights, $\alpha_{r\,j}$ and $\beta_{r\,j}$;
- the burning mass $\dot{\mathcal{M}}^{\mathrm{ff}}_{\mathrm{F}\,i}$, given by Eq. (4.117) is split according to $\alpha_{r\,j}$ and $\beta_{r\,j}$ among the three modelled reactions;

The stoichiometric coefficients in the chemical scheme, Eq.s (4.110 – 4.112), allow to compute the rates of production/consumption of each chemical species. For the generic, j-th class, these rates are expressed as:

$$\dot{\mathcal{M}}^{\mathrm{ff}}_{\mathrm{O_2}\,j} = \left[\alpha_{r\,j}\beta_{r\,j}\left(x+\frac{y}{4}-\frac{z}{2}\right)+(1-\alpha_{r\,j})\beta_{r\,j}\,\frac{x-z}{2}\right]\frac{M_{\mathrm{O_2}}}{M_F}\,\dot{\mathcal{M}}^{\mathrm{ff}}_{\mathrm{F}\,j} \tag{4.118}$$

$$\dot{\mathcal{M}}^{\mathrm{ff}}_{\mathrm{CO_2}\,j} = -\alpha_{r\,j}\beta_{r\,j}\,x\,\frac{M_{\mathrm{CO_2}}}{M_F}\,\dot{\mathcal{M}}^{\mathrm{ff}}_{\mathrm{F}\,j} \tag{4.119}$$

$$\dot{\mathcal{M}}^{\mathrm{ff}}_{\mathrm{H_2O}\,j} = -\alpha_{r\,j}\beta_{r\,j}\,\frac{y}{2}\,\frac{M_{\mathrm{H_2O}}}{M_F}\,\dot{\mathcal{M}}^{\mathrm{ff}}_{\mathrm{F}\,j} \tag{4.120}$$

$$\dot{\mathcal{M}}^{\mathrm{ff}}_{\mathrm{CO}\,j} = -\left[(1-\alpha_{r\,j})\beta_{r\,j}\,x+(1-\beta_{r\,j})\,z\right]\frac{M_{\mathrm{CO}}}{M_F}\,\dot{\mathcal{M}}^{\mathrm{ff}}_{\mathrm{F}\,j} \tag{4.121}$$

$$\dot{\mathcal{M}}^{\mathrm{ff}}_{\mathrm{H_2}\,j} = -(1-\alpha_{r\,j})\beta_{r\,j}\,\frac{y}{2}\,\frac{M_{\mathrm{H_2}}}{M_F}\,\dot{\mathcal{M}}^{\mathrm{ff}}_{\mathrm{F}\,j} \tag{4.122}$$

$$\dot{\mathcal{M}}^{\mathrm{ff}}_{\mathrm{C_aH_b}\,j} = -(1-\beta_{r\,j})\,z\,\frac{M_{\mathrm{C_aH_b}}}{M_F}\,\dot{\mathcal{M}}^{\mathrm{ff}}_{\mathrm{F}\,j} \tag{4.123}$$

with:

$$M_{\mathrm{X}} \quad \text{for} \quad \mathrm{X} = \mathrm{O_2}, \mathrm{CO_2}, \mathrm{H_2O}, \mathrm{CO}, \mathrm{H_2}, \mathrm{C_aH_b}. \tag{4.124}$$

the molar masses of the chemical species considered. The total rates of production/destruction of the chemical species involved in flame-front reactions are then obtained summing over the PDF classes:

$$\dot{\mathcal{M}}^{\mathrm{ff}}_{\mathrm{X}} = \sum_{j=1}^{N_{\mathrm{PDF}}} \dot{\mathcal{M}}^{\mathrm{ff}}_{\mathrm{X}\,j} \quad \text{for} \quad \mathrm{X} = \mathrm{O_2}, \mathrm{CO_2}, \mathrm{H_2O}, \mathrm{CO}, \mathrm{H_2}, \mathrm{C_aH_b}. \tag{4.125}$$

This procedure introduces additional sources of carbon monoxide CO and unburned hydrocarbons $\mathrm{C_aH_b}$, due to the existence of rich classes. These compounds are subsequently oxidized in the homogeneous burned gas zone, according to the post-flame reaction mechanisms described in Section 4.1.3.

4.8 Summary of the model equations

4.8.1 3-zone thermodynamic model

Cylinder gas. (detailed in Section 4.1.4)

$$\dot{\mathcal{M}}_i = \dot{\mathcal{M}}_i^{\text{va}} + \dot{\mathcal{M}}_i^{\text{bb}} + \dot{\mathcal{M}}_i^{\text{ff}} + \dot{\mathcal{M}}_i^{\text{po}} \quad \text{with} \quad i = 1, \dots, N_{SP} \tag{4.20}$$

$$\dot{p} = R\rho\dot{T} + RT\dot{\rho} + T\rho\dot{R} \tag{4.26}$$

Reactive chage zone. (detailed in Section 4.3.1)

$$\dot{\mathcal{M}}_{i\,\text{rc}} = \frac{\mathcal{M}_{\text{rc}}}{\mathcal{M}}\dot{\mathcal{M}}_i^{\text{in}} + \frac{\mathcal{M}_{i\,\text{rc}}}{\mathcal{M}}\dot{\mathcal{M}}^{\text{out}} + \dot{\mathcal{M}}_i^{\text{ent}} + \dot{\mathcal{M}}_i^{\text{ev}} + \dot{\mathcal{M}}_i^{\text{ff}} + \dot{\mathcal{M}}_i^{\text{po}} \quad \text{with} \quad i = 1, \dots, N_{\text{SP}} \tag{4.35}$$

$$\dot{\mathcal{H}}_{\text{rc}} = V_{\text{rc}}\,\dot{p} - \frac{V_{\text{rc}}}{V}\,Q_W + \dot{Q}_{\text{ff}} + \dot{Q}_{\text{po}} + h_0^L\,\dot{\mathcal{M}}^{\text{ev}} + \left(h_0^{\text{in}}\,\dot{\mathcal{M}}^{\text{in}} + \frac{\mathcal{H}_{\text{rc}}}{\mathcal{M}_{\text{rc}}}\,\dot{\mathcal{M}}^{\text{out}}\right)\frac{\mathcal{M}_{\text{rc}}}{\mathcal{M}} \tag{4.36}$$

Fresh gas zone. (detailed in Section 4.3.1)

$$\dot{\mathcal{M}}_{i\,\text{fg}} = \frac{\mathcal{M}_{\text{fg}}}{\mathcal{M}}\dot{\mathcal{M}}_i^{\text{in}} + \frac{\mathcal{M}_{i\,\text{fg}}}{\mathcal{M}}\dot{\mathcal{M}}^{\text{out}} + \left(\dot{\mathcal{M}}_i^{\text{ent}} + \dot{\mathcal{M}}_i^{\text{ev}}\right)\frac{\mathcal{M}_{\text{fg}}}{\mathcal{M}_{\text{rc}}} - \frac{Y_{i\,\text{fg}}}{Y_{F\,\text{fg}}}\,\dot{\mathcal{M}}_F^{\text{ff}} \quad \text{with} \quad i = 1, \dots, N_{\text{SP}} \tag{4.39}$$

$$\dot{\mathcal{H}}_{\text{fg}} = V_{\text{fg}}\,\dot{p} - \frac{V_{\text{fg}}}{V}\,Q_W + h_0^L\,\dot{\mathcal{M}}_i^{\text{ev}}\frac{\mathcal{M}_{\text{fg}}}{\mathcal{M}_{\text{rc}}} + \left[(h_0^{\text{in}}\,\dot{\mathcal{M}}^{\text{in}} + \frac{\mathcal{H}_{\text{fg}}}{\mathcal{M}_{\text{fg}}}\left(\dot{\mathcal{M}}^{\text{out}} - \dot{\mathcal{M}}^{\text{ff}}\right)\right]\frac{\mathcal{M}_{\text{fg}}}{\mathcal{M}} \tag{4.40}$$

4.8.2 Liquid Phase

Liquid parcel evaporating surface. (Detailed in Section 4.4.1)

$$\dot{\mathcal{S}}_L^i = \underbrace{\frac{6}{\rho_L\,D_{32}^{\text{inj}}\,(t)}\,\dot{\mathcal{M}}_{\text{inj}}^i}_{\text{production (inj)}} - \underbrace{\frac{2}{3}\,\frac{\mathcal{S}_L^i}{\mathcal{M}_L^i}\,\dot{\mathcal{M}}_{\text{ev}}^i}_{\text{destruction (ev)}} \tag{4.50}$$

Atomization model. (Detailed in Section 4.4.2)

$$\frac{D_{32}^{\text{inj}}}{D_{\text{noz}}} = \mathcal{K}_{\text{ato}}\,(Re_f\,We_f)^{-0.28} \tag{4.53}$$

Drop parcel dynamics. (Detailed in Section 4.4.3)

$$\dot{\mathcal{P}}_L^i = \underbrace{\frac{1}{2}\,C_D\,\rho_g\,S_d^i\,\left(u_p^{\parallel}(\mathcal{X}_L^i) + u_t^{\parallel}(\mathcal{X}_L^i) - u_d^i\right)^2}_{\text{drag force}} + \underbrace{\mathcal{K}_v\,u_{\text{inj}}\,\dot{\mathcal{M}}_{\text{inj}}}_{\text{injection}} - \underbrace{u_d^i\,\dot{\mathcal{M}}_{\text{ev}}^i}_{\text{evaporation}} \tag{4.59}$$

$$\dot{\mathcal{X}}_L^i = u_d^i = \frac{\mathcal{P}_L^i}{\mathcal{M}_L^i} \tag{4.55}$$

Drop parcel evaporation. (Detailed in Section 4.4.3)

$$\dot{\mathcal{M}}_L^i = \underbrace{-\pi\, n^i\, D_{32}^i\, \frac{\lambda_g}{c_{p\,g}}\, \frac{Sh}{Le}\, \log\left(1+B_M\right)}_{\dot{\mathcal{M}}_{\text{ev}}^i} + \dot{\mathcal{M}}_{\text{inj}}^i \tag{4.62}$$

$$\dot{\mathcal{H}}_L^i = \dot{\mathcal{M}}_{\text{ev}}^i \left[\frac{c_{p\,L}\,\left(T_\infty - T_d^i\right)}{B_T} - H_L - \frac{\mathcal{H}_L^i}{\mathcal{M}_L^i}\right] + h_0^{\text{inj}}\dot{\mathcal{M}}_{\text{inj}}^i \tag{4.64}$$

4.8.3 Gas Phase

Spray penetration. (Detailed in Section 4.5)

$$x_p = \tilde{x}\, x^+ \tag{4.67}$$

$$\tilde{x} = \mathcal{K}_p\, \tilde{t}\, \left(1+\tilde{t}^{\frac{n}{2}}\right)^{-\frac{1}{n}} \tag{4.68}$$

Spray spreading rate. (Detailed in Section 4.5)

$$\tan\frac{\alpha}{2} = \mathcal{K}_a \left[\left(\frac{\rho_g}{\rho_f}\right) - 0.0043\sqrt{\frac{\rho_f}{\rho_g}}\right] \tag{4.69}$$

Reactive charge volume and air entrainment. (Detailed in Section 4.5)

$$\dot{V}_{\text{rc}} = \frac{d}{dt}\left[\frac{\pi}{3}\, x^3\, \tan^2\frac{\alpha}{2}\, \frac{1+2\,\tan\frac{\alpha}{2}}{\left(1+\tan\frac{\alpha}{2}\right)^3}\right] \tag{4.70}$$

$$\dot{\mathcal{M}}_i^{\text{ent}} = \dot{V}_{\text{rc}}\, \left(1+\alpha_{t\,\text{ent}}\right)\, \rho_i \quad \text{with} \quad i = 1, \ldots, N_{\text{SP}} \tag{4.75}$$

4.8.4 Small-scale mixing: Y_F PDF

Mixture fraction discretization. (Detailed in Section 4.6)

$$Y_F^j = \frac{j-1}{N_{\text{PDF}}-1} \quad \text{with} \quad j = 1, 2, ..., N_{\text{PDF}} \tag{4.76}$$

Mass and momentum entering the PDF. (Detailed in Section 4.6)

$$\dot{\mathcal{M}}_{\text{so}\,j}^{\text{pdf}} = \begin{cases} \overbrace{\dot{\mathcal{M}}^{\text{ent}} + \frac{\mathcal{M}_{\text{rc}}}{\mathcal{M}}\dot{\mathcal{M}}^{\text{va}}}^{\text{entrained ambient gas}} - \overbrace{\sum_{k=2}^{N_{\text{PDF}}} \frac{1-Y_F^k}{Y_F^k} \sum_{i=1}^{N_P} C_{ik}^{\text{em}}\, \dot{\mathcal{M}}_i^{\text{ev}}}^{\text{ambient gas for fuel dilution}} & j = 1 \\ \underbrace{\frac{1}{Y_F^j}\sum_{i=1}^{N_P} C_{ij}^{\text{em}}\, \dot{\mathcal{M}}_i^{\text{ev}}}_{\text{ambient gas + fuel}} & j = 2, \ldots, N_{\text{PDF}} \end{cases} \tag{4.83}$$

$$\dot{\mathcal{P}}^{\mathrm{pdf}}_{\mathrm{so}\,j} = \begin{cases} \overbrace{u_a \left(\dot{\mathcal{M}}^{\mathrm{ent}} + \frac{\mathcal{M}_{\mathrm{rc}}}{\mathcal{M}} \dot{\mathcal{M}}^{\mathrm{va}} \right)}^{\text{entrained ambient gas}} - \overbrace{\frac{\mathcal{P}_0}{\mathcal{M}_0} \sum_{k=2}^{N_{\mathrm{PDF}}} \frac{1 - Y_F^k}{Y_F^k} \sum_{i=1}^{N_P} C_{ik}^{\mathrm{em}} \dot{\mathcal{M}}_i^{\mathrm{ev}}}^{\text{ambient gas for fuel dilution}} & j = 1 \\ \underbrace{\frac{\mathcal{P}_0}{\mathcal{M}_0} \frac{1 - Y_F^j}{Y_F^j} \sum_{i=1}^{N_P} C_{ij}^{\mathrm{em}} \dot{\mathcal{M}}_i^{\mathrm{ev}}}_{\text{ambient gas for fuel dilution}} + \underbrace{\sum_{i=1}^{N_P} u_{d\,i}\, C_{ij}^{\mathrm{em}} \dot{\mathcal{M}}_i^{\mathrm{ev}}}_{\text{fuel vapor}} & j = 2, \ldots, N_{\mathrm{PDF}} \end{cases} \tag{4.84}$$

with:

$$C_{ij}^{\mathrm{em}} = \begin{cases} \frac{Y_F^{j+1} - Y_{i\,F}^{\mathrm{sat}}}{Y_F^{j+1} - Y_F^j} & Y_F^j \leq Y_{i\,F}^{\mathrm{sat}} < Y_F^{j+1} \\ \frac{Y_{i\,F}^{\mathrm{sat}} - Y_F^{j-1}}{Y_F^j - Y_F^{j-1}} & Y_F^{j-1} \leq Y_{i\,F}^{\mathrm{sat}} < Y_F^j \\ 0 & \text{elsewhere} \end{cases} \tag{4.82}$$

Discrete PDF mixing mechanism: transport of mass and momentum. (Detailed in Section 4.6)

$$\dot{\mathcal{M}}_l^{\wedge} = \sum_{j=1}^{N_{\mathrm{PDF}}} \sum_{k=1}^{j} \dot{\mathcal{M}}_l^{j \wedge k} \quad \text{and} \quad \dot{\mathcal{P}}_l^{\wedge} = \sum_{j=1}^{N_{\mathrm{PDF}}} \sum_{k=1}^{j} \dot{\mathcal{P}}_l^{j \wedge k} \tag{4.99}$$

with:

$$\begin{aligned} \dot{\mathcal{M}}_j^{j \wedge k} &= -\rho_j \dot{V}_{\mathrm{Sweep}}^{j \wedge k} \frac{V_j V_k}{V_{\mathrm{tot}}^{5/3}} \sqrt{N_{\mathrm{PDF}}} \\ \dot{\mathcal{M}}_k^{j \wedge k} &= -\rho_k \dot{V}_{\mathrm{Sweep}}^{j \wedge k} \frac{V_j V_k}{V_{\mathrm{tot}}^{5/3}} \sqrt{N_{\mathrm{PDF}}} \end{aligned} \tag{4.91}$$

and:

$$\begin{aligned} \dot{\mathcal{P}}_j^{j \wedge k} &= -\frac{\mathcal{P}_j}{\mathcal{M}_j} \cdot \dot{\mathcal{M}}_j^{j \wedge k} \\ \dot{\mathcal{P}}_k^{j \wedge k} &= -\frac{\mathcal{P}_k}{\mathcal{M}_k} \cdot \dot{\mathcal{M}}_k^{j \wedge k} \end{aligned} \tag{4.92}$$

4.8.5 Combustion

Flame front reaction. (Detailed in Section 4.7)

$$\alpha_r \beta_r \left[\mathrm{C}_x\mathrm{H}_y\mathrm{O}_z + \left(x + \frac{y}{4} - \frac{z}{2} \right) \mathrm{O}_2 \longrightarrow x\,\mathrm{CO}_2 + \frac{y}{2}\,\mathrm{H}_2\mathrm{O} \right] \tag{4.110}$$

$$(1 - \alpha_r) \beta_r \left[\mathrm{C}_x\mathrm{H}_y\mathrm{O}_z + \frac{x - z}{2}\,\mathrm{O}_2 \longrightarrow x\,\mathrm{CO} + \frac{y}{2}\,\mathrm{H}_2 \right] \tag{4.111}$$

$$(1 - \beta_r) \left[\mathrm{C}_x\mathrm{H}_y\mathrm{O}_z \longrightarrow z\,\mathrm{CO} + \mathrm{C_aH_b} \right] \tag{4.112}$$

with

$$\beta_r = \frac{0,98}{\phi} \frac{4x + y - 2z}{2x - 2z} \tag{4.113}$$

and:

$$\alpha_r = \max\left(0, \frac{\max(0.98, \phi)\,\dfrac{4x + y - 2z}{\phi} - 2x + 2z}{2x + y}\right) \tag{4.114}$$

Average burning rate. (Detailed in Section 4.7)

$$\begin{aligned} \dot{\mathcal{M}}_j^{\mathrm{ff}} &= \frac{\dot{\mathcal{M}}_{\mathrm{F}}^{\mathrm{ff}}}{\bar{Y}_F}\,\mathrm{P}_F(j) \quad \text{with} \quad j = 1, \ldots, N_{\mathrm{PDF}} \\ \dot{\mathcal{M}}_{\mathrm{F}\,j}^{\mathrm{ff}} &= \dot{\mathcal{M}}_{\mathrm{F}}^{\mathrm{ff}}\,\mathrm{P}(j) \end{aligned} \tag{4.117}$$

Chapter 5

Validation of the Spray Model

This chapter presents three validation cases that were studied during this PhD. The cases are designed to test the following physical aspects of the development of a free spray in GDI conditions:

- dynamics in a quiescent environment;
- interaction with a tumble vortex;
- dynamics in a variable-density environment.

These studies were performed in parallel with the development of the 0D model and the results obtained motivated several modelling choices. The different blocks of the spray model, added throughout this work, were validated on these test cases.

The results presented here were all obtained with the final version of the 0D model and are therefore comparable with one another.

In all three cases, reference data are provided by 3D RANS simulations performed with the IFP-C3D solver (Velghe et al., 2011). Experimental data were used to calibrate the Lagrangian injection model in the quiescent environment case which corresponds to the MAGIE experiment (Dumas et al., 2012). For the following cases, derived from MAGIE with minor geometry modifications, the same calibration was used.

5.1 Constant-volume vessel: the MAGIE experiment

Part of the validations of the spray model developed so far during this PhD work were performed on a constant volume vessel test case, by comparing the results provided by the 0D model to experimental data and 3D RANS simulations. The test case consists of an injection of iso-octane into a constant volume chamber through a three hole symmetrical injector. Different thermodynamic conditions representative of early injections in a homogeneous DI-SI engine at high and low load were investigated.

A system simulation test bench was built in the Simcenter Amesim in order to model the experiment. The DI-SI engine combustion chamber component of the IFP-Engine library, in which the developments concerning the spray are integrated, was adapted imposing a null rotation speed, reducing the cylinder to a constant-volume vessel.

5.1.1 Test case

The constant volume vessel used for injection visualizations has a cubical shape with $1.4\,10^{-3} m^3$ volume. It is capable to reproduce high pressure ($1 - 150$ bar) and temperature ($20 - 200\,^{\circ}$C)

Table 5.1: Constant-volume vessel: gas operating conditions investigated in the MAGIE experiment. Only the high-load points are considered for this validation.

		Low Load			High Load		
		Gas p bar (abs)	Gas T °C	Gas ρ kg/m^3	Gas p bar (abs)	Gas T °C	Gas ρ kg/m^3
Ref. Pt.	#0	0.29	41	0.32	1.54	33	1.75
Iso ρ	$\#1_d$	0.31	60	0.32	1.95	115	1.75
	$\#2_d$	0.37	125	0.32	2.00	125	1.75
Iso p	$\#1_p$	0.29	60	0.30	1.54	90	1.48
	$\#2_p$	0.29	90	0.28	1.54	115	1.38
	$\#3_p$	0.29	125	0.25	1.54	125	1.35
(RANS only)	$\#4_p$				1.54	225	1.07

conditions that can be found in ICE combustion chambers. Four optical windows of 70 mm diameter provide access for the light source and cameras to perform Mie Scattering and Schlieren imaging.

An axisymetric three-nozzle injector with a global spray angle of 90° was adopted. The inclination of the three jet axes with respect to the injector axis is 38° which grants minimal interaction between the jets so to be representative of isolated sprays (Dumas et al., 2012).

The operating conditions for the experiments were chosen around two reference points representing typical low and high load engine operation. Gas temperature variations from the reference points at constant pressure and at constant density were also investigated as summarized in Table 5.1. The injection pressure is 200 bar and the injector tip temperature (which corresponds to the liquid fuel temperature) is maintained at 90 °C for all the operating points investigated. Injected fuel mass is 3.75 mg (724 μs) for low load operation and 24.9 mg (3320 μs) for high load.

Since the saturation pressure of iso-octane at 90 °C is 0.57 bar, flash boiling occurs at the low-load operating points. This condition not being dealt with in the evaporation and atomization models, only the high-load conditions were retained for validation.

5.1.2 Experimental data

Post-processed experimental data for this test case were available from previous measurements performed at IFPEN within the framework of the MAGIE (Modélisation et Approche Générique de l'Injection Essence – Modelling and Generic Approach of Gasoline Injection) collaborative project (Dumas et al., 2012).

Schlieren imaging was used in the experiment to investigate the vapour phase. This technique uses the refractive-index gradients in the measurement field to investigate density gradients and, therefore, fuel mass fraction distribution in the spray. The images are acquired placing a luminous source and a camera on two opposite sides of the cell, as shown in Fig 5.1.

Image post-processing on Schlieren images produced spray tip penetration length and

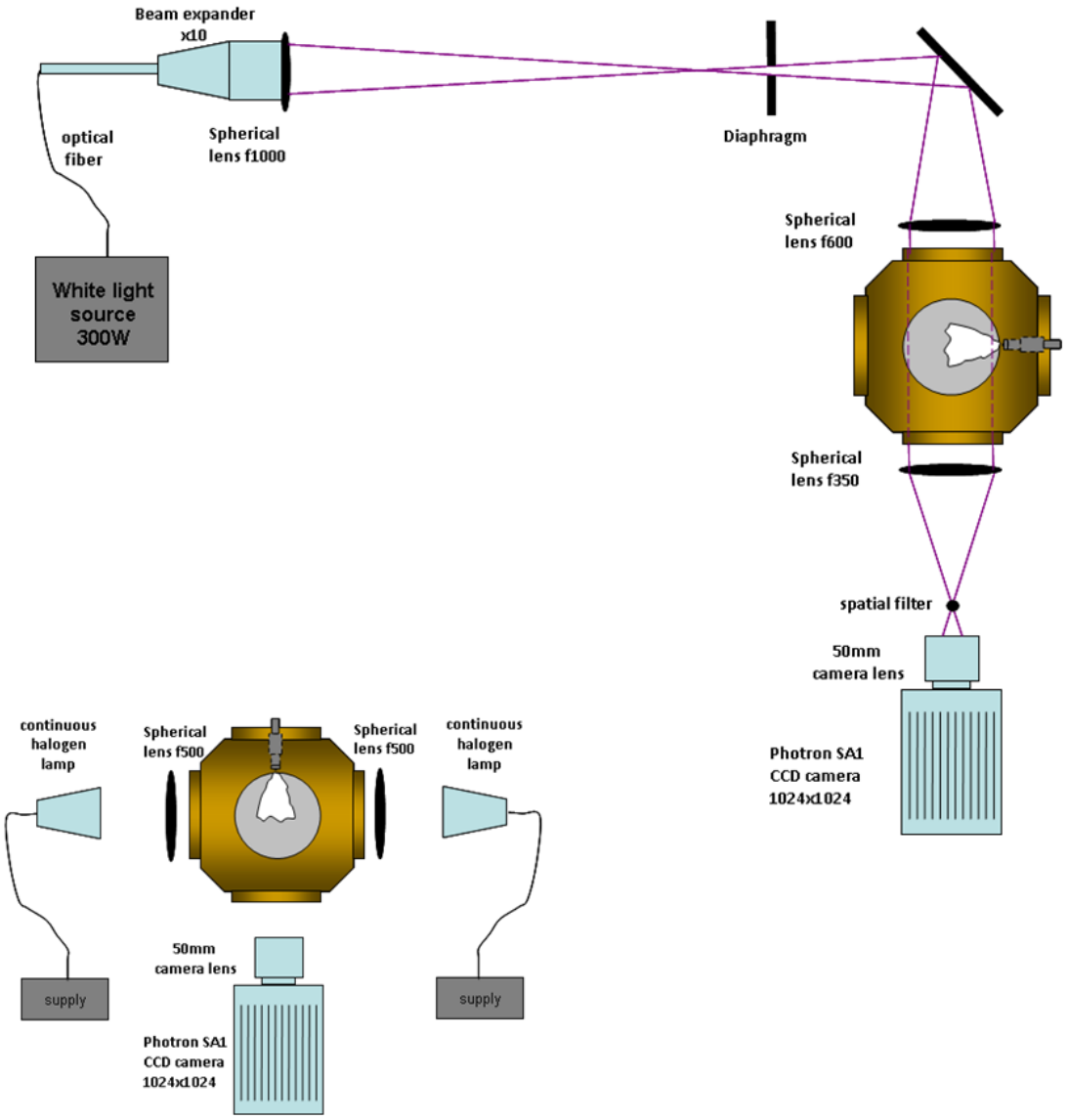

Figure 5.1: Optical setup for Schlieren (top-right) and Mie scattering (bottom-left) visualizations (source Dumas et al. (2012)).

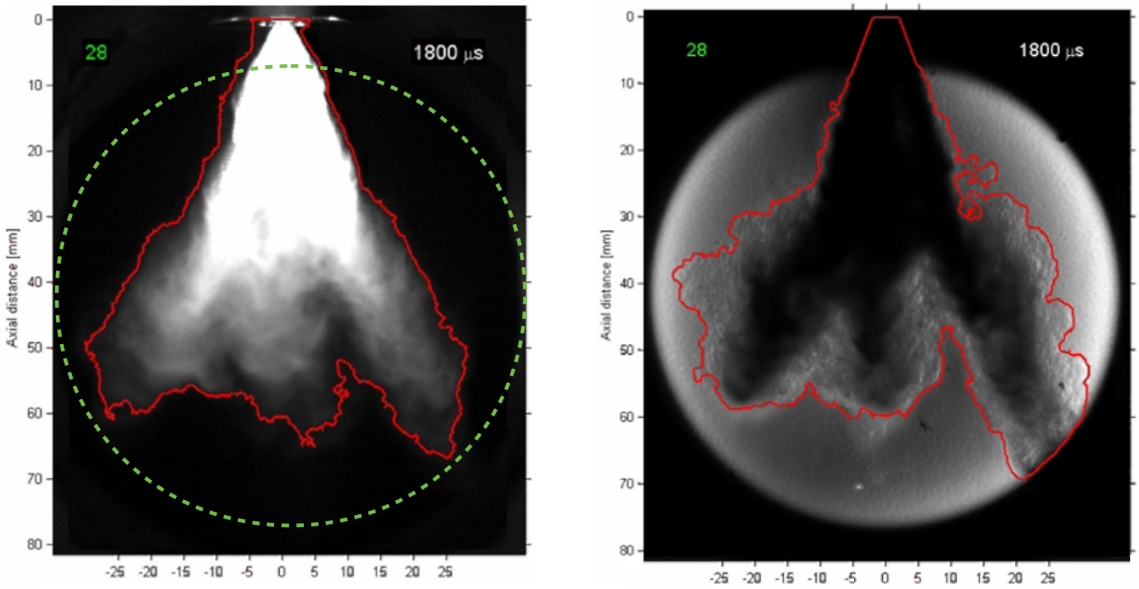

(a) Mie Scattering – liquid contour. **(b)** Schlieren imaging – vapor contour.

Figure 5.2: An example of the spray images obtained with the two techniques (Image from Dumas et al. (2012)). The white circle in the Schlieren figure (b pane), is the image of the back window used to illuminate the vessel. It is indicated by a dotted line on Mie Scattering figure (a pane) as a reference.

velocity as well as the global spray angle of the three jets.

Mie scattering, employed to investigate the liquid phase, captures the light scattered by the liquid fuel drops. The axis of the camera is perpendicular to that of the light sources, as shown in Fig. 5.1. Time evolution of liquid penetration length, velocity and global angle were likewise available.

With both techniques ten consecutive acquisitions were performed and averaged before post-processing, to acquire a statistically mean spray evolution. Figure 5.2 shows an example of instantaneous images acquired with the two techniques. A red line identifies the liquid (Mie) and vapour (Schlieren) contours used to define the spray penetration and spreading rate.

Penetrations

The gaseous and liquid spray penetrations were evaluated on the injector axis, z, at the maximum distance where fuel vapour or liquid were detected. This selects *de facto* the most penetrating jet. Penetration on the jet axis, x, can be obtained knowing the target inclination angle $\beta = 38°$ that the injector axis forms with the jet axes. Hence the two penetrations, z_p and x_p respectively, are related through:

$$x_p = \frac{z_p}{\cos\beta} \tag{5.1}$$

Spray angle

The measurements of the spray angle α provided by the experiment are derived from the spray images by measuring the spray width l_a at a given distance from the injector tip $z_a = 15\,mm$, as shown in Fig. 5.3a. This implies that the measured spray angle includes the three jets.

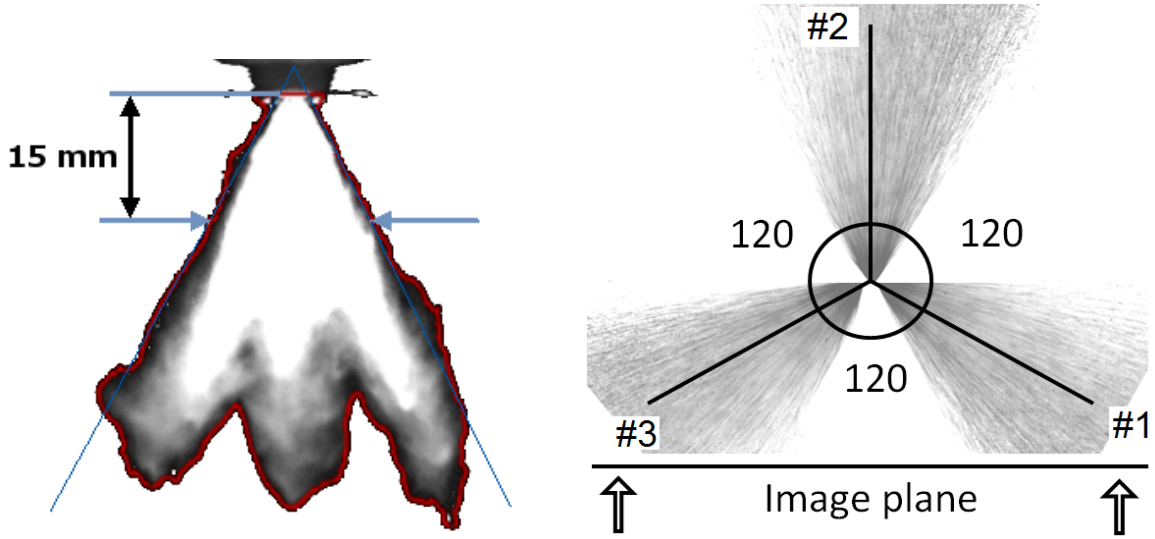

(a) Definition **(b)** Top view

Figure 5.3: Experimental spray angle.

Furthermore the plane containing the axes of the two external jets (n. 1 and 3), forms an angle γ with the image plane. Some corrections are therefore necessary in order to obtain the spray angle, ϑ of a single jet from the available data.

Denoting with β', x'_p and ϑ' respectively, the projections of β, x_p and ϑ on the image plane, it can be proved that:

- $\tan\beta' = \tan\beta\,\cos 30°$
- $x'_p = x_p \dfrac{\cos\beta}{\cos\beta'}$

Hence, the real spray angle can be computed as:

$$\tan\frac{\vartheta}{2} = \tan\frac{\vartheta'}{2}\frac{x'_p}{x_p} = \tan\frac{\vartheta'}{2}\frac{\cos\beta}{\cos\beta'} \tag{5.2}$$

The projected single-spray angle ϑ' is obtained from the measured global angle α as follows:

$$\vartheta' = \alpha - 2\,\beta' \tag{5.3}$$

5.1.3 3D numerical simulations

The main purpose of running RANS simulations here is to access those data that are not directly available from experiments, either because the related physical quantities were not investigated or because of the limits of the available techniques. In particular, the following data – needed to validate the different substeps of the 0D model – cannot be derived just by post-processing the experimental data:

liquid and vapour penetrations outside the measurement field: the optical access of the cell is limited in size, which restrains the observation field to a maximum distance of about 70 mm from the injector tip;

drop size distribution: required to validate the breakup and evaporation aspects of the developed model. The drop size distribution is not available in the experimental database and it is an input parameter[1] of the RANS simulations. To identify the most realistic characterization in 3D simulations, it was chosen to iterate through different initial conditions for primary atomization and choose the one that gives the best fit with experimental penetrations. The retained value was then compared to those proposed in literature for the same experience to avoid simulation setup errors;

spray volume and **ambient gas mass** within the spray to validate the gas entrainment model;

liquid and vapour mass of fuel to validate the evaporation model;

fuel mass fraction distribution to validate the mixture formation model.

The CFD simulations were performed with IFP-C3D (Velghe et al., 2011), an RANS code developed at IFP Energies nouvelles to perform engine simulations. The Sauter Mean Diameter (SMD) was set to $100\,\mu m$ for all cases – in agreement with Khan et al. (2012) – since the code provides a secondary atomization model that takes into account the ambient gas thermodynamic conditions.

Post processing

Spray penetration. The spray tip penetration on the nozzle axis direction, x_p, is derived from the three-dimensional fields obtained from the CFD simulations through the implementation of the following criteria.

Liquid phase penetration x_p is defined as the radius of a sphere – centered at the injector tip – containing $X_{\%}\%$ of the liquid mass in the domain.

$$X_{\%} = 90,\ 95,\ 98$$

Vapor phase penetrations are defined as the maximum of the distances from the injector tip of the cells satisfying the following criterion

$$Y_F^{\text{cell}} > Y_F^{\text{cr}} \tag{5.4}$$

where Y_F^{cell} is the average fuel mass fraction in the cell and Y_F^{cr} is a constant threshold; here:

$$Y_F^{\text{cr}} = 10^{-5},\ 10^{-3},\ 10^{-2} \tag{5.5}$$

Jet volume and spreading angle Likewise, the reactive charge volume is computed as the summing the volumes of the cells that satisfy the criterion defined in Eq. 5.4.

An estimation of the spreading angle α of a single jet is derived, knowing the spray volume, V_{spr}, and penetration on the jet axis, x_p, and assuming a conical shape corrected with a semisphere at the spray tip, which is the same shape assumption used in the 0D model: this allows to obtain comparable results from 3D and 0D data.

The jet volume, is obtained as the sum of the cone and the semisphere:

$$V_{\text{spr}} = \frac{\pi}{3} a_p^3 \tan^2\frac{\alpha}{2} + \frac{2\pi}{3} a_p^3 \tan^3\frac{\alpha}{2} \tag{5.6}$$

[1] In all 3D RANS simulations performed in this work, the drop-size distribution is obtained injecting identical drops (uniform initial distribution) that are subsequently subject to a secondary atomization model.

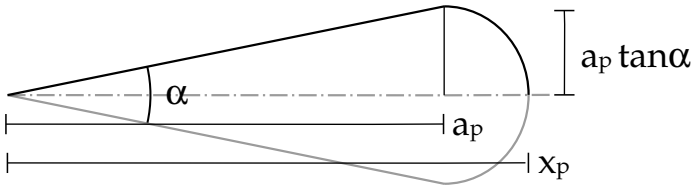

Figure 5.4: The assumed shape of a 3D single jet, used to determine the spreading rate based on its volume and penetration is obtained as the combination of a cone and a semisphere at its base.

with a_p the cone height, obtained as:

$$a_p = \frac{x_p}{1 + \tan\frac{\alpha}{2}} \tag{5.7}$$

from the tip penetration.

Mixture formation. A discrete PDF like the one presented in § 4.6 was derived from the CFD data dividing the fuel mass fraction, Y_F, into 31 classes. The i-th class is characterized by the two values $Y^i_{F\,\min}$ and $Y^i_{F\,\max}$ that delimit its fuel mass fraction interval.

Each time-step, the code cycles through the cells and identifies each of them as member of a class i so that :

$$Y^i_{F\,\min} < Y^{\text{cell}}_F < Y^i_{F\,\max} \tag{5.8}$$

and sums the cell values of the following quantities to the respective class values:

- gas mass;
- fuel vapour mass;
- cell volume;
- momentum;
- kinetic energy;

so to describe how these extensive quantities are divided among the fuel mass fraction classes.

The mean value, $\bar{Y}_F$, and variance, $\sigma^2_{Y_F}$, of Y_F within the spray volume are also calculated during the post-processing loop described above. The variance takes into account the two contributions:

- variation of the cell values Y^{cell}_F in the domain;
- the sub-grid variance, $\tilde{\sigma}^2_{Y_F}$, of Y_F transported by the turbulence model[2];

leading to the expression:

$$\sigma^2_{Y_F} = \frac{1}{\mathcal{M}^{tot}_F} \sum_{i=1}^{N_{\text{cells}}} \left[\left(Y^i_F - \bar{Y_F}\right)^2 + \left(\tilde{\sigma}^i_{Y_F}\right)^2 \right] \mathcal{M}^i_F \tag{5.9}$$

with $\mathcal{M}^i_F$ the fuel mass contained in the i-th cell, $\mathcal{M}^{tot}_F$ the fuel mass contained in the spray volume, $\bar{Y_F}$ the average fuel mass fraction on the spray and N_{cells} the number of cells in the spray.

These data will prove useful in future validations of the mixture formation model.

[2] The dynamics of sub-grid variance is modelled, in the RANS code, by a transport equation for $\sigma^2_{Y_F}$ and an algebraic equation for its dissipation rate. The details of this approach are described by Colin et al. (2003).

5.1.4 0D numerical simulations

0D simulation were performed with the developed model. This section presents the values of relevant model parameters and a comparison of the results obtained with 0D and 3D.

Model parameters

Table 5.2 synthetizes the calibration parameter set adopted to run the 0D model. It is assumed that the values of $\mathcal{K}_{t\,\mathrm{ev}}$, $\mathcal{K}_{t\,\mathrm{en}}$ and $\mathcal{K}_{\beta}^{\mathrm{pdf}}$ do not influence the results of this validation case, since the gas is at rest at the beginning of the injection.

Table 5.2: Three-nozzle injection in a constant-volume vessel (MAGIE experiment): calibration of the 0D model.

Evaporation				Spray			Mixing			
$\mathcal{K}_{\mathrm{ato}}$	N_P	$\mathcal{K}_v$	$\mathcal{K}_{t\,\mathrm{ev}}$	$\mathcal{K}_p$	$\mathcal{K}_a$	$\mathcal{K}_{t\,\mathrm{en}}$	N_{CL}	$\mathcal{K}_{\alpha}^{\mathrm{pdf}}$	$\mathcal{K}_{\beta}^{\mathrm{pdf}}$	$\mathcal{K}_{\mathcal{P}}^{\mathrm{pdf}}$
3.00	20	1.00	2.50	1.40	1.00	1/600	100	1.7	30	$5.0\,10^3$

The values chosen for these parameters result from the model calibration to globally match the reference (3D and measurements) data on the operating points considered. In particular:

- $\mathcal{K}_{\mathrm{ato}}$ is used to fine-tune the evaporation rate targeting the liquid and vapour fuel masses;
- $\mathcal{K}_p$ targets the spray penetration
- $\mathcal{K}_{\alpha}^{\mathrm{pdf}}$ and $\mathcal{K}_{\mathcal{P}}^{\mathrm{pdf}}$ target the time-evolution of the PDF variance.

Results

The results obtained from experiments, 3D RANS computations and the 0D model are presented in this section, both for the isobaric (constant pressure) and isopycnic (constant density) variations. Test conditions are summarized in Table 5.1.

Vapor penetration. Vapor penetrations obtained with the 0D model are compared to experimental (Schlieren) and 3D RANS results. In particular:

- Figure 5.5 presents the evolution for the reference point, #0, and points $\#1_d$ and $\#2_d$ of the isopycnic variation;
- Figure 5.6 presents the evolution for points $\#1_p$, $\#2_p$, $\#3_p$ and $\#4_p$ of the isobaric variation.

All the curves show a good agreement between experimental data and both simulations (0D and 3D). Experimental data are only available until the spray tip reaches the optical window boundary. Due to the spray/wall interaction, penetration in RANS slows down when the spray tip approches a wall (around $t = 4\,\mathrm{ms}$ for all cases): this phenomenon is not taken into account by the 0D model, leading to deviations towards the end of the simulation.

Concerning the dependency on the thermodynamic conditions, the vapor penetrations provided by 0D model at constant density (Fig. 5.5 pane (d)) does not depend on temperature since, in the Siebers model adopted, density is the only thermodynamic parameter of the gas phase take into account. Little negative trends appear in experimental and 3D RANS data.

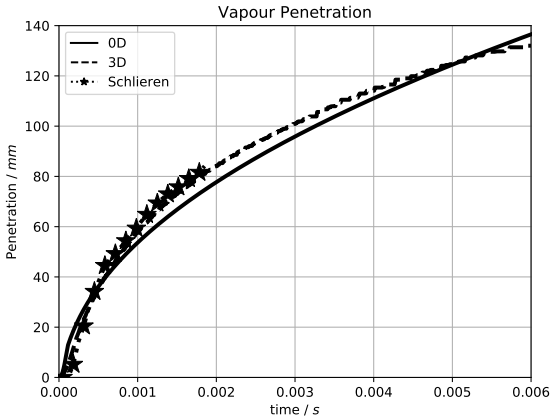

(a) Reference point #0: $p_0 = 1.54\,\text{bar}$ and $T_0 = 33\,°\text{C}$.

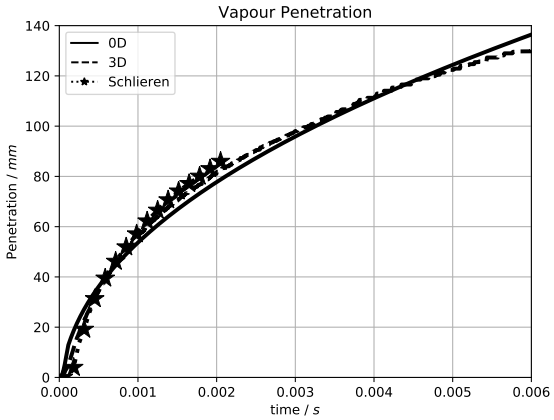

(b) Point #1_d: $p_0 = 1.95\,\text{bar}$ and $T_0 = 115\,°\text{C}$.

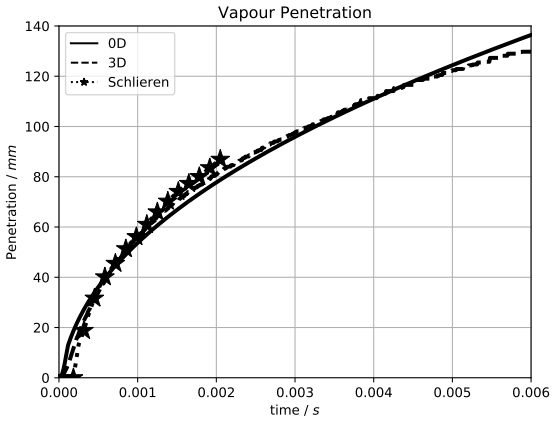

(c) Point #2_d: $p_0 = 2.00\,\text{bar}$ and $T_0 = 125\,°\text{C}$.

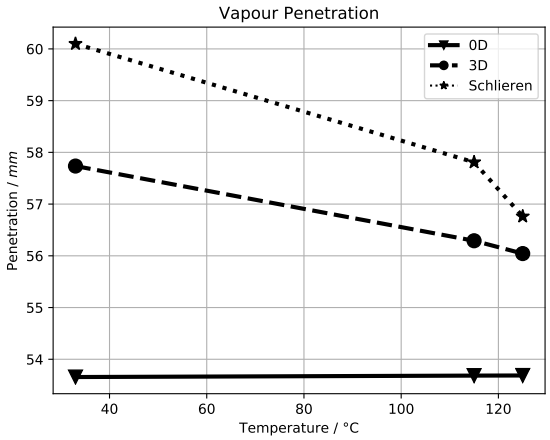

(d) Temperature sensitivity analysis at $t = 1\,\text{ms}$.

Figure 5.5: Constant-volume vessel (MAGIE): reference point and **isopycnic** variations (Table 5.1)) – spray **vapor penetration**. (a) – (c): time evolution in different operating conditions. (d): sensitivity to the initial temperature T_0 (also includes the reference point shown in Fig. 5.5 (a)). Solid lines for 0D, dashed lines for 3D and dotted lines for experiment.

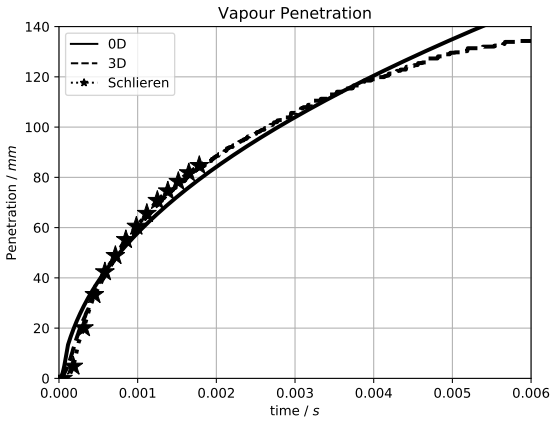

(a) Point $\#1_p$: $p_0 = 1.54\,\text{bar}$ and $T_0 = 90\,°\text{C}$.

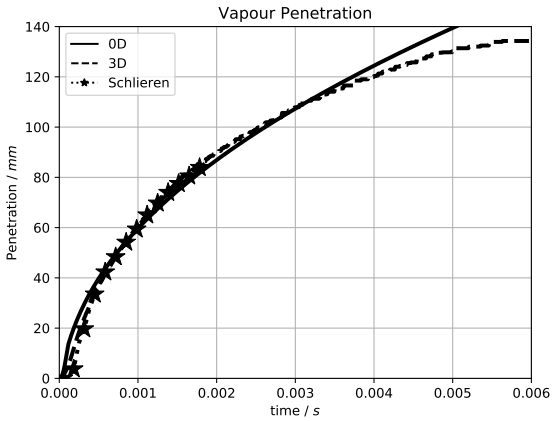

(b) Point $\#2_p$: $p_0 = 1.54\,\text{bar}$ and $T_0 = 115\,°\text{C}$.

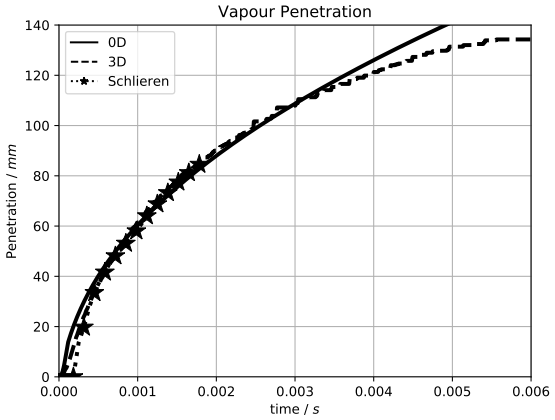

(c) Point $\#3_p$: $p_0 = 1.54\,\text{bar}$ and $T_0 = 125\,°\text{C}$.

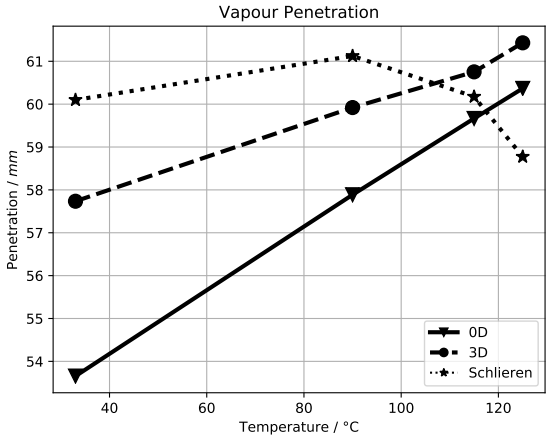

(d) Temperature sensitivity analysis at $t = 1\,\text{ms}$.

Figure 5.6: Constant-volume vessel (MAGIE): **isobaric** variations (Table 5.1)) – spray **vapor penetration**. (a) – (c): time evolution in different operating conditions. (d): sensitivity to the initial temperature T_0 (also includes the reference point shown in Fig. 5.5 (a)). Solid lines for 0D, dashed lines for 3D and dotted lines for experiment.

At constant pressure, on the other hand, sprays show a tendency to penetrate more quickly at higher temperatures. A slight positive trend that appears in RANS data is also found with the 0D model (Fig. 5.6 pane (d)). Though this trend is hardly visible in experimental data, an increase in gas temperature and the consequent density reduction are expected to accelerate the penetration (Siebers, 1998).

Liquid penetration. Similar considerations apply to the liquid penetrations show in Fig. 5.7 (isopycnic variation) and Fig. 5.8 (isobaric variation). The 0D values of the liquid penetration, X_L,are obtained integrating the momentum equations of each drop parcel according to Eq. (4.55), recalled here:

$$\dot{\mathcal{X}}_L^i = u_d^i = \frac{\mathcal{P}_L^i}{\mathcal{M}_L^i} \quad \text{with} \quad i = 1, \dots, N_\text{P} \tag{4.55}$$

and taking the maximum value at current time:

$$X_L = \max_{i=1}^{N_\text{P}} \mathcal{X}_L^i \tag{4.61}$$

The accuracy of this method decreases with time, because of error accumulation throughout the integration: the drop dynamics model describes the forces that act on each drop parcel, these are subsequently integrated to obtain the drop momentum, $\mathcal{P}_L^i$, and velocities, $\dot{\mathcal{X}}_L^i$, which are again integrated to obtain the penetrations, $\mathcal{X}_L^i$. This leads, in particular, to an underestimation of the liquid penetrations starting from $t = 3\,\text{ms}$ with respect to RANS data (experimental data are unavailable at this time, due to the saturation of the optical window).

Spreading angle. The spreading angles – shown in Fig. 5.9 (reference point isopycnic variations) and Fig. 5.10 (isobaric variations) – are globally well described. Angles in 0D and RANS are evaluated with respect to the volume of the gas phase, while the liquid phase (Mie scattering images) is used for the experiments. Furthermore, given the noise level in the experimental signal, the (d) panes in Fig.s 5.9 – 5.10 show the mean value in the $t = 2 - 3\,\text{ms}$ interval.

The 0D model expresses the spreading angle as a function of the thermodynamic conditions in the vessel which do not vary during the simulation, leading to a constant output. The values obtained with CFD and experiments at the beginning of the injection should not be taken into account, since they are derived dividing the spray volume (CFD) or area (Mie) by the spray penetration x_p which amplifies the inaccuracies for small x_p values.

No effect of temperature is visible in 0D data at constant density (Fig. 5.9 pane (d)), since density is the only thermodynamic parameter of the gas phase take into account in Eq. (4.69), used for the spray angle. The trend visible in RANS data (Fig. 5.10 pane (d)) at constant pressure is well represented by the 0D model: higher temperatures lead to lower densities and to a lower momentum transfer to the gas phase, so that the spray spreads less. This trend is not observed in the experimental data.

Spray volume. The spray volumes obtained from RANS data and with the 0D model are shown in Fig.5.11 (reference point isopycnic variations) and Fig.5.12 (isobaric variations): both figures show a plot of the data from all the operating points against time (pane (a)) and a plot against temperature at selected times (pane (b)).

Spray volumes are almost constant through isopycnic temperature variation, because of the insensitivity of the models adopted for penetration and spreading rate to thermodynamic

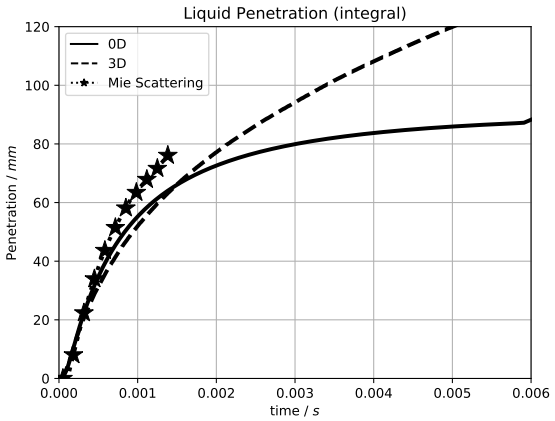

(a) Reference point #0: $p_0 = 1.54\,\text{bar}$ and $T_0 = 33\,°\text{C}$.

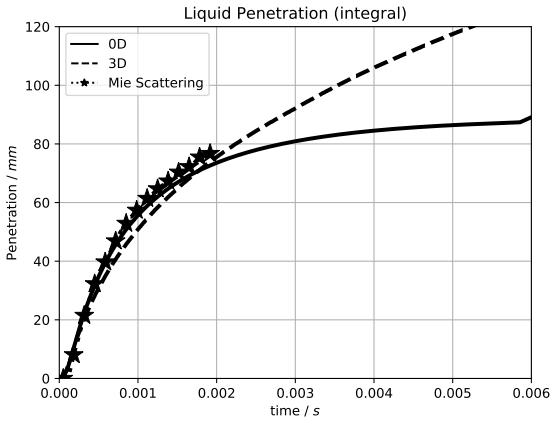

(b) Point #1_d: $p_0 = 1.95\,\text{bar}$ and $T_0 = 115\,°\text{C}$.

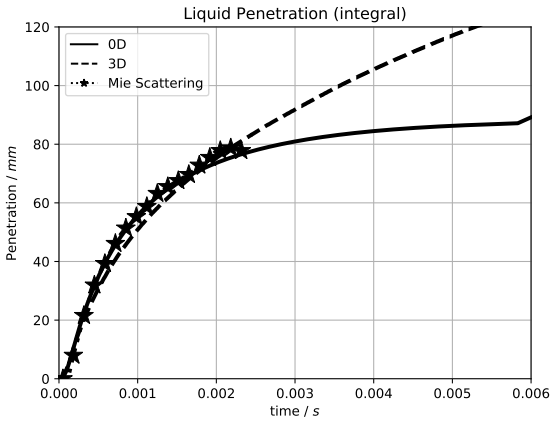

(c) Point #2_d: $p_0 = 2.00\,\text{bar}$ and $T_0 = 125\,°\text{C}$.

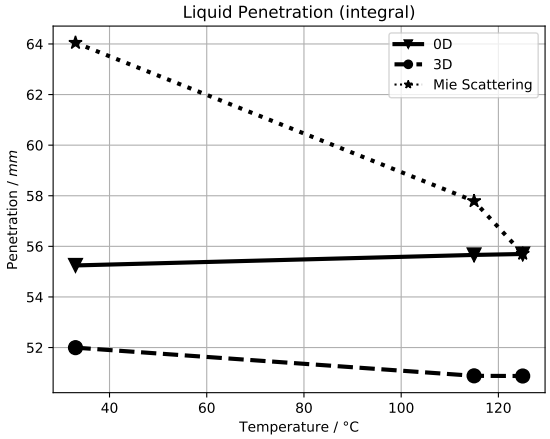

(d) Temperature sensitivity analysis at $t = 1\,\text{ms}$.

Figure 5.7: Constant-volume vessel (MAGIE): reference point and **isopycnic** variations (Table 5.1)) – spray **liquid penetration**. (a) – (c): time evolution in different operating conditions. (d): sensitivity to the initial temperature T_0 (also includes the reference point shown in Fig. 5.5 (a)). Solid lines for 0D, dashed lines for 3D and dotted lines for experiment.

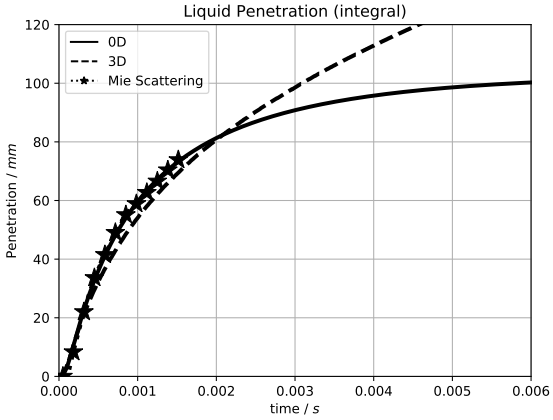

(a) Point $\#1_p$: $p_0 = 1.54\,\text{bar}$ and $T_0 = 90\,°\text{C}$.

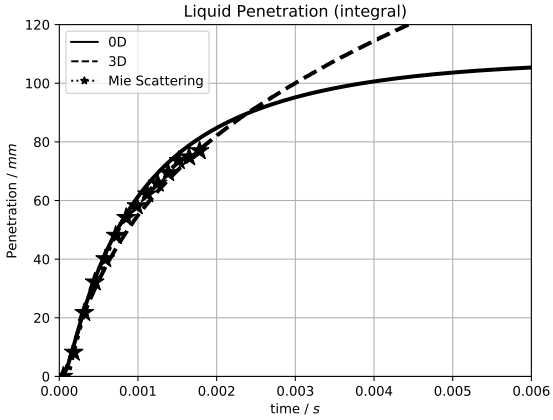

(b) Point $\#2_p$: $p_0 = 1.54\,\text{bar}$ and $T_0 = 115\,°\text{C}$.

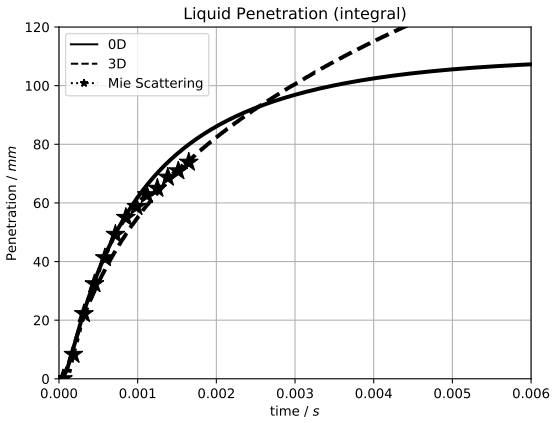

(c) Point $\#3_p$: $p_0 = 1.54\,\text{bar}$ and $T_0 = 125\,°\text{C}$.

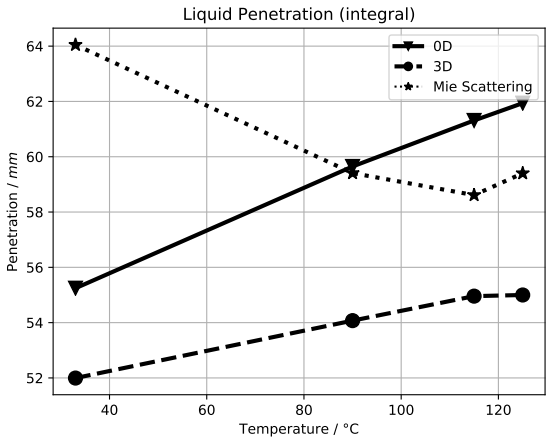

(d) Temperature sensitivity analysis at $t = 1\,\text{ms}$.

Figure 5.8: Constant-volume vessel (MAGIE): **isobaric** variations (Table 5.1)) – spray **liquid penetration**. (a) – (c): time evolution in different operating conditions. (d): sensitivity to the initial temperature T_0 (also includes the reference point shown in Fig. 5.5 (a)). Solid lines for 0D, dashed lines for 3D and dotted lines for experiment.

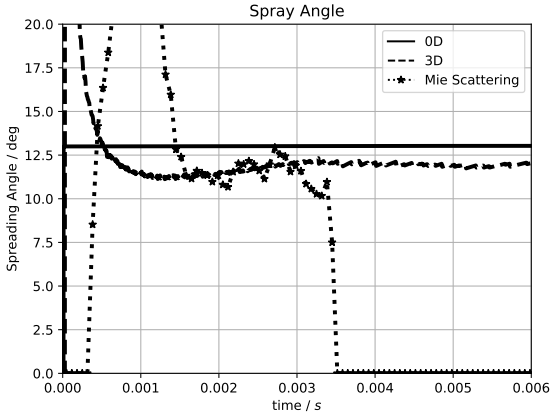

(a) Reference point #0: $p_0 = 1.54\,\text{bar}$ and $T_0 = 33\,°\text{C}$.

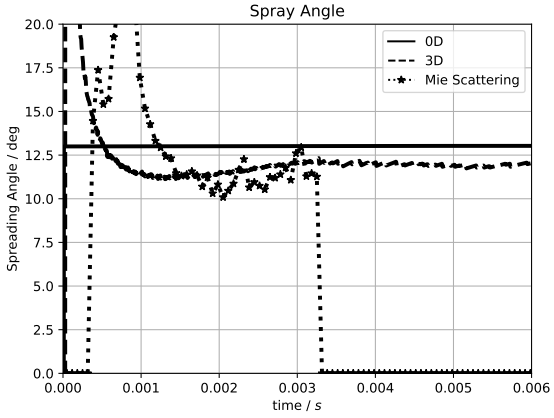

(b) Point #1_d: $p_0 = 1.54\,\text{bar}$ and $T_0 = 115\,°\text{C}$.

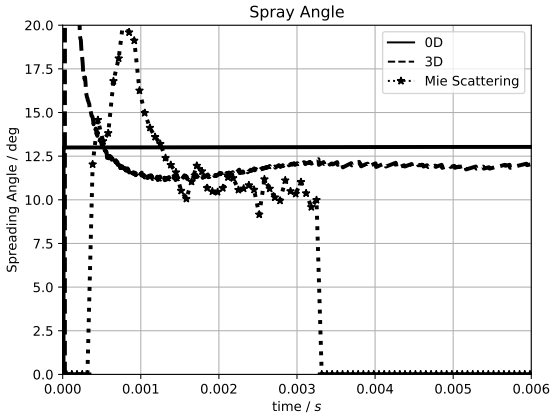

(c) Point #2_d: $p_0 = 1.54\,\text{bar}$ and $T_0 = 125\,°\text{C}$.

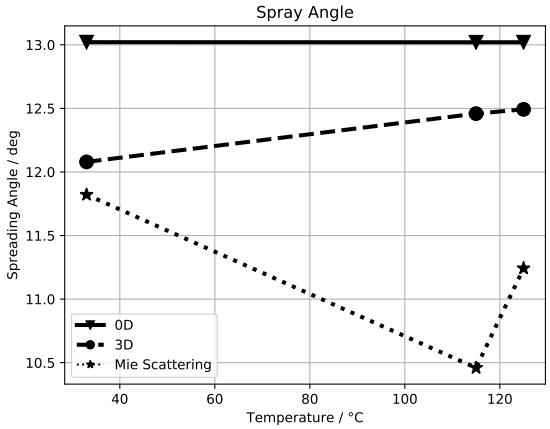

(d) Temperature sensitivity analysis at $t = 3\,\text{ms}$.

Figure 5.9: Constant-volume vessel (MAGIE): reference point and **isopycnic** variations (Table 5.1)) – spray **spreading angle**. (a) – (c): time evolution in different operating conditions. (d): sensitivity to the initial temperature T_0 (also includes the reference point shown in Fig. 5.5 (a)). Solid lines for 0D, dashed lines for 3D and dotted lines for experiment.

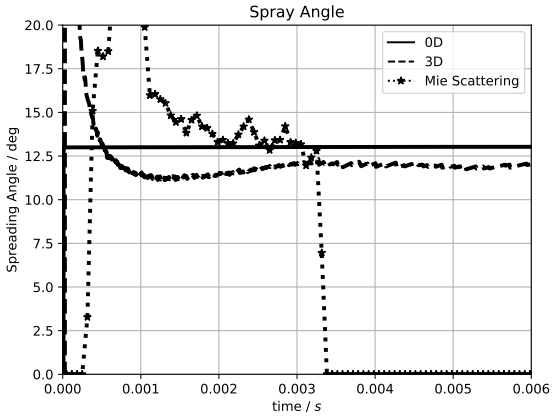

(a) Point $\#1_p$: $p_0 = 1.54\,\text{bar}$ and $T_0 = 90\,°\text{C}$.

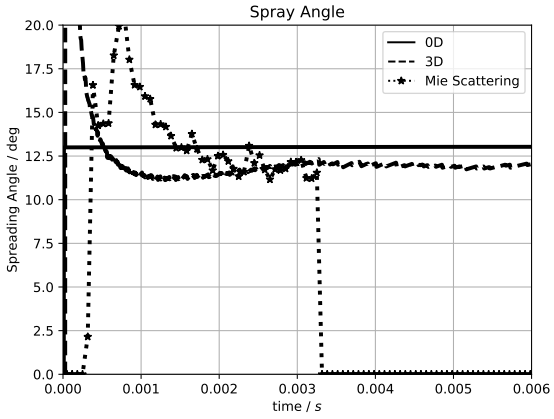

(b) Point $\#2_p$: $p_0 = 1.54\,\text{bar}$ and $T_0 = 115\,°\text{C}$.

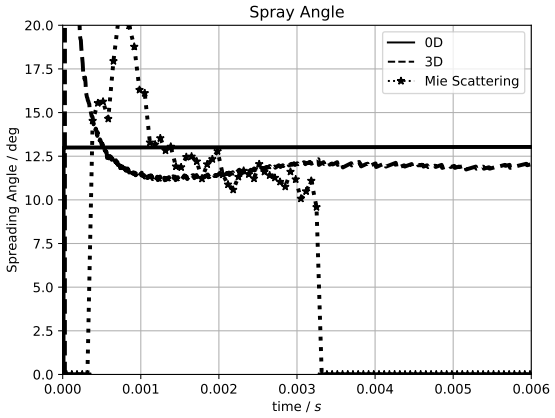

(c) Point $\#3_p$: $p_0 = 1.54\,\text{bar}$ and $T_0 = 125\,°\text{C}$.

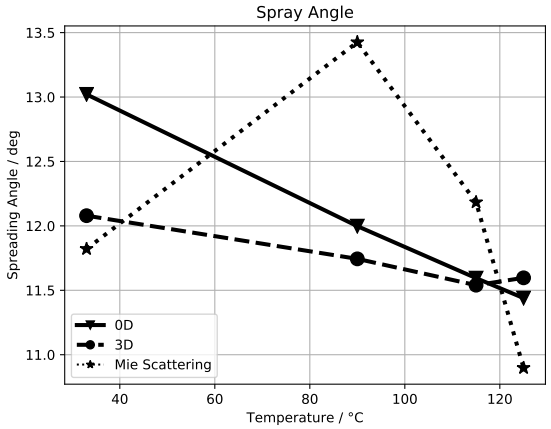

(d) Temperature sensitivity analysis at $t = 3\,\text{ms}$.

Figure 5.10: Constant-volume vessel (MAGIE): **isobaric** variations (Table 5.1)) – spray **spreading angle**. (a) – (c): time evolution in different operating conditions. (d): sensitivity to the initial temperature T_0 (also includes the reference point shown in Fig. 5.5 (a)). Solid lines for 0D, dashed lines for 3D and dotted lines for experiment.

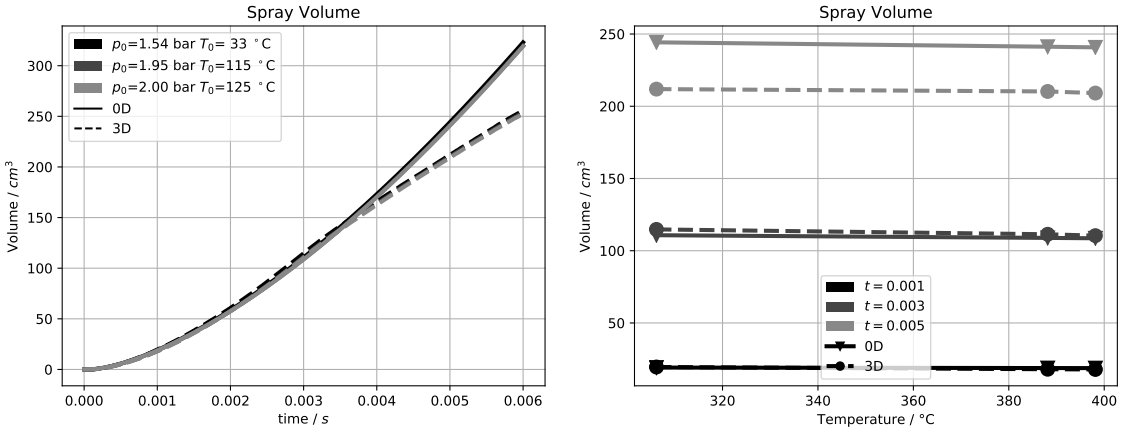

(a) Time evolution for different operating points (identified by shades of grey).

(b) Temperature sensitivity analysis at $t = 1\,\text{ms}$, $t = 3\,\text{ms}$ and $t = 5\,\text{ms}$ (identified by shades of grey).

Figure 5.11: Constant-volume vessel (MAGIE): reference point and **isopycnic** variations (Table 5.1)) – **spray volume**. Left pane (a): time evolution for different operating conditions. Right pane (b): sensitivity to initial temperature T_0 for different times after SOI. Solid lines for 0D and dashed lines for 3D.

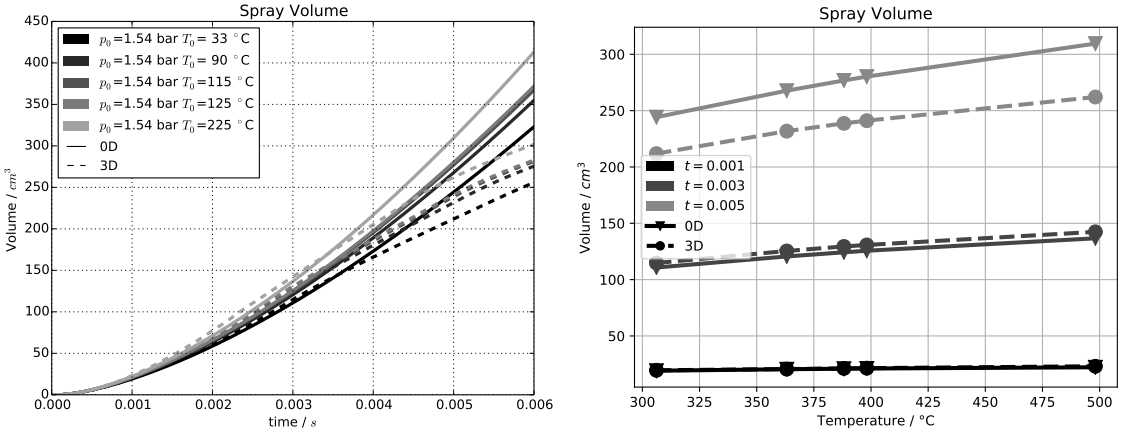

(a) Time evolution for different operating points (identified by shades of grey).

(b) Temperature sensitivity analysis at $t = 1\,\text{ms}$, $t = 3\,\text{ms}$ and $t = 5\,\text{ms}$ (identified by shades of grey).

Figure 5.12: Constant-volume vessel (MAGIE): reference point and **isobaric** variations (Table 5.1)) – **spray volume**. (a) – (c): time evolution in different operating conditions. (d): sensitivity to the initial temperature T_0 (also includes the reference point shown in Fig. 5.5 (a)). Solid lines for 0D and dashed lines for 3D.

variation at constant density. The three curves in the left pane (a) of Fig. 5.11 collapse on oneanother while the right pane (b) shows constant data.

Isobaric data, Fig. 5.12, show, on the other hand, a significative trend that is well represented by the 0D model.

In both Fig.s 5.11 – 5.12 deviations appear after $t = 4\,\text{ms}$ because of the influence of the solid wall that slows down the approaching spray tip: this effect is well represented in 3D RANS while the 0D model does not take it into account.

Evaporation. The description of evaporation can be evaluated following the values of liquid and vapor fuel mass, in the following figures:

- the evolution of the liquid fuel mass and its sensitivity to gas temperature variation at constant density (Table 5.1) is shown in Fig. 5.13;
- the evolution of the liquid fuel mass and its sensitivity to gas temperature variation at constant pressure (Table 5.1) is shown in Fig. 5.14;
- the evolution of the fuel vapor mass and its sensitivity to gas temperature variation at constant density (Table 5.1) is shown in Fig. 5.15;
- the evolution of the fuel vapor mass and its sensitivity to gas temperature variation at constant pressure (Table 5.1) is shown in Fig. 5.16;

All figures present:

- a left pane (a) with a plot against time, for all the cases belonging to the respective parametric variation (isopycnic or isobaric);
- a left pane (b) with a plot against temperature, for three different timestamps ($t = 1\,\text{ms}$, $t = 3\,\text{ms}$ and $t = 5\,\text{ms}$).

Both the time evolutions and the pronounced temperature trends are well represented.

Mixing. The description of mixing provided by the 0D model can be evaluated following the values of the average mixture fraction, $\bar{Y}_F$, and its variance, $\sigma^2_{Y_F}$, in the following figures:

- the evolution of the average mixture fraction, $\bar{Y}_F$, and its sensitivity to gas temperature variation at constant density (Table 5.1) is shown in Fig. 5.17;
- the evolution of the average mixture fraction, $\bar{Y}_F$, and its sensitivity to gas temperature variation at constant pressure (Table 5.1) is shown in Fig. 5.18;
- the evolution of the mixture fraction variance, $\sigma^2_{Y_F}$, and its sensitivity to gas temperature variation at constant density (Table 5.1) is shown in Fig. 5.19;
- the evolution of the mixture fraction variance, $\sigma^2_{Y_F}$, and its sensitivity to gas temperature variation at constant pressure (Table 5.1) is shown in Fig. 5.20.

The figures adopt the usual data presentation consisting of time plots (a) and temperature plots (b).

The average mixture fraction, $\bar{Y}_F$, is globally well represented in both Fig.s 5.17 – 5.18, representing the isopycnic and isobaric temperature variations, respectively. The plots show a change in slope around 3 ms, which corresponds to the end of injection. Deviations appear at the beginning of injection, due to the small masses of fuel and air involved, and towards the end of the simulation when the spray tip approaches the chamber walls: the 0D model does

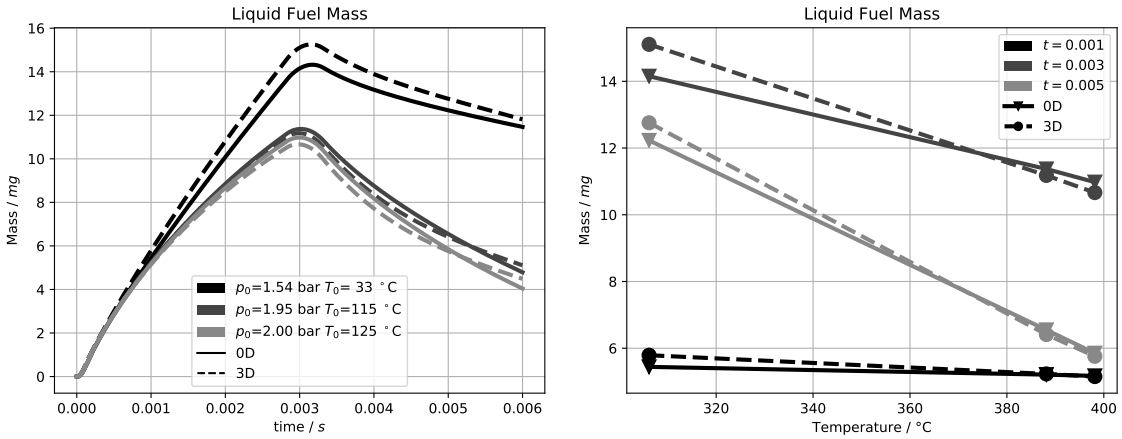

(a) Time evolution for different operating points (identified by shades of grey).

(b) Temperature sensitivity analysis at $t = 1$ ms, $t = 3$ ms and $t = 5$ ms (identified by shades of grey).

Figure 5.13: Constant-volume vessel (MAGIE): reference point and **isopycnic** variations (Table 5.1)) – **liquid fuel mass**. Left pane (a): time evolution for different operating conditions. Right pane (b): sensitivity to initial temperature T_0 for different times after SOI. Solid lines for 0D, dashed lines for 3D and dotted lines for experiment.

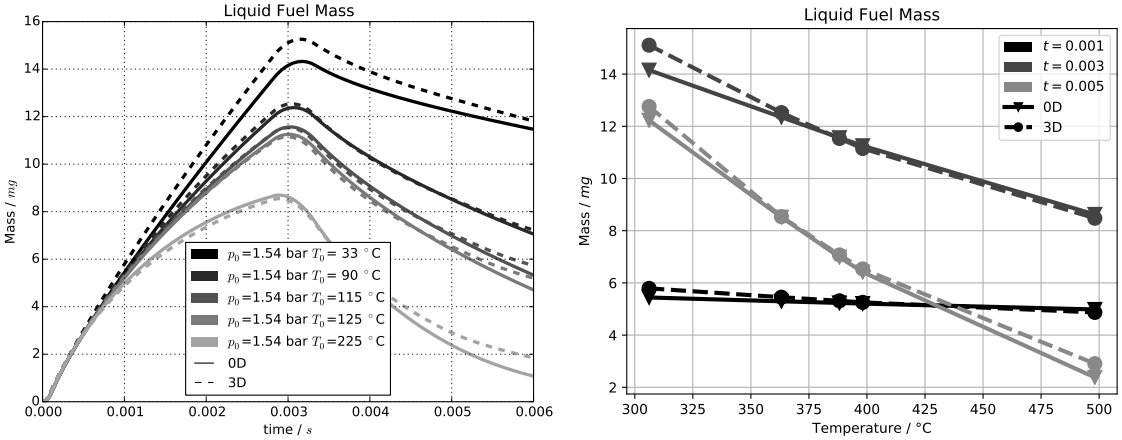

(a) Time evolution for different operating points (identified by shades of grey).

(b) Temperature sensitivity analysis at $t = 1$ ms, $t = 3$ ms and $t = 5$ ms (identified by shades of grey).

Figure 5.14: Constant-volume vessel (MAGIE): reference point and **isobaric** variations (Table 5.1)) – **liquid fuel mass**. Left pane (a): time evolution for different operating conditions. Right pane (b): sensitivity to initial temperature T_0 for different times after SOI. Solid lines for 0D and dashed lines for 3D.

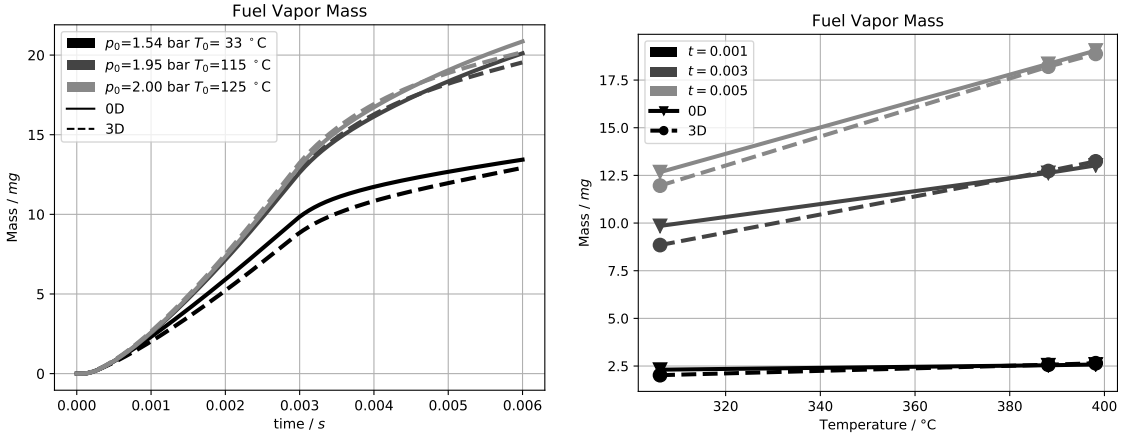

(a) Time evolution for different operating points (identified by shades of grey).

(b) Temperature sensitivity analysis at $t = 1\,\text{ms}$, $t = 3\,\text{ms}$ and $t = 5\,\text{ms}$ (identified by shades of grey).

Figure 5.15: Constant-volume vessel (MAGIE): reference point and **isopycnic** variations (Table 5.1)) – **fuel vapor mass**. Left pane (a): time evolution for different operating conditions. Right pane (b): sensitivity to initial temperature T_0 for different times after SOI. Solid lines for 0D and dashed lines for 3D.

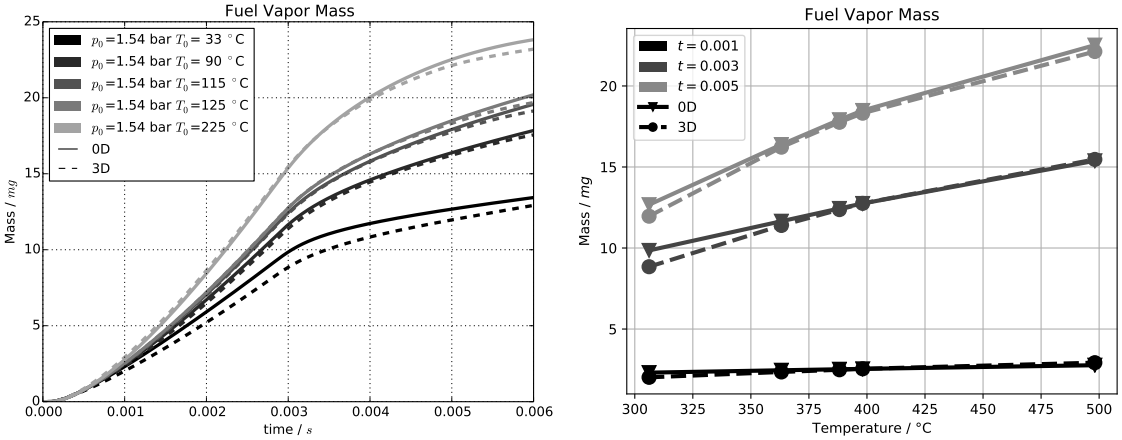

(a) Time evolution for different operating points (identified by shades of grey).

(b) Temperature sensitivity analysis at $t = 1\,\text{ms}$, $t = 3\,\text{ms}$ and $t = 5\,\text{ms}$ (identified by shades of grey).

Figure 5.16: Constant-volume vessel (MAGIE): reference point and **isobaric** variations (Table 5.1)) – **fuel vapor mass**. Left pane (a): time evolution for different operating conditions. Right pane (b): sensitivity to initial temperature T_0 for different times after SOI. Solid lines for 0D and dashed lines for 3D.

not reproduce the wall effect and overestimates the air entrainment leading to lower values of $\bar{Y}_F$. The temperature trend (b panes) is underestimated by the 0D model, particularly at $t = 1\,\mathrm{ms}$. Furthermore, the 0D model underestimates $\bar{Y}_F$ towards the end of the simulation, as it overestimates air entrainment.

Concerning the mixture fraction variance, $\sigma^2_{Y_F}$, the trends in the isobaric temperature variation (Fig. 5.20) are well represented. In the isopycnic variation (Fig. 5.19), on the other hand, the 0 model underestimates the temperature trend.

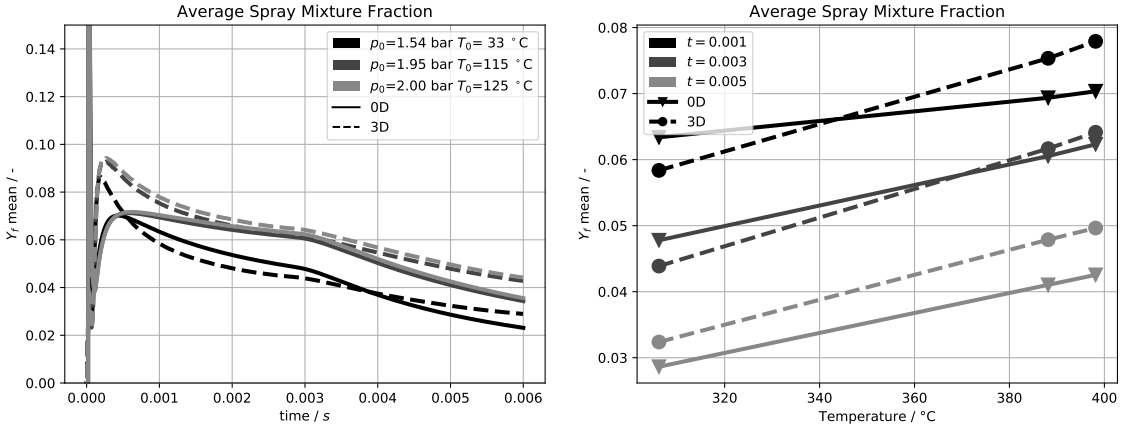

(a) Time evolution for different operating points (identified by shades of grey).

(b) Temperature sensitivity analysis at $t = 1\,\text{ms}$, $t = 3\,\text{ms}$ and $t = 5\,\text{ms}$ (identified by shades of grey).

Figure 5.17: Constant-volume vessel (MAGIE): reference point and **isopycnic** variations (Table 5.1)) – spray **average mixture fraction**. Left pane (a): time evolution for different operating conditions. Right pane (b): sensitivity to initial temperature T_0 for different times after SOI. Solid lines for 0D and dashed lines for 3D.

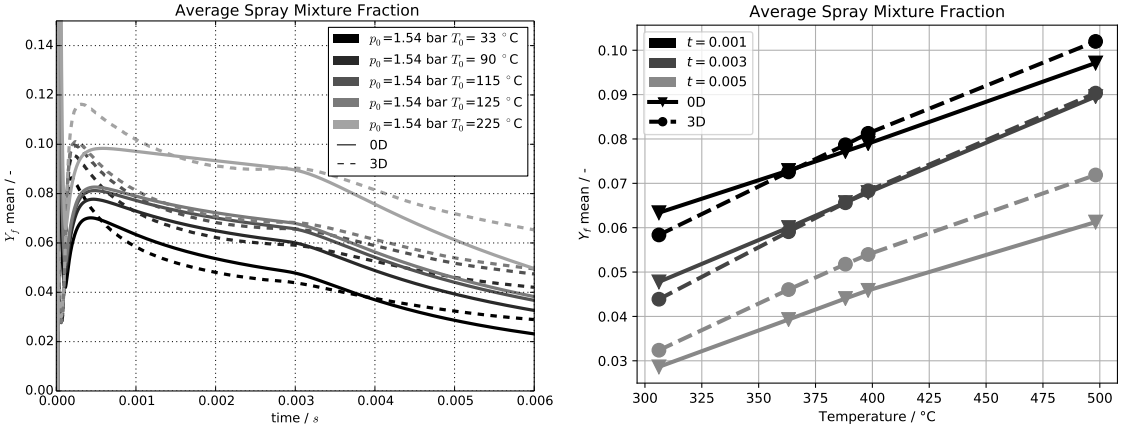

(a) Time evolution for different operating points (identified by shades of grey).

(b) Temperature sensitivity analysis at $t = 1\,\text{ms}$, $t = 3\,\text{ms}$ and $t = 5\,\text{ms}$ (identified by shades of grey).

Figure 5.18: Constant-volume vessel (MAGIE): reference point and **isobaric** variations (Table 5.1)) – spray **average mixture fraction**. Left pane (a): time evolution for different operating conditions. Right pane (b): sensitivity to initial temperature T_0 for different times after SOI. Solid lines for 0D and dashed lines for 3D.

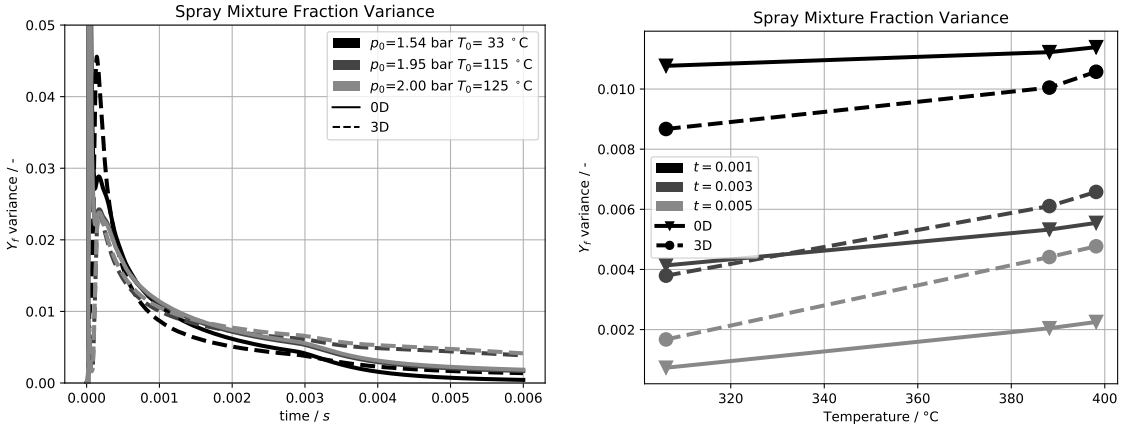

(a) Time evolution for different operating points (identified by shades of grey).

(b) Temperature sensitivity analysis at $t = 1\,\text{ms}$, $t = 3\,\text{ms}$ and $t = 5\,\text{ms}$ (identified by shades of grey).

Figure 5.19: Constant-volume vessel (MAGIE): reference point and **isopycnic** variations (Table 5.1)) – spray **mixture fraction variance**. Left pane (a): time evolution for different operating conditions. Right pane (b): sensitivity to initial temperature T_0 for different times after SOI. Solid lines for 0D and dashed lines for 3D.

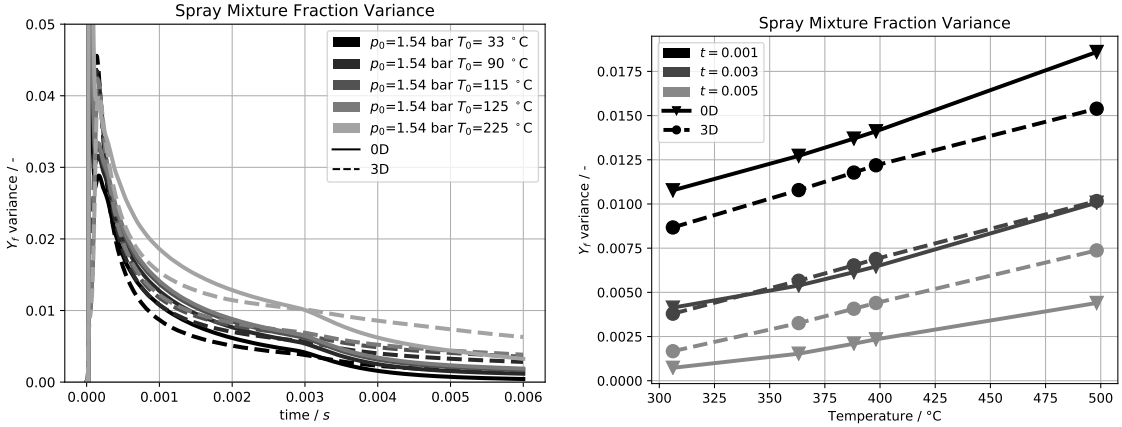

(a) Time evolution for different operating points (identified by shades of grey).

(b) Temperature sensitivity analysis at $t = 1\,\text{ms}$, $t = 3\,\text{ms}$ and $t = 5\,\text{ms}$ (identified by shades of grey).

Figure 5.20: Constant-volume vessel (MAGIE): reference point and **isobaric** variations (Table 5.1)) – spray **mixture fraction variance**. Left pane (a): time evolution for different operating conditions. Right pane (b): sensitivity to initial temperature T_0 for different times after SOI. Solid lines for 0D and dashed lines for 3D.

5.1.5 PDF convergence and computational cost

This section presents a convergence test of the PDF-based mixing model and an assessment of the computational cost of the spray model. The accuracy and resolution of the fuel mass fraction distribution and the computational cost both depend directly on the number of classes used, N_{PDF}, so that a compromise between computation time and accuracy has to be found.

The levels of probability defined by Eq. (4.103) depend linearly on the number of classes N_{PDF} used to discretize the Y_F domain. The probability density defined as:

$$p(j) = \frac{P(j)}{\Delta Y_F} = P(j)\, N_{\mathrm{PDF}} \tag{5.10}$$

is expected to be insensitive to variation of N_{PDF}, if the latter is sufficiently high to provide a good resolution.

A convergence test was run in the operating conditions corresponding to the high load reference point, Table 5.1.

Figure 5.21 shows a collection of $p(j)$ profiles obtained with N_{PDF} ranging from 50 to 400. The PDF domain is expressed in terms of equivalence ratio, and four plots, obtained at different times after the start of injection (SOI), compare the profiles corresponding to each value of the N_{PDF}. The profiles show a good convergence for $N_{\mathrm{PDF}} > 100$, proving a coherent formulation of the mixing model: in particular, two peaks appear for $\phi < 0.5$ in simulations with $N_{\mathrm{PDF}} = 200$ and $N_{\mathrm{PDF}} = 300$.

The normalization factor defined in Eq. (4.98), and used in Eq. (4.91) is obtained in order to satisfy the convergence criterion:

$$\lim_{N_{\mathrm{PDF}} \to \infty} \frac{d\, p(j)}{d\, N_{\mathrm{PDF}}} = 0 \tag{5.11}$$

While the resolution improves increasing N_{PDF}, the computational cost increases as well, so that a compromise must be found, depending on the application. It is found that the CPU time increases with $\approx (N_{\mathrm{PDF}})^{3.3}$, and the following expression:

$$t_{\mathrm{CPU}} = 1.15\ (N_{\mathrm{PDF}})^{3.3} \tag{5.12}$$

was retained as a trend line. Figure 5.22 shows CPU time, measured on the convergence test for different PDF discretizations (N_{PDF} ranging from 50 to 400) and compares them to the trend line in Eq. (5.12). The represented computation times correspond to the simulation of $t = 6\,\mathrm{ms}$.

The computation time rapidly increases with N_{PDF}. It was chosen here to run most of the validations with $N_{\mathrm{PDF}} = 100$ classes, which provide a good resolution at an acceptable computational cost (40 s/6 ms).

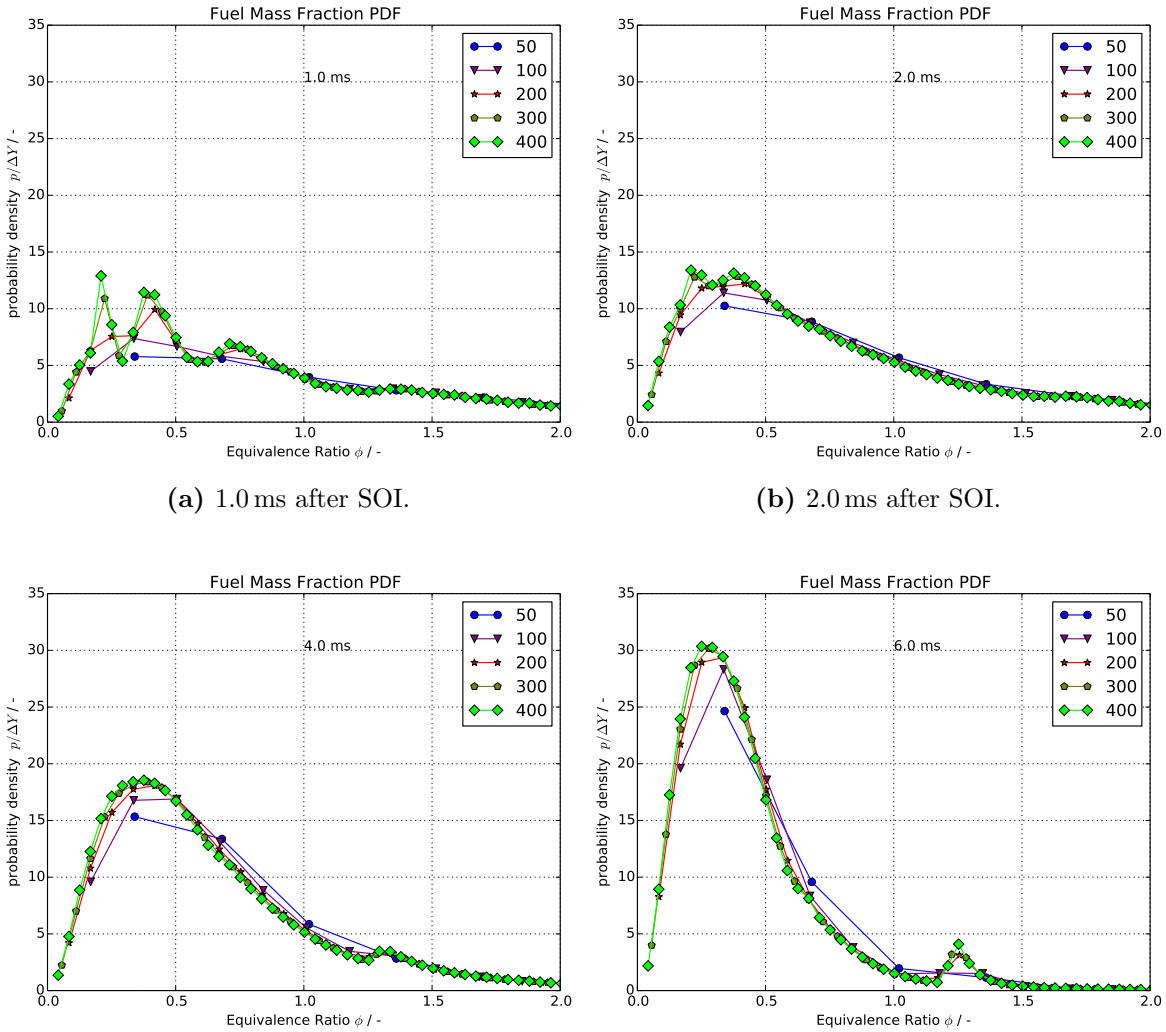

(a) 1.0 ms after SOI.

(b) 2.0 ms after SOI.

(c) 4.0 ms after SOI.

(d) 6.0 ms after SOI.

Figure 5.21: Mixture formation model convergence test: the probability density profiles obtained with N_{PDF} ranging from 50 to 400 in terms of equivalence ratio are compared at different times after the Start of Injection (SOI). The profiles converge for high N_{PDF}.

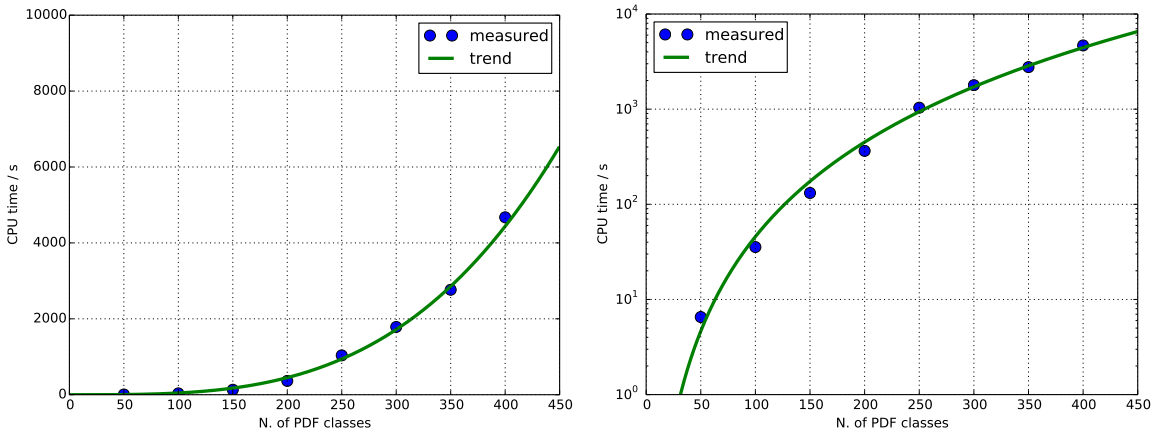

(a) Linear scale. **(b)** Logaritmic time scale.

Figure 5.22: Mixture formation model computational cost: the measured computational cost is shown as a function of N_{PDF} (blue dots) in both linear and semi-logaritmic scale. The trend line defined by Eq. (5.12) is also shown (green solid line).

5.2 Constant-volume vessel with tumble flow

Intake valves and ducts of spark-ignition engines are specially designed in order to produce a coherent vortex – called tumble – whose axis is perpendicular to that of the cylinder.

The tumble flow enhances combustion velocity by increasing the in-cylinder turbulence level, the advantages of a shorter combustion period being: an increased thermodynamic efficiency, the possibility of extending the flammability limit (lean burning) or of using slow burning fuel (Hill and Zhang, 1994).

The existence of a rotational velocity field in the gas phase influences the spray development, accelerating in particular:

air entrainment, as a consequence of the transverse air flow that introduces additional air in the reactive charge zone;

fuel evaporation, since the additional air flow increases the relative velocity between the gas and liquid phases and the fuel mass fraction;

small-scale mixing, because of turbulence generated by tumble.

This section presents a validation case designed to test the response of the spray model to these interaction phenomena. 3D RANS numerical simulations are used as a reference to calibrate the 0D model and evaluate its predictivity. No experimental data is available for this case.

5.2.1 3D numerical simulations

The chosen geometry is the cubical constant-volume vessel described in Section 5.1.1 (volume $1.4 \times 10^{-3}\,\mathrm{m}^3$) equipped with a single hole injector (nozzle diameter 0.2 mm). It is a simplification of the MAGIE cell, with the three-hole injector replaced with a single hole of the same diameter.

The change in geometry allows to isolate the effects of the spray/tumble interaction, eliminating the interference between the different spray jets.

The gas field is initialized with a y-wise rigid vortex, centered in the domain, as shown in Fig. 5.23, and with different initial angular velocities, ω_0. The turbulent kinetic energy is initialized with a uniform field and the values, summarized in Table 5.3, are chosen close to the equilibrium values for a constant-speed vortex, in order to minimize turbulence intensity variations during the simulation. This allows to correlate the small-scale effects with the turbulence intensity.

Accordingly, the simulated points are described by the following initial tumble velocities, ω_0:

$$\omega_0 = 100, 200, \ldots, 600\,\mathrm{rad/s} \tag{5.13}$$

which correspond roughly to engine speeds ranging from 1000 rpm to 6000 rpm, and the following thermodynamic conditions:

- $p_0 = 1.54\,\mathrm{bar}$;

Table 5.3: Single-hole injection with y-wise (tumble) vortex: summary of the initial conditions.

k_0 ($\mathrm{m}^2/\mathrm{s}^2$)	2.5	3.5	4.5	7.5	11.0	16.0	21.0
ω_0 (rad/s)	0	100	200	300	400	500	600

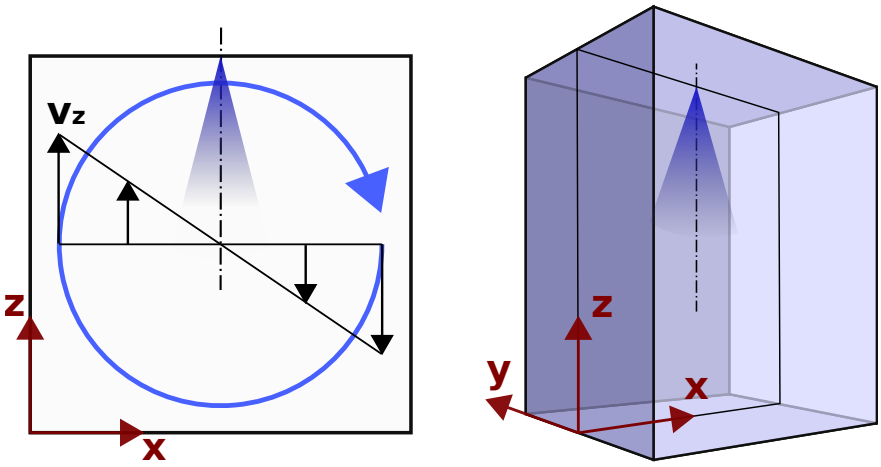

(a) Schematic representation of the geometry.

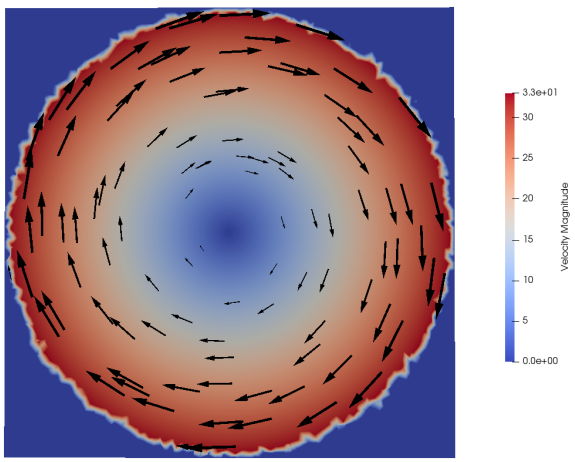

(b) $\omega_0 = 600\,\mathrm{rad/s}$ case: initial velocity field in the x–z plane.

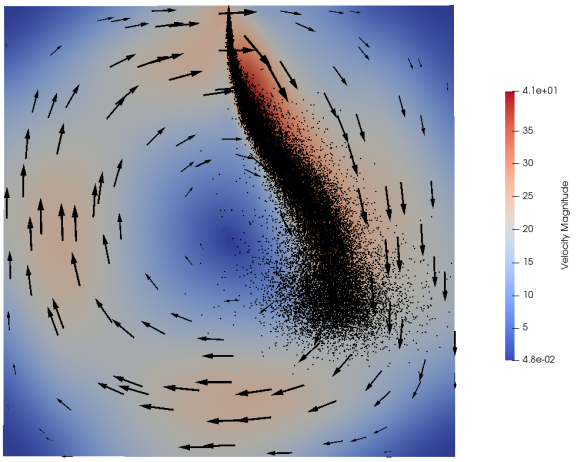

(c) $\omega_0 = 600\,\mathrm{rad/s}$ case: velocity field and disperse phase at 3.2 ms after SOI, in the x–z plane.

Figure 5.23: Three-dimensional case for the investigation of the influence of tumble on spray dynamics. The cubic box size is 112 mm, the nozzle is located at the center of the top face and injection axis is parallel to z. The initial y-wise vortex is 112 mm wide and centered in the domain.

- $T_0 = 115\,°\mathrm{C}$;

corresponding to operating point iso-p #2 in the MAGIE experiment (Table. 5.1). A single injection of 3.32 ms duration is performed at $t = 0$, thus introducing 8.3 mg of iso-octane in the chamber, corresponding to a mean equivalence ratio of about 0.07[3].

5.2.2 0D numerical simulations and validation

This section presents the modelling hypotheses adopted for the 0D simulation and compares the obtained results to the reference data (3D RANS).

0D model calibration and setup

Table 5.4 shows the values of the calibration parameters used to tune the 0D model for this validation case. Their values are held constant through the different cases for a given geometry.

Table 5.4: Single-hole injection with y-wise (tumble) vortex: calibration of the 0D model.

Evaporation				Spray			Mixing			
$\mathcal{K}_{\mathrm{ato}}$	N_P	$\mathcal{K}_v$	$\mathcal{K}_{t\,\mathrm{ev}}$	$\mathcal{K}_p$	$\mathcal{K}_a$	$\mathcal{K}_{t\,\mathrm{en}}$	N_{CL}	$\mathcal{K}_\alpha^{\mathrm{pdf}}$	$\mathcal{K}_\beta^{\mathrm{pdf}}$	$\mathcal{K}_{\mathcal{P}}^{\mathrm{pdf}}$
2.40	20	1.00	2.00	1.50	1.60	1/550	61	0.7	40	$5.0\,10^3$

Tumble entrainment Factor. Equations (4.72) and (4.74), recalled here to ease the reader, define the tumble entrainment factor as the ratio of the entrained mass with a given tumble intensity ω_y to that in a quiescent environment:

$$\alpha_{t\,\mathrm{en}} = \frac{\mathcal{M}_{\mathrm{sp}}^{\mathrm{air}}(\omega, t)}{\mathcal{M}_{\mathrm{sp}}^{\mathrm{air}}(0, t)} - 1 \tag{5.14}$$

and the linear model used to describe it:

$$\alpha_{t\,\mathrm{en}} = \mathcal{K}_{t\,\mathrm{en}}\omega_y \tag{5.15}$$

with $\mathcal{K}_{t\,\mathrm{en}}$ a calibration parameter.

Figure 5.24 shows the correlation between the tumble entrainment factor, $\alpha_{t\,\mathrm{en}}$, and the tumble velocity, ω_y. In particular, the top panes plot $\alpha_{t\,\mathrm{en}}$ and ω_y against time, for the different cases. The two quantities are averaged over the time interval $t \in [0.002; 0.004]$, where both have stable values, leading to a point in the $(\omega_y, \alpha_{t\,\mathrm{en}})$ space for each validation case. The bottom pane compares the linear model in Eq. (5.14) to the reference points obtained from 3D results: the approach adopted is sufficient to capture the trend and give satisfying results over the observed ω_t range, taken as representative of real engine conditions.

[3]The injections are performed in a relatively large combustion vessel, designed to investigate the free spray evolution. This lead to a very low value of the mean equivalence ratio.

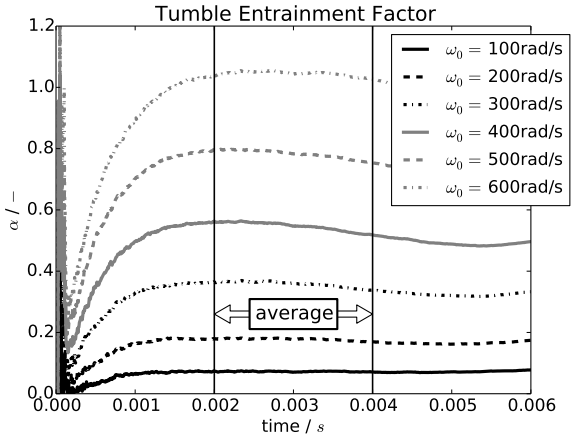

(a) Entrainment factor.

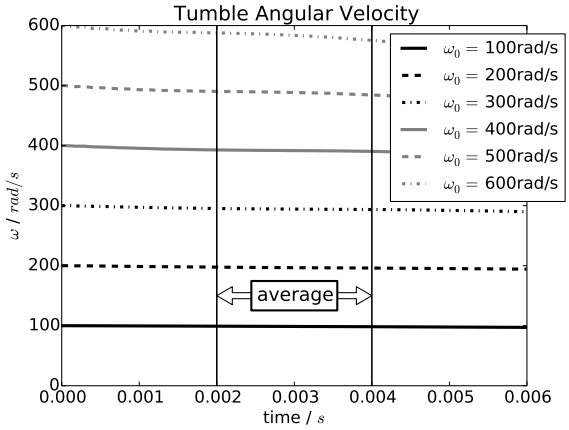

(b) Angular velocity.

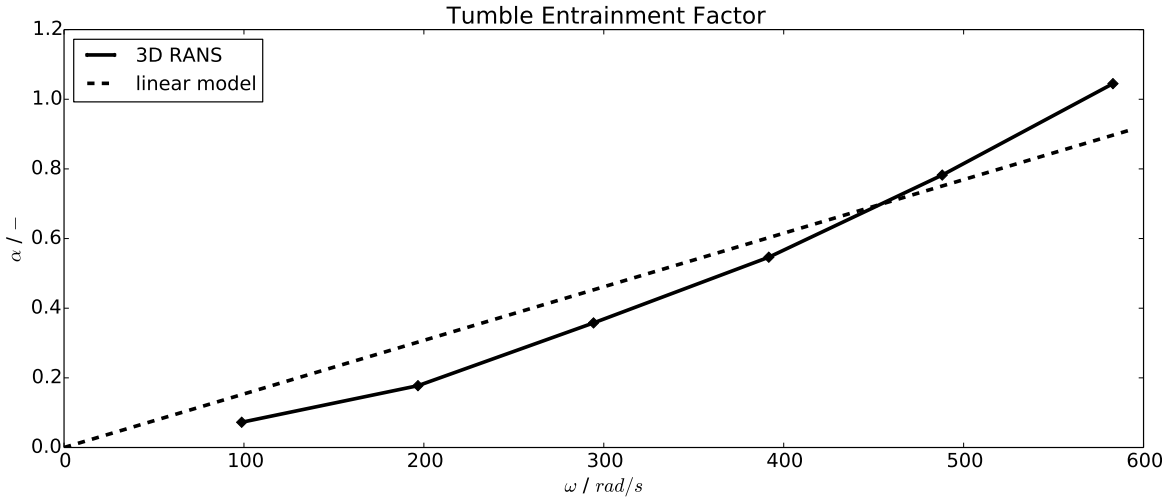

(c) Tumble entrainment factor against average angular velocity.

Figure 5.24: Influence of tumble flow on air entrainment in 3D RANS simulations. Top panels plot the time evolution of the tumble entrainment factor defined by Eq. (5.14) (left) and the average tumble angular velocity (right). Bottom panel shows the correlation of the average of these two quantities over the time interval indicated in the top panels.

Results

Penetration and spreading rate. Simulation results are shown in Fig. 5.25. since the thermodynamic conditions, p_0 and T_0, are the same in all cases, all the penetration and spreading angle curves coincide in 0D model.

Nevertheless, some differences appear in the 3D RANS results. Penetrations vary slightly because of two combined effects: on the one hand tumble increases the spray diffusion reducing penetration, on the other it deviates the spray moving its tip away from the injector axis. The spreading rate present a more pronounced case-by-case variation due to its definition in 3D based on Eq. (5.4), that provides an estimation based on the actual volume and penetration. With this definition, the spreading rate obtained with 3D RANS simulation includes the effect of tumble that is modelled separately in 0D, via Eq. (5.14).

Spray mass. The vortex intensity is, on the other hand, taken into account in the computation of the spray mass, shown in Fig. 5.26:

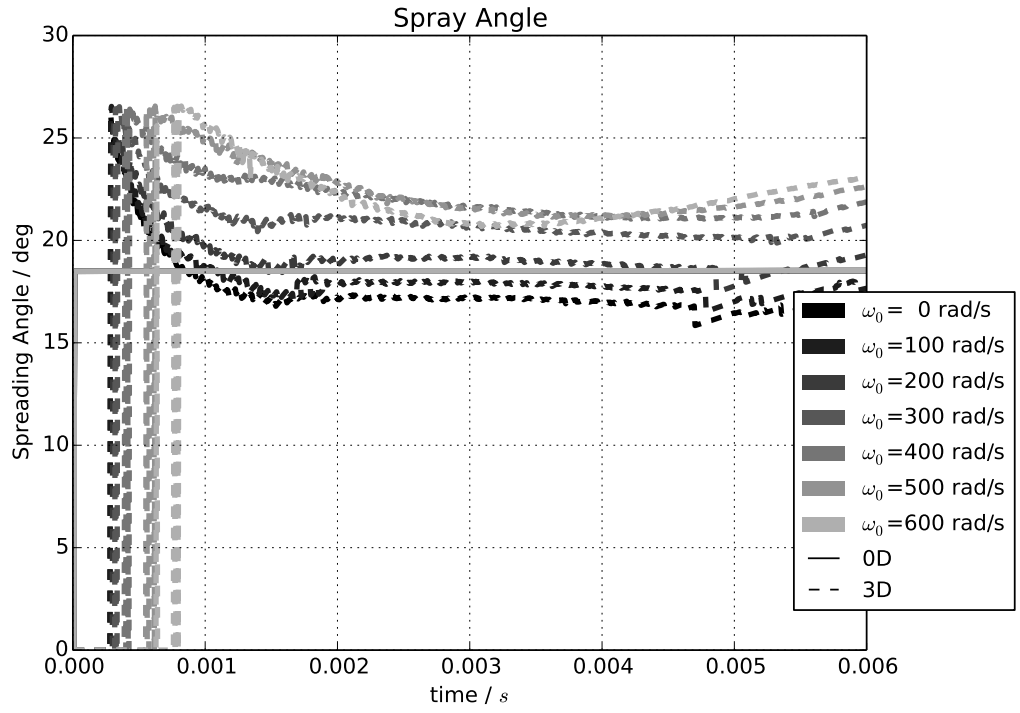

(a) Spreading angle.

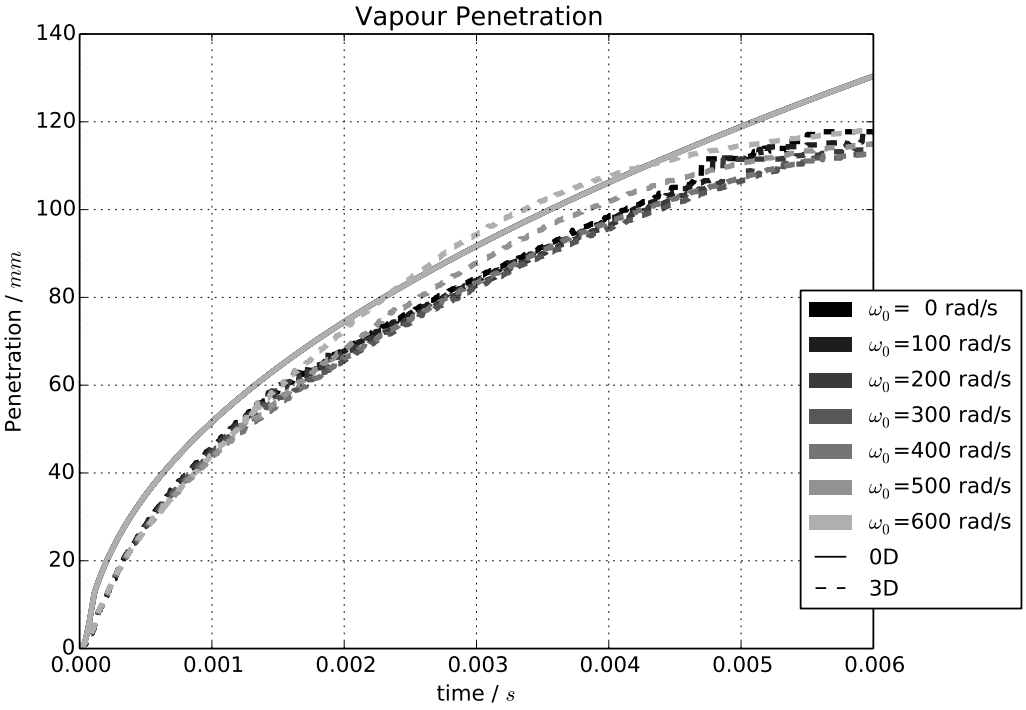

(b) Gas penetration.

Figure 5.25: Constant-volume vessel with tumble flow – evolution of the reactive charge zone: the different shades of grey identifiy the initial tumble velocity, ω_0. Solid lines: 0D. Dashed lines: 3D (reference). (a): spreading angle. (b): gas penetration.

- panel (a) plots the spray mass against time, for different values of the inital tumble velocity ω_0;
- panel (b) plots it against the initial tumble velocity, ω_0, at different times after SOI ($t = 1\,\text{ms}$, $t = 3\,\text{ms}$ and $t = 5\,\text{ms}$).

The 0D model evaluates the entrained air mass based on the spray spreading rate and penetration, Eq. (4.70). Without the correction introduced with Eq.s (4.74 – 4.75), the spray mass would be insensitive to ω_0, the solid lines (representing the 0D model) in Fig. 5.26 (a) would be superimposed and no trend would appear in Fig. 5.26 (b).

The linear correction adopted in the 0D model – defined in Eq.s (4.74 – 4.75) – allows to represent the trend found in 3D RANS data, compensating the deviations observed on spreading rate and penetration (Fig. 5.25). Nevertheless, a difference in curvature appears in Fig. 5.26 (b): the entrained air mass at 5 ms is overestimated for $\omega_0 \in [100; 500]$ showing the limitation of such linear approximation.

Evaporation Results concerning the evolution of liquid and vapor fuel masses are shown in Fig. 5.27 and Fig. 5.28, respectively.

The time evolution of liquid (Fig. 5.27:(a)) and vapor fuel (Fig. 5.28:(a)) masses is well represented. Increasing ω_0 enhances evaporation. This leads to increased fuel vapor masses and reduced liquid fuel masses: this phenomenon is well represented by the 0D, as a result of taking the transverse gas velocity – as defined in Eq.s (4.56 – 4.57) – into account in the evaporation model: without this modification all the curves in panels (a) would collapse into one, as the thermodynamic conditions are the same in all cases shown.

The (b) panels in Fig.s 5.27 – 5.28 show the liquid and vapor fuel masses respectively, at three times after SOI. Positive trends are visible at 3 ms and 5 ms, in both 0D and 3D results. The different curvatures show that the 0D model overestimates evaporation for $\omega_0 \in [100; 500]$, i.e. when the air entrainment is also overestimated.

Mixing. Large scale mixing, as a results of air entrainment and fuel evaporation within the reactive charge zone, leads to the quantification of the average fuel mass fraction, $\bar{Y_F}$, shown in Fig. 5.29. The level of accuracy is a consequence of the good agreement of air entrainment and fuel evaporation with the reference data (3D RANS results). Increasing ω_0 accelerates fuel evaporation and enhances air entrainment: the latter effect prevails leading to lower values of $\bar{Y_F}$ at higher ω_0.

Small scale mixing is synthesized by the fuel mass fraction variance, $\sigma^2_{Y_F}$, shown in Fig. 5.30. The trends are negative with ω_0, since tumble enhances fuel/air mixing.

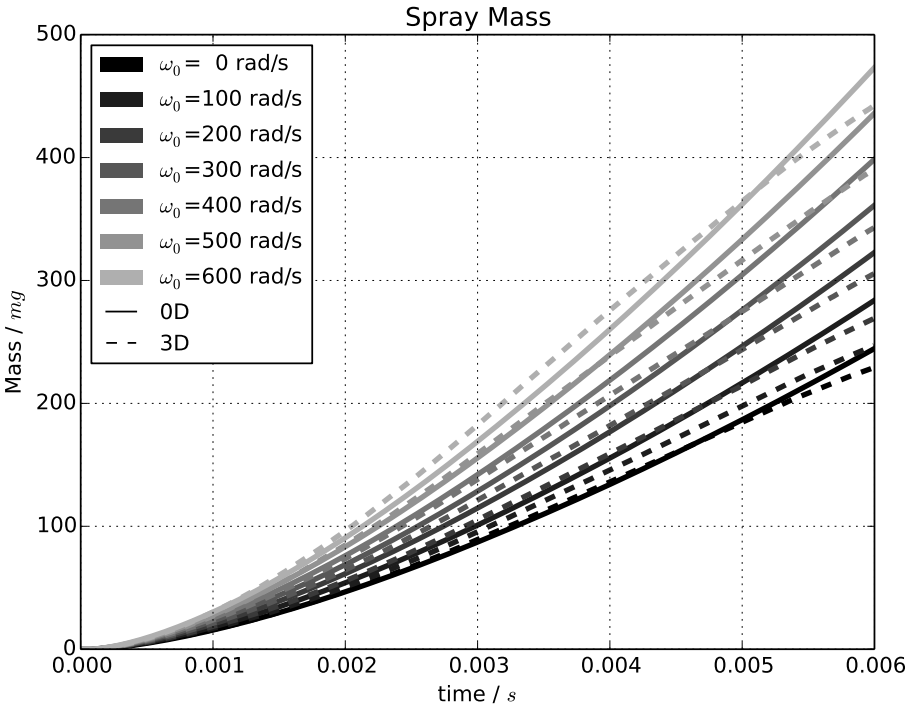

(a) Spray mass against time: the different shades of grey identifiy the initial tumble velocity, ω_0. Solid lines: 0D. Dashed lines: 3D (reference).

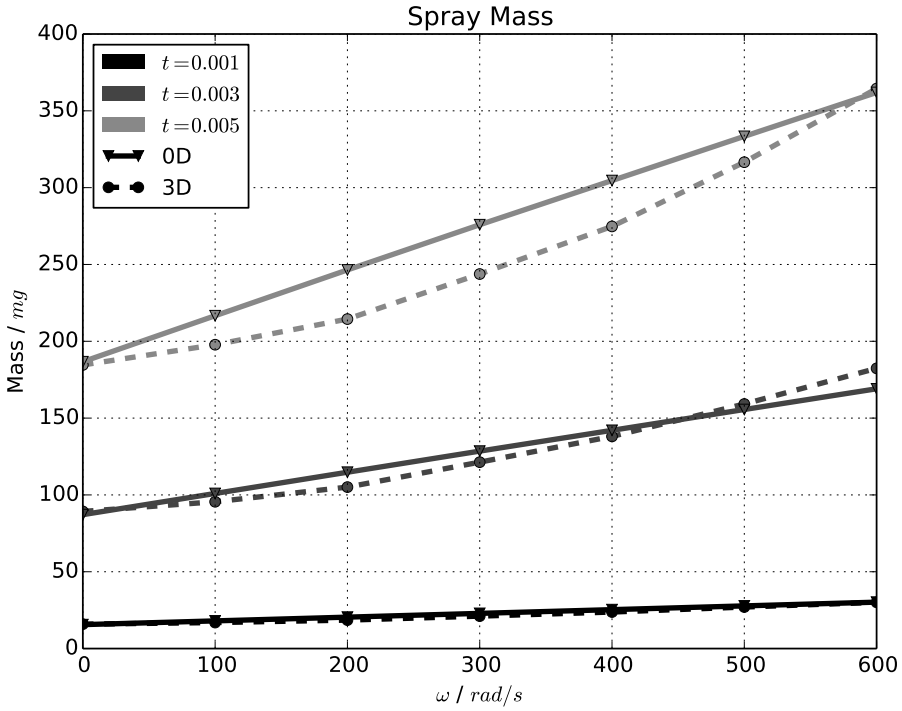

(b) Spray mass against initial tumble velocity: the different shades of grey identify the timestamps. Solid lines: 0D. Dashed lines: 3D (reference).

Figure 5.26: Constant-volume vessel with tumble flow – evolution of the reactive charge zone. (a): spray mass against time for different tumble intensities, ω_0. (b): spray mass against the tumble intensity, ω_0, at different times after SOI.

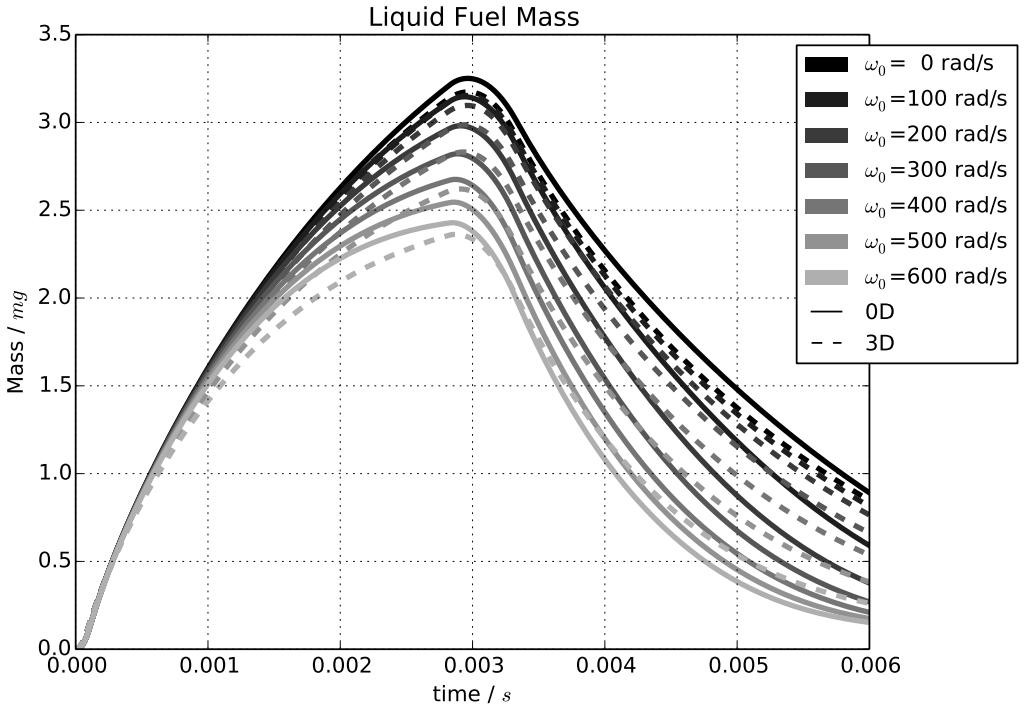

(a) Liquid fuel mass against time: the different shades of grey identifiy the initial tumble velocity, ω_0. Solid lines: 0D. Dashed lines: 3D (reference).

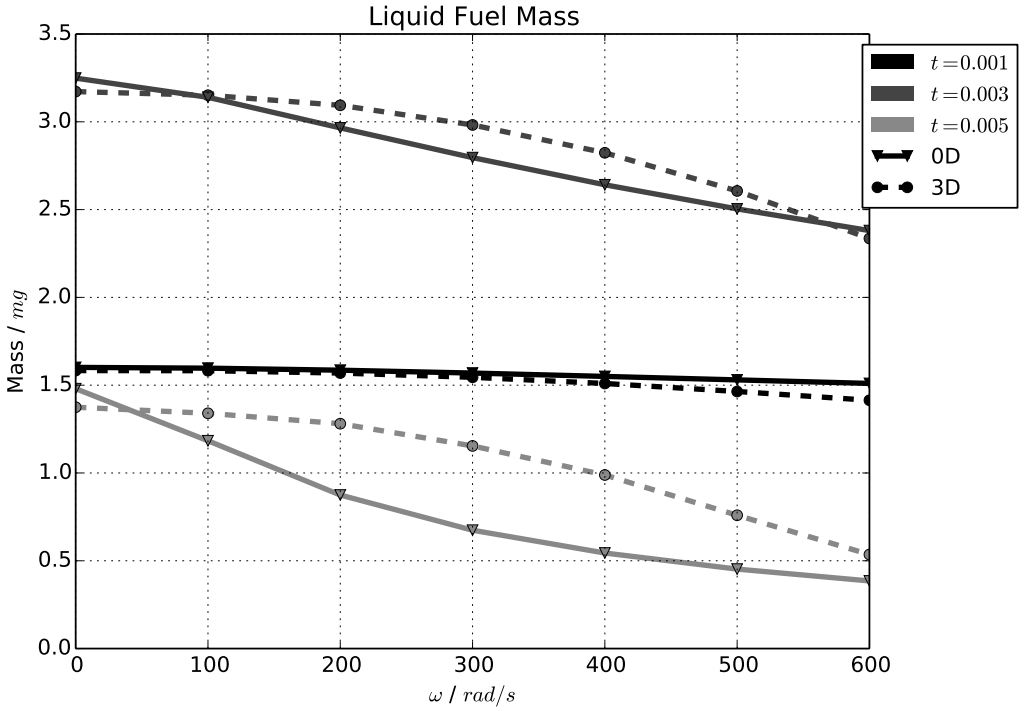

(b) Liquid fuel mass against initial tumble velocity: the different shades of grey identify the timestamps. Solid lines: 0D. Dashed lines: 3D (reference).

Figure 5.27: Constant-volume vessel with tumble flow – fuel evaporation. (a): liquid fuel mass against time for different tumble ω_0 intensities. (b): liquid fuel mass against the tumble intensity, ω_0, at different times after SOI.

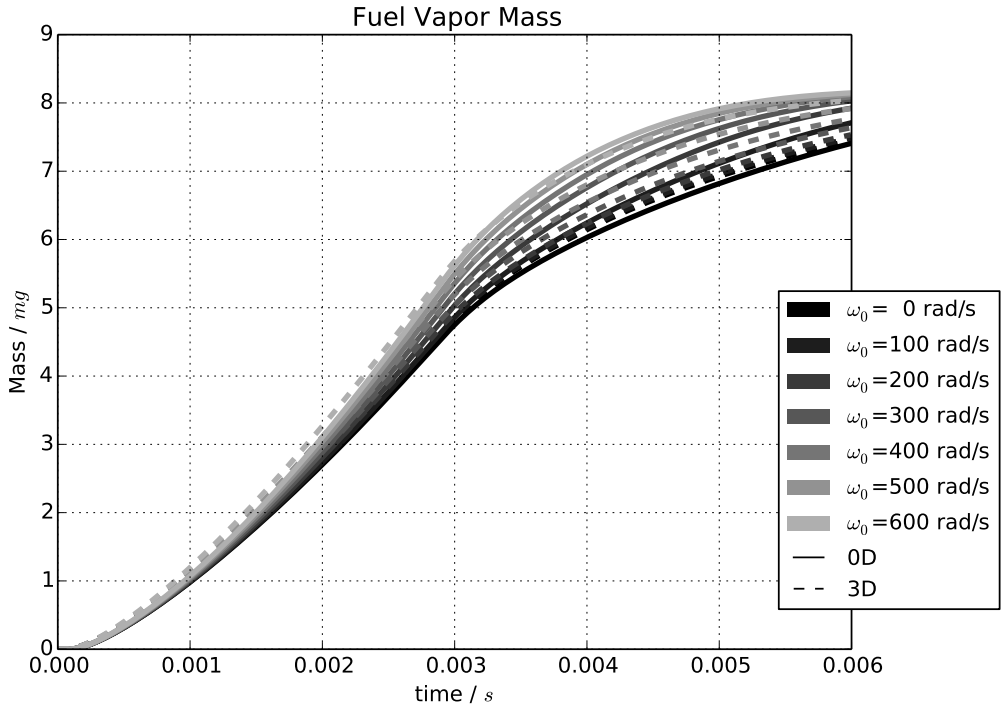

(a) Fuel vapor mass against time: the different shades of grey identifiy the initial tumble velocity, ω_0. Solid lines: 0D. Dashed lines: 3D (reference).

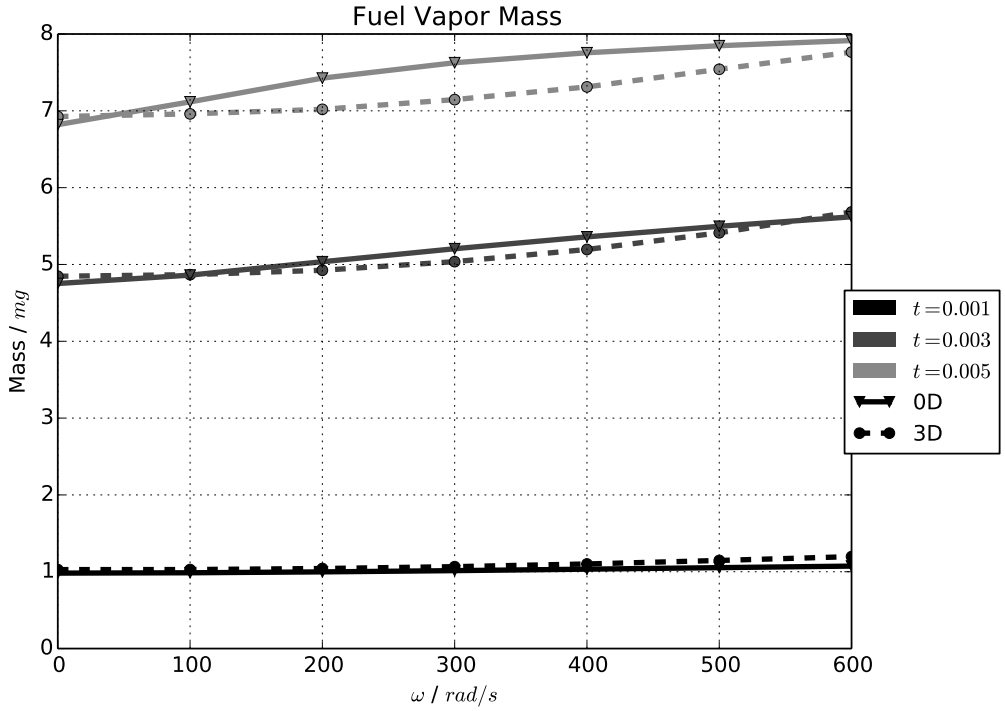

(b) Liquid fuel mass against initial tumble velocity: the different shades of grey identify the timestamps. Solid lines: 0D. Dashed lines: 3D (reference).

Figure 5.28: Constant-volume vessel with tumble flow – fuel evaporation. (a): fuel vapor mass against time for different tumble intensities, ω_0. (b): fuel vapor mass against the tumble intensity, ω_0, at different times after SOI.

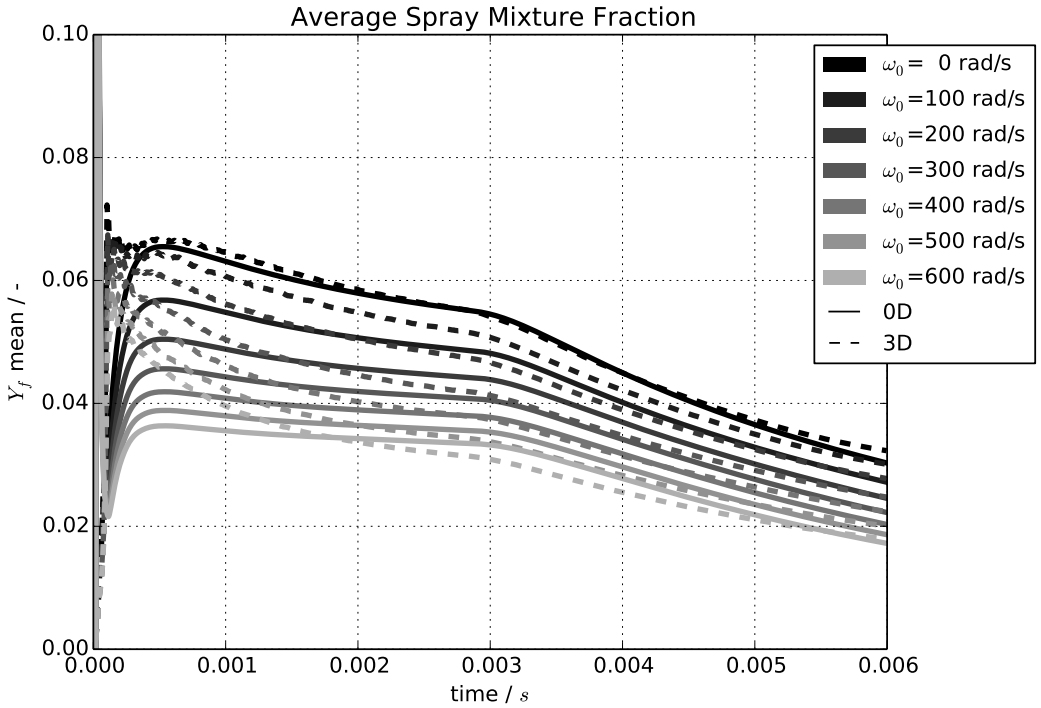

(a) Average fuel mass fraction against time: the different shades of grey identifiy the initial tumble velocity, ω_0. Solid lines: 0D. Dashed lines: 3D (reference).

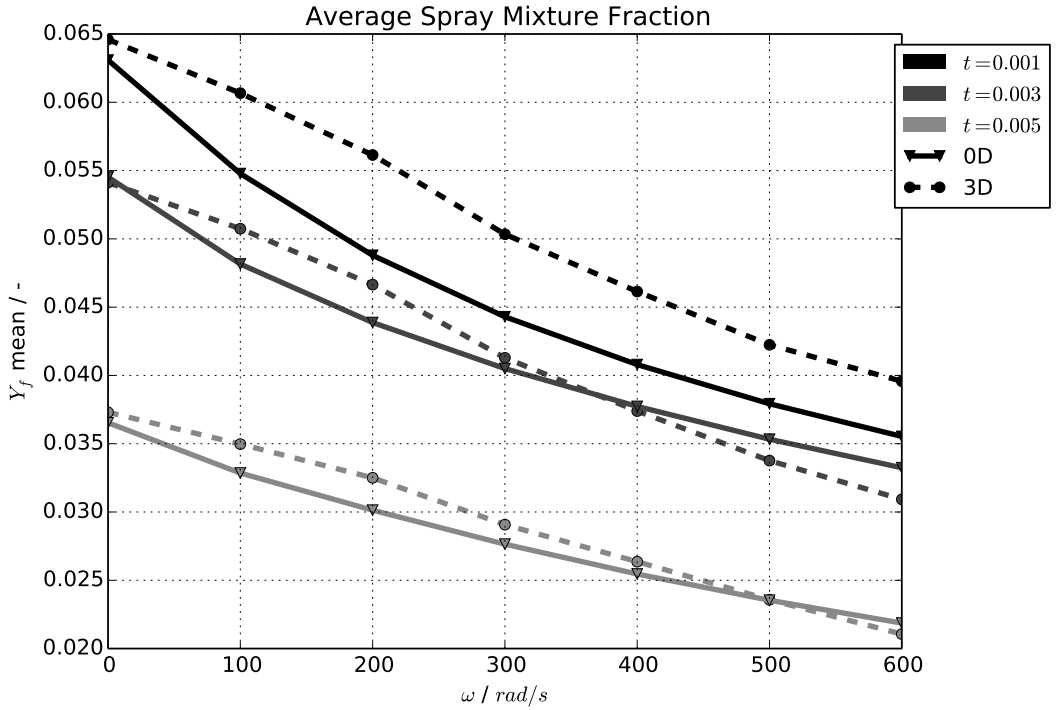

(b) Average fuel mass fraction against initial tumble velocity: the different shades of grey identify the timestamps. Solid lines: 0D. Dashed lines: 3D (reference).

Figure 5.29: Constant-volume vessel with tumble flow – fuel mass fraction (Y_F). (a): average fuel mass fraction, $\bar{Y_F}$, on the reactive charge zone against time for different tumble intensities, ω_0. (b): average fuel mass fraction, $\bar{Y_F}$, against the tumble intensity, ω_0, at different times after SOI.

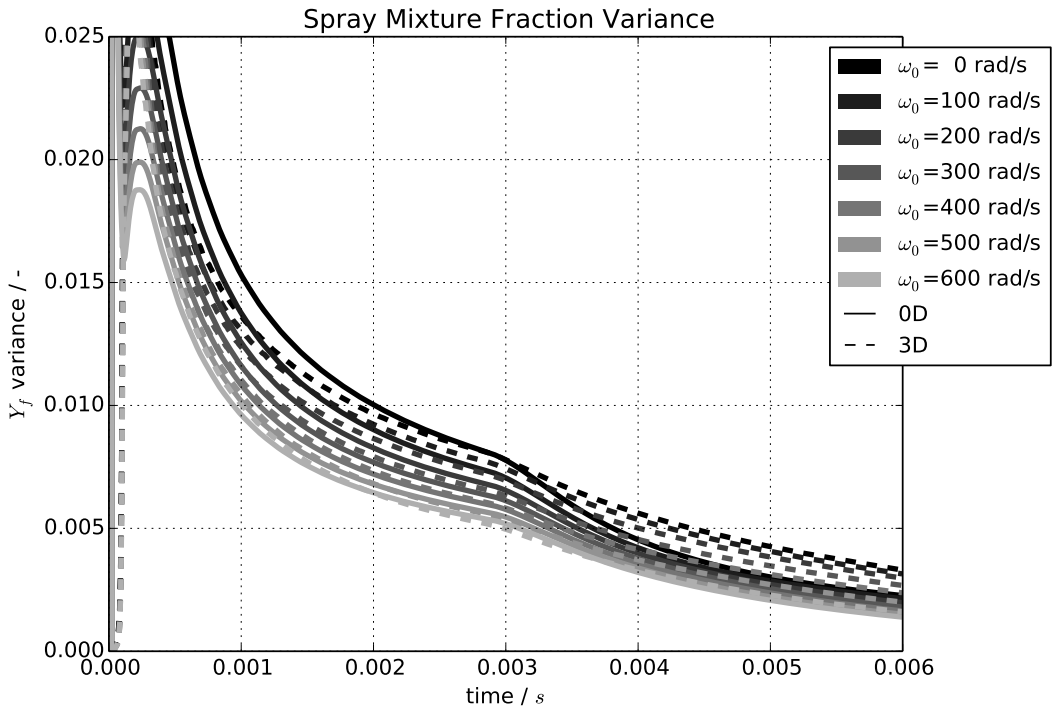

(a) Fuel mass fraction variance against time: the different shades of grey identifiy the initial tumble velocity, ω_0. Solid lines: 0D. Dashed lines: 3D (reference).

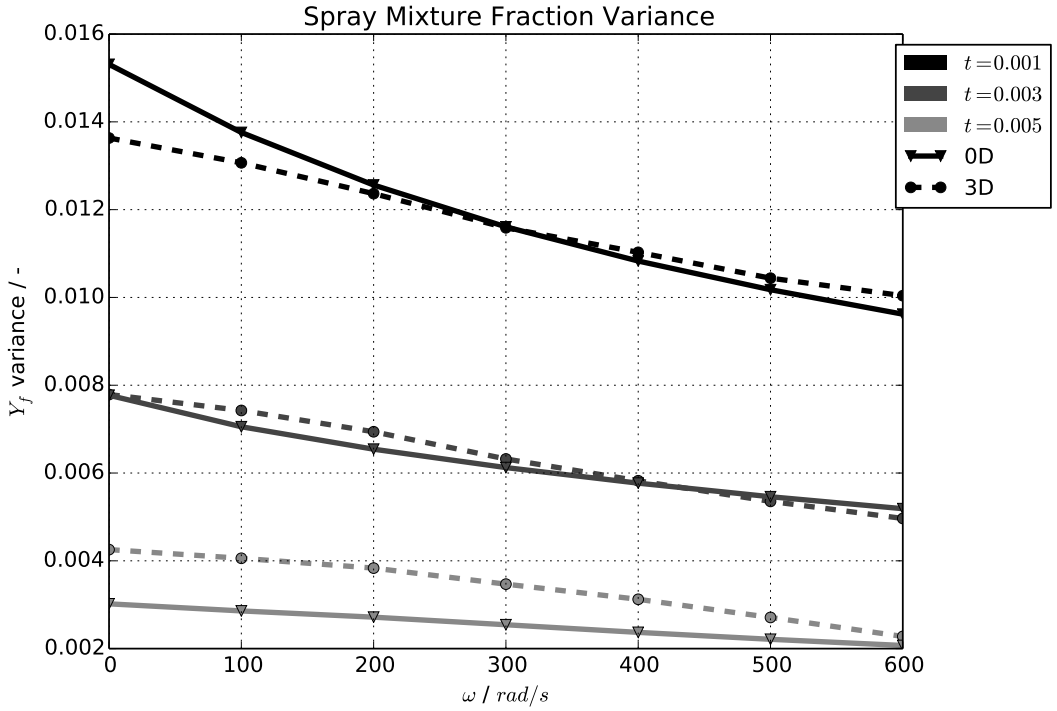

(b) Fuel mass fraction variance against initial tumble velocity, ω_0: the different shades of grey identify the timestamps. Solid lines: 0D. Dashed lines: 3D (reference).

Figure 5.30: Constant-volume vessel with tumble flow – fuel mass fraction (Y_F) distribution. (a): fuel mass fraction variance, $\sigma^2_{Y_F}$, on the reactive charge zone against time for different tumble intensities, ω_0. (b): fuel mass fraction variance, $\sigma^2_{Y_F}$, against the tumble intensity, ω_0, at different times after SOI.

5.3 Variable-volume vessel

Both the validation cases discussed so far involve fuel injections in constant-volume vessels, with constant thermodynamic conditions. In real engine operation, however, significant variations of density, pressure and temperature may occur throughout spray evolution and mixture formation, especially when injection takes place during the compression stroke.

The test case presented in this section is dedicated to the investigation of spray dynamics in such variable thermodynamic conditions. For this purpose, the geometry described in Fig. 5.31 was adopted. It consists of a closed cylinder filled with air at rest, with a single-nozzle injector whose axis corresponds to that of the cylinder.

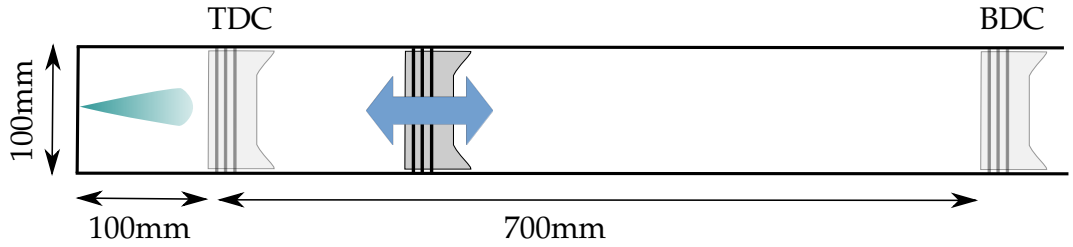

Figure 5.31: Single hole injection in a variable-volume vessel: geometry. The vessel consists of a closed cylinder where fuel (C_8H_{18}) is injected along the piston axis.

In order to have density variations of the order of those encountered in DI-SI engines on the one hand, and to avoid spurious influences on the results due to the presence of walls, the following choices were made in the setup:

- a realistic compression ratio (value set at 8), to sweep the same pressure range as in an engine;
- a realistic crank speed (value set at 3000 rpm), to have a comparable compression duration;
- no interaction between the spray and the piston wall (squared cylinder at TDC).

The latter constraint leads, on the other hand, to very high values of the piston velocity (70 m/s) and stroke (70 cm), that can hardly be found in automotive ICEs. Moreover, a constant piston velocity profile was adopted, so that piston position (and chamber volume) are linear in time (and crank angle).

The velocity field induced by the piston motion on the gas phase, because of its elevated values, has a considerable impact on spray development. Such an impact is accounted for by the model through Eq. (4.58): this correction proved necessary in order to get consistent results in terms of evaporation rate and liquid penetration. The intensity of this velocity field produces non-negligible effects on both those quantities, because it modifies the reactive velocity between the two phases, introducing additional drag and enhancing the evaporation rate.

Four cases were studied with this geometry, all consisting of an iso-octane injection at the beginning of a compression or expansion stroke. The initial conditions of the four simulations are summarized in Table 5.5, and are taken to be representative of a turbocharged engine at high and low load.

Temperature values corresponding to high pressure are the result of an adiabatic compression from ambient conditions. Moreover, the initial conditions of the two expansion cases are chosen to approximately match the final conditions of the compression cases, in order

Table 5.5: Single-hole injection in a variable-volume vessel: summary of the operating conditions. The indexes 0 and 1 refer to the start and end of stroke respectively. Injection starts 10 °CA after stroke start.

		V_0	V_1	p_0	p_1	T_0	T_1
compression	#1	$1570\,\text{cm}^3$	$196\,\text{cm}^3$	0.8 bar	≈ 15.0 bar	300 K	≈ 690 K
	#2			1.6 bar	≈ 30.0 bar	350 K	≈ 800 K
expansion	#1	$196\,\text{cm}^3$	$1570\,\text{cm}^3$	15.0 bar	≈ 0.8 bar	690 K	≈ 300 K
	#2			30.0 bar	≈ 1.6 bar	800 K	≈ 350 K

to investigate spray behaviour in the same pressure and temperature range and isolate the effects of density variation.

5.3.1 3D numerical simulations

Reference data to validate the 0D model is obtained through 3D RANS simulations performed with the FP-C3D (Velghe et al., 2011) code.

Since the piston velociy is constant in this case, a gas velocity field, parallel to the cylinder axis, was imposed as initial condition to provide a smooth connection between the fixed (cylinder head) and moving (piston surface) boundaries and avoid wave effects. The value of the initial velocity, $u(z)$, varies along the piston axis as:

$$u(z) = u_p \frac{z}{z_p} \tag{5.16}$$

with z a coordinate along the cylinder axis that has its origin on the cylinder head, z_p its value on the piston surface, and u_p the piston velocity.

The computational domain consists of a moving mesh that stretches according to piston motion and is remapped four times per stroke to maintain an optimal cell aspect ratio. The mesh size of the compression cases ranges between:

- 230 910 nodes at BDC (−180 °CA);
- 151 072 nodes at TDC (0 °CA);

while that of the expansion cases ranges between:

- 156 583 nodes at TDC (−180 °CA);
- 248 883 nodes at BDC (0 °CA).

Post processing

The post processing used to extract 0D information such as spray penetration and spreading rate, fuel masses and mixing is the same as described in Section 5.1.3.

5.3.2 0D numerical simulations and validation

0D model calibration

Table 5.6 summarizes the calibration parameter set used to run the 0D model on this validation case. The values are the same as in the constant-volume vessel with tumble flow

validation case discussed in Section 5.2, since the same single-nozzle injector is adopted in the two cases. Though small adjustments could be introduced to optimize the results on each validation case, priority was given to the aim of preserving the same model calibration in similar geometries.

Table 5.6: Single-hole injection in a variable-volume vessel: calibration of the 0D model.

Evaporation				Spray			Mixing			
$\mathcal{K}_{\text{ato}}$	N_P	$\mathcal{K}_v$	$\mathcal{K}_{t\,\text{ev}}$	$\mathcal{K}_p$	$\mathcal{K}_a$	$\mathcal{K}_{t\,\text{en}}$	N_{CL}	$\mathcal{K}_\alpha^{\text{pdf}}$	$\mathcal{K}_\beta^{\text{pdf}}$	$\mathcal{K}_{\mathcal{P}}^{\text{pdf}}$
2.40	20	1.00	2.00	1.50	1.60	1/550	61	0.7	40	$5.0\,10^3$

Results

The results obtained with the 0D model are presented in the following and compared to 3D RANS (reference) data. All the relevant quantities are plotted against the crank angle (°CA).

Vapor penetration and spreading angle. The vapor penetration is displayed in Fig. 5.32: the (a) plot shows the compression cases, while the (b) plot shows the expansion cases. Likewise, the spreading angle is displayed in Fig. 5.33: the(a) plot shows the compression cases while the (b) plot shows the expansion cases. Both figures show that the model proposed by Naber and Siebers (1996) for the spray penetration and spreading angle adopted here leads to good results in variable-volume conditions, requiring no correction. Shorter penetrations and larger spray angles are obtained at higher pressures, with both 0D and 3D in the expansion case as well as in the compression: it is a consequence of the higher density that increases the drag force on the fuel drops and the shear between the jet and the surrounding air.

The decreasing penetration visible in 3D at the end of the compression stroke, Fig. 5.32:(a), is due to the effect of the gas velocity field induced by the piston, that becomes more important as the latter approaches the cylinder head. An similar behavior is shown by the 0D model, despite the fact that the expressions for the spray penetration and spreading angle – in Eq.s (4.67) and (4.69), respectively – give an instantaneous value of the two quantities, based only on the thermodynamic conditions of the injected fuel and the surrounding air. Moreover, the values of the spray penetration and spreading angle given by the Naber and Siebers (1996) model at a certain time t, are based on the assumption that the thermodynamic conditions at t were constant since the beginning of the injection. In other words, this model does not take into account the *history* of the spray.

These approximations explain the overestimation during compression, Fig. 5.32:(a), and underestimation during expansion, Fig. 5.32:(b), of the spray penetrations.

Spray volume and mass. The volume of the reactive charge zone and the total (fuel vapor and air) mass it contains are shown in Fig.s 5.34 – 5.35.

It is interesting to point out the differences in time evolution between the reactive charge volume (Fig. 5.34) and the reactive charge mass (Fig. 5.35) during compression (a) and expansion (b). While the reactive charge mass is monotonous in all cases, since large scale mixing is an irreversible process, the volume has a peak in the second half of the compression stroke and decreases when the effect of compression is greater than that of mixing.

Since sprays tend to penetrate more at low density, the reactive charge volumes, Fig. 5.34, decrase when p_0 is increased. The opposite is observed with reactive charge masses, Fig. 5.35,

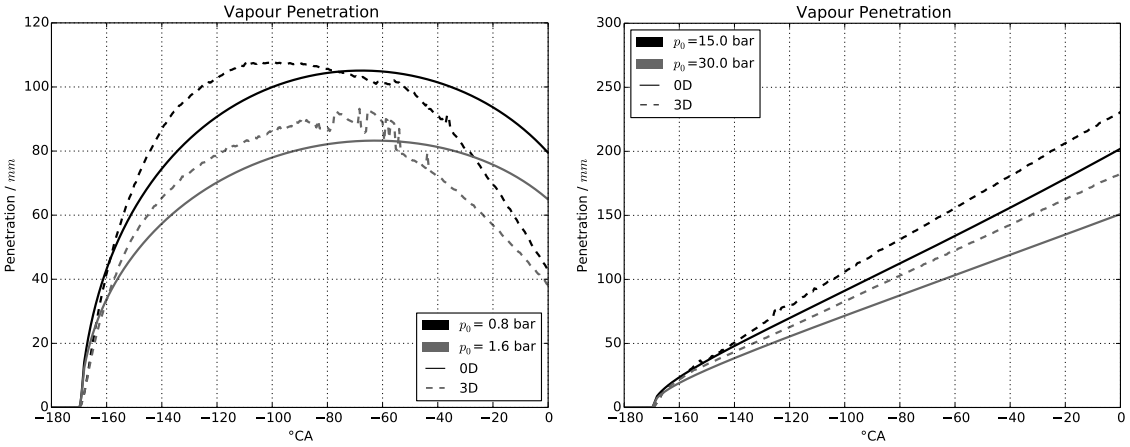

(a) Injection during compression. **(b)** Injection during expansion.

Figure 5.32: Variable-volume vessel – **vapor penetration**. (a): injection during compression. (b): injection during expansion. Solid lines for 0D and dashed lines for 3D (reference).

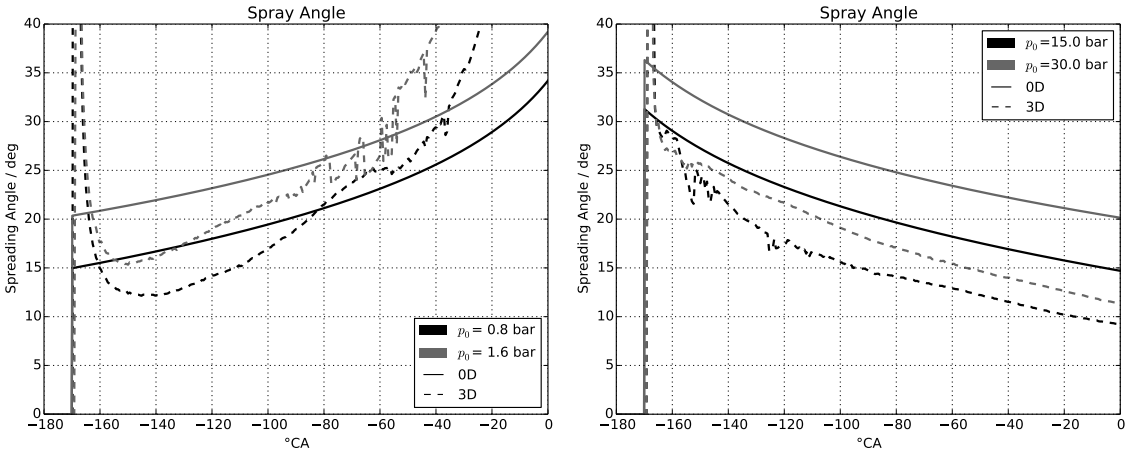

(a) Injection during compression. **(b)** Injection during expansion.

Figure 5.33: Variable-volume vessel – **spreading angle**. (a): injection during compression. (b): injection during expansion. Solid lines for 0D and dashed lines for 3D (reference).

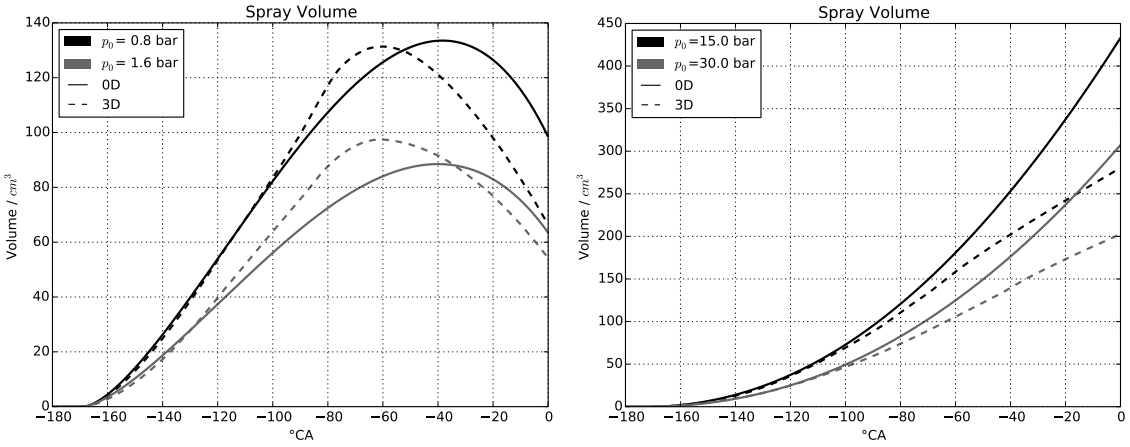

(a) Injection during compression. **(b)** Injection during expansion.

Figure 5.34: Variable-volume vessel – **spray volume**. (a): injection during compression. (b): injection during expansion. Solid lines for 0D and dashed lines for 3D (reference).

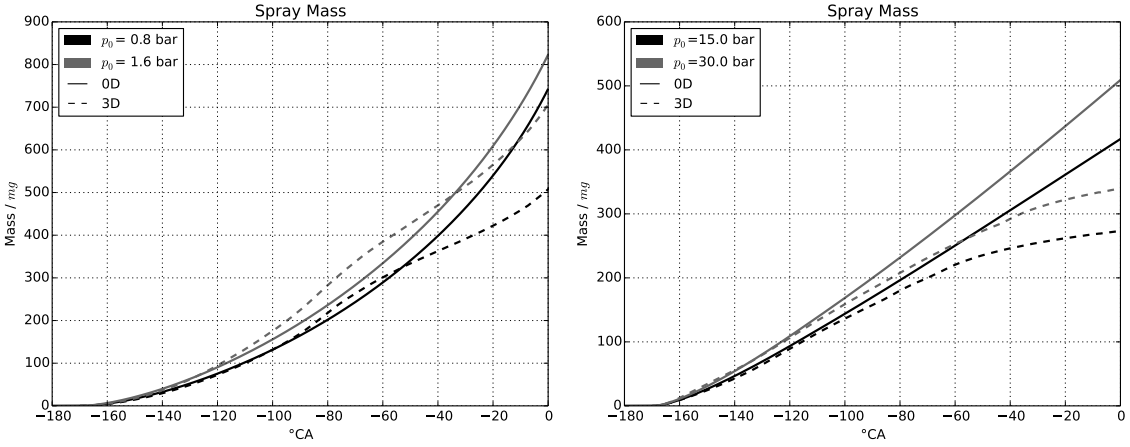

(a) Injection during compression. **(b)** Injection during expansion.

Figure 5.35: Variable-volume vessel – **spray mass**. (a): injection during compression. (b): injection during expansion. Solid lines for 0D and dashed lines for 3D (reference).

showing that the density increase with p_0 overcompensates the volume reduction resulting in more entrained air mass.

The results match the reference data (3D RANS) at the beginning of injection and diverge towards the end of the stroke. In particular, the values of mass and volume given by the 0D model are always overestimated towards the end of both the compression and expansion strokes. Concerning the values of spray penetration and spreading angle, on which the air entrainment model is based, it can be observed that the former (Fig. 5.32) are overestimated at the end of compression and underestimated at the end of expansion while the opposite happens to the latter (Fig. 5.33). This results in an overestimation of the reactive charge mass in both compression and expansion.

Evaporation The liquid and vapor fuel masses are displayed in Fig.s 5.36 and 5.37, respectively, with split plots between compression (a) and expansion (b) cases. In both the compression and expansion cases, evaporation is accelerated at high-load conditions. This is a consequence of the slightly higher gas temperature and of the greater density: increasing the gas mass reduces Y_F^∞ and increases the available energy for heating up the liquid phase, with a net positive effect on the evaporation rate.

Deviations from the shape seen in the previous validation cases are due to the variable thermodynamic conditions and to the gas velocity induced by the piston motion along its axis: both effects lead to higher evaporation rates close to the top dead center, which is reach at the end of compression simulations and at the beginning of expansion ones. The effect of piston motion, in particular, required the integration of the additional gas velocity component u_p – defined by Eq. (4.58) – in order to include the stroke-wise gas velocity. As described in section 4.4.3, the evaporation model takes into account both the effects of tumble and piston motion, in the definition of the gas flow around the evaporating drops.

Mixing Large scale mixing, as a results of air entrainment and evaporation, leads to the average mixture fraction shown in Fig. 5.38. The level of accuracy is a consequence of the good agreement of entrainment and evaporation with the reference data (RANS).

The characteristic peaks at SOI are a consequence of the small fuel and air mass involved: since $\bar{Y}_F$ is a mass ratio its value lacks accuracy when numerator and denominator tend to zero. Moreover, while both the fuel vapor mass and the entrained air clearly vary with the thermodynamic conditions – in both the compression and expansion case – variations in $\bar{Y}_F$ are less evident.

Small scale mixing is synthesized by the mixture fraction variance, shown in Fig. 5.39: the 0D model qualitatively agrees with the reference data, though a consistent underestimation of the variance appears in the expansion cases (b). This is particularly evident at the beginning of spray development, when the reactive charge mass is very low: the relevant difference between the 0D model results and the reference data has little global effect in this phase.

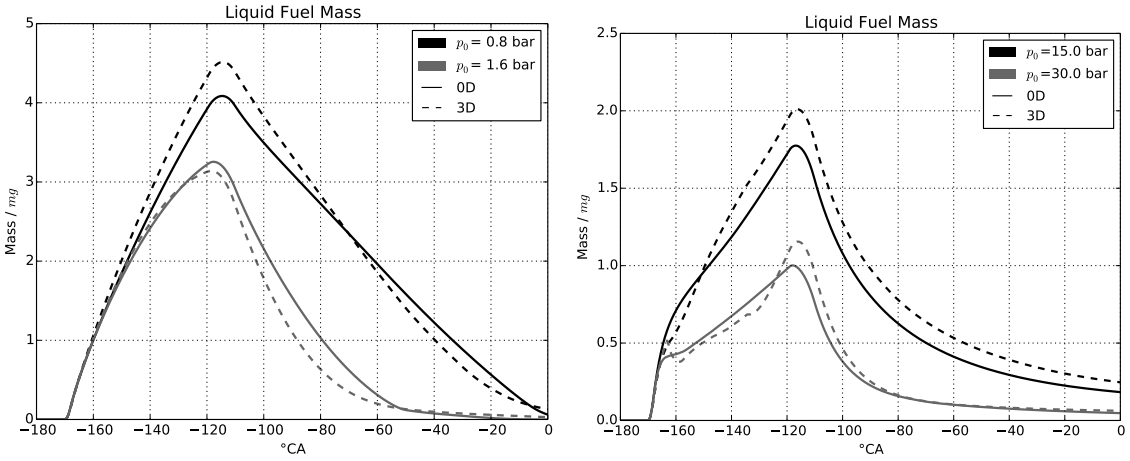

(a) Injection during compression. **(b)** Injection during expansion.

Figure 5.36: Variable-volume vessel – **liquid fuel mass**. (a): injection during compression. (b): injection during expansion. Solid lines for 0D and dashed lines for 3D (reference).

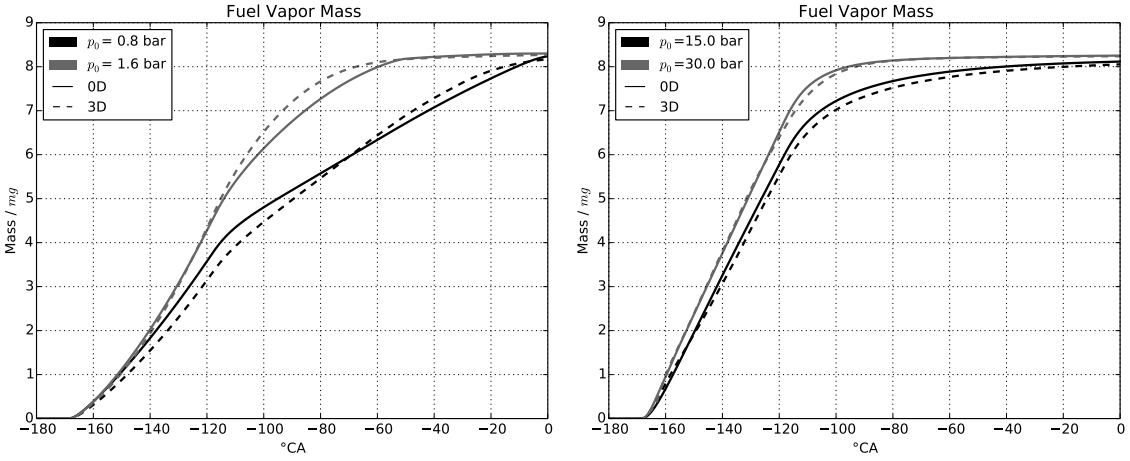

(a) Injection during compression. **(b)** Injection during expansion.

Figure 5.37: Variable-volume vessel – **fuel vapor mass**. (a): injection during compression. (b): injection during expansion. Solid lines for 0D and dashed lines for 3D (reference).

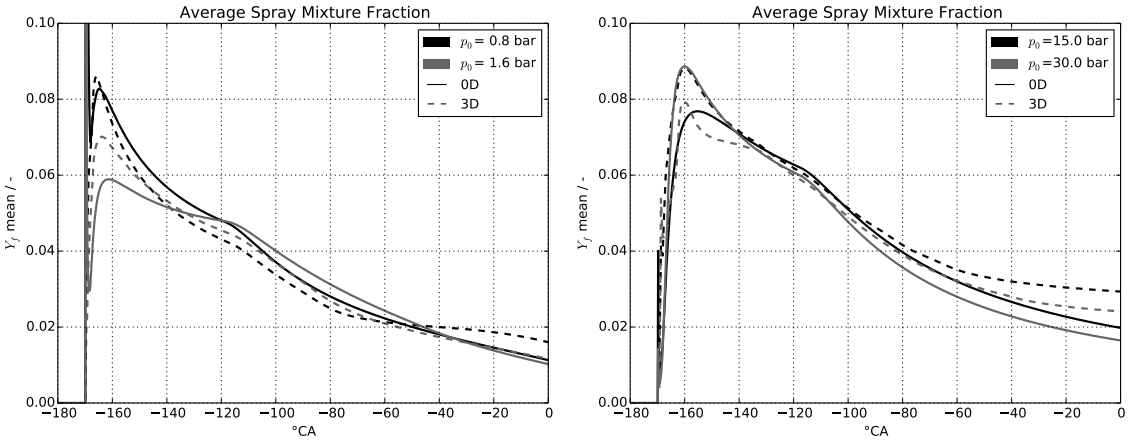

(a) Injection during compression. **(b)** Injection during expansion.

Figure 5.38: Variable-volume vessel – **average mixture fraction**. (a): injection during compression. (b): injection during expansion. Solid lines for 0D and dashed lines for 3D (reference).

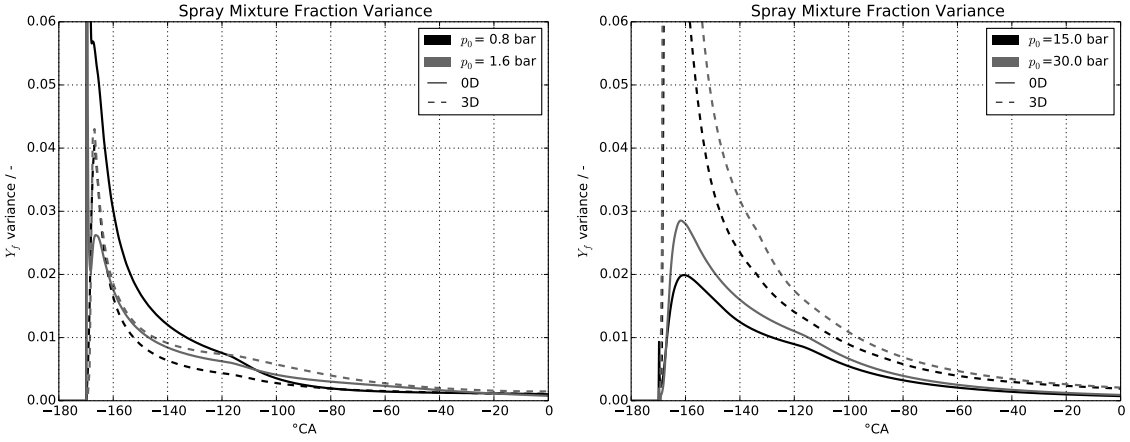

(a) Injection during compression. **(b)** Injection during expansion.

Figure 5.39: Variable-volume vessel – **mixture fraction variance**. (a): injection during compression. (b): injection during expansion. Solid lines for 0D and dashed lines for 3D (reference).

5.4 Conclusion

The validation cases presented in this chapter were used to test the response of the 0D model developed in this PhD work. In particular, the constant-volume vessel injections from the MAGIE experiment provides a variety of constant thermodynamic conditions injection experiments, representative of gasoline engine operation. The 0D model was run on this set of experiments with a unique set of calibration parameters and compare to experimental and 3D RANS data, showing a good response in the different thermodynamic conditions.

Subsequently, the constant-volume vessel with rotating flow (Tumble) validation case served as a base to test the response of the 0D spray model to the aerodynamics in the injection environment. The introduction of a correction in the 0D air entrainment model allowed to represent the sensitivity of spray development to the kinetic energy of the surrounding gas.

Finally, the variable-volume vessel (Cylinder) was used to simulate spray development in an environment where the thermodynamic conditions vary during the experiment. These two latter validation cases are purely numerical experiments, realized with a single-hole injector in order to eliminate the jet-to-jet interaction.

It is interesting to comment on the values of the calibration parameters shown in Table 5.7 and used to adjust the 0D model to fit best with the reference data. The differences can be explained by the change in geometry between the different cases. In particular, the MAGIE experiment uses a three-hole injector while the tumble and cylinder cases use a single-hole injector. Focusing on a single jet, the presence of other neighboring jets in the MAGIE experiment provides an additional source of momentum in the direction of the injection axis. This leads to a reduction of the shear forces that explains the smaller spreading angle (smaller $\mathcal{K}_a$) and worse atomization (a higher value of $\mathcal{K}_{\text{ato}}$ leads to larger drops).

Table 5.7: Summary of the 0D model calibration parameters.

Geometry		Evaporation				Spray			Mixing			
case	N_{holes}	$\mathcal{K}_{\text{ato}}$	N_P	$\mathcal{K}_v$	$\mathcal{K}_{t\,\text{ev}}$	$\mathcal{K}_p$	$\mathcal{K}_a$	$\mathcal{K}_{t\,\text{en}}$	N_{CL}	$\mathcal{K}_\alpha^{\text{pdf}}$	$\mathcal{K}_\beta^{\text{pdf}}$	$\mathcal{K}_{\mathcal{P}}^{\text{pdf}}$
MAGIE	3	3.00	20	1.00	2.50	1.40	1.00	1/600	100	1.7	30	$5.0\,10^3$
Tumble	1	2.40	20	1.00	2.00	1.50	1.60	1/550	61	0.7	40	$5.0\,10^3$
Cylinder	1	2.40	20	1.00	2.00	1.50	1.60	1/550	100	0.7	40	$5.0\,10^3$

Chapter 6

Validation of the Complete Combustion Model: the ICAMDAC Engine

This chapter presents the validation of the 0D spray model, coupled to the CFM1D combustion model, in real engine operating conditions. The investigation includes:

- an evaluation of the spray model – like the ones presented in Chapter 5 – where the spray characterization obtained with the 0D model is compared with 3D RANS data on four selected engine operating conditions;
- a validation of the whole DI-SI combustion chamber model where the engine performances obtained with the 0D model are compared with experimental data on the whole operating map.

6.1 Description of the test case

The engine prototype realized in the framework of the ICAMDAC[1] project (de Francqueville, 2013; Maligne et al., 2013) – issued from a collaboration between IFPEN, IMFT[2], PRISME[3], PSA and Renault – is used as a case study for these investigations.

The geometric characteristics of the ICAMDAC engine are summarized in Table 6.1. The engine prototype was realized in two versions:

[1]Instabilités et Combustions Anormales dans les Moteurs Downsizés à Allumage Commandé.
[2]Institut de Mécanique des Fluides de Toulouse.
[3]Laboratoire Pluridisciplinaire de Recherche Ingéniérie des Systèmes, Mécanique, Énérgetique, University of Orléans.

Table 6.1: ICAMDAC: summary of the engine geometry.

displacement	399.5 cm^3	compression ratio	10.6 : 1
dead volume	42.2 cm^3	injector	6-nozzle axysimmetrical
bore	77 mm		(Continental)
stroke	85.8 mm	injector position	central

Table 6.2: ICAMDAC: summary of the engine operating points simulated with 3D RANS.

	#1	#2	#3	#4
Speed (rpm)	1200	1200	3000	4000
IMEP (bar)	6.0	17.0	6.0	18.0
SOI (°CA)	-278.6	-308.6	-275.2	-275.2
DOI (°CA)	9.01	27.68	22.66	82.67
fuel mass (mg/stroke)	15.2	52.2	15.2	46.4
spark advance (°CA)	14.1	-15.0	18.1	1.0

full metal with a regular piston, to evaluate performance on a test bed in fired conditions;

optical with a transparent piston, used to evaluate in-cylinder aerodynamics with Particle Image Velocimetry (PIV) in motored condition (no combustion).

The fuel used in the fired tests is pure iso-octane (C_8H_{18}).

The ICAMDAC engine is a downsized DI-SI engine, designed for homogeneous stoichiometric operation. In homogeneous operation, injections take place early, during the intake stroke, so that fuel vapor has the time to fill the combustion chamber, and completely mix with ambient air before ignition. Differently, in stratified operation, injection takes place late, in the compression stroke, so that the in-cylinder mixture is not homogeneous: a small portion of the mixture, confined in a portion of the combustion chamber is close to stoichiometry, the rest being filled with air for a globally lean operation.

If, on the one hand, the engine is classified as homogeneous because of the reasons discussed above, the equivalence ratio distribution still presents small scale gradients (Iafrate, 2016) at ignition that have an impact on flame propagation.

The ICAMDAC project is dedicated to the investigation of instabilities and abnormal combustions in downsized SI engines, due to the high level of turbocharging (de Francqueville, 2013). The experimental database consists of a speed-load operating map with typical calibration as well as particular operating points dedicated to the investigation of abnormal combustions (knock and rumble).

6.2 Mixture formation in different operating conditions

This section presents compares the results obtained with the 0D model to the reference data (3D RANS), on four different engine operating conditions that were studied in detail.

The analysis focuses on spray characteristics and aims to test the behavior of the developed spray model in real engine conditions.

6.2.1 3D numerical simulations

The four operating points detailed in Table 6.2 were chosen to validate the 0D spray model against 3D RANS data: RANS simulations had already been performed in the framework of the ICAMDAC project, so that mesh and combustion model parameter set could be reused in this work. All the operating points in Table 6.2 belong to the operating map, with the exception of a rumble point (1200 rpm and 17 bar IMEP) that presents a late ignition.

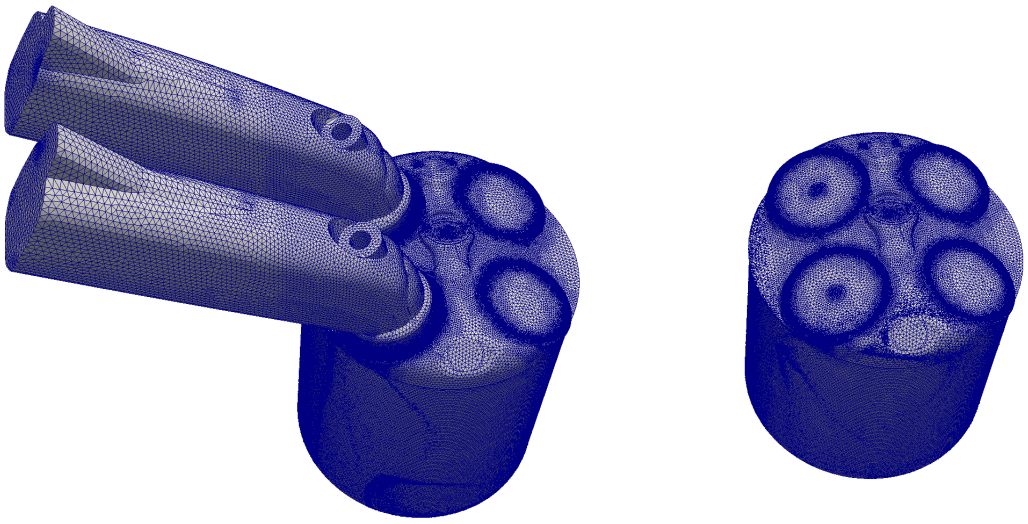

(a) 160 °CA before TDC (open valves).

(b) 120 °CA before TDC (closed valves).

Figure 6.1: ICAMDAC engine: mesh used for the 3D RANS simulations. The intake ducts are resolved, to have a better prediction of the aerodynamics inside the cylinder, until IVC.

Mesh. The computational domain consists of a moving mesh that stretches according to piston motion and is remapped 34 times per stroke to maintain an optimal cell aspect ratio.

Intake valves and ducts are also meshed to provide a good prediction of the aerodynamics inside the combustion chamber. Fig. 6.1 shows the computational domain and mesh surface at −169 °CA and −120 °CA: since intake valves close at −151.6 °CA, the domain includes the intake ducts in the first case but not in the second; this allows to save computational time.

The mesh size depends on remapping and ranges between:

- 2 670 161 nodes (including the intake valves and ducts) at IVO (−357 °CA), when all four simulations begin;
- 264 332 nodes at firing TDC (0 °CA).

Initial conditions. Simulations are initialized with a null velocity field and uniform thermodynamic conditions, as summarized in Table 6.3. Fuel is injected at 50 °C and the initial drop diameter is fixed at 20 μm, a secondary atomization model describes subsequent break-up and indirectly provides a drop size distribution.

Table 6.3: ICAMDAC: initial conditions for 3D RANS computations.

	#1	#2	#3	#4
Speed (rpm)	1200	1200	3000	4000
IMEP (bar)	6.0	17.0	6.0	18.0
p_0 (bar)	0.770	1.770	0.765	1.580
T_0 (°C)	-278.6	-308.6	-275.2	-275.2

CFD code. As in the test cases discussed in the previous chapter, the 3D simulations were performed with IFP-C3D (Velghe et al., 2011), a RANS code developed at IFP Energies nouvelles for engine simulations.

Validation of the numerical setup. Mesh, tuning parameters boundary and initial conditions used to simulate these engine operating points were generated and set up at IFPEN in the framework of a previous research project, ICAMDAC (de Francqueville, 2013). In detail, inlet and exhaust temperature and pressure profiles from engine testbed measurements on the ICAMDAC monocylinder are imposed as boundary conditions.

Combustion model parameters are tuned to best fit the measured cylinder pressure profiles, as shown in Fig. 6.2 (a) for the #1 operating point.

The original numerical setup includes a correction of the trapped mass and mean fuel concentration at IVC, to match the air mass estimated from measurements. This is common practice in engine simulations because of the high sensitivity of output power and combustion duration to air mass and equivalence ratio: an inevitable small error in these quantities can result in a poor prediction of cylinder pressure.

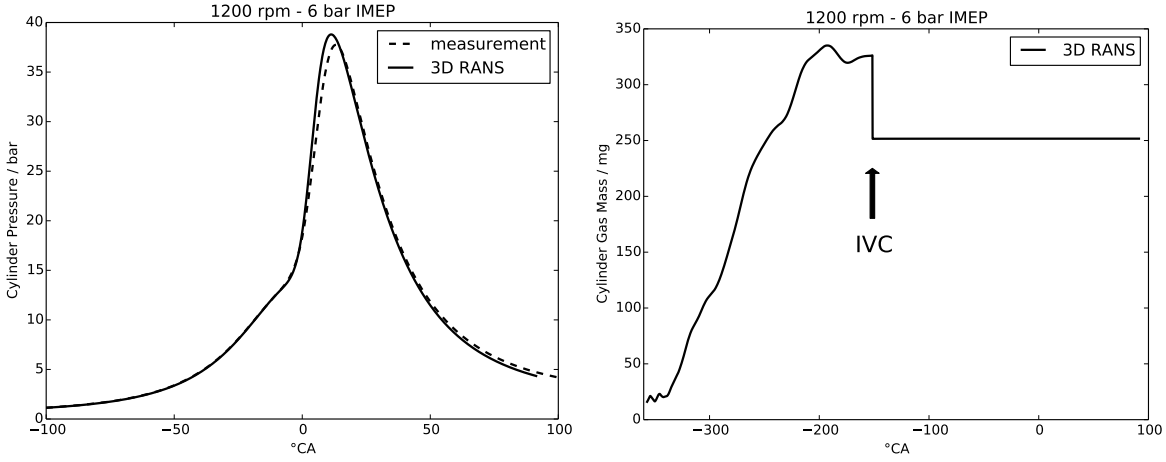

(a) Cylinder pressure

(b) Trapped mass

Figure 6.2: 3D RANS simulations of the ICAMDAC engine – operating point #1: the combustion model is tuned to best represent cylinder pressure (a). A correction of the trapped mass and composition is performed at Inlet Valve Closing (IVC) (b): the amount of this correction ($\approx 30\%$) suggests a problem with the measurements or an incorrect description of valve permeability.

Fig. 6.2 (b) plots the in-cylinder gas mass against the crank angle: IVC separates the intake phase (on the left) from the compression-expansion phases where mass is constant. The negative step ($\approx 30\%$) visible at IVC identifies the mass correction. Its value turns out to be high and suggests a problem in measured intake pressure.

Since the 0D model uses the same boundary conditions as RANS (intake and exhaust pressure and temperature) and it does not allow to correct the gas mass at IVC, it was chosen here to remove the correction in 3D RANS, to better compare simulation data. Results obtained in this way are more suitable to be used as reference data to validate the 0D spray model, even though less accurate in terms of combustion.

6.2.2 0D numerical simulations

The parameter set summarized in Table 6.4 was adopted for the 0D simulations.

Table 6.4: ICAMDAC engine: calibration of the 0D spray model and comparison with the other validation test cases.

Geometry		Evaporation				Spray			Mixing		
case	N_{holes}	$\mathcal{K}_{\text{ato}}$	N_P	$\mathcal{K}_v$	$\mathcal{K}_{t\,\text{ev}}$	$\mathcal{K}_p$	$\mathcal{K}_a$	$\mathcal{K}_{t\,\text{en}}$	N_{CL}	$\mathcal{K}_\alpha^{\text{pdf}}$	$\mathcal{K}_\beta^{\text{pdf}}$
ICAMDAC	6	3.00	20	1.00	2.00	0.87	0.70	1/450	100	1.5	40
MAGIE	3	3.00	20	1.00		1.40	1.00		100	1.7	
Cylinder	1	2.40	20	1.00	2.00	1.50	1.60	1/550	100	0.7	40

The values indicated in Table 6.4 were obtained focusing on the respective variables and targeting the reference data (3d RANS). The atomization coefficient, $\mathcal{K}_{\text{ato}}$, is the value that provides the best fit of the liquid and vapor fuel mass. Likewise, the spray penetration and spreading angle coefficients, $\mathcal{K}_p$ and $\mathcal{K}_a$ respectively, target the penetration and spray mass while the $\mathcal{K}_\alpha^{\text{pdf}}$ coefficient is obtained targeting the mixture fraction variance.

It is interesting to point out that some of the changes – with respect to the injector shape – follow the trend outlined in section 5.4. In particular, $\mathcal{K}_a$, used to fine-tune the spreading angle, decreases as the number of injector holes increases. As seen in section 5.4, this behavior can be explained with a reduction of the shear forces resulting from the interference between jets that, in turn, produces narrower jets.

Spray penetration

Results concerning the vapor and liquid penetrations are discussed in the following paragraphs.

Vapor penetration. Fig. 6.3 shows the gas penetrations for the four operating points investigated, comparing the 0D model with the 3D reference data.

The 0D model, that describes the gas penetrations of a free jet, does not take into account the influence of solid walls: the results show a good agreement between the 0D model and 3D data during the free jet penetration phase. 3D data saturates on the piston wall and follows its movement after the impact, while the 0D spray continues to penetrate until its volume has filled the cylinder: at this point the computation of the gas penetration – used until then to estimate the air entrainment – stops as its value is no longer needed to continue the simulation.

This behavior is observed in all operating points except the high-speed high-load one, #4, where the maximum penetration reached in 0D is smaller than the injector-piston distance, as appears in Fig. 6.3 plot (d). In this case, the gas penetration is underestimated but its effect on the spray volume and mass, shown in Fig.s 6.6 – 6.7, is compensated by the effect of tumble on air entrainment, described in the 0D model by Eq.s (4.74 – 4.75).

The enhanced spray tip velocity in 3D, for case #4, can be a consequence of the high level of tumble: the rotating flow advects fuel vapor towards the piston on one side and away from it on the other, increasing the gas penetration defined – in 3D – as the maximum distance of fuel vapor from the injector tip.

Liquid penetration. Figure 6.4 plots liquid penetrations comparing the results obtained from the 0D model with the reference data extracted from 3D RANS simulations. The following two phases can be identified:

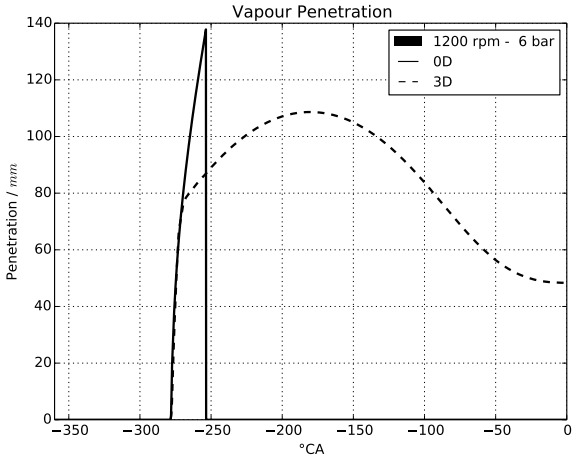

(a) Operating point #1.

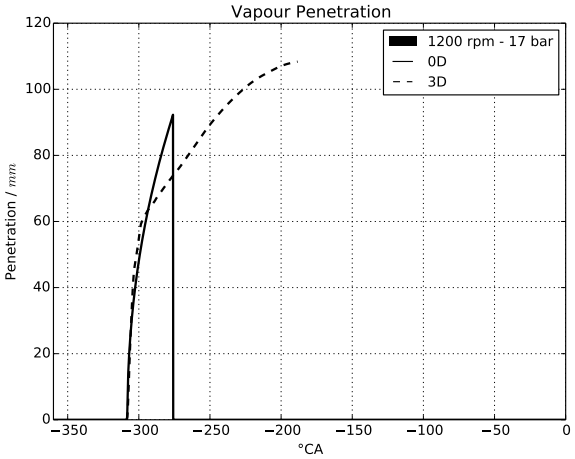

(b) Operating point #2.

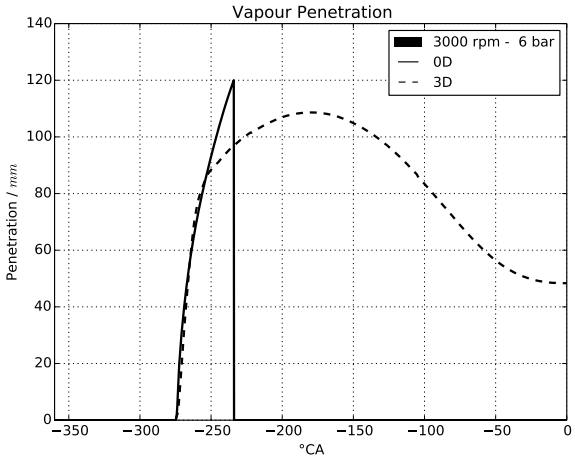

(c) Operating point #3.

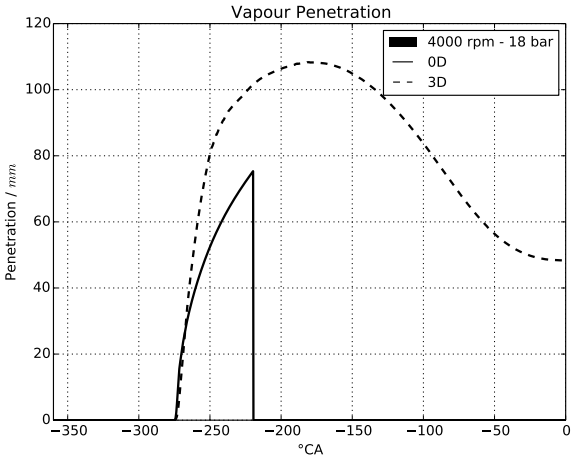

(d) Operating point #4.

Figure 6.3: Mixture formation in the ICAMDAC engine – **gas penetration**: the four plots compare 0D (solid lines) and 3D reference data (dashed lines) for each of the operating points in Table 6.2. The 0D model calculates the gas penetration until the spray has filled the combustion chamber.

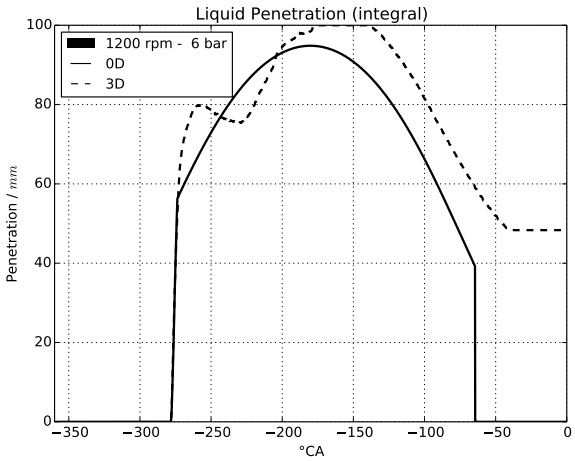

(a) Operating point #1.

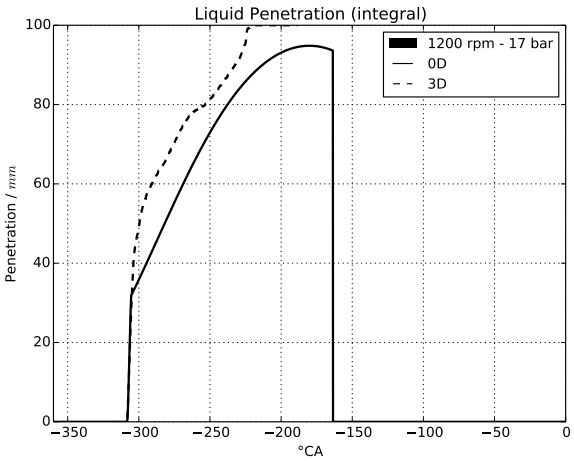

(b) Operating point #2.

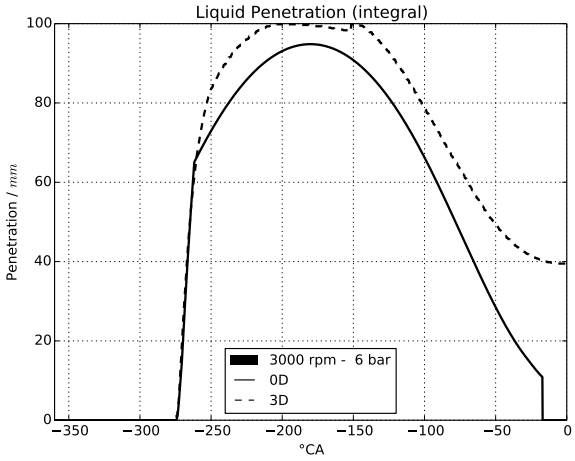

(c) Operating point #3.

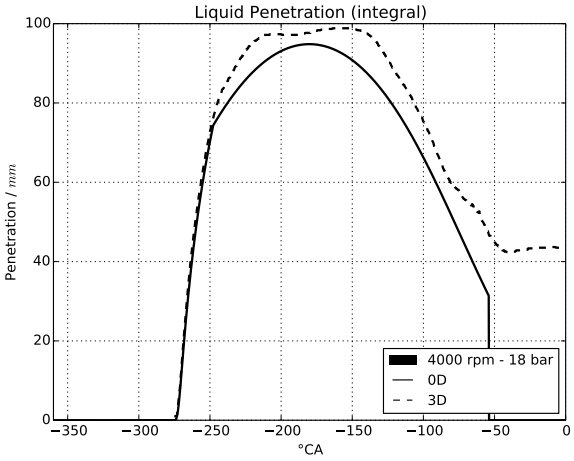

(d) Operating point #4.

Figure 6.4: Mixture formation in the ICAMDAC engine – **liquid penetration**: the four plots compare 0D (solid lines) and 3D reference data (dashed lines) for each of the operating points in Table 6.2. The 0D model calculates the liquid penetration until the disperse phase has completely evaporated.

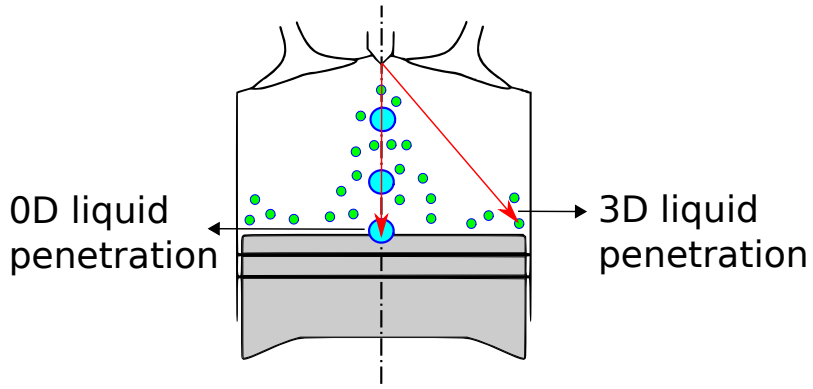

Figure 6.5: Description of the liquid phase. 0D drop parcels – represented by big blue spheres in the image – are assumed to move along the injection axis and their dynamics is frozen after reaching the piston wall. Liquid drops in 3D simulations – represented by small green spheres in the image – are free to move in the three spatial directions and are always treated as a disperse phase. After reaching the piston wall, some drops find themselves close to the piston/liner interface, leading to greater penetrations in 3D than in 0D.

- an initial fast propagation, typical of free sprays and characterized by a quasi linear penetration;
- a slower propagation, when the spray tip approaches the piston wall.

While there is good match between 0D an 3D in the first phase, noticeable differences arise in the second. In particular:

- the transition between the two phases is smooth in 3D data while it presents a brusque slope variation in 0D;
- the 0D model gives a more regular behavior after the impact;
- 3D simulations generally present greater liquid penetrations close to the piston wall.

These discrepancies can be explained pointing out the different modelling approaches adopted to describe the liquid phase in 0D and 3D.

Drop parcel positions are computed in the 0D model integrating drop velocities given by momentum equation, Eq (4.59). A set of spatial coordinates locates each drop parcel along the injection axis and saturates at the intersection with the piston surface: the maximum penetration over the drop parcels is taken as a value for liquid phase penetration. Since only one dimension is resolved, all the drop parcels are assumed to collide with the piston surface in the same point, i.e. at the intersection with the injection axis. After the impact, the liquid parcels are treated as attached to the piston and follow its regular oscillation.

In 3D simulations, on the other hand, liquid drops are free to move in the three resolved directions and the liquid penetrations – calculated as the maximum distance from the injector tip – also take into account the two additional degrees of freedom. This leads to generally higher values when drops migrate towards the intersection between piston and liner boundaries, as shown in Fig. 6.5.

Furthermore, the solid wall has an indirect effect on the liquid phase as its presence slows down the approaching gas stream.

The absence of a film model in 3D simulations explains the less regular behavior during the second phase: the liquid drops are always treated as a disperse phase and continue moving in response to the aerodynamics, producing the observed instabilities in the liquid penetration.

Large scale mixing

The large scale mixing is described by the spray volume and mass, discussed in the following paragraphs.

Reactive charge zone volume. Fig. 6.6 plots the volume of the reactive charge zone against the crank angle for the four operating points investigated. The transition from an initial free-jet propagation to a cylinder-guided deformation of the reactive charge zone after the charge has filled the cylinder is smoother in 3D than in 0D for the reasons explained above. This transition appears earlier in 0D than in 3D: 0D simulations show a transition during the intake stroke, shortly after the injection while 3D simulations predict it at the beginning of the compression stroke, after IVC (151.5 °CA).

Reactive charge mass. The same conclusions as for the spray volume evolution can be drawn following the spray masses in Fig. 6.7. Discrepancies between 0D and 3D in the trapped mass are a consequence of the different description of intake, assumed to be more predictive in 3D. In particular, the reactive charge mass presents a maximum t 1200 rpm and 1200 bar IMEP (Fig. 6.7 plot a): its subsequent decrease indicates the appearance of backflow towards IVC. The intensity of this backflow is more pronounced in 0D.

It is interesting, in order to locate the evolution of large scale mixing in the engine cycle, to build normalized indicators such as the crank angles indicating when the charge mass (air mixed with fuel) attains 50% (CA_{50}^{sp}) and 90% (CA_{90}^{sp}) of the in-cylinder gas mass.

The values of CA_{50}^{sp} and CA_{90}^{sp} are traced in Fig. 6.8 with red crosses for the results obtained with the 0D and blue circles for 3D reference data.

The 0D model gives good predictions of CA_{50}^{sp} while deviations from the reference data appear in the values of CA_{90}^{sp}. The two being indicators of the free-jet and cylinder-guided propagation, respectively, this observation is consistent with the fact that the 0D model does not take into account the wall boundary effects on spray propagation.

Evaporation

The description of evaporation by the 0D model is evaluated in the following paragraphs, comparing the liquid and vapor fuel masses obtained with the reference data (3D RANS results). Both quantities are the output of the liquid phase model based on homogeneous drop parcels, described in Section 4.4.

Liquid fuel mass. Figure 6.9 shows the liquid mass against the crank angle in the four operating points investigated. The values obtained with the 0D model summing the masses of all drop parcels (solid line) are compared with 3D RANS (reference) data.

The 0D model describes well the two phases of the liquid mass evolution, i.e:

during injection the evaporation rate is always smaller than the injection rate, resulting in an increase of the liquid mass;

after injection only evaporation is active and the liquid mass decreases.

This behavior is typical of GDI sprays. In Diesel conditions – at high loads – injections often present an equilibrium phase where the evaporation and injection rates are equal and liquid mass is stable: this happens when the spray tip reaches the *liquid length* (Siebers, 1998, 1999).

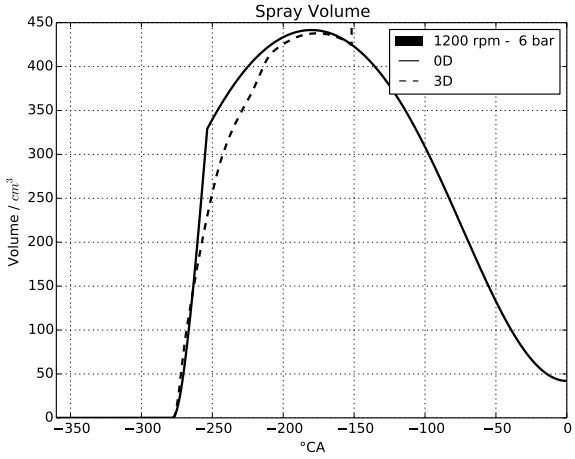

(a) Operating point #1.

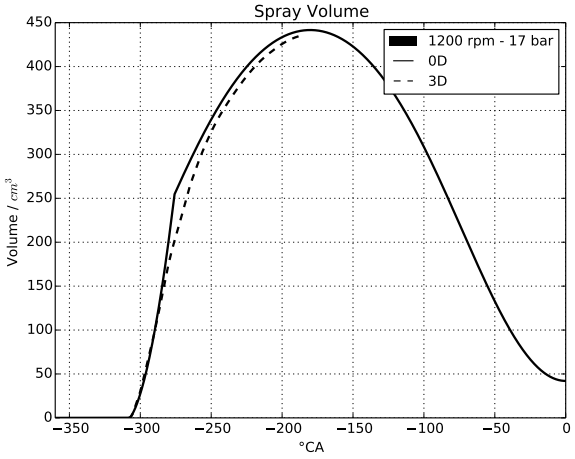

(b) Operating point #2.

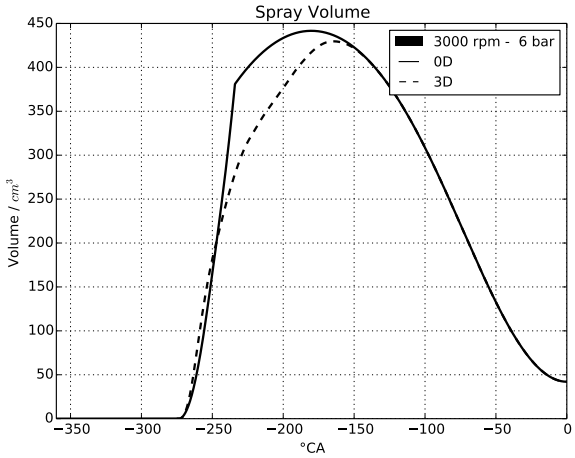

(c) Operating point #3.

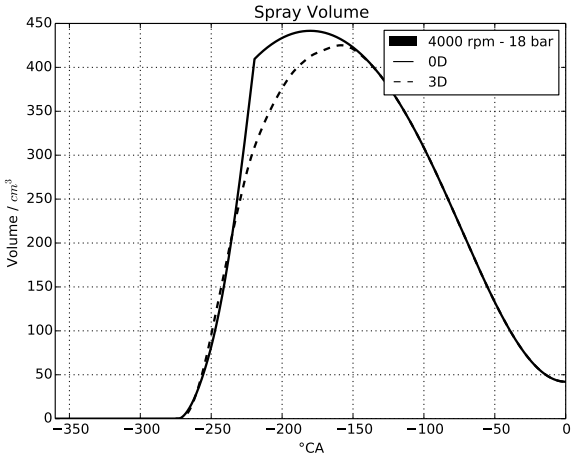

(d) Operating point #4.

Figure 6.6: Mixture formation in the ICAMDAC engine – **spray volume**: the four plots compare 0D (solid lines) and 3D reference data (dashed lines) for each of the operating points in Table 6.2.

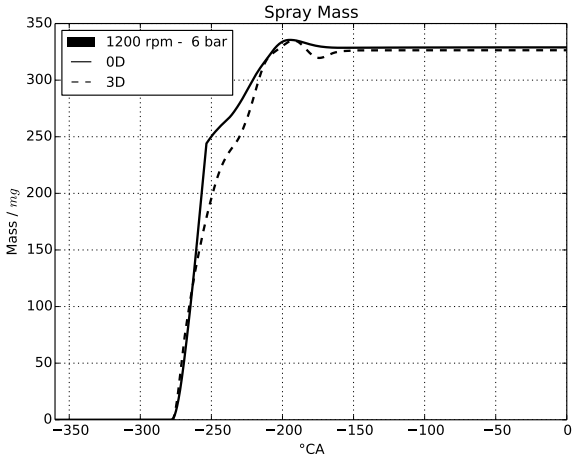

(a) Operating point #1.

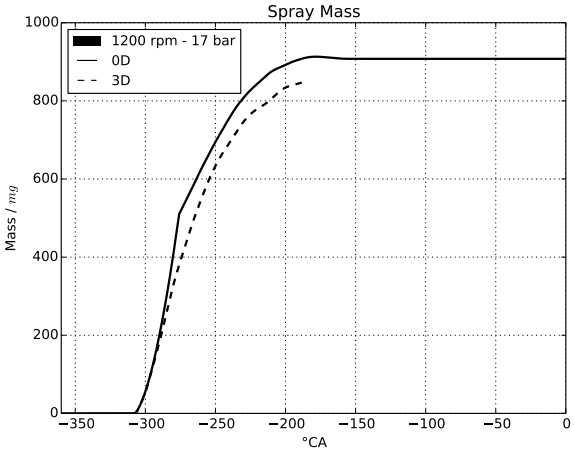

(b) Operating point #2.

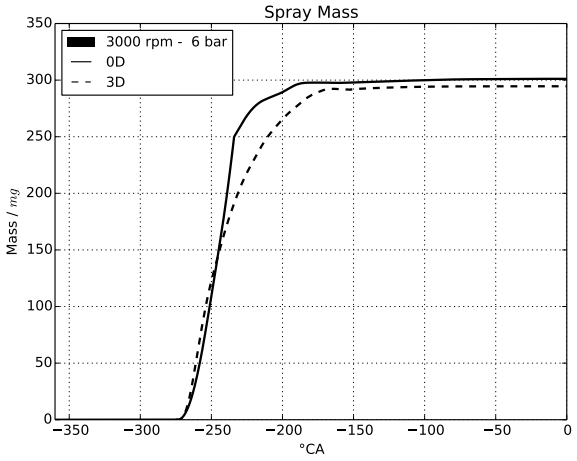

(c) Operating point #3.

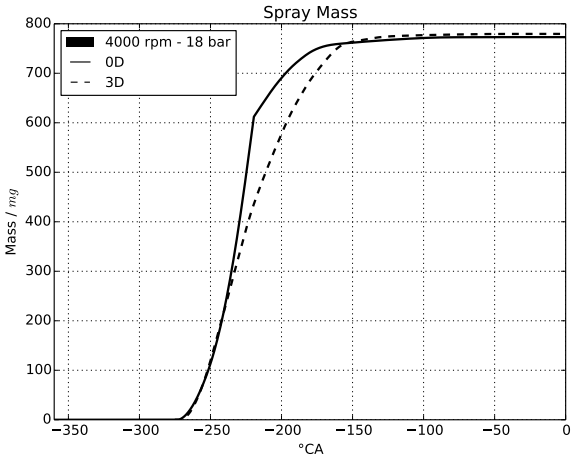

(d) Operating point #4.

Figure 6.7: Mixture formation in the ICAMDAC engine – **spray mass**: the four plots compare 0D (solid lines) and 3D reference data (dashed lines) for each of the operating points in Table 6.2.

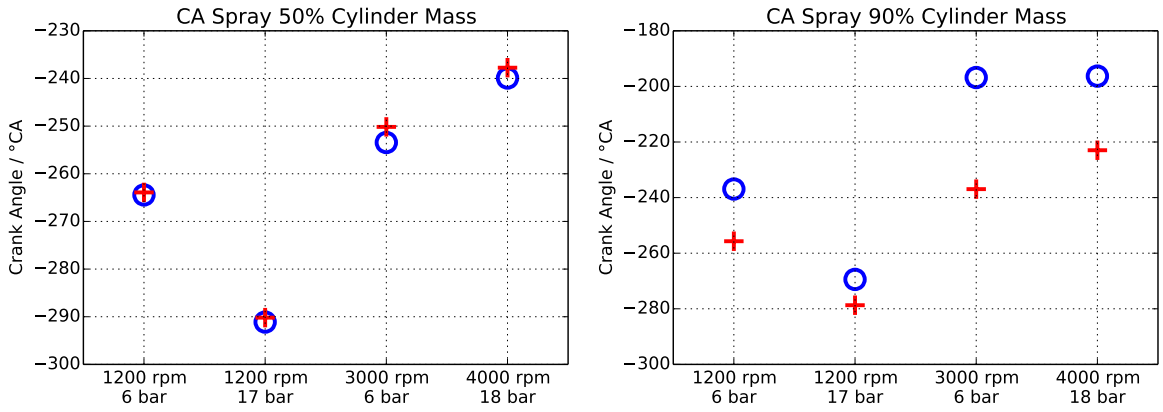

(a) Charge attains 50% of in-cylinder gas.

(b) Charge attains 90% of in-cylinder gas.

Figure 6.8: Mixture formation in the ICAMDAC engine – **charge propagation indicators**: the two plot show the values of the crank angle when the reactive mixture (spray) attains 50% and 90%, respectively, of the in-cylinder gas mass (air and fuel vapor) for each of the operating points in Table 6.2. Results obtained with the 0D model (red crosses) are compared with the reference 3D data (blue circles).

A small negative step is visible in 3D RANS results relative to operating point #3 (3000 rpm – 6 bar IMEP) – shown in Fig. 6.9 (b) – at IVC (−152 °CA). This effect is explained by the presence of liquid drops backflow into the intake manifold, at the end of the intake stroke. At IVC, when connection between cylinder and intake ducts is broken, the latter are cut out of the computational domain and the liquid mass they contain is lost. Fig. 6.10 shows the computational domain at −155 °CA, shortly before IVC (−151.6 °CA). Liquid drops are visible at the end of the intake ducts, close to the valves, confirming the hypothesis of disperse phase backflow.

In real engine operation, this phenomenon has no effect on the in-cylinder mean equivalence ratio, since the fuel that backflows into the intake manifold at cycle n is aspirated back into the cylinder at $n+1$. This could be taken into account in 3D RANS by simulating multiple cycles. With a single-cycle simulation, like the ones performed in this study, backflow results in a reduction of the mean equivalence ratio.

Fuel vapor mass. Fig. 6.11 plots the fuel vapor mass against the crank angle in the four operating points investigated. The displayed behaviors reflect those of the liquid mass shown in Fig. 6.9.

Discrepancies in the vapor mass at the end of evaporation – particularly visible in the low-load points, 1200 rpm IMEP = 6 bar IMEP and 3000 rpm IMEP = 6 bar IMEP – is again a consequence of backflow.

At 1200 rpm backflow of air and fuel vapor is more pronounced in 3D than in 0D, but detected by both models, as shown in Fig. 6.7 (a): the spray mass presents a maximum and then decreases because of backflow. The little discrepancy in trapped mass results from the different description of a phenomenon – vapor fuel backflow – that both models take into account. In particular, the 0D profile in ig. 6.7 (a) is always increasing showing that the evaporation rate overcomes the backflow resulting in a positive contribution to the fuel vapor mass.

At 3000 rpm liquid drops flow back in the intake ducts in 3D – as shown in Fig. 6.10 – while the 0D model always locates the disperse phase inside the combustion chamber

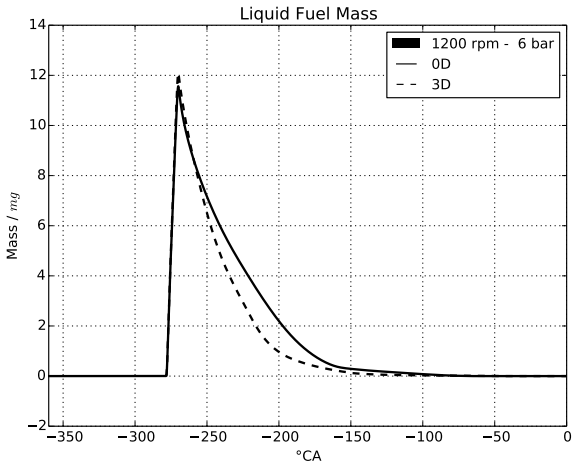

(a) Operating point #1.

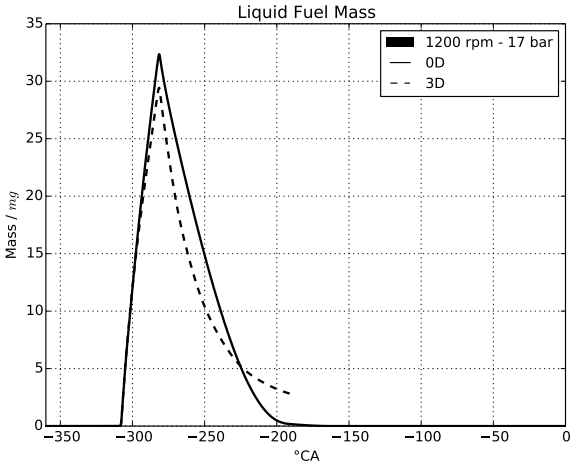

(b) Operating point #2.

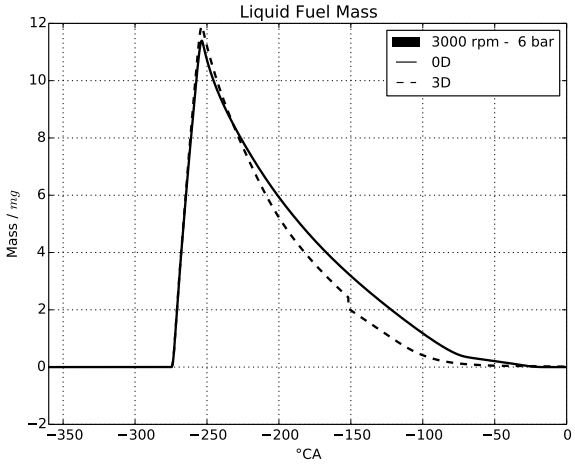

(c) Operating point #3.

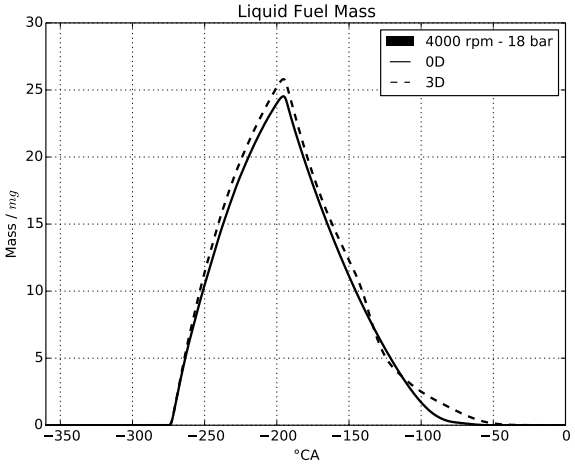

(d) Operating point #4.

Figure 6.9: Mixture formation in the ICAMDAC engine – **liquid fuel mass**: the four plots compare 0D (solid lines) and 3D reference data (dashed lines) for each of the operating points in Table 6.2.

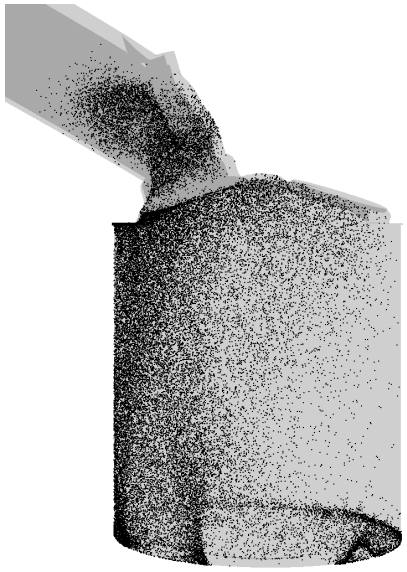

Figure 6.10: 3D RANS simulation of the 3000 rpm 6 bar IMEP operating point. The image shows a snapshot of the disperse phase in the computational domain at −155 °CA, right before IVC (−151.6 °CA). Particles in the intake ducts are a result of backflow.

(and more precisely along the injection axis). In this case, the pronounced discrepancy in trapped fuel mass results from a phenomenon – liquid fuel backflow – that the 0D model does not take into account.

Similarly to what was done with spray mass, Fig. 6.12 shows the crank angle when the evaporated fuel mass attains 50% (CA_{50}^{ev}) and 90% (CA_{90}^{ev}) of the injected mass.

Predictions of CA_{50}^{ev} given by the 0D model are good for all operating points. Those of CA_{90}^{ev} match the reference data at high load and overestimate them at low load: this behavior corresponds to the overestimation of the evaporation rates visible in Fig. 6.9, plots (a) and (b).

Small-scale mixing

The mixing model based on the discrete PDF, described in Section 4.6, is validated in the following paragraphs.

Average mixture fraction. The evolution of average fuel mass concentration Y_F in the spray zone – shown in Fig. 6.13 – is a result of fuel evaporation, spray entrainment and valve flow. Very rich values at injection start later stabilize around the stoichiometric concentration.

The 0D model fails to predict the average mass fraction at the beginning of injection, because of the small masses involved in the ratio. However some remarkable tendencies concerning the concentration peak, such as:

- the intensity decrease with charge;
- the duration increase with charge;

are consistent between 0D and 3D.

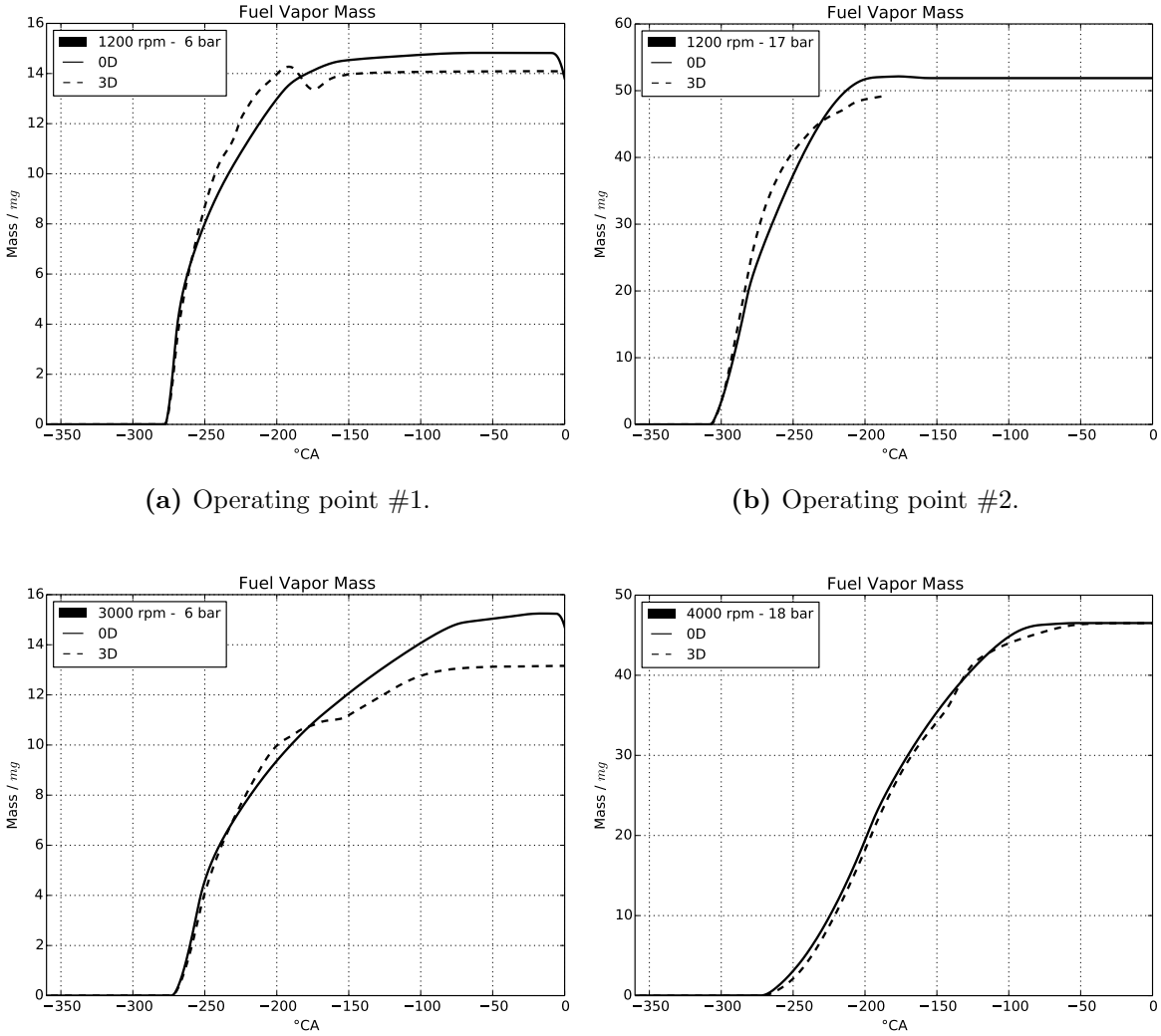

(a) Operating point #1.

(b) Operating point #2.

(c) Operating point #3.

(d) Operating point #4.

Figure 6.11: Mixture formation in the ICAMDAC engine – **fuel vapor mass**: the four plots compare 0D (solid lines) and 3D reference data (dashed lines) for each of the operating points in Table 6.2.

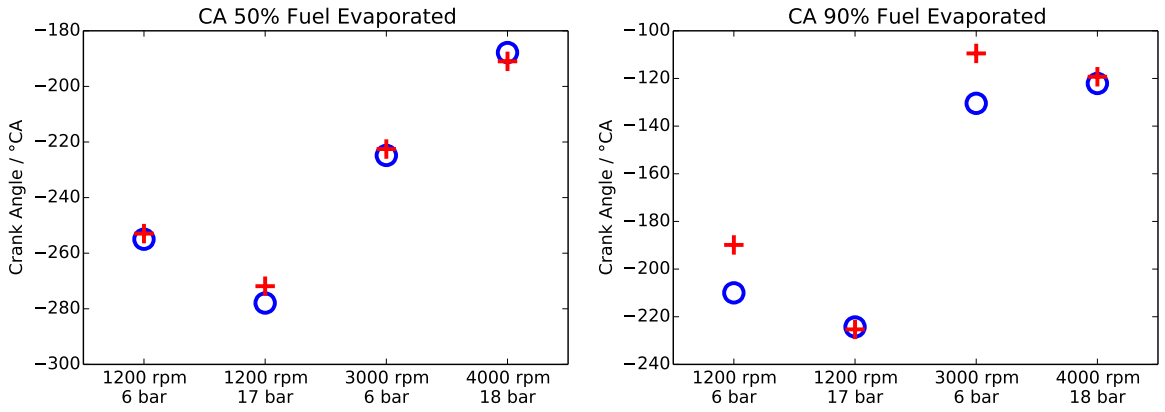

(a) Evaporated mass attains 50% of injected mass. **(b)** Evaporated mass attains 90% of injected mass.

Figure 6.12: Mixture formation in the ICAMDAC engine – **charge propagation**: The two plot show the values of the crank angle when the evaporated fuel mass attains 50% and 90% of the injected mass for each of the operating points in Table 6.2.

Mixture Fraction Variance Fig. 6.14 shows the variance of Y_F giving an indication of mixture heterogeneity. In both 0D and 3D RANS data, variance tends to decrease with time as a result of mixing: the rich and lean pockets tend to disappear as the mixture becomes more homogeneous. Nevertheless, the comparison is not as good as in the validation cases shown in Chapter 5, pointing out the limitations of the mixing model.

Taking operating point #1 as an example, Fig. 6.13:(a) shows that the mean mixture fraction is approximately $\bar{Y_F} \approx 0.045$ while the probability distributions, shown in Fig. 6.15 at six different times during an engine cycle, tend to shrink with time. In the last time sample, shown in panel (f), almost all the charge is concentrated in the two classes corresponding to $Y_F = 0.04$ and $Y_F = 0.05$. Because of the finite discretization, the final state always involves two classes, unless the mean mixture fraction, $\bar{Y_F}$, corresponds exactly to one of the N_{PDF} values, Y_F^j, used in the discretization.

Operating point #4 (4000 rpm – 18 bar IMEP) presents a variance peak at $-120\,^{\circ}$CA in 3D simulation that is not reproduced by the 0D model. At this point 90% of the injected mass has already evaporated, as Fig. 6.12 shows a $\mathrm{CA}_{90}^{\mathrm{ev}} \approx -120$.

This behavior reveals the presence of a small mass of liquid evaporating at high Y_F and therefore – under the hypothesis that evaporating drops are in equilibrium with their saturated vapor – at high temperature. This hypothesis can be verified setting a threshold and recalculating the mixture fraction variance for $Y_F < 0.2$. This truncation removes the variance peak in the 3D distribution with little effect on the average mixture fraction. Fig. 6.16 shows mean (a) and variance (b) of the three distributions.

The spatial distribution of the locations where liquid fuel heats up and evaporates at $Y_F > 0.2$ is shown in Fig. 6.17. The computational domain is outlined in light blue and cells with $Y_F > 0.2$ are highlighted in red at three different timings ($-120\,^{\circ}$CA, $-96\,^{\circ}$CA and $-76\,^{\circ}$CA).

The highlighted rich cells are located close to solid walls, in particular at the piston/liner interface, where gas temperature is higher. During intake and compression solid walls are hotter than the gas mixture resulting in the former heating the latter. Hot spots are therefore located near the edges where the surface-area-to-volume ratio increases heat transfer.

Figure 6.18 shows a comparison the probability class distributions obtained with the 0D model (light blue bars), from 3D data (magenta circles and solid line) and the truncated 3D

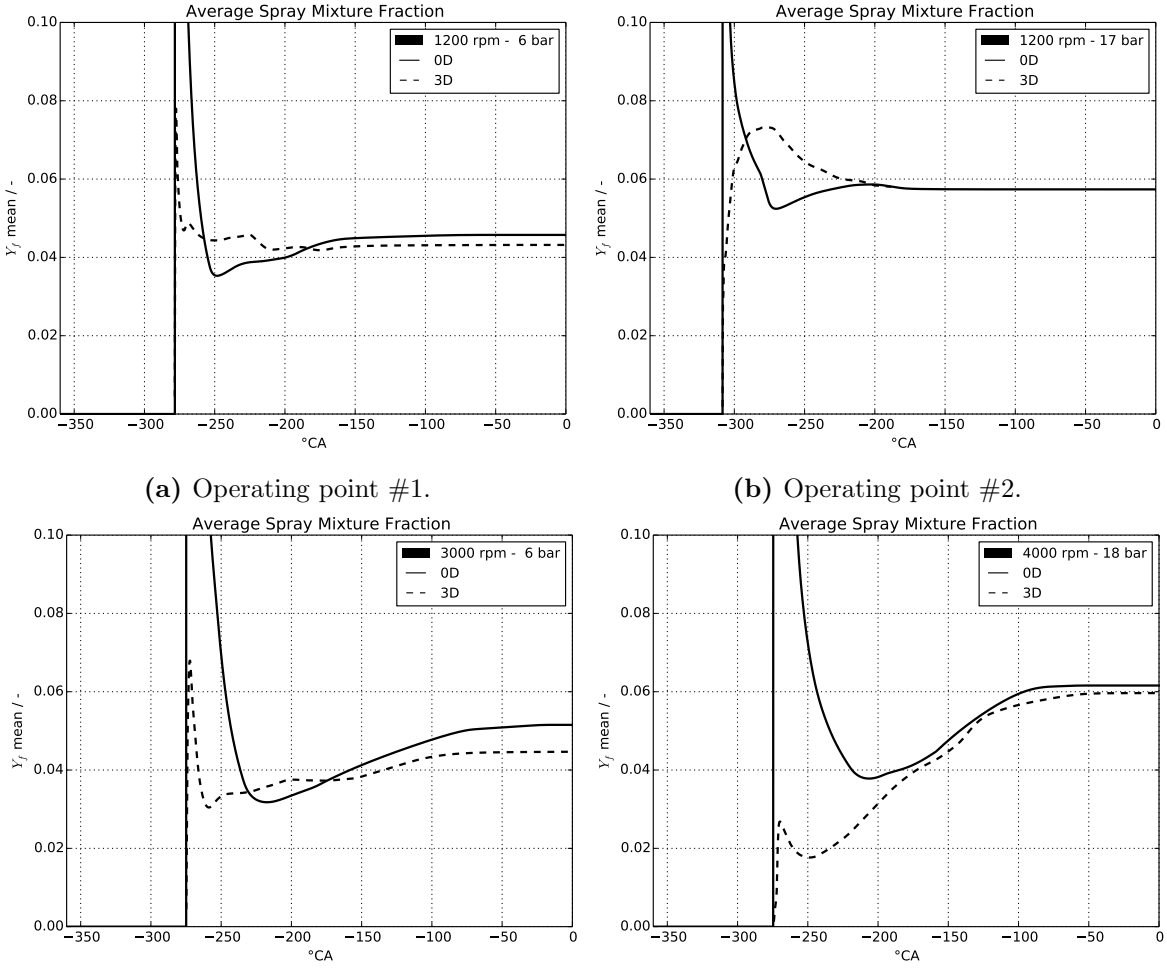

(a) Operating point #1.

(b) Operating point #2.

(c) Operating point #3.

(d) Operating point #4.

Figure 6.13: Mixture formation in the ICAMDAC engine – **average mixture fraction** Y_F: the four panes plot compare 0D (solid lines) and 3D reference data (dashed lines) for each of the operating points in Table 6.2.

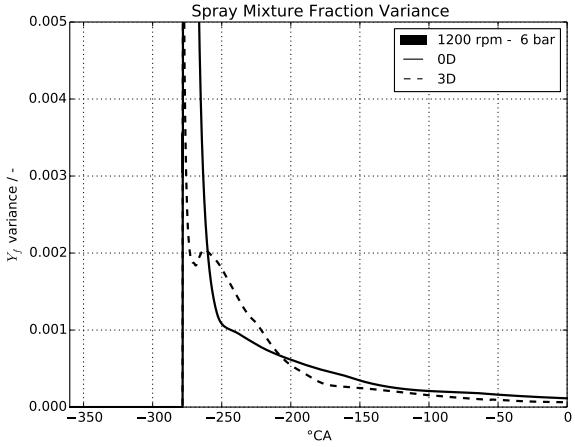

(a) Operating point #1.

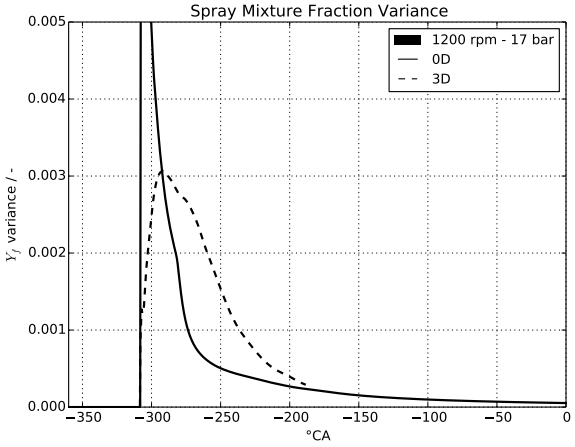

(b) Operating point #2.

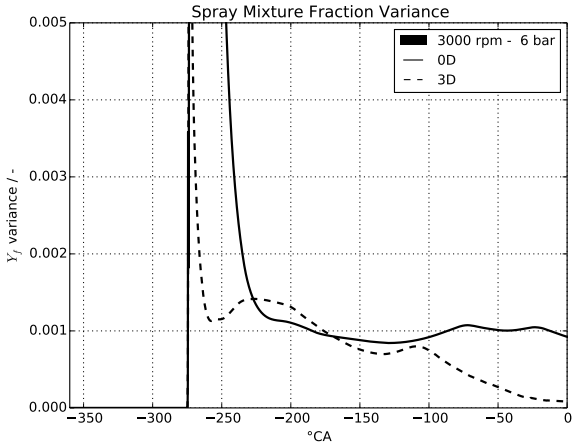

(c) Operating point #3.

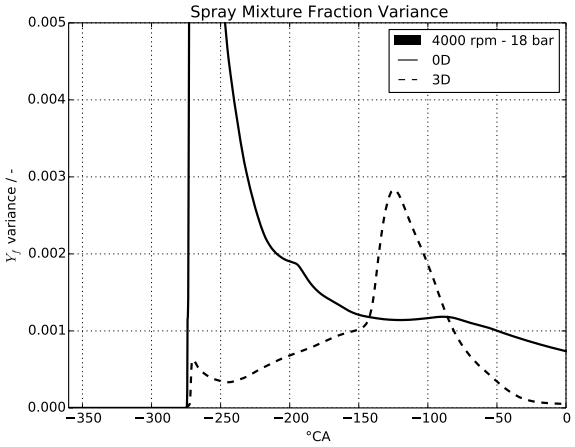

(d) Operating point #4.

Figure 6.14: Mixture formation in the ICAMDAC engine – **mixture fraction Y_F variance**: the four panes plot compare 0D (solid lines) and 3D reference data (dashed lines) for each of the operating points in Table 6.2.

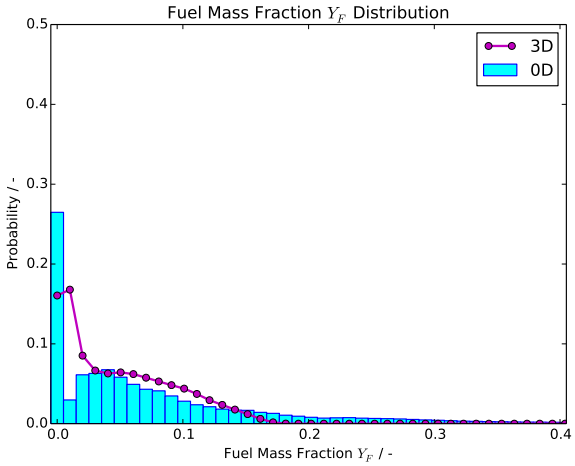

(a) 270 °CA before firing TDC.

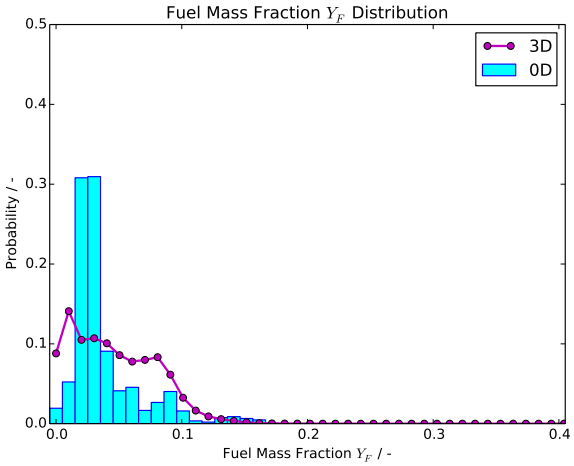

(b) 225 °CA before firing TDC.

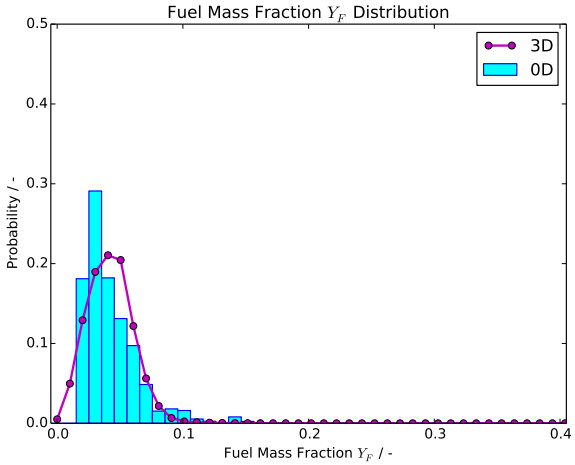

(c) 180 °CA before firing TDC.

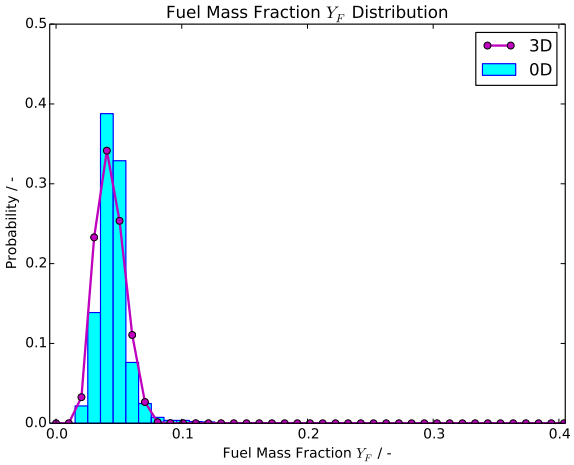

(d) 90 °CA before firing TDC.

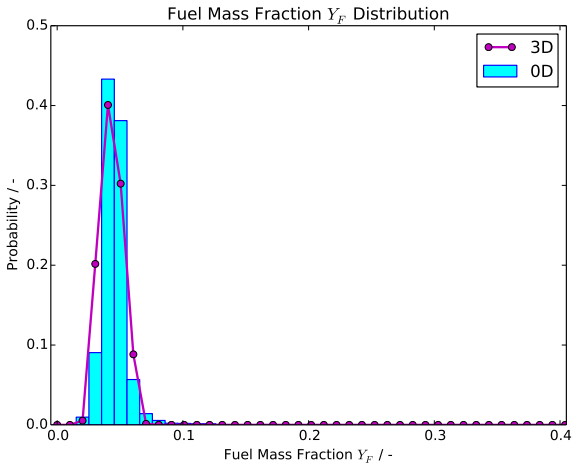

(e) 45 °CA before firing TDC.

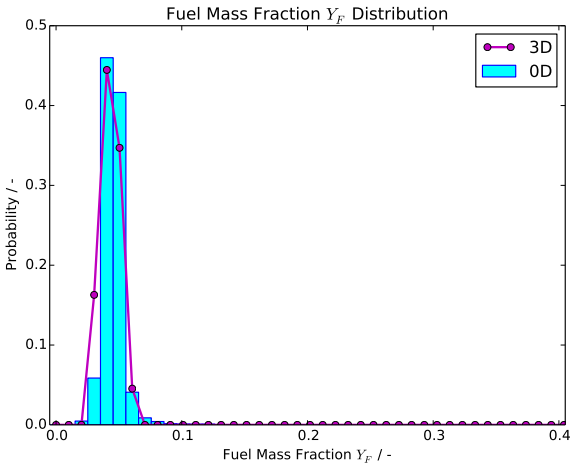

(f) At firing TDC.

Figure 6.15: Mixture formation in the ICAMDAC engine – **fuel mass fraction Y_F distribution**: the six plots compare 0D results (blue bars) to 3D RANS reference data (dashed lines) for each of the #1 operating point in Table 6.2.

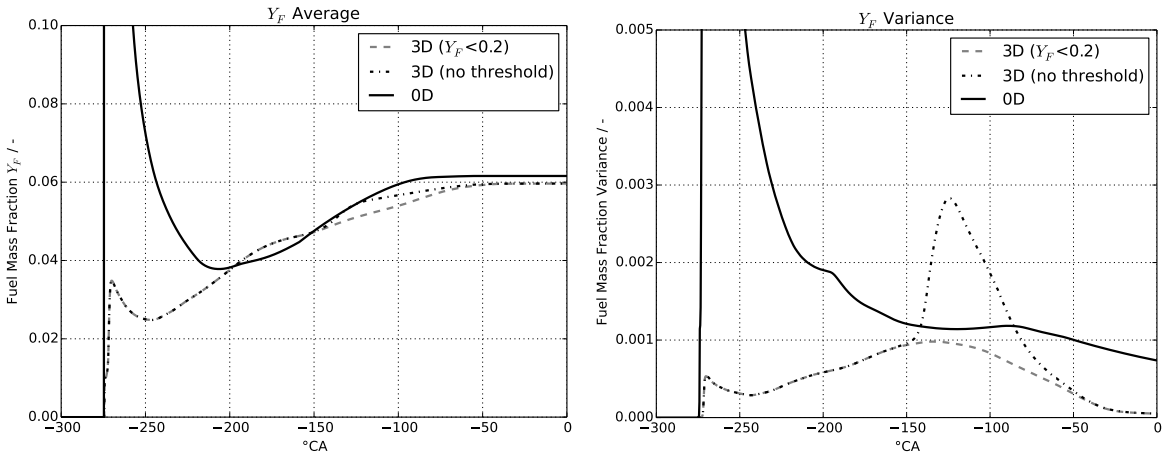

(a) Average mixture fraction $\bar{Y}_F$. **(b)** Mixture fraction variance.

Figure 6.16: ICAMDAC engine: operating point at $N = 4000\,\text{rpm}$ and IMEP $= 18\,\text{bar}$. The two plots show the **average mixture fraction** $\bar{Y}_F$ (a) and its **variance** (b) against the crank angle. Solid line for 0D, black dash dotted line for 3D, grey dashed line for 3D with threshold $Y_F < 0.2$. Cutting off cells with higher fuel concentrations attenuates the variance peak at at 125 °CA before TDC with little effect on the mean value.

(a) 120 °CA before TDC. **(b)** 96 °CA before TDC. **(c)** 76 °CA before TDC.

Figure 6.17: ICAMDAC engine: operating point at $N = 4000\,\text{rpm}$ and IMEP $= 18\,\text{bar}$. The three plots show the computational domain in light blue at different crank angles. The cells with a fuel mass concentration greater than 0.2 ($Y_F > 0.2$) are highlighted in red, suggesting an accumulation of hot drops at the piston/liner interface.

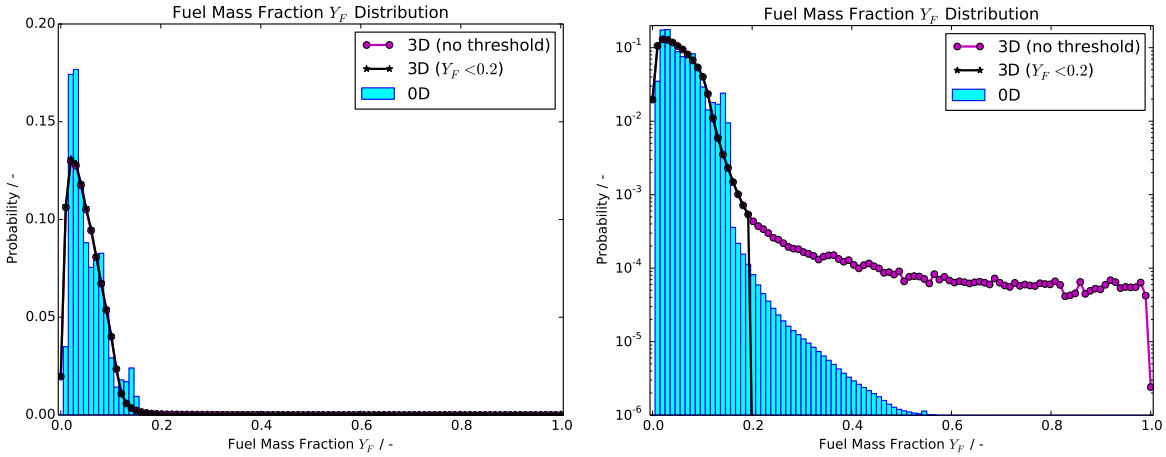

(a) Linear plot. **(b)** Semi-log plot.

Figure 6.18: ICAMDAC engine: operating point at $N = 4000$ rpm and IMEP $= 18$ bar. The two plots show the **mixture fraction Y_F distribution** in linear (a) and log scale (b) at 125 °CA before TDC. Blue bars for 0D, red circles & solid line for 3D, black stars and solid line for 3D with threshold $Y_F < 0.2$ The log plot confirms that the variance peak in Fig 6.16 (a) results from a small amount of mass (probability $< 10^{-4}$ per class) at $Y_F > 0.2$.

distribution (blue stars and solid line) obtained for $0 < Y_F < 0.2$, to complete the analysis The linear scale plot in pane (a) of Fig. 6.18 shows that:

- the two distributions obtained from 3D data are superimposed;
- the 0D model gives a satisfying description of Y_F distribution;
- the visible mass spans the $0 < Y_F < 0.2$ range.

The semi-logarithmic scale plot in pane (b) of Fig. 6.18 shows, on the other hand:

- the original 3D distribution is quasi uniform in the $0.2 < Y_F < 1$ range, with a probability of 10^{-4};
- the 0D distribution decreases exponentially for $Y_F > 0.2$;
- truncating the 3D distribution at $Y_F = 0.2$ amounts to cutting 0.8% of the vapor mass out[4].

This confirms the hypothesis that the variance peak in Fig. 6.16 results from a small mass that, because of the high liquid temperature, evaporates at high Y_F.

[4]Obtained assigning a probability of 10^{-4} to the 80 classes in the $0.2 < Y_F < 1$ interval.

6.3 Combustion and emissions on the whole operating map

This section presents a comparison between the result of the 0D model developed in this PhD work and the experimental characterization of the ICAMDAC monocylinder engine on test bed.

The operating points considered in this study cover the whole engine map realized in the framework of the ICAMDAC project (de Francqueville, 2013): engine response to iso-speed charge variations was tested at 1200, 2000, 3000 and 4000 rpm on engine test bed.

Both tests and simulations are run on an iso-octane fueled engine. Spark advance is set to optimize engine performance (p_{max} at 13 °CA after TDC) at low loads and delayed to limit knock for higher loads. Maximum charge for each speed is defined by limitations on combustion timing ($CA_{50} < 30$ °CA after TDC) and exhaust temperature ($T_{exh} < 850$ °C). Fuel is delivered with a single injection per cycle, starting around 280 °CA before TDC, i.e. midway during the intake stroke.

Engine performance

The following paragraphs discuss the parameters that characterize engine performance.

Heat release. The following plots compare experimental heat release rates to the results obtained with the 0D model. The aim is to determine if the modified combustion model taking into account equivalence ratio heterogeneity can predict flame propagation correctly. Spark timing in 0D simulation is the same as in test bed experiment.

Information on combustion duration and phasing – which are directly related to engine performance – is given in terms of CA_{XX}:

- CA_{10}, i.e. the crank angle when 10% of the charge is burned (Fig. 6.19), identifies the start of combustion and – for a given spark advance – gives an estimation of the ignition lag;
- CA_{50}, i.e. the crank angle when 50% of the charge is burned (Fig. 6.20), expresses combustion phasing;
- CA_{90}, i.e. the crank angle when 90% of the charge is burned, identifies the end of combustion.

Combustion duration (Fig. 6.21) is defined here as the crank angle sweeped while burning from 10% to 90% of the charge:

$$DUR = CA_{90} - CA_{10} \tag{6.1}$$

Comparison between combustion timings (Fig. 6.20) and durations (Fig. 6.21) show an overall matching of the burning rate obtained with and without the spray model.

Slightly longer combustion durations are obtained with the spray model, due to the effect of stratification on flame speed at 4000 rpm, where the mean equivalence ratio (Fig. 6.22) is correctly predicted.

Mean equivalence ratios are shown in Fig. 6.22: values of ϕ at ignition obtained with the homogeneous model and the spray model are compared to the measured equivalence ratio in the exhaust manifold. The engine model with detailed spray description is globally leaner than the homogeneous model. This can be explained by the thermal effect of fuel evaporation on

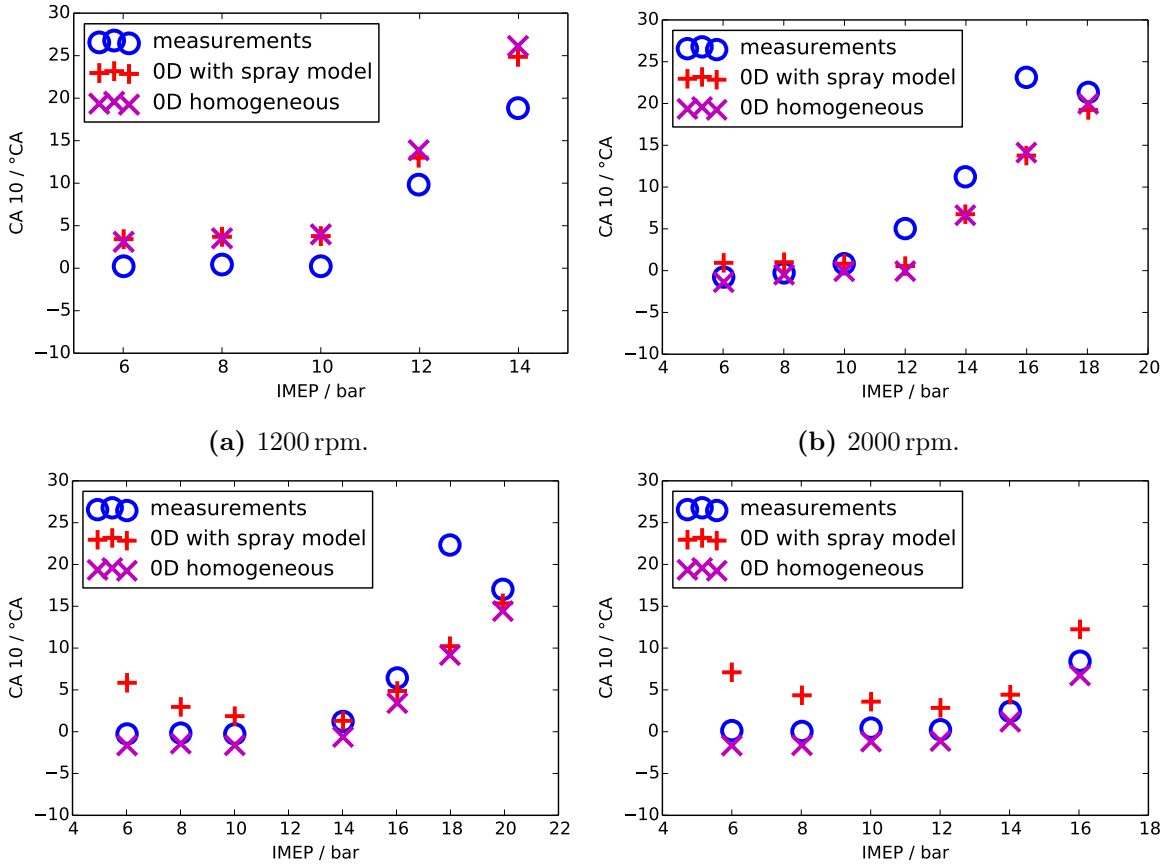

(a) 1200 rpm. **(b)** 2000 rpm.

(c) 3000 rpm. **(d)** 4000 rpm.

Figure 6.19: ICAMDAC engine: **heat release**. The values of CA_{10} are plotted against the nominal IMEP for four different crank speeds. Red "+" for the developed 0D model (with detailed spray description), magenta "X" for the base 0D model (no spray description) and blue "O" for test bed measurements. The operating points shown cover the whole engine map realized in the framework of the ICAMDAC project (de Francqueville, 2013).

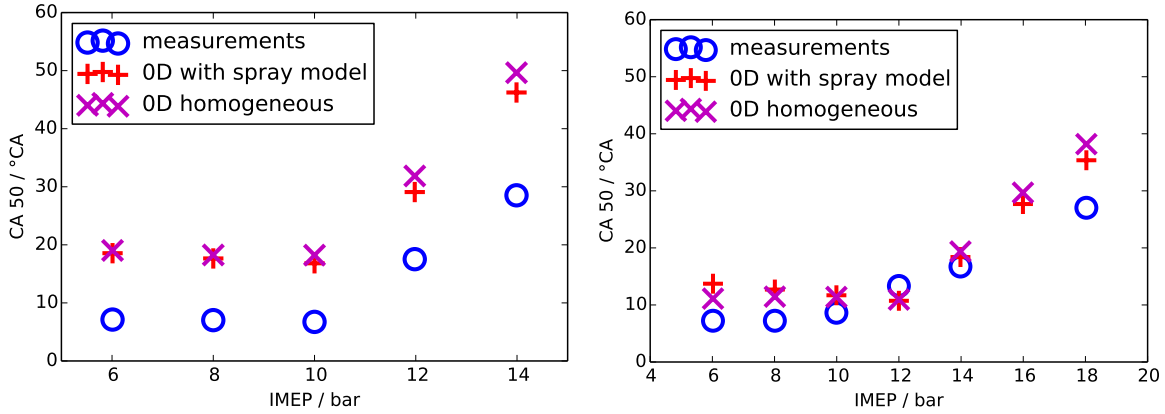

(a) 1200 rpm.

(b) 2000 rpm.

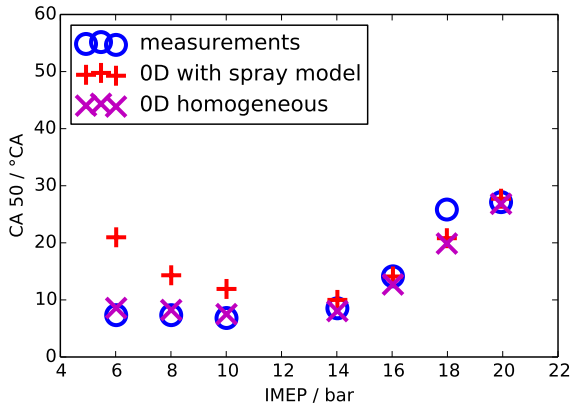

(c) 3000 rpm.

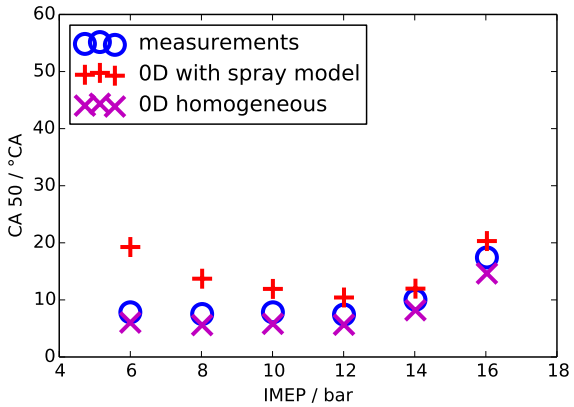

(d) 4000 rpm.

Figure 6.20: ICAMDAC engine: **heat release**. The values of CA_{50} are plotted against the nominal IMEP for four different crank speeds. Red "+" for the developed 0D model (with detailed spray description), magenta "X" for the base 0D model (no spray description) and blue "O" for test bed measurements. The operating points shown cover the whole engine map realized in the framework of the ICAMDAC project (de Francqueville, 2013).

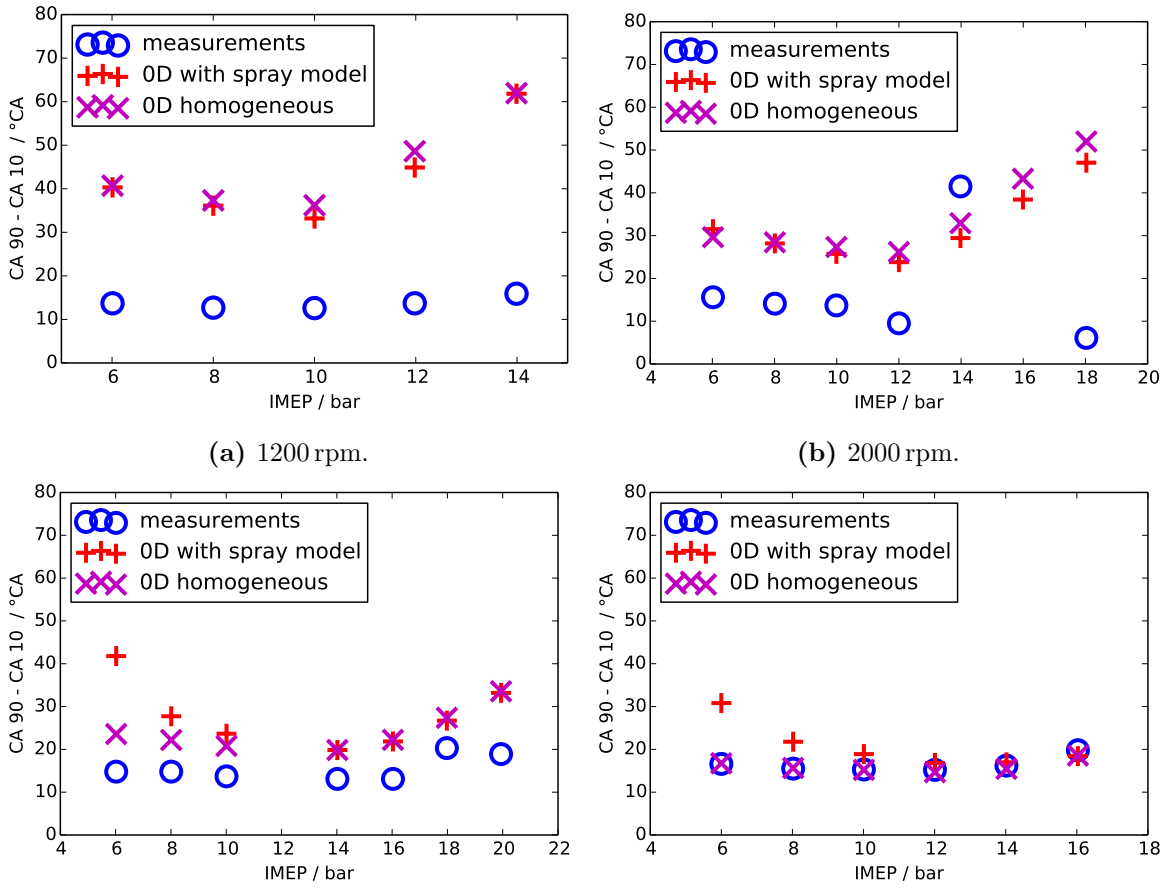

(a) 1200 rpm. **(b)** 2000 rpm.

(c) 3000 rpm. **(d)** 4000 rpm.

Figure 6.21: ICAMDAC engine: **heat release**. The values of combustion duration $CA_{90} - CA_{10}$ are plotted against the nominal IMEP for four different crank speeds. Red "+" for the developed 0D model (with detailed spray description), magenta "X" for the base 0D model (no spray description) and blue "O" for test bed measurements. The operating points shown cover the whole engine map realized in the framework of the ICAMDAC project (de Francqueville, 2013).

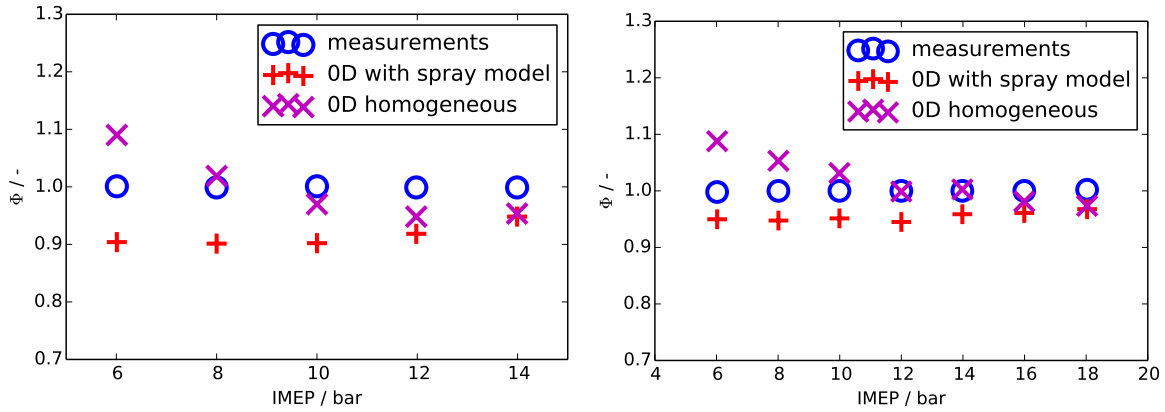

(a) 1200 rpm. **(b)** 2000 rpm.

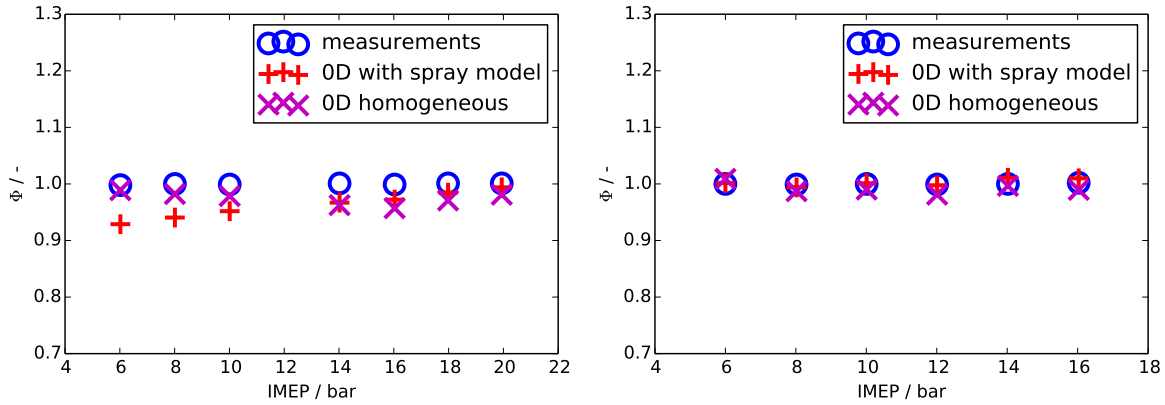

(c) 3000 rpm. **(d)** 4000 rpm.

Figure 6.22: ICAMDAC engine. The values of the **equivalence ratio** are plotted against the nominal IMEP for four different crank speeds. Red "+" for the developed 0D model (with detailed spray description), magenta "X" for the base 0D model (no spray description) and blue "O" for test bed measurements. The operating points shown cover the whole engine map realized in the framework of the ICAMDAC project (de Francqueville, 2013).

air filling: the heat required to evaporate injected fuel, cools down the air reducing its density and increasing the volumetric efficiency. The different volumetric efficiency shown by the two simulations has an impact on the intensities of tumble and turbulence which, combined with the discrepancy in the equivalence ratio, has a strong effect on combustion duration. In particular, the increased aerodynamics caused by the enhanced air flow accelerates flame propagation while the lower equivalence ratio decelerates it.

It is therefore difficult to isolate the flame speed reduction due to stratification in the final data. The high load points at 4000 rpm show a similar air filling (Fig. 6.22 (d)) and are therefore well adapted to underline the different flame propagation speed between the homogeneous and stratified models, *cæteribus paribus*. The values of CA_{50} (Fig. 6.20 (d)) and combustion duration (Fig. 6.21 (d)) show a slightly slower combustion and a longer ignition lag with the new stratified combustion model.

Emissions

Pollutant species concentrations depend on the local thermochemical properties of the reactive mixture, in particular:

nitrogen oxydes (NO and NO_2) formation is promoted by high temperatures and oxygen availability (stoichiometric and lean mixtures);

carbon monoxyde (CO) and unburnt hydrocarbons (HC) formation is mainly related to the lack of oxygen (rich mixtures) and flame extinction.

For globally stoichiometric mixtures, stratification plays an essential role in CO and HC production: increasing the inhomogeneity increases the occurrence of rich mixture pockets that constitute local sources of these compounds. For this reason, it is expected to find higher concentrations of CO and HC in operating points with more pronounced stratification.

Because of the difficulties with the description of the heat release, it was not possible to test the emissions predicted by the post-oxydation models and compare the results obtained with the homogeneous and stratified models. Such a test, required to achieve a thorough validation of the proposed model, is left as a perspective for future works.

The following analysis proposes instead some correlations between the relevant spray characteristics obtained with the 0D model and the pollutant concentrations measured at the engine test bed. The aim is to investigate the potential of the spray model as a tool to predict pollutant formation and guide future developments and studies.

Figures 6.23 – 6.24 correlate the measured concentrations of CO and HC to the mixture fraction variance, $\sigma^2_{Y_F}$, at CA_{10} and to the end of evaporation crank angle, CA^{ev}_{90}, respectively. $\sigma^2_{Y_F}$ and CA^{ev}_{90} are chosen as indicators of mixture heterogeneity and of the presence of liquid during flame propagation, respectively. The two representations of CO and HC concentrations reflect, as expected, the same behavior in both Fig.s 6.23 – 6.24, in particular:

HC concentrations are monotonic in mixture fraction variance ($\sigma^2_{Y_F}$), end of evaporation crank angle (CA^{ev}_{90}) and speed: HC production increases with mixture heterogeneity and decreases with speed;

CO concentrations present a maximum as a function of heterogeneity and speed.

The HC profiles in Fig. 6.23 are easily explained by the assumption that – for a globally stoichiometric mixture – wider mixture fraction distributions present a higher density of rich pockets where the occurence of unburnt hydrocarbons is higher. Likewise, the HC profile in Fig. 6.24 reflects the production of unburnt hydrocarbons due to the presence of liquid during combustion.

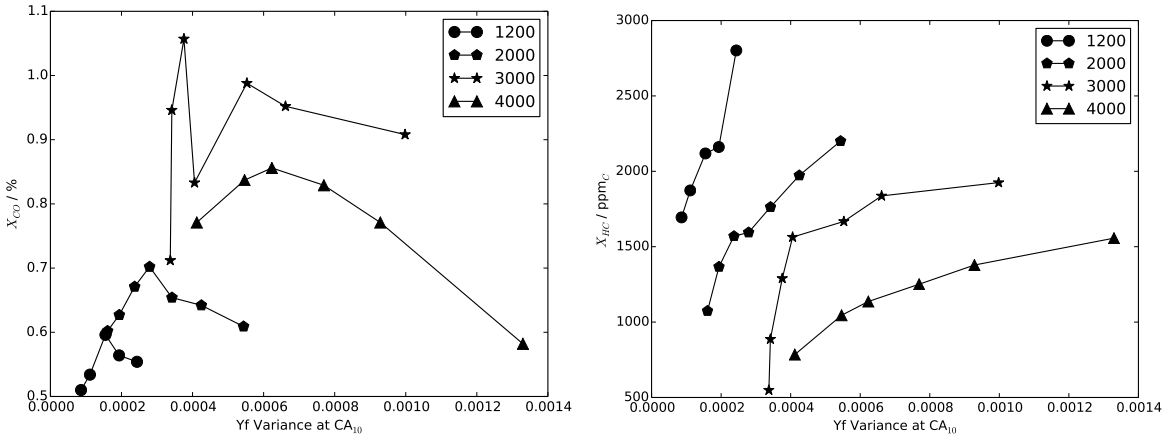

(a) CO **(b)** HC

Figure 6.23: ICAMDAC engine: pollutant emissions. The values of of the measured CO and HC concentrations are plotted against the variance of the mixture fraction, Y_F, at CA_{10}, obtained with the spray model for four different crank speeds. The operating points shown cover the whole engine map realized in the framework of the ICAMDAC project (de Francqueville, 2013).

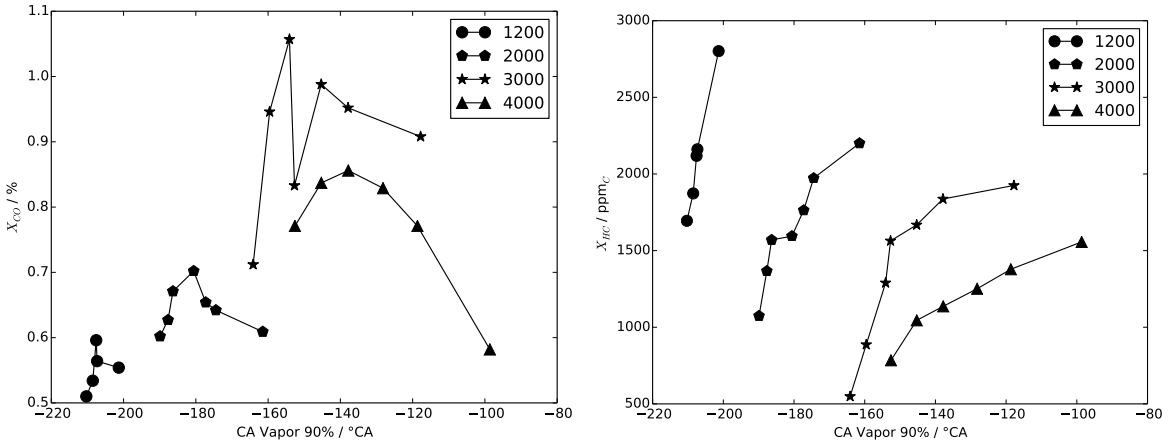

(a) CO **(b)** HC

Figure 6.24: ICAMDAC engine: pollutant emissions. The values of the measured CO and HC concentrations are plotted against the end of evaporation crank angle, CA_{90}^{ev}, obtained with the spray model for four different crank speeds. The operating points shown cover the whole engine map realized in the framework of the ICAMDAC project (de Francqueville, 2013).

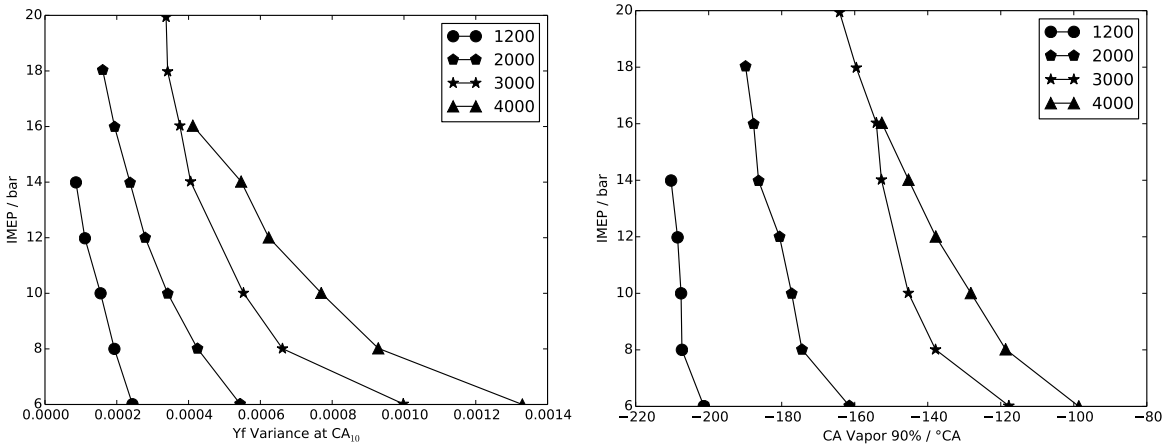

(a) IMEP against $\sigma^2_{Y_F}$. **(b)** IMEP against $\mathrm{CA}^{\mathrm{ev}}_{90}$.

Figure 6.25: ICAMDAC engine: correlation between engine charge and spray statistics. The values of the mesured IMEP are plotted against the computed mixture fraction variance, $\sigma^2_{Y_F}$, and the end of evaporation crank angle, $\mathrm{CA}^{\mathrm{ev}}_{90}$, for four different crank speeds. The operating points shown cover the whole engine map realized in the framework of the ICAMDAC project (de Francqueville, 2013).

The maximum on the CO profiles is, on the other hand, counterintuitive. One possible explanation is the concurrent effect of rich pockets and elevated gas temperature: while the former increase CO production the latter increases its post-oxydation in the burnt gas, thus reducing its concentration in the exhaust gas. Figure 6.25 shows the correlation between measured IMEP and the calculated values of mixture fraction variance, $\sigma^2_{Y_F}$, and end of evaporation crank angle, $\mathrm{CA}^{\mathrm{ev}}_{90}$, showing that charge heterogeneity decreases with charge and, therefore, with burnt gas temperature. This observation allows to couple the two identified effects:

- at low load, CO post-oxydation due to the increasing temperature prevails and a reduction of CO concentration is observed as IMEP increases.
- at high load, CO production due to rich pockets prevails and an increase of CO concentration with IMEP is observed.

6.3.1 Computation time

During this PhD work, a spray model detailing atomization, evaporation, fuel/air mixing and flame propagation in a heterogenous mixture was developed and integrated to an existing SI engine model (CFM1D).

The prevoius sections compare the results obtained with the new model (CFM1D+spray) with those of the reference model (CFM1D) and describe the additional information provided by the the former and unavailable with the latter.

A computational cost is associated to the additional detail level provided by the new model, since:

- new state variables and ordinary differential equations (ODE) increase the number of computations per time step;
- stability issues introduced with the new model might increase time resolution.

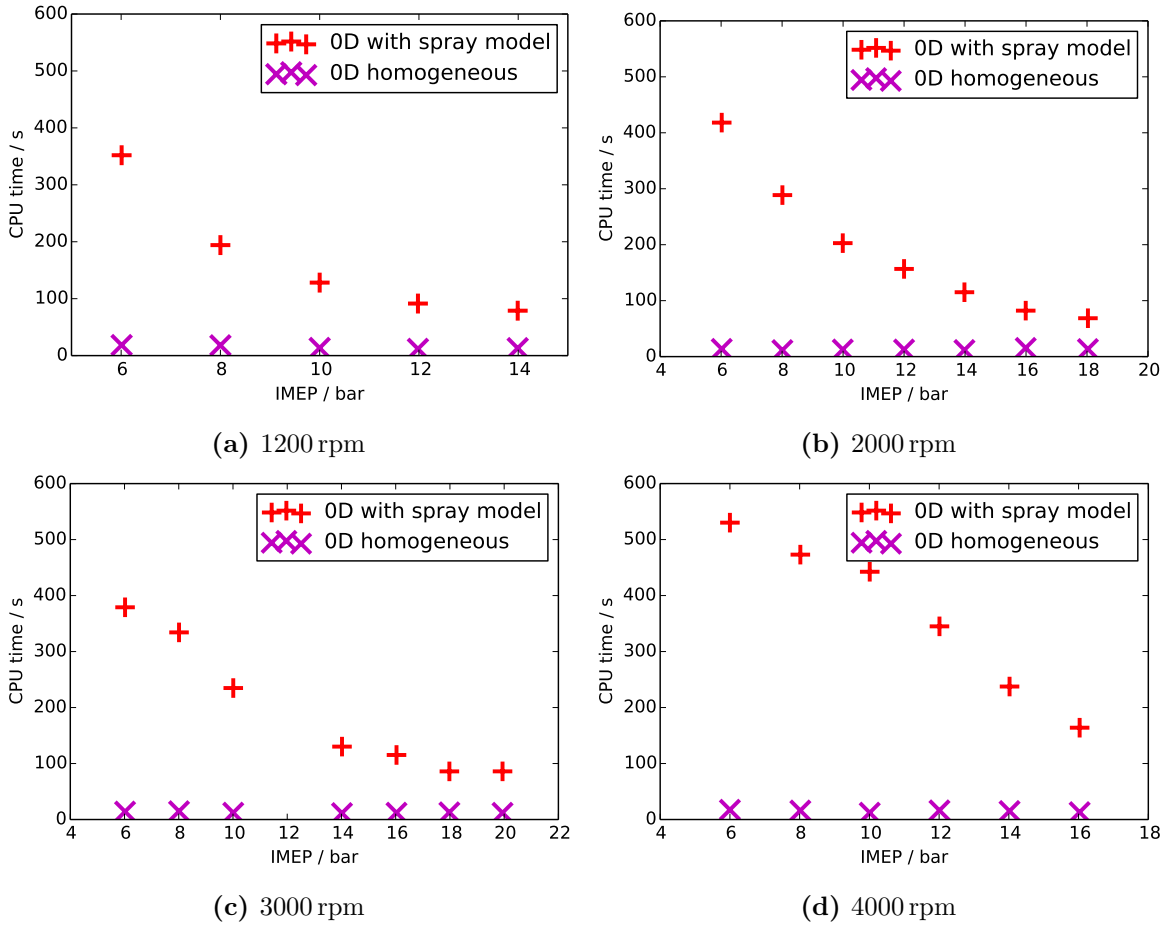

(a) 1200 rpm **(b)** 2000 rpm

(c) 3000 rpm **(d)** 4000 rpm

Figure 6.26: ICAMDAC engine. The values of the **CPU time** per engine cycle are plotted against the nominal IMEP for four different crank speeds. Computation time with the 0D stratified model (red crosses) are compared to those of the base homogeneous 0D model (magenta Xes).

The parcel-based evaporation model and the class-based mixing model, are particularly sensitive to these issues since the number of state variables introduced is proportional to the number of parcels for the former, and to the number of classes for the latter.

A comparison of the computation times per engine cycle with the base homogeneous engine model and with the spray model developed in this work is presented in Fig. 6.26. As expected, the engine model detailing spray dynamics has a sensibly higher computation cost due to the more detailed description of the physic phenomena. In particular:

- the base engine model with homogeneous combustion (CFM1D) runs in $11\,\mathrm{s} - 15\,\mathrm{s}$ per engine cycle;
- the new engine model with detailed spray dynamics and stratified combustion (CFM1D-GDI) runs in $70\,\mathrm{s} - 470\,\mathrm{s}$ per engine cycle, i.e. $5 - 32$ times slower.

CPU time with the spray model has a negative trend against IMEP, which can be explained by the increasing chamber temperatures leading to faster evaporation: the parcel-based evaporation model and the class-based PDF model – whose computational cost is a result of the large number of state variables involved – are therefore run on shorter physical durations.

As summarized in Table 6.4, the computations shown in this chapter are run with 20 drop parcels for the evaporation model and 100 classes for the discrete-PDF mixing model.

Conclusions and Perspectives

The objective of this PhD work is the development and validation of a 0D combustion model of DI-SI engine combustion for system simulation.

Starting from the existing CFM1D model for SI combustion, a new spray model, detailing the main phenomena related to direct injection, was developed.

The liquid phase is discretized in homogeneous drop parcels, each containing drops of the same diameter, temperature, location and velocity. This discretization is achieved dividing the injection profile into equal mass elements, each generating a single drop parcel. An empirical model was used to describe atomization and provide an initial drop size, based on the thermodynamic conditions of the liquid fuel and cylinder gas as well as on the injector geometry and injection rate. The evolution of the liquid phase and the evaporation rate are obtained via an evaporation model, that treats the liquid parcels as separate collection of isolated drops. The level of detail of the evaporation model allows to account for multi-component fuels.

In parallel, a gas zone model describes the air entrainment and large-scale fuel/air mixing based on empirical correlations for the spray penetration and spreading angle. The multi-zone approach allows to describe stratified combustion. The fuel evaporation rate and the air entrainment rate feed a small-scale mixing model that describes the state of the mixture with a discrete fuel mass fraction PDF. The mixing model makes no assumption on the PDF shape and is therefore adapted to describe multiple injections. The model provides information on stratification and partial premixing that can be used in knock prediction.

The spray model was initially tested on a validation case consisting of an injection of iso-octane into a 1.4L, constant volume, chamber with quiescent gas, through a three-hole symmetrical injector. Different experimental thermodynamic conditions, representative of early injections in a homogeneous GDI engine working at high and low load operations, were investigated. Temperature variations from the reference points at constant pressure and at constant density were also investigated. Results obtained with the 0D model were compared with 3D RANS simulations and optical measurements obtained from a previous project.

The same geometry was subsequently used to test the model response to the presence of a tumble vortex, of variable intensity. This validation case is designed to test the response of the spray model to the interaction with tumble, in terms of evaporation, air entrainment and mixing, through the production of turbulent kinetic energy. The results obtained on this test case motivated the introduction of a correction – function of the tumble velocity – that enhances the entrainment rate. This correction allowed to describe the effect that in-cylinder aerodynamics has on large-scale mixing.

The spray model was then used to simulate injections in a variable-volume vessel in order to test its ability to describe the development of a spray within a gas whose thermodynamic conditions vary during the injection. The results obtained in this study brought to the introduction of a correction in the liquid phase model, to take into account the piston velocity

in the computation of the liquid/gas relative velocity: this provides a better description of liquid penetration and evaporation rate.

Finally, a validation of the spray model on a real mono-cylinder engine was carried out. Four operating points were analyzed, comparing the results obtained with the 0D model concerning spray penetration, fuel evaporation and mixing with 3D RANS results. The 0D model was subsequently run on a whole engine operating map. Results in term of combustion duration are compared to those obtained with the original CFM1D model (with no spray description) and to test bed measurements. Some tendencies are outlined between the spray characteristics (liquid mass, evaporation duration, mixing) obtained with the 0D model and the pollutant emissions measured at the engine test bed, in order to show the potential of a detailed description of the GDI spray.

This PhD work opens various perspectives for future works.

- A thorough validation of the combustion model, showing the model ability to predict pollutant emission will point out possible refinements to the coupling of the spray and combustion models.
- The discrete PDF, only applied so far to the fresh gas, could be used to describe the mixing-controlled post-oxidation reactions in the exhaust gas.
- The parcel-based liquid phase model can be used to predict the mass of liquid fuel colliding with the cylinder walls. This information can be used to develop a liquid film model: predicting the liquid fuel mass present in the cylinder during combustion has an interest in connection with soot formation modelling.

Appendix A

SAE Paper 2015-24-2471: Development of a Quasi-Dimensional Spray Evaporation and Mixture Formation Model for Direct-Injection Spark-Ignition Engines

Development of a Quasi-Dimensional Spray Evaporation and Mixture Formation Model for Direct-Injection Spark-Ignition Engines

2015-24-2471
Published 09/06/2015

Federico Pellegrino and Alessio Dulbecco
IFP Energies Nouvelles

Denis Veynante
CNRS & Ecole Centrale Paris

CITATION: Pellegrino, F., Dulbecco, A., and Veynante, D., "Development of a Quasi-Dimensional Spray Evaporation and Mixture Formation Model for Direct-Injection Spark-Ignition Engines," SAE Technical Paper 2015-24-2471, 2015, doi:10.4271/2015-24-2471.

Abstract

This paper presents a phenomenological quasi-dimensional model of the processes that lead to charge preparation in a Direct-Injection Spark-Ignition (DI-SI) engine, focusing on the physics of atomization and drop evaporation, spray development and the mutual interaction between these phenomena. Atomization and drop evaporation are addressed by means of constant-diameter drop parcels, which provide a discrete drop-size distribution. A discrete Probability Density Function (PDF) approach to fuel/air mixing is proposed, based on constant-mixture-fraction classes that interact with each other and with the drop parcels. The model has been developed in the LMS Imagine.Lab Amesim™ system simulation platform for multi-physical modeling and integrated in a generic SI combustion chamber submodel, CFM1D [15], of the IFP-Engine library.

The validation of the approach is performed on an experimental test case consisting of a high pressure isooctane injection in a constant volume vessel for which mie-scattering and high-speed schlieren visualizations for different thermodynamic conditions were performed at IFPEN within the framework of the French government MAGIE R&D project. Liquid and vapor penetration as well as spray angle data from experiments are then used to tune the RANS CFD simulations performed with the IFP-C3D code. CFD provides further data which is not directly available from the experiments such as drop size and charge distributions as well as spray properties outside the optical measurement field, which are then used to tune and validate the 0D model.

Good accordance is found between validation data and the results obtained with the proposed model showing the advantages of a detailed - though phenomenological - description of the main phenomena involved.

Introduction

Major objectives of today's automotive industry are the reduction of pollutant emissions and the increase of the overall efficiency of powertrains, leading to the development of new concepts of Internal Combustion Engines (ICE). The well-known advantages of charge stratification in ultra-lean gasoline [20, 7] engines and engine downsizing [6] suggest that an increase in the diffusion of DI-SI architectures is foreseeable in the near future.

Gasoline Direct Injection (GDI) consists of injecting the liquid fuel directly in the combustion chamber. Injection timing varies depending on engine operation strategy:

- in homogeneous charge engines, injection takes place during the intake stroke or at the beginning of compression, so that the fuel has enough time to mix;
- in stratified charge engines, fuel is injected during the end of the compression stroke, so that the reactive mixture is confined in a portion of the chamber: shape of the piston, tumble and swirl flows all help containing the charge.

GDI offers many advantages with respect to traditional homogeneous charge SI engines. In particular in highly stratified DI-SI engines, the fact that the charge is confined in a portion of the combustion chamber leads to

- moderately rich mixtures near the spark plug, reducing the risk of misfiring and producing higher flame speeds;
- lean mixtures far from the spark plug which lowers the risk of knock, thus allowing higher compression ratios;
- decreased pumping losses since power regulation can be achieved acting on the injected fuel mass instead of throttling the intake air flow;
- less thermal losses since an air layer separates the flame from cylinder walls.

The advantages of stratified DI-SI have caused the spread of this technology on the automotive market during the last two decades with introduction of stratified charge engine concepts by major constructors.

Another significant trend in recent research on SI engines is the introduction of the downsizing technology, consisting in the reduction of the engine combustion chamber volume conserving the engine output power. This is achieved with the assistance of a turbocharger or supercharger that increases the mass of air in the cylinder thus allowing to burn more fuel.

Downsizing allows the engine to run at higher Indicated Mean Effective Pressures (IMEP) with an increase of the global efficiency. Adopting DI in downsized engines allows to:

- benefit from the latent heat of vaporization of the injected fuel to cool fresh gases and increase the volumetric efficiency of the engine;
- reduce the residence time of the reactive mixture at high temperature and pressure before ignition. The consequent benefit on the knock limit allows to achieve higher compression ratios.

Furthermore, thanks to the flexibility on fuel injection timing, Variable Valve Timing (VVT) or Variable Valve Actuation (VVA) systems can be integrated into the engine architecture, this allowing to adopt new control strategies. As an example, by delaying the Exhaust Valve Closing (EVC) timing it is possible to prolong the valve overlap interval, thus producing a better scavenging of the combustion chamber; this leads, moreover, to an internal cooling of the combustion chamber with, once more, benefits on knock limit [17].

DI-SI systems challenge simulation with the description of new phenomena with respect to traditional spark-ignition engines. Injecting liquid fuel in the combustion chamber introduces the necessity to manage physics related to atomization process, fuel evaporation and reactive mixture formation: this for properly estimating the engine performance in terms of pollutant emissions and specific fuel consumption, but also for identify the frontiers of the multi-dimensional calibration domain to not cross for avoiding the appearance of unwanted phenomena such as cylinder wall or piston wetting or incomplete evaporation during flame propagation, since both cause soot production.

A crucial point is the description of fuel/air mixture stratification, which conditions important aspects of the combustion process such as the turbulence/flame interaction with an additional source of flame front wrinkling provided by the non-homogeneity of the laminar flame speed in the mixture [14, 8, 9], the pollutant formation kinetics which is highly dependent on local thermochemical state of the mixture [19], as well as the appearance of abnormal combustions such as knock or super knock which, once again, strongly depend on mixture heterogeneities [3]. Furthermore the spray/wall interaction has interesting future perspectives with respect to soot emission modeling, which is one of the major challenges.

System Simulation for ICEs

ICEs are very complex systems including a large number of components and their operation involves many branches of physics. System simulation is a powerful tool to reproduce the behavior of the powertrain as a whole, since it allows to investigate the interactions between the different components in both stable and transient conditions. It can serve different purposes in the automotive industry, such as:

- testing for different possible architectures to optimize the choice of components;
- development, testing and optimization of control strategies;
- evaluation of the effects of engine calibration on combustion performance.

The evolution of experimental techniques together with the progress of CFD modeling in the last decades improved the knowledge and understanding of the physical phenomena taking place in combustion chambers as well as in other components. All this provides the expertise necessary to the development and validation of physical phenomenological models of components for system simulation, This modeling approach, because of its increasing capability to get accurate numerical prediction of the real system, is increasingly replacing test bench in most applications due to the short time needed to run a simulation and the reduced cost to perform tests of exploitation.

The objective of this work is to develop a spray model for system simulation applications, to address the injection-related issues in DI-SI engines that lead to the preparation of the charge for combustion.

Literature Review

This section provides a brief review of the 0D models of direct-injection ICEs discussed in literature. Since direct injection for spark-ignition is a relatively new concept - at least from the point of view of numerical simulation - all the available literature discussing spray-related issues mainly covers Diesel direct injection.

The 0D phenomenological combustion model for common rail Diesel engines presented by [2] uses the empirical correlation proposed by [18] for atomization that provides an initial drop diameter for the whole spray. Fuel evaporation is accounted for via a steady-state D^2 model, where the evaporation constant τ_{ev} is used as a calibration parameter.

The Universal Diesel Engine Simulator (UniDES) proposed by [10] uses the Hiroyasu model equations for the spray penetration and cone angle to predict the air entrainment in the spray. Droplet evaporation is reproduced with the Spalding D^2 model and the initial drop size is provided with Kawamura's equation. Fuel/air mixing is described with a simplified PDF model based on the interaction of fixed-equivalence ratio classes.

The 0D combustion model developed at IFPEN [4, 12] for Diesel engines uses Naber's model for spray penetration [13] and air entrainment. The calculation of the evaporation rate is based on the concept of liquid length [16] which does not require an atomization model. Mixture evolution is described providing model equation for the mean and variance of a β-PDF function [4].

Model Description

The proposed spray model has been developed on the LMS Imagine. Lab Amesim™ multi-physics platform for system simulation. The model is articulated in five main blocks that exchange information as summarized in Fig. 1.

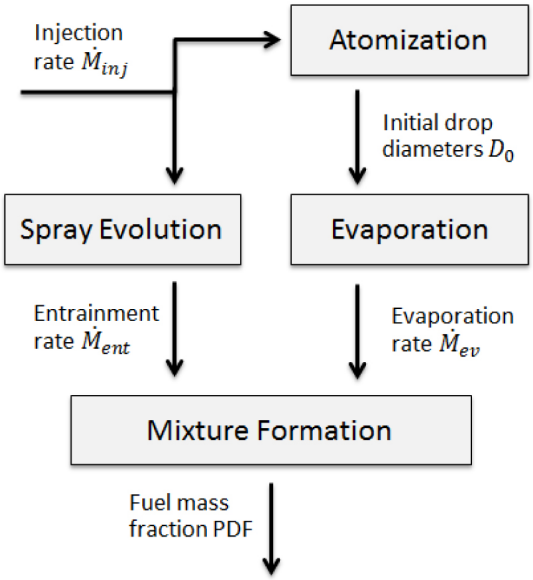

Figure 1. Overview of the spray model.

It accounts for the relevant physical phenomena related to DI engines architectures, from injection to reactive charge formation.

Liquid Fuel Mass Injection

To account for the variability of the injector rate profile and the different ambient gas conditions that can be encountered during injection, it is important to have a detailed description of the drop size distribution within the combustion chamber, since the latter affects the evaporation rate the liquid penetration and soot pollutant emissions.

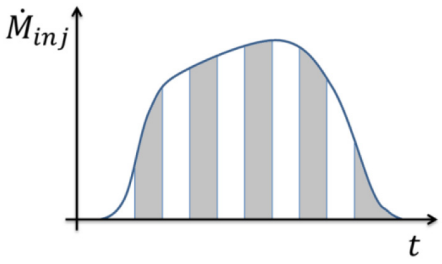

Figure 2. Discretization of the injected mass.

Accordingly, the evaporation model proposed here is obtained dividing the injected liquid phase into parcels of drops, Fig. 2. Each parcel is characterized by a mean representative drop and is fully described by the following quantities:

- mass;
- momentum;
- and temperature.

Each of these variables is transported by balance equations providing evaporation rate, drag force and heat flux, according to Eq. (6), Eq. (4) and Eq. (7), respectively.

Atomization

A drop-size distribution can be represented by the Sauter Mean Diameter, defined as

$$\mathrm{SMD} = \frac{\sum D_i^{\,3}}{\sum D_i^{\,2}} \tag{1}$$

where the sum spans all the fuel drops and D_i is the diameter of the i-th drop. The empirical correlation proposed by Varde [18]

$$\frac{SMD}{D_{noz}} = K_{SMD}\left(Re_l\, We_g\right) \tag{2}$$

where D_{noz} is the nozzle diameter - was retained here to provide the initial drop diameters for the parcel-based fuel drop distribution of the evaporation model, with the addiction of the calibration parameter K_{SMD}.

One of the advantages of Eq. (2) is that the influence of the injection system is expressed in terms of injection velocity, u_{inj} - which appears in the following expression for Re_l and We_g instead of pressure drop through the nozzle orifice:

$$Re_l = \frac{u_{inj}\, D_{noz}}{\nu_l} \qquad We_g = \frac{\rho_g\, u_{inj}^{\,2}\, D_{noz}}{\sigma_l} \tag{3}$$

ν_l and σ_l being, respectively, the liquid fuel viscosity and surface tension. This circumstance suits the purpose best since combustion chamber models in the IFP-Engine library take the injected mass flow rate as an input, the injectors being modeled in separate blocks.

Moreover, the use of this brake up model allows to capture the influence of

- injection pressure;
- injection temperature;
- injected fuel properties;
- and injector hole geometry.

As an example, Fig. 3 shows the influence of the mass flow rate on the SMD.

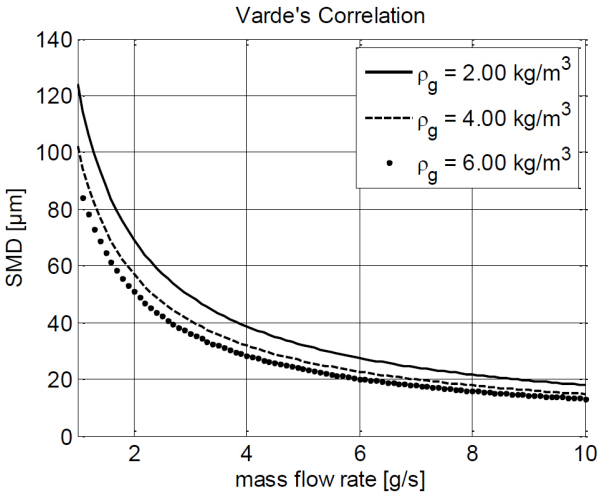

Figure 3. Varde's correlation: Sauter mean diameter against the injection rate, for different gas densities. Fuel is isooctane (σ_l = 18.77 10^{-3} N/m and ν_l = 5.0 10^{-6} m^2/s), D_{noz} = 200µm.

The applicability of Eq. (2) is, however, limited to plain orifice atomizers and does the approach is not sensitive to detailed injector geometry features such as the aspect ratio of the injector nozzle. Accordingly, a change in the aspect ratio of the injector nozzle would require an adjustment of the calibration parameter of the model.

Evaporation

The dynamics of liquid drops are here described under the assumption that the surrounding gas is at rest. The relative velocity generating the drag force is therefore related the injected drop velocity only. This is true when describing injections taking place in a constant-volume high-temperature high-pressure vessel, which is the case here. For engine configurations a representative velocity of the gas phase will have to be taken into account to correctly estimate the relative velocity of the two phases. If the effects of gravity are neglected, variations of momentum, $\dot{\mathcal{P}}$, are solely due to the drag force of the surrounding gas; the second law of dynamics is then

$$\dot{\mathcal{P}} = -\frac{1}{2} C_D \rho_g S {u_d}^2 \tag{4}$$

where ρ_g is the gas density and the surface S is the projection of the liquid body in the direction of the flow which - for a spherical drop having a diameter equal to D - is a circle $S = \pi D^2/4$, u_d is the drop velocity, and the drag coefficient C_D is given by the expression

$$C_D = \frac{24}{Re_g}\left(1 + \frac{{Re_g}^2}{6}\right) \tag{5}$$

which satisfies the viscous limit $24/Re_g$ when $Re_g \rightarrow 0$. The Reynolds number is calculated with the gas viscosity, drop diameter and relative velocity between the two phases.

Evaporation rate, $\dot{\mathcal{M}}_d$, and heat flux towards the liquid phase, $\dot{\mathcal{H}}_d$, are described by Eq. (6) and Eq. (7) following the approach proposed in [1]

$$\dot{\mathcal{M}}_d = -\pi D \frac{\lambda_g}{c_{p\,g}} Sh \log(1 + B_M) \tag{6}$$

$$\dot{\mathcal{H}}_d = -\dot{\mathcal{M}}_d \left[\frac{c_{p\,l}(T_\infty - T_d)}{B_T} - H_L\right] \tag{7}$$

where the following terms appear:

the drop diameter D

the chamber gas thermal conductivity λ_g

the chamber gas constant-pressure specific heat $c_{p\,g}$

the Sherwood Number Sh, defined as the ratio of the convective mass fraction coefficient to the diffusive mass fraction coefficient;

the Spalding mass transfer number B_M, calculated from the saturation and far field values ($Y_F{}^s$ and $Y_F{}^\infty$) of the fuel mass fraction:

$$B_M = \frac{Y_F{}^s - Y_F{}^\infty}{1 - Y_F{}^s} \tag{8}$$

The temperature field in the liquid drop is assumed to be uniform, variations between the surface and the core of the drop are not taken into account. Figure 4 shows the results obtained for an isolated drop evaporating in air at different velocities.

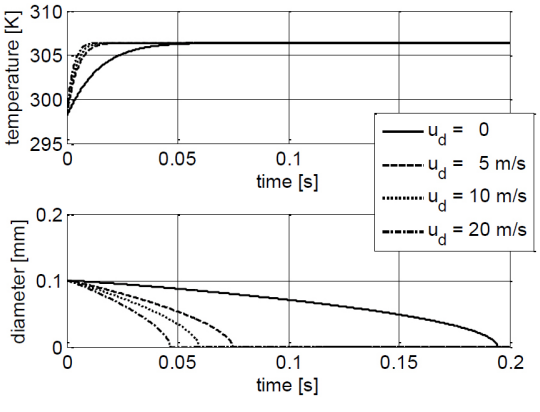

Figure 4. Evolution of the diameter and temperature of an evaporating drop subject to forced convection, for different velocities. Evaporating fuel is isooctane, surrounding gas is air at 2 bar and 100 °C. Drop velocity u_d is held constant.

Spray Penetration and Air Entrainment

The spray region is modeled as a cone that evolves freely into the combustion chamber, incorporating air as it penetrates.

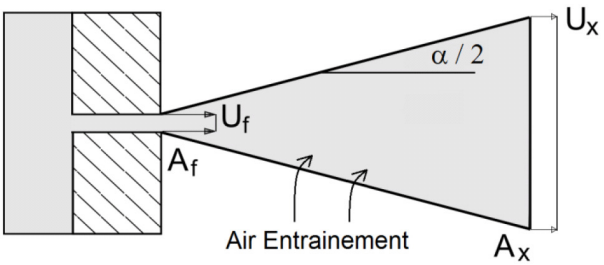

Figure 5. Penetration and entrainment model.

Spray tip penetration is calculated with the relation based on momentum conservation provided by Naber [13]. The normalized penetration length, $\tilde{x} = x/x^+$, is calculated as a function of the non-dimensional time, $\tilde{t} = t/t^+$,

$$\tilde{x} = \mathcal{K}_x \left[\frac{1}{(\tilde{t})^n} + \frac{1}{(\tilde{t})^{n/2}}\right]^{-1/n} \quad (9)$$

The two quantities being normalized with respect to

$$x^+ = \frac{D_f\sqrt{\rho_l/\rho_g}}{tan\left(\frac{\alpha}{2}\right)} \quad (10)$$

and

$$t^+ = \frac{x^+}{u_{inj}} \quad (11)$$

with α the spreading angle of the model spray, given by

$$tan\,{}^{\alpha}/_{2} = \mathcal{K}_\alpha \left[\left(\frac{\rho_g}{\rho_f}\right)^{0,19} - 0{,}0043\left(\frac{\rho_f}{\rho_g}\right)^{0,5}\right] \quad (12)$$

u_{inj} the injection velocity and $D_f = \sqrt{\mathcal{K}_D}\, D_{noz}$ the diameter of the nozzle flow; $\mathcal{K}_x$ $\mathcal{K}_\alpha$ and $\mathcal{K}_D$ are calibration parameters.

The air entrainment rate is then calculated from the spray volume variation, $\dot{V}$, as

$$\dot{\mathcal{M}}_{entr} = \rho_{ga}\,\dot{V} \quad (13)$$

where ρ_{ga} is the density of the chamber gas outside the spray region.

Mixture Formation

A mixing model based on a discrete Probability Density Function (PDF) has been chosen to account for fuel mass fraction non-homogeneities within the spray. The model is based on the approach outlined by [10] for Diesel simulations.

Non-homogeneities in the in-cylinder fuel mass fraction, Y_F, range -theoretically - in the $0 \le Y_F \le 1$interval, the two limit conditions correspond to pure air and pure fuel vapor. In the adopted modeling approach, the domain of variability of Y_F is discretised in N values

$${Y_F}^i = \frac{i-1}{N-1} \quad \text{with} \quad i = 1, \dots, N \quad (14)$$

The air and fuel vapor masses contained in the spray region are organized into classes and each class, characterized by its mean ${Y_F}^i$, contributes to filling PDF.

Focusing on the PDF classes, the N values of ${Y_F}^i$ do not change with time and are only calculated once at the beginning of the simulation when the model is initialized. On the other hand, the relative importance of each class on the global PDF depends on the mass, $\mathcal{M}_i$, it contains. Each class i is also characterized by a momentum, $\mathcal{P}_i$, and velocity, u_i, that evolve according to governing equations.

Boundary conditions for mass and momentum evolution are provided as follows. The saturation mixture fraction $Y_{F\,s}$ is attributed to the evaporating mass $\dot{\mathcal{M}}_{ev}$ coming from a given evaporating liquid fuel mass parcel: the corresponding mass of air

$${\dot{\mathcal{M}}_{ev}}^{air} = \frac{(1 - Y_{F\,s})}{Y_{F\,s}}\,\dot{\mathcal{M}}_{ev} \quad (15)$$

is subtracted from the entrained mass flow $\dot{\mathcal{M}}_{entr}$. A mass flow of $\dot{\mathcal{M}}_{ev}/Y_{F\,s}$ (which includes air and fuel vapor) is attributed to the couple of classes corresponding to $Y_{F\,s}$, as indicated in the following for $Y_{F\,new}$. The entrained mass flow $\dot{\mathcal{M}}_{entr}$, decreased of ${\dot{\mathcal{M}}_{ev}}^{air}$ feeds the first class with $Y_{F1} = 0$, corresponding to pure air. The two values $\dot{\mathcal{M}}_{ev}$ and $\dot{\mathcal{M}}_{entr}$ are provided by evaporation and entrainment submodels.

Boundary conditions on momentum are provided likewise. Entrained air is supposed to be at rest before entrainment while evaporated fuel enters the mechanism at injection velocity

$$\dot{\mathcal{P}}_{ev} = u_{inj}\,\dot{\mathcal{M}}_{ev} \quad (16)$$

$$\dot{\mathcal{P}}_{entr} = 0 \quad (17)$$

Moreover, according to [10] an additional variable characterizing the class can be defined: the fictive radius R_i, expressed by

$$R_i = \left(\frac{3\,\mathcal{M}_i}{4\pi\,\rho_i}\right)^{1/3} \quad (18)$$

with ρ_i the density of the i-th class, is useful to express the mixing law between classes. Fuel vapor and air densities are evaluated for a perfect gas at cylinder pressure

$$\rho_F = \frac{p_{cyl}\, M_F}{R\, T_f} \qquad \rho_A = \frac{p_{cyl}\, M_A}{R\, T_{cyl}} \tag{19}$$

where T_F is the temperature of the evaporating fuel, T_{cyl} is the average temperature of the cylinder, M_A and M_F are the molar masses of air and fuel and R the universal gas constant. The densities of the two boundary classes are combined with a mass-weighted average

$$\rho_i = \left(\frac{Y_F{}^i}{\rho_F} + \frac{1 - Y_F{}^i}{\rho_A} \right)^{-1} \tag{20}$$

and generate the values for all the intermediate classes. The two boundary classes are fed by the gas mass flows entering the spray: the evaporating fuel and the entrained air feed the concerned PDF classes as specified above. A mechanism of interaction between the classes describes the mixing process as a continuous mass transfer from the two boundaries towards the equilibrium Y_F through the intermediate classes of the PDF.

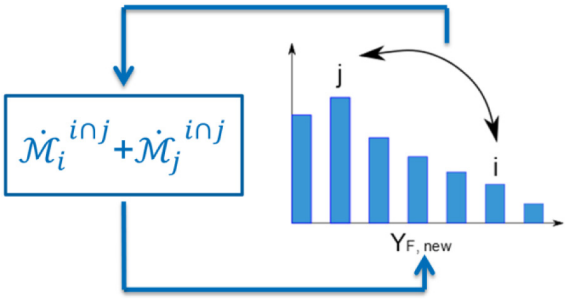

Figure 6. Fuel mass fraction discrete PDF approach: mixing model.

The classes are represented as spheres that penetrate one another and lose part of their mass that feeds a third class of intermediate Y_F:

- the interference of the two spheres representing the i-th and j-th classes generates a volume, $V_{Sweep}{}^{i\cap j}$, where mass belonging to the two original classes is enclosed;
- the enclosed mass flow rates, $\dot{\mathcal{M}}_i^{\,i\cap j}$ and $\dot{\mathcal{M}}_j^{\,i\cap j}$, mix generating a blend characterized by the mass fraction $Y_{F\,new}{}^{i\cap j}$, computed as

$$Y_{F\,new}{}^{i\cap j} = \dot{\mathcal{M}}_i^{\,i\cap j}\, Y_i + \dot{\mathcal{M}}_j^{\,i\cap j}\, Y_j \tag{21}$$

- the mass flow rate $\dot{\mathcal{M}}_i^{\,i\cap j} + \dot{\mathcal{M}}_j^{\,i\cap j}$ is transferred to the class corresponding to the calculated $Y_{F\,new}{}^{i\cap j}$.

In each time-step, the model cycles on all the possible interactions between non-empty classes, for each couple i and j (i denotes the smaller of the two):

- a sweep volumetric flow (L^3T^{-1}) is calculated as

$$\frac{d}{dt} V_{Sweep}{}^{i\cap j} = \pi\, \mathrm{R}_i{}^2 \left| u_i - u_j \right| \tag{22}$$

where the class velocities are evaluated via mass and momentum by $u_i = \mathcal{M}_i / \mathcal{P}_i$. This represents the interference volume over an infinitesimal time step, which is a cylinder having the same diameter as the smaller sphere and whose height grows with the relative velocity between the two entities.

- The mass flows leaving the two mixing classes are then calculated by

$$\dot{\mathcal{M}}_i^{\,i\cap j} = \mathcal{K}_{PDF}\ \rho_i\ \frac{d}{dt} V_{Sweep}{}^{i\cap j}\ \frac{\mathrm{R}_i{}^2 \mathrm{R}_j{}^4}{V_{tot}{}^2} \tag{23}$$

$$\dot{\mathcal{M}}_j^{\,i\cap j} = \mathcal{K}_{PDF}\ \rho_j\ \frac{d}{dt} V_{Sweep}{}^{i\cap j}\ \frac{\mathrm{R}_i{}^2 \mathrm{R}_j{}^4}{V_{tot}{}^2} \tag{24}$$

where $\mathcal{K}_{PDF}$ is a calibration parameter allowing to act on the portion of interference mass that actually mixes, which is directly correlated to the statistical mixing velocity.

- Momentum is transported with the mass from the two origin classes to the destination according to the following relations

$$\dot{\mathcal{P}}_i^{\,i\cap j} = \frac{\mathcal{P}_i}{\mathcal{M}_i} \dot{\mathcal{M}}_i^{\,i\cap j} \tag{25}$$

$$\dot{\mathcal{P}}_j^{\,i\cap j} = \frac{\mathcal{P}_j}{\mathcal{M}_j} \dot{\mathcal{M}}_j^{\,i\cap j} \tag{26}$$

- These two mass and momentum flows are joined and mixed into a new one whose mass fraction is $Y_{F\,new}{}^{i\cap j}$, calculated according to Eq. (21);
- two classes k and k+1 belonging to the PDF are identified, so that $Y_{F\,k} \le Y_{F\,new}{}^{i\cap j} \le Y_{F\,k+1}$.
- finally the flow is split proportionally to $Y_{F\,k+1} - Y_{F\,new}{}^{i\cap j}$ and $Y_{F\,new}{}^{i\cap j} - Y_{F\,k}$ and added to the two classes, k and k+1 respectively, so that total mass and momentum are conserved.

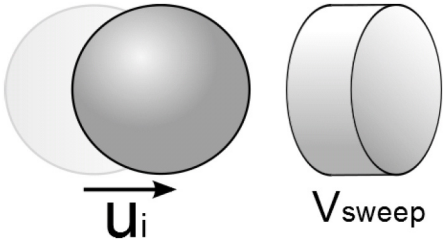

Figure 7. Fuel mass fraction discrete PDF approach: Interpretation of the sweep volume.

Fig. 8 shows a qualitative evolution of the fuel mass fraction PDF in time, from the initial conditions towards the equilibrium of the reactive charge, in an ideal case where time is enough to achieve homogeneous conditions.

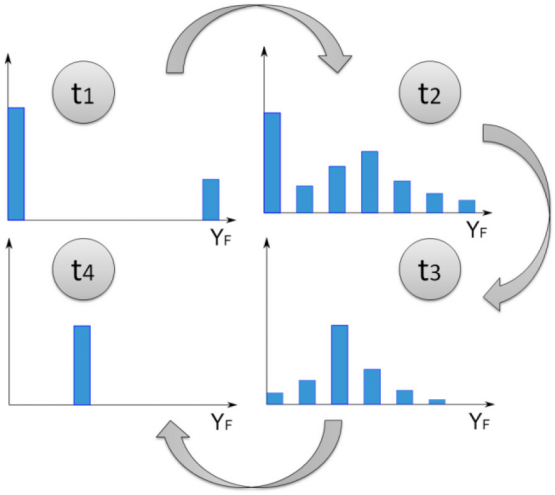

Figure 8. Fuel mass fraction discrete PDF approach: qualitative representation of a time evolution.

Model Validation

Validations of the spray model presented in this work were performed on a test case, by comparing the results provided by the 0D model to experimental data and 3D RANS simulations.

The test case consists of an injection of isooctane into a constant volume chamber through a three hole symmetrical injector. Different thermodynamic conditions representative, of early injection strategy in a homogeneous charge DI-SI engine running at high and low load operation were investigated.

Accordingly, a system simulation test bench was built in Amesim in order to simulate the experiment. The new DI-SI engine combustion chamber component, in which the developments concerning the spray are integrated, was adapted for being representative of the vessel injection case. For this purpose, he piston position was held constant by replacing the crankshaft with a zero displacement constraint, resulting in a constant volume vessel.

Test Case

The constant volume vessel used for injection visualizations has a cubical shape with 1.4 10^{-3} m^3 volume. It is capable of reproducing high pressure (0 ÷ 150 *bar*) and temperature (20 ÷ 200°C) thermodynamic conditions that can be found in ICE combustion chambers. Four optical windows of 70 *mm* diameter provide access for the light source and cameras to perform mie-scattering and schlieren imaging.

A symmetric three-hole-nozzle injector with a global spray angle of 90° was adopted. The inclination of the three jets with respect to the injector axis is 38° which grants minimal interaction between the jets so that each of them can be representative of an isolated spray [5].

The operating conditions for the experiments were chosen around two reference points which represent early injection strategy at low and high load engine operation. Temperature variations from the reference points at constant pressure and at constant density were investigated.

Since the saturation pressure of isooctane at 90°C is 0.57 *bar* flash boiling occurs in the low-load operating points. As this phenomenon cannot be described by the evaporation and atomization models, only the high-load operating conditions were retained for validation, Tab. 1.

Table 1. Operating conditions for the validation test case: high-load operating point.

Operating point		Pressure (bar)	Temperature (°C)	Density (kg/m³)
	#0	1.54	33	1.75
Iso ρ	#1	1.95	115	1.75
	#2	2.00	125	1.75
Iso p	#1	1.54	90	1.48
	#2	1.54	115	1.38
	#3	1.54	125	1.35

The injection pressure is 200 *bar* and the injector tip temperature is maintained at 90°C in all the investigated operating points investigated. Injected fuel mass is 3.75 *mg* (injection duration: 724 μs) for low load operation and 24.9 *mg* (injection duration: 3320 μs) for high load operation.

Experimental Data

Post-processed experimental data for this test case were already available from previous measurements performed at IFPEN within the framework of the MAGIE (Modélisation et Approche Générique de l'Injection Essence - Modeling and Generic Approach of Gasoline Injection) collaborative project [5].

Schlieren imaging was used to investigate the vapor phase. This technique uses the refractive-index gradients in the measurement field to investigate density and, therefore, fuel mass fraction distribution in the spray. Images are acquired placing a luminous source and a camera on two opposite sides of the cell. Image post-processing of schlieren images results in spray tip penetration length and velocity as well as the global spray angle of the three jets.

Mie scattering, employed for the liquid phase, captures the light scattered by the liquid fuel drops. The axis of the camera is perpendicular to that of the light sourcs. Time-resolved liquid penetration length and velocity as well as global angle data were likewise available.

For both experimental techniques, the average images were obtained from ten raw instantaneous images.

3D CFD Simulations

CFD simulations of the test cases were performed with a RANS code, in order to provide additional information - useful for the 0D model development and validation - which is not directly available from the experimental data. In particular:

- penetration lengths outside the optical window;
- spray volume;
- masses of air and fuel in the spray;
- fuel mass fraction PDF.

The simulations were tuned in order to fit the experimental data on penetration and cone angle acting, in particular, on the initialization of the liquid phase. The initial drop-size distribution used agrees with the one adopted by authors who simulated the same experiment [11].

The spray region is defined as the union of the cells whose fuel mass fraction is above a threshold, here fixed to 10^{-3}. Spray volume and penetration are calculated accordingly.

The mean value and variance of fuel mass fraction Y_F are derived from CFD data with a total mass weighted average on cell values. In particular, the variance takes into account the two contributions due to

- non uniform cell value of Y_F over the domain;
- sub grid variance ${\sigma_Y}^2$ transported by the turbulent combustion model, under the assumption of a β-PDF distribution.

The overall variance of the fuel mass fraction can then be expressed as:

$$var(Y_F) = \frac{1}{\mathcal{M}_{tot}} \sum_{i=1}^{N_c} \left[\left({Y_F}^i - \overline{Y_F} \right)^2 - ({\sigma_Y}^i)^2 \right] \mathcal{M}_i \qquad (27)$$

where N_c is the number of cells in the spray zone, $\mathcal{M}_i$ the gas mass in the i-th cell, ${Y_F}^i$ the fuel mass fraction in the i-th cell and $\overline{Y_F}$ its average over the domain.

The fuel mass fraction PDF is derived using the cell values of the fuel mass fraction: the mass contained in each cell is split between the two neighbor classes according to Eq. (21). This operation does not yet take into account the sub-grid distribution mentioned above.

Reference Point Results

This section presents penetration, spray volume and evaporation results for the reference point (point #0 in Tab. 1).

Penetrations (Fig. 9) show a good agreement with CFD. A slight bias can be noticed in the vicinity of the wall (located at 112mm), as spray/wall interaction is not taken into account by the 0D model. An acceptable agreement is found with Schlieren data as well, up a distance corresponding to the end of the optical window (75mm from the injector tip). At the beginning of injection, when the spray is not well developed, the 0D model fits experimental data rather than CFD, which is less reliable because of the strong effect of boundary conditions.

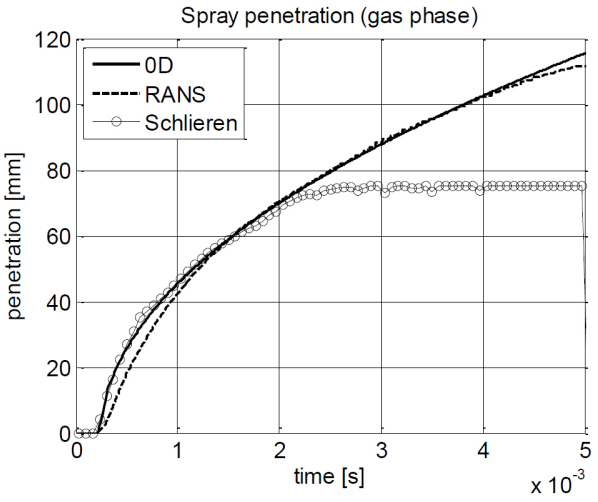

Figure 9. Reference point: spray tip penetration.

Figure 10 shows that the spray volume computed by the 0D model well agrees with the one given by CFD computations. Nevertheless it is shown that deviations are found for times greater than 4 ms after SOI, when the spray tip approaches the cell walls, in which conditions the validity of the conical shape assumption drops.

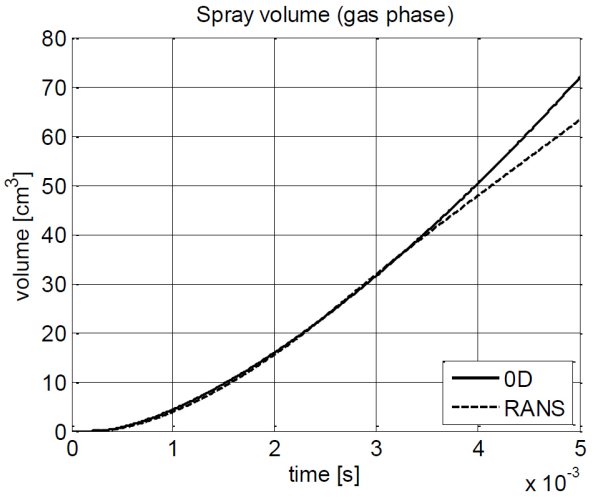

Figure 10. Reference point: spray volume.

The spreading angles are well described, considering that no time variation can be described by the 0D model, since it expresses the angle as a function of chamber thermodynamic conditions which do not vary during the injection. The spreading angle values obtained with CFD and experiments at the beginning of the injection cannot be taken into account, since they are derived from the volume (CFD) or the spray image area (mie), for a conical spray, whose height is the penetration x_p. This method amplifies the inaccuracies for small x_p.

Experimental values are less reliable than CFD here since the single-jet spreading angle is derived numerically from the overall spray under the assumption that the jet axis equals follows the target indicated by the constructor [5].

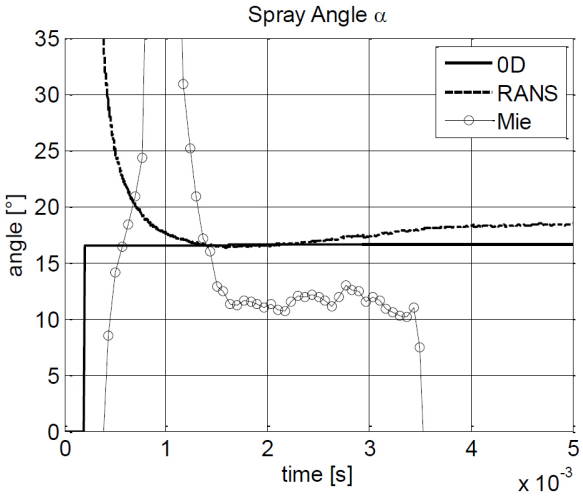

Figure 11. Reference point: spray spreading angle.

Computed liquid and gaseous fuel masses (Fig. 12 and Fig. 13) in the spray are in good agreement with CFD, showing that the model is capable of describing evaporation correctly

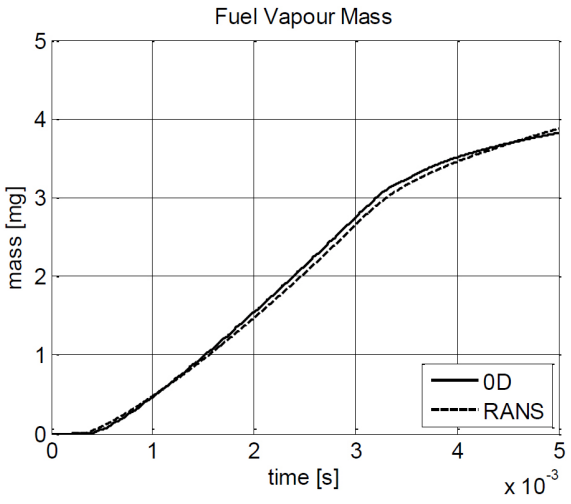

Figure 12. Reference point: fuel vapor mass.

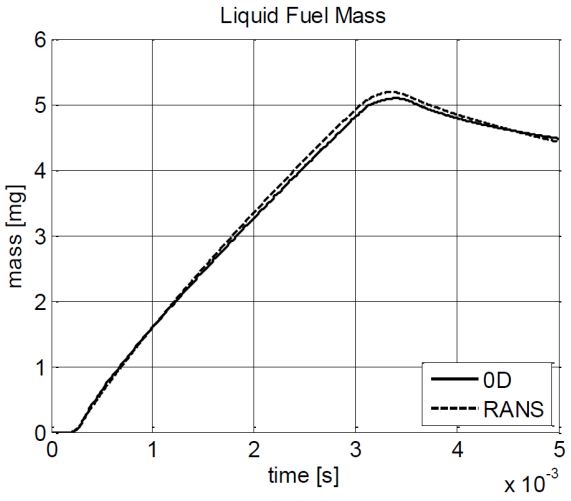

Figure 13. Reference point: liquid fuel mass.

The following plots show the evolution of fuel mass fraction distribution within the spray. The computed results for the mean value (Fig. 14) agree with CFD data. This follows from the good agreement found on the vapor mass and spray volume, and confirms that the entrained air mass in the spray is computed consistently. Deviations are unavoidable at the beginning of injection, due to the little masses involved. As shown in Fig. 10 and Fig. 12, the volume of the spray - therefore the air mass - and the fuel vapor mass are close to zero during the first 0.5 ms after SOI.

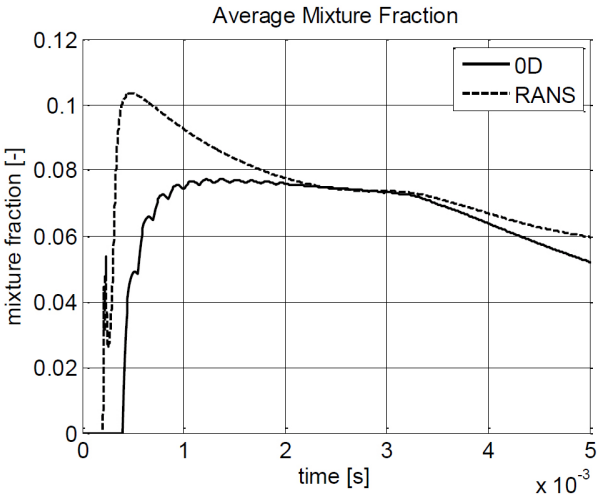

Figure 14. Reference point: spray average fuel mass fraction.

Variance is also reasonably well represented (Fig. 15). The two values are nevertheless affected by the discretization of the liquid mass which causes the second order discontinuities observed on 0D data. The fuel parcel discretization is also responsible for the little delay of 0D with respect to RANS, shown in Fig. 14 and Fig. 15, since it postpones the beginning of evaporation to the time when the first liquid fuel parcel is full.

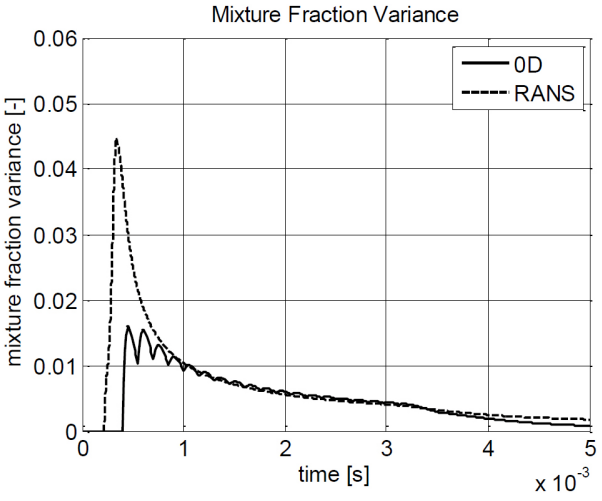

Figure 15. Reference point: fuel mass fraction variance.

Figure 16 shows a comparison of 0D and CFD discrete PDF at different times after SOI.

Such a level of detail in the description of stratification is useful for future development of models for the evaluation of the exhaust gas composition and the prediction of abnormal combustions.

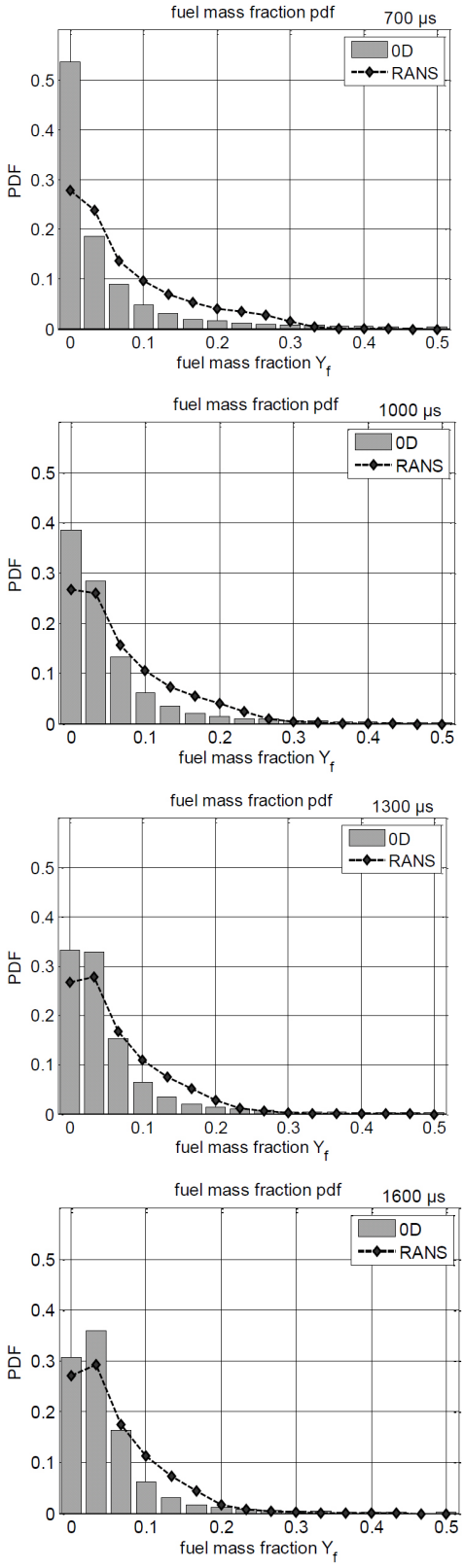

Figure 16. Reference point: fuel mass fraction PDF, at different timings.

Parametric Variations

The calibrated model was then tested on the whole experimental database, spanning the operating points listed in Tab. 1.

Constant pressure parametric variations from the reference point are shown below - to summarize the capability of the model to account for variations of the operating conditions. The main spray-characterizing quantities are plotted against the chamber temperature, which varies across the operating points investigated (#0, iso-p #1, #2 and #3, in Tab. 1). Results on iso-ρ temperature variations are not shown here.

Spray penetrations are shown here at two different timings: 1 and 2 ms after SOI, Fig. 17 and Fig. 18 respectively. The 0D data is in good agreement with experimental data in the near-nozzle region while in the far field they approach CFD results.

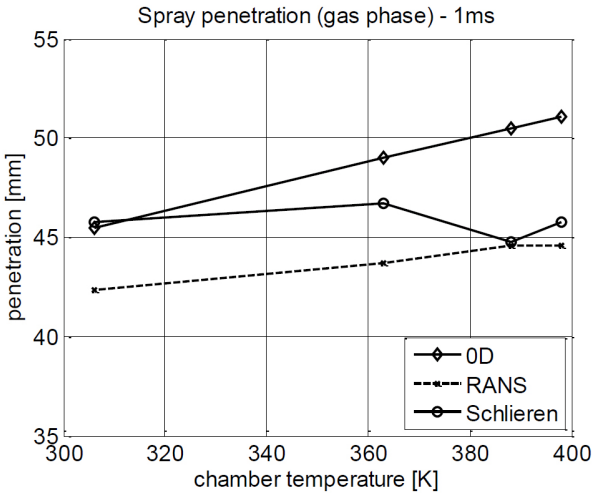

Figure 17. Parametric variations: spray tip penetration against temperature, 2ms after SOI.

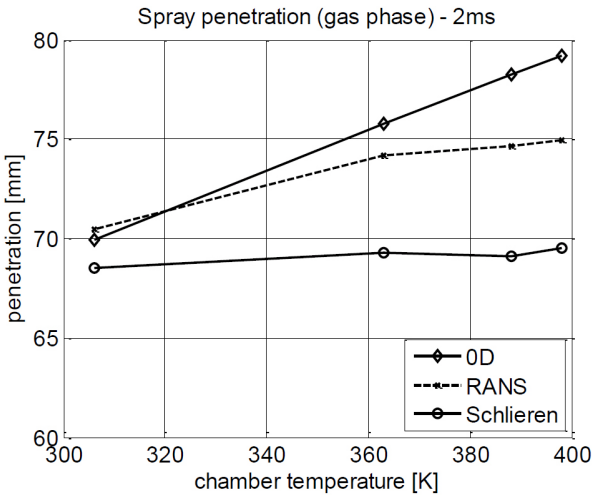

Figure 18. Parametric variations: spray tip penetration against temperature, 2ms after SOI.

Penetration and volume (Fig. 19) data show that Naber's model [13] responds correctly to temperature variations, whose influence on spray development is well described.

Fuel vapor mass (at 2ms and 4ms after SOI, Fig. 20 and Fig. 21, respectively) agree with CFD data: a strong dependency on temperature is found in both cases, showing that the evaporation model is capable of responding to in-cylinder thermodynamic variations.

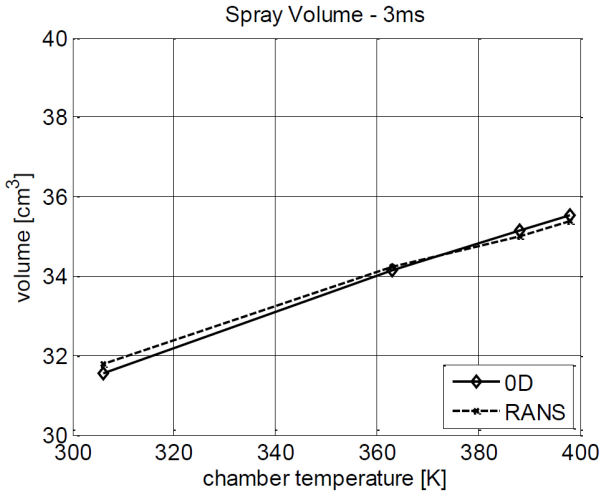

Figure 19. Parametric variations: spray volume against temperature, 3ms after SOI.

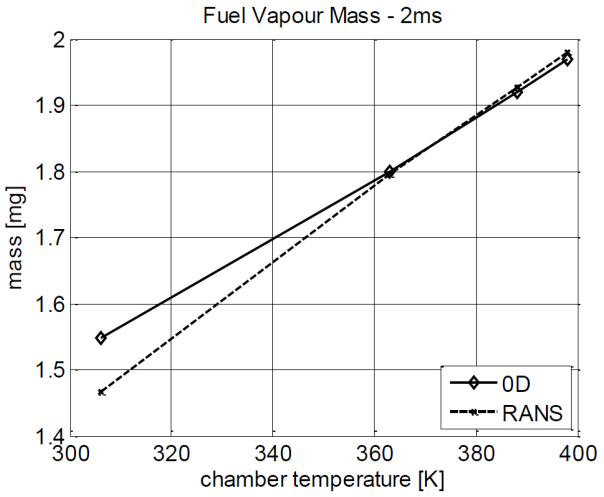

Figure 20. Parametric variations: fuel vapor mass against temperature, 2ms after SOI.

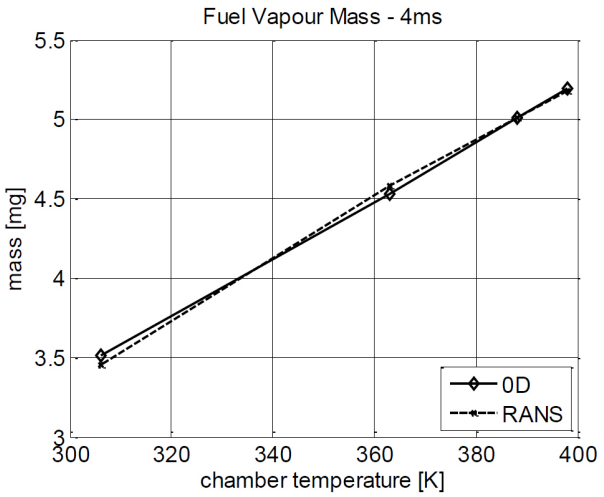

Figure 21. Parametric variations: liquid fuel mass against temperature, 4ms after SOI.

The average mixture fraction in the spray reflects the soundness of the evaporation and entrainment models.

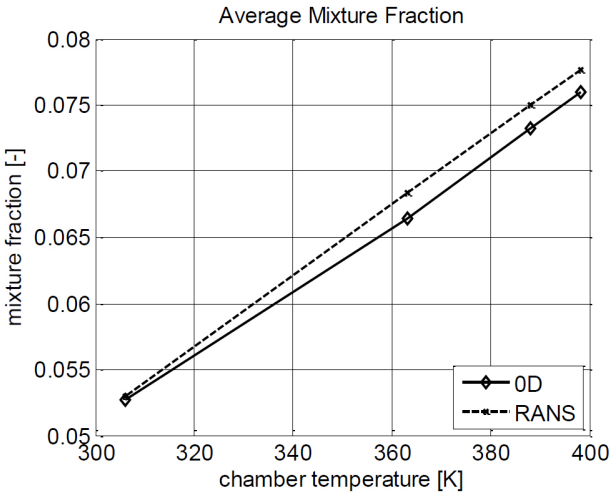

Figure 22. Parametric variations: average fuel mass fraction against temperature, 2ms after SOI.

The mixture fraction variance plot in Fig. 22 summarizes the response of the PDF mixing model to temperature variations: the trend is represented correctly though the poor fit suggests further investigation.

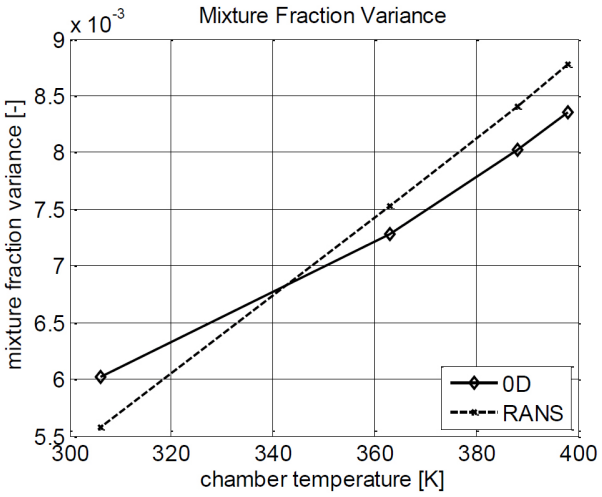

Figure 23. Parametric variations: fuel mass fraction variance against temperature, 2ms after SOI.

Conclusions

A spray model was devised and developed within the existing CFM1D [15] combustion model of the IFP-Engine library. The model addresses atomization and drop evaporation with a discrete size distribution, air entrainment and gaseous penetration explicitly and proposes a discrete PDF-based approach to describe stratification, so to give an accurate prediction of the evaporation rate and account for fuel vapor distribution within the combustion chamber.

Validation was performed on an experimental test case consisting of a high pressure isooctane injection in a constant volume vessel for which mie-scattering and high-speed schlieren visualizations for different thermodynamic conditions - previously performed at IFPEN within the framework of the MAGIE collaborative project - were available.

Liquid and vapor penetrations as well as spray angle data from experiments were then used to tune RANS CFD simulations performed with the IFP-C3D code. CFD provides further data which is not directly available from the experiments such as drop size and charge distributions as well as spray properties outside the measurement field, which are then used to tune and validate the 0D model.

The new approach showed its potential in describing the spray evolution in modern DI-SI engines. The model was tested on a range of thermodynamic conditions. Calibration of the 0D model was performed on the reference point, so to test the model in different thermodynamic conditions and verify its response to parametric variations.

The new approach can reproduce the effects of temperature variations on evaporation and atomization without recalibration.

Moreover this approach - because of its physical bases - gives access to useful information related to the spray - namely, the description of the fuel mass fraction stratification has interesting perspectives of coupling with a combustion model: the emission of pollutants can be detailed for the different fuel mass fraction classes to take into account the effects of stratification on combustion. Information on temperature and charge stratification is also useful to predict the presence of the *hot-spots*, that could initiate abnormal combustions.

Nevertheless, some improvements are still needed in order to apply the proposed model to an engine case. The coupling of the spray propagation with the tumble flow can be used to correct the penetration and entrainment. The inclusion of a turbulence-related source to the class mixing mechanism is likewise necessary to get reliable predictions in engine injections.

References

1. Abramzon B. and Sirignano W.A.. Droplet vaporization model for spray combustion calculations. *International Journal of Heat and Mass Transfer*, 32(9):1605-1618, 1989.
2. Barba, C., Burkhardt, C., Boulouchos, K., and Bargende, M., "A Phenomenological Combustion Model for Heat Release Rate Prediction in High-Speed DI Diesel Engines with Common Rail Injection," SAE Technical Paper 2000-01-2933, 2000, doi:10.4271/2000-01-2933.
3. Bradley D. Autoignitions and detonations in engines and ducts. *Philosophical Transactions of the Royal Society A: Mathematical, Physical and Engineering Sciences*, 370(1960):689-714, 2012.
4. Dulbecco Alessio. *Modeling of Diesel HCCI combustion and its impact on pollutant emissions applied to global engine system simulation*. PhD thesis, INPT Toulouse, 2010.
5. Dumas Jean Pierre, Hermant Laurent, and Kashdan Julian. Experimental characterisation of multi-hole injector spray behaviour in a high pressure/temperature chamber database for gasoline direct injection. MAGIE project - tasks 3c & 4b, IFPEN, 2012.
6. Fraser, N., Blaxill, H., Lumsden, G., and Bassett, M., "Challenges for Increased Efficiency through Gasoline Engine Downsizing," *SAE Int. J. Engines* 2(1):991-1008, 2009, doi:10.4271/2009-01-1053.
7. Geiger, J., Grigo, M., Lang, O., Wolters, P. et al., "Direct Injection Gasoline Engines - Combustion and Design," SAE Technical Paper 1999-01-0170, 1999, doi:10.4271/1999-01-0170.
8. Jérôme Hélieand Arnaud Trouvé. Turbulent flame propagation in partially premixed combustion. *Symposium (International) on Combustion*, 27:891-898, 1998.
9. Jérôme Hélie and Arnaud Trouvé. A modified coherent flame model to describe turbulent flame propagation in mixtures with variable composition. *Symposium (International) on Combustion*, 28:193-201, 2000.
10. Inagaki, K., Ueda, M., Mizuta, J., Nakakita, K. et al., "Universal Diesel Engine Simulator (UniDES): 1st Report: Phenomenological Multi-Zone PDF Model for Predicting the Transient Behavior of Diesel Engine Combustion," SAE Technical Paper 2008-01-0843, 2008, doi:10.4271/2008-01-0843.
11. Khan M M,Helie J,Gorokhovski M,Wood A,Wigley G,Kashdan J, Dumas J P,Mojtabi M, andGuibert P. Numerical analysis of multihole gasoline direct injection sprays. ICLASS, 2012.
12. Mauviot Gilles, Albrecht Antoine, and Poinsot Thierry J.. A new 0d approach for diesel combustion modeling coupling probability density function with complex chemistry. 2006.
13. Naber, J. and Siebers, D., "Effects of Gas Density and Vaporization on Penetration and Dispersion of Diesel Sprays," SAE Technical Paper 960034, 1996, doi:10.4271/960034.
14. Poinsot Thierry, Veynante Denis, Trouvé Arnaud, and Ruetsch G.. Turbulent flame propagation in partially premixed flames. *Proceedings of the CRT Summer Program*, pages 111-141, 1996.
15. Richard S., Bougrine S., Font G., Lafossas F.-A., and le Berr F. On the reduction of a 3d cfd combustion model to build a physical 0d model for simulating heat release, knock and pollutants in si engines. *Oil and Gas Science and Technology*, 64(3):223-242, 2009.
16. Siebers, D., "Liquid-Phase Fuel Penetration in Diesel Sprays," SAE Technical Paper 980809, 1998, doi:10.4271/980809.
17. Turner, J., Popplewell, A., Patel, R., Johnson, T. et al., "Ultra Boost for Economy: Extending the Limits of Extreme Engine Downsizing," *SAE Int. J. Engines* 7(1):387-417, 2014, doi:10.4271/2014-01-1185.
18. Varde, K., Popa, D., and Varde, L., "Spray Angle and Atomization in Diesel Sprays," SAE Technical Paper 841055, 1984, doi:10.4271/841055.

19. Vervisch P.E., Colin O., J.-Michel B., and Darabiha N. No relaxation approach (NORA) to predict thermal no in combustion chambers. *Combustion and Flame*, 158(8):1480-1490, 2011.

20. Zhao Fuquan, Lai M-C, and Harrington David L. Automotive spark-ignited direct-injection gasoline engines. *Progress in energy and combustion science*, 25(5):437-562, 1999.

Contact Information

Federico Pellegrino
Engine and Vehicle Modeling Department
IFP Energies nouvelles
1 et 4 avenue de Bois-Préau
92852 Rueil-Malmaison Cedex - France
federico.pellegrino@ifpen.fr

Definitions/Abbreviations

IFPEN - IFP Energies nouvelles

DI - Direct Injection

SI - Spark Ignition

GDI - Gasoline Direct Injection

SOI - Start of Injection

EOI - End of Injection

Mie - Experimental technique to visualize a disperse liquid phase through light scattering

Schlieren - Experimental technique to visualize density gradients in a fluid

PDF - Probability Density Function

ICE - Internal Combustion Engine

VVT - Variable Valve Timing

VVA - Variable Valve Actuation

IVO - Inlet Valve Opening

IVC - Inlet Valve Closing

EVO - Exhaust Valve Opening

EVC - Exhaust Valve Closing

The Engineering Meetings Board has approved this paper for publication. It has successfully completed SAE's peer review process under the supervision of the session organizer. The process requires a minimum of three (3) reviews by industry experts.

ISSN 0148-7191

http://papers.sae.org/2015-24-2471

Appendix B

THIESEL 2018: Development and Validation of a Quasi-Dimensional Spray Model for DI-SI engines

Development and Validation of a Quasi-Dimensional Spray Model for DI-SI engines

F. Pellegrino[1, 2], A. Dulbecco[1] and D. Veynante[2, 3]

[1]IFPEN, 1-4 av. du Bois-Préau, 92852 Rueil-Malmaison, France.
E-mail: alessio.dulbecco@ifpen.fr
Telephone: +33 (0)1 47 52 72 24
[2]CentraleSupélec. Université Paris Saclay.
[3]Laboratoire EM2C. CNRS.

Abstract. Future constraints on pollutant emissions pushed car manufacturers towards Gasoline Direct Injection (GDI) technologies to improve engine performances. New challenges are hence introduced in terms of combustion optimization due to a more complex phenomenology while system models require additional calibration parameters. This study presents the development and validation of a Quasi Dimensional (QD) model of GDI spray for system simulation. The proposed model focuses on physics of atomization and drop evaporation and fuel/air mixing. The liquid phase is discretized in parcels grouping drops of the same size. An empirical atomization model based on injection velocity, fuel characteristics and thermodynamic conditions provides initial diameters. A Lagrangian model including drag-inertia dynamics, heat-up and forced convection describes drop parcel penetration and evaporation. Fuel / air mixing is described using a discrete Probability Density Function (PDF) approach, based on constant-mixture-fraction classes interacting with each other and with the drop parcels. The model was implemented in the Simcenter Amesim™ software platform for multi-physical modeling and integrated in a generic Spark Ignition (SI) combustion chamber submodel, CFM1D, from the IFP-Engine library. Fuel evaporation, spray dynamics and mixture formation modeling approaches, inspired by literature on Diesel engines, were adapted to GDI operating conditions. The model was first validated on a constant-volume vessel with quiescent gas in different thermodynamic conditions from experiments and 3D RANS CFD simulations performed with IFP-C3D. A tumble vortex in a constant volume vessel, in a first time, and rapid variations of the vessel volume, in a second time, were then investigated to test the model response to in-cylinder flow aerodynamics and variable thermodynamic conditions, respectively, in terms of fuel evaporation, spray development and fuel/air mixing and equivalence ratio distribution. Computations of fuel injections in a motored engine complete the model validation campaign in variable thermodynamic conditions and with realistic aerodynamics and the results were compared to both experiments and CFD computations. The model predicts with a good accuracy spray properties such as liquid and gas penetration, spray volume, mass and mixture fraction distribution.

1. Model description

1.1 Liquid phase description

The liquid phase is discretized in *parcels*, containing drops of the same diameter, temperature, location and velocity. This discretization is achieved dividing the injection profile into equal mass elements, each generating a single drop parcel.

1.1.1 Discretization of the liquid phase

The drop parcels are described by evolution equations for the state variables listed in Table 1.

Table 1. Drop parcel state variables.

Mass	$\mathcal{M}$	Momentum	$\mathcal{P}$
Surface	$\mathcal{S}$	Enthalpy	$\mathcal{H}$

Their variations result of fuel injection, evaporation and liquid/gas drag force for momentum. The use of both total mass and surface as state variable allows defining an average diameter at all times and

describe its evolution due to the injection of new drops and evaporation of the existing ones. The integration of momentum provides the drop parcel position along the injection axis, $\mathcal{X}$.

1.1.2 Injection and atomization

The initial diameter of the drops injected at the instant *t* is given by the empirical model of Varde *et al.* (1984):

$$\frac{D_{32}^{inj}}{D_{NOZ}} = K_{ato}(Re\ We)^{-0.28} \tag{1}$$

where the Sauter Mean Diameter, D_{32}, is expressied as a function of the nozzle diameter, D_{NOZ}, Reynolds and Weber numbers of the nozzle flow. The injected drops feeding a generic, *i*-th, parcel will therefore increase its surface with a contribution:

$$\dot{\mathcal{S}}^i\big|_{inj} = \frac{6\,\dot{\mathcal{M}}_{inj}}{\rho_L\, D_{32}^{inj}} \tag{2}$$

with $\dot{\mathcal{M}}_{inj}$ the injection rate and ρ_L the liquid fuel density.

1.1.3 Evaporation

The Abramzon and Sirignano (1989) model describes the evaporation rate, $\dot{\mathcal{M}}_{ev}^i$, of each drop parcel. The surface destruction contribution associated with evaporation is:

$$\dot{\mathcal{S}}^i\big|_{ev} = -\frac{2}{3}\frac{\mathcal{S}^i}{\mathcal{M}^i}\,\dot{\mathcal{M}}_{ev}^i \tag{3}$$

The evaporation model accounts for an inter-phase convection velocity obtained by combining liquid drop and gaseous phase velocities, resulting from the tumble vortex intensity, Fig. 2 (left).

1.2 Gas phase description

Spray penetration and spreading rate are described by the Naber and Siebers (1996) model. The air entrainment rate, $\dot{\mathcal{M}}_{entr}$, corresponds to the rate of expansion of the spray conical region. Its value is corrected to account for tumble effects on fuel/air mixing.

1.3 Mixture formation and stratification

The non-homogeneity of the reactive charge is modeled by a discrete PDF: the fuel mixture fraction, Y_F, axis is divided in equal intervals, each identifying a *class*. The evaporating mass of the *i*-th parcel, $\dot{\mathcal{M}}_{ev}^i$, is attributed to and shared between contiguous classes containing the saturation fuel mixture fraction value at drop liquid/gas interface.The entrained mass, $\dot{\mathcal{M}}_{entr}$, is attributed to the $Y_F = 0$ class.

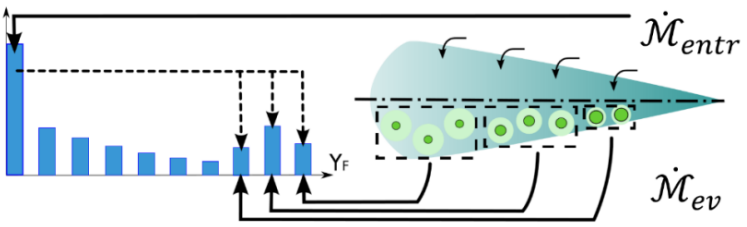

Fig. 1. Interaction between the fuel evaporation and entrainment models and the discrete mixture fraction PDF.

An interaction mechanism, based on the model proposed by Inagaki *et al.* (2008), describes mixing as a mass flow from the pure air and air saturated with fuel classes towards the equilibrium class corresponding to the mean mixture fraction, $\bar{Y}_F$, Fig. 1.

2. Results and validation tests

The proposed 0D spray model provides several characteristics that are useful in engine computations:

- Liquid and gas penetrations and air entrainment rates enter predictions of fuel/air mixing and fuel drop impacts on solid walls that can generate films;
- The evaporation rate provides the amount of liquid in the combustion chamber, which is a key parameter for soot formation, and the fuel/air mixing;
- The mixture fraction PDF – combined to a combustion model – can be used to improve the prediction of heat release rates and pollutant formation in GDI engines.

The results obtained with the 0D spray model were compared against 3D RANS simulations, the latter validated by means of experimental data, in different geometries, to provide an exhaustive validation.

2.1 Constant volume vessel

The test case consists of an injection of isooctane into a 1.4L, constant volume, chamber with quiescent gas, through a three-hole symmetrical injector. Different experimental thermodynamic conditions, representative of early injections in a homogeneous GDI engine working at high and low load operations, were investigated. Temperature variations from the reference points at constant pressure and at constant density were also investigated. Results obtained with the 0D model were compared with 3D RANS simulations and optical measurements (Mie and Schlieren) performed during the MAGIE project (Dumas *et al.*, 2012).

The same geometry was used to test the model response to the presence of a tumble vortex, whose intensity can reach 600rad/s.This validation case is designed to test the response of the spray model to the interaction with tumble, in terms of evaporation, air entrainment and mixing, through the production of turbulent kinetic energy. Validation results for this case are shown in Fig. 2.

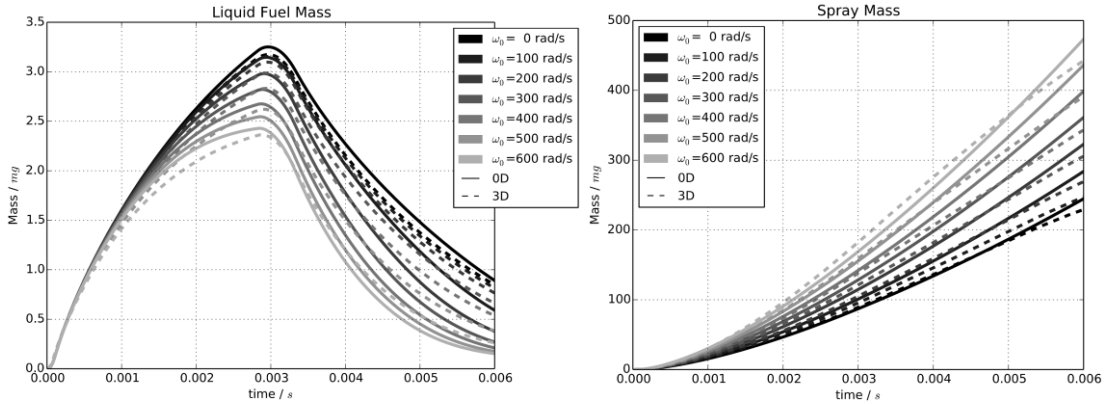

Fig. 2. Constant volume vessel with initial tumble flow: liquid fuel mass (left) and total spray mass (right). 0D model results (solid line) are compared to 3D RANS reference data (dashed line).

2.3 Variable volume vessel

This test case investigates the spray dynamics in variable thermodynamic conditions. The configuration consists of a closed cylinder filled with air at rest, with a single-nozzle injector aligned with the piston axis. The particularly long stroke associated with this geometry is required to reach a realistic compression ratio (8) and crank speed (3000rpm), and a large dead volume to avoid any interaction between spray and walls. Validation results for this case are shown in Fig. 3.

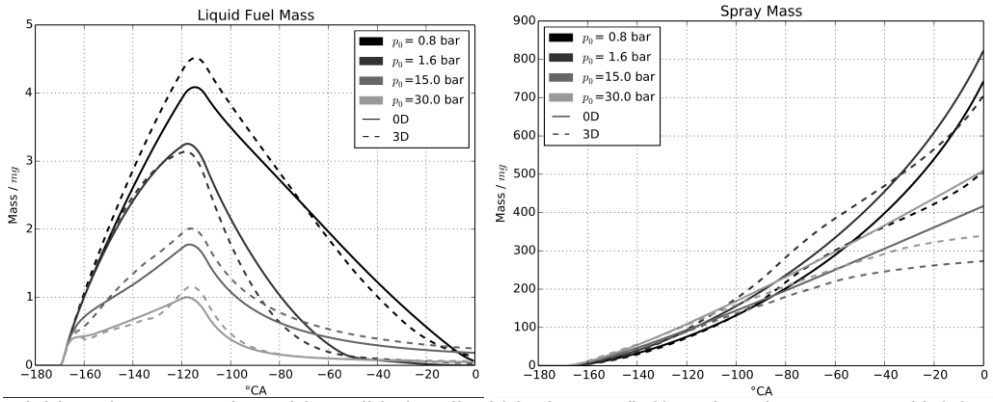

Fig. 3. Variable-volume vessel used for validation: liquid fuel mass (left) and total spray mass (right). 0D model results (solid line) are compared to 3D RANS reference data (dashed line).

2.4 Motored engine

Finally, the model response to the combined effect of variable thermodynamic conditions and tumble is tested for iso-octane injections in the ICAMDAC engine in motored conditions (de Franqueville, 2013) and validated against 3D RANS simulations (Fig. 4).

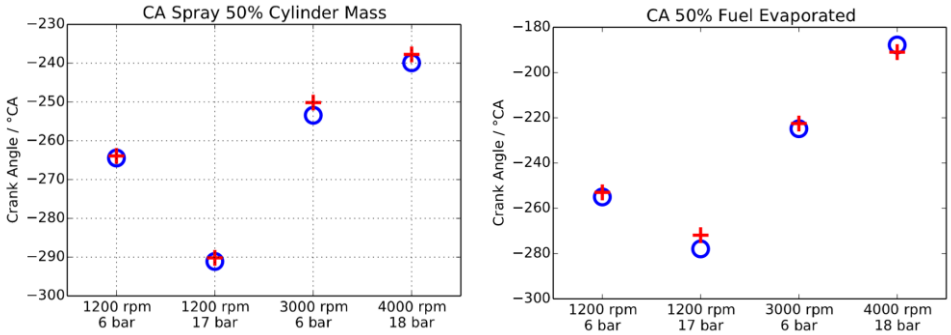

Fig. 4. Motored engine validation: crank angles when the spray fills half of the cylinder volume (left) and when half of the injected mass has evaporated (right). Blue O: 3D RANS; Red +: 0D model.

References

B. Abramzon and W. Sirignano (1989) Droplet vaporization model for spray combustion calculations. International Journal of Heat and Mass Transfer, 32(9):1605–1618.

J. P. Dumas, L. Hermant, and J. Kashdan (2012) Experimental characterisation of multi-hole injector spray behaviour in a high pressure/temperature chamber - database for gasoline direct injection. MAGIE project - tasks 3c & 4b, IFPEN.

L. de Francqueville (2013) Essais sur monocylindre opaque : Base de données moteur allumage commandé. Projet ICAMDAC – phase 4.2, IFPEN.

K. Inagaki, M. Ueda, J. Mizuta, and K. Nakakita (2008) Universal diesel engine simulator (UniDES): 1st report : Phenomenological multi-zone pdf model for predicting the transient behavior of diesel engine combustion. SAE Technical Paper 2008-01-0843.

J. D. Naber and D. L. Siebers (1996) Effects of Gas Density and Vaporization on Penetration and Dispersion of Diesel Sprays. SAE Technical Paper 960034.

F. Pellegrino, A. Dulbecco and D. Veynante (2015) Development of a Quasi-Dimensional Spray Evaporation and Mixture Formation Model for Direct-Injection Spark-Ignition Engines. SAE Technical Paper 2015-24-2471

K. Varde, D. Popa, and L. Varde (1984) Spray angle and atomization in diesel sprays. SAE Technical Paper 841055.

Appendix C

Résumé du manuscrit (en français)

C.1 Introduction

Ce manuscrit présente le développement d'un modèle 0D de combustion dans les moteurs à allumage commandé à injection directe. Le modèle proposé est développé a partir d'un modèle de combustion existant, CFM1D, adapté aux moteurs à allumage commandé sans injection directe (injection indirecte ou carburation).

Les développements réalisés dans ces travaux de thèse portent sur la prise en compte de l'injection directe en détaillant les différents aspects tels quels l'atomisation, l'évaporation de carburant, son mélange avec le comburant, la description des fluctiations de richesse dans la chambre de combustion et la propagation de la flamme dans un mélange imparfait.

C.2 Description du modèle

C.2.1 Modélisation de la phase liquide

La phase liquide est discretisée en parcelles de gouttes, ayant les mêmes charactéristiques en termes de : diamètre, temperature, position et vitesse. L'évolution temporelle de l'état de ces parcelles est décrite par des équations de conservation pour les variables suivantes:

- la masse totale de la parcelle, $\mathcal{M}_L^i$;
- la surface totale de contact entr, $\mathcal{S}_L^i$, entre la phase liquide et la phase gas;
- l'enthalpie totale, $\mathcal{H}_L^i$
- la quantité de mouvement, $\mathcal{P}_L^i$
- la distance de l'injecteur, $\mathcal{X}_L^i$

À partir de ces variables d'état, le quantités suivantes sont dérivées :

- le nombre de gouttes:

$$n^i = \frac{6}{\rho_L \, \pi} \frac{\mathcal{M}_L^i}{{D_{32}^i}^3} = \frac{\rho_L^2}{36 \, \pi} \frac{{\mathcal{S}_L^i}^3}{{\mathcal{M}_L^i}^2} \tag{C.1}$$

- le diamètre des gouttes:

$$D_{32}^i = \frac{6 \, \mathcal{M}_L^i}{\rho_L \, \mathcal{S}_L^i} \tag{C.2}$$

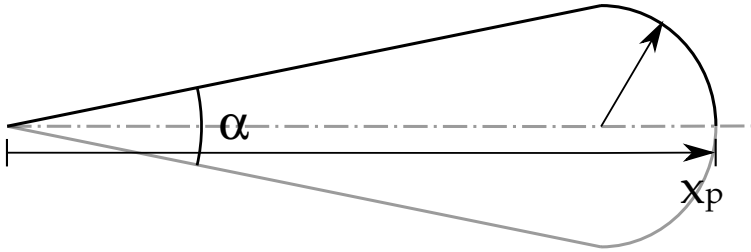

Figure C.1: Modélisation de la zone de mélange air/carburant : le jet est décrit comme l'union d'une cône et d'une semisphère.

L'équation de conservation de la surface de contact :

$$\dot{\mathcal{S}}_L^i = \underbrace{\frac{6}{\rho_L \, D_{32}^{\text{inj}}(t)} \dot{\mathcal{M}}_{\text{inj}}^i}_{\text{(injection)}} - \underbrace{\frac{2}{3} \frac{\mathcal{S}_L^i}{\mathcal{M}_L^i} \dot{\mathcal{M}}_{\text{ev}}^i}_{\text{(évaporation)}} \tag{C.3}$$

se compose de deux termes :

- le premier, dû à l'injection, qui introduit des nouvelles gouttes dont le diamètre, D_{32}^{inj} est donné par le modèle d'atomisation ;
- le deuxième, qui décrit la réduction de surface due à l'évaporation et n'altère pas la valeur de numbre de gouttes, n^i

Le modèle d'atomisation. La corrélation empirique proposée par Varde et al. (1984) a été retenue pour calculer la condition initiale du diamètre des gouttes :

$$\frac{D_{32}^{\text{inj}}}{D_{\text{noz}}} = \mathcal{K}_{\text{ato}} \, (Re_f \, We_f)^{-0.28} \tag{C.4}$$

avec l'introduction du paramètre de calibration $\mathcal{K}_{\text{ato}}$.

Le modèle d'évaporation. L'évolution des gouttes dans la chambre de combustion est décrite par un modèle Lagrangien dérivé de la littérature. Le flux thermique par convection forcée et le taux d'évaporation sont donnés par le modèle de Abramzon and Sirignano (1989). L'équilibre dynamique des parcelles de gouttes est établi prenant en compte la force de trainée de la phase gas sur la phase dispersée résultant de la vitesse des gouttes et de l'aérodynamique dans la chambre de combustion.

C.2.2 Modélisation de la phase gas

La déscription macroscopique du mélange air/carburant, est obtenue en couplant le modèle d'évaporation avec le modèle de propagation de spray proposé par Naber and Siebers (1996). Ce modèle fournit les valeurs de la pénétration du spray, x_p, et de son angle d'ouverture, α, qui sont ensuite utilisées pour calculer le volume de la zone de mélange, modélisée comme l'union d'un cône et d'une semisphère, Fig. C.1. L'évolution temporelle du volume de cette zone fournit la valeur du taux d'entrainement de chaque espèce pendant la formation du melange:

$$\dot{\mathcal{M}}_i^{\text{ent}} = \dot{V}_{\text{rc}}^{\text{Sieb}} \, (1 + \alpha_{t\,\text{ent}}) \, \rho_i \quad \text{with} \quad i = 1, \ldots, N_{\text{SP}} \tag{C.5}$$

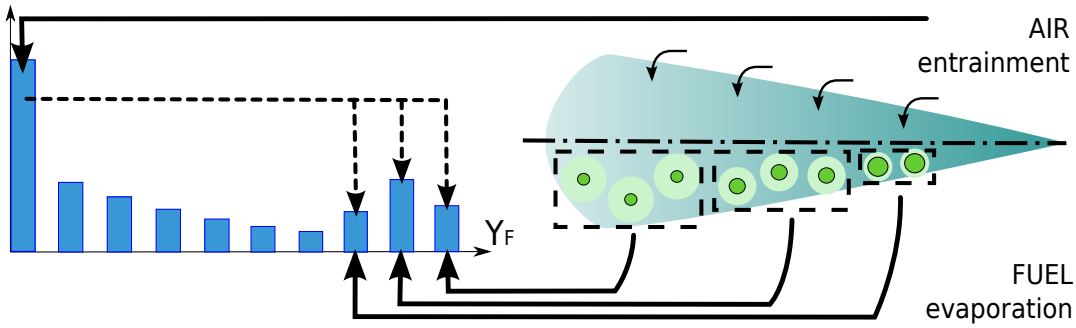

Figure C.2: La PDF de richesse et son interaction avec les modèles d'évaporation et d'entrainement d'air.

où $V_{\mathrm{rc}}^{\mathrm{Sieb}}$ est le volume du jet en Fig. C.1, et $\alpha_{t\,\mathrm{ent}}$ un facteur prenant en compte le gain sur l'entrainement d'air dû au tumble.

Stratification à petite échelle. La non-homogéneité de la zone de mélange est modélisée par une PDF discrète sur le domaine de la fraction massique de carburant, Y_F, comme montré en Fig. C.2. L'axe des fraction massiques, Y_F, est discrétisé en intervalles identiques, chacun identifiant une *classe* de richesse. La masse s'évaporant de chaque parcelle de gouttes est attribuée à la classe de la PDF corréspondante à la fraction massique de saturation de la parcelle liquide i-ème, $Y_{F\,i}^{s}$, elle-même fonction de la température du liquide.

C.2.3 Modélisation de la combustion

Réaction au front de flamme. Le schéma de reaction adopté pour le front de flamme est obtenu comme combinaison de trois réactions :

$$\alpha_r\beta_r\left[\mathrm{C}_x\mathrm{H}_y\mathrm{O}_z + \left(x+\frac{y}{4}-\frac{z}{2}\right)\mathrm{O}_2 \longrightarrow x\,\mathrm{CO}_2 + \frac{y}{2}\,\mathrm{H}_2\mathrm{O}\right] \tag{C.6}$$

$$(1-\alpha_r)\beta_r\left[\mathrm{C}_x\mathrm{H}_y\mathrm{O}_z + \frac{x-z}{2}\,\mathrm{O}_2 \longrightarrow x\,\mathrm{CO} + \frac{y}{2}\,\mathrm{H}_2\right] \tag{C.7}$$

$$(1-\beta_r)\left[\mathrm{C}_x\mathrm{H}_y\mathrm{O}_z \longrightarrow z\,\mathrm{CO} + \mathrm{C}_\mathrm{a}\mathrm{H}_\mathrm{b}\right] \tag{C.8}$$

Les réactions en Eq. (C.8) representent, respectivement, une combustion complète, une combustion incomplète et un transfert d'hydrocarbures imbrûlés dans les gas brûlés. Les poids de réactions, α_r et β_r, dépendent de la richesse, ϕ :

$$\alpha_r = \max\left(0, \frac{\max(0.98,\phi)\,\dfrac{4x+y-2z}{\phi} - 2x + 2z}{2x+y}\right) \tag{C.9}$$

$$\beta_r = \frac{0,98}{\phi}\frac{4x+y-2z}{2x-2z} \tag{C.10}$$

Intéraction du front de flamme avec la PDF de richesse. La vitesse de flamme laminaire est obtenue en moyennant les vitesses de flamme propres à chaque classe de la PDF de richesse :

$$\bar{s}_L = \sum_{j=1}^{N_{\mathrm{PDF}}} s_L^j\, P_F(j) \tag{C.11}$$

Les taux de production/destruction de chaque espèce sont obtenus en applicant le schéma cinétique en Eq. (C.8) à chaque classe de la PDF de richesse :

$$\dot{\mathcal{M}}^{\mathrm{ff}}_{\mathrm{O_2}\,j} = \left[\alpha_{r\,j}\beta_{r\,j}\,\left(x+\frac{y}{4}-\frac{z}{2}\right)+(1-\alpha_{r\,j})\beta_{r\,j}\,\frac{x-z}{2}\right]\,\frac{M_{\mathrm{O_2}}}{M_F}\,\dot{\mathcal{M}}^{\mathrm{ff}}_{\mathrm{F}\,j} \tag{C.12}$$

$$\dot{\mathcal{M}}^{\mathrm{ff}}_{\mathrm{CO_2}\,j} = -\alpha_{r\,j}\beta_{r\,j}\,x\,\frac{M_{\mathrm{CO_2}}}{M_F}\,\dot{\mathcal{M}}^{\mathrm{ff}}_{\mathrm{F}\,j} \tag{C.13}$$

$$\dot{\mathcal{M}}^{\mathrm{ff}}_{\mathrm{H_2O}\,j} = -\alpha_{r\,j}\beta_{r\,j}\,\frac{y}{2}\,\frac{M_{\mathrm{H_2O}}}{M_F}\,\dot{\mathcal{M}}^{\mathrm{ff}}_{\mathrm{F}\,j} \tag{C.14}$$

$$\dot{\mathcal{M}}^{\mathrm{ff}}_{\mathrm{CO}\,j} = -\left[(1-\alpha_{r\,j})\beta_{r\,j}\,x+(1-\beta_{r\,j})\,z\right]\,\frac{M_{\mathrm{CO}}}{M_F}\,\dot{\mathcal{M}}^{\mathrm{ff}}_{\mathrm{F}\,j} \tag{C.15}$$

$$\dot{\mathcal{M}}^{\mathrm{ff}}_{\mathrm{H_2}\,j} = -(1-\alpha_{r\,j})\beta_{r\,j}\,\frac{y}{2}\,\frac{M_{\mathrm{H_2}}}{M_F}\,\dot{\mathcal{M}}^{\mathrm{ff}}_{\mathrm{F}\,j} \tag{C.16}$$

$$\dot{\mathcal{M}}^{\mathrm{ff}}_{\mathrm{C_aH_b}\,j} = -(1-\beta_{r\,j})\,z\,\frac{M_{\mathrm{C_aH_b}}}{M_F}\,\dot{\mathcal{M}}^{\mathrm{ff}}_{\mathrm{F}\,j} \tag{C.17}$$

with:

$$M_{\mathrm{X}} \quad \text{for} \quad \mathrm{X} = \mathrm{O_2}, \mathrm{CO_2}, \mathrm{H_2O}, \mathrm{CO}, \mathrm{H_2}, \mathrm{C_aH_b}. \tag{C.18}$$

C.3 Validation et résultats

Le modèle 0D proposé reproduit plusieurs caractéristiques du spray et du mélange qui sont utiles en calcul moteur :

- Les pénétrations liquides et gazeuses et le taux d'entrainement d'air permettent de prédire le mélange air/carburant ;
- le taux d'évaporation est également déterminant dans la formation du mélange ;
- la PDF sur la richesse – combinée au modeéle de combustion – permet d'améliorer la prediction du dégagement d'énergie et de la formation des polluants.

Les résultats obtenus avec le modéle 0D proposé ont été comparés aux résultats de calcul 3D, réalisés avec le code RANS IFP-C3D sur trois différentes géométries, pour fournir une validation exhaustive.

C.3.1 Bombe à volume constant

Le cas test constiste en une série d'injections d'iso-octane réalisées dans une bombe á volume constante de 1.4 L contenant de l'air au repos. L'éxpérience est réalisée en différentes conditions thermodynamiques, representatives d'injections précoces (pendant la phase d'admission) dans un moteur GDI homogène en condition de faible et forte charge. Les résultats ont été comparés aux calculs RANS et aux mesures optiques (Mie et Schlieren) réalisées dans le cadre du projet MAGIE (Dumas et al., 2012).

La même géométrie a ensuite été utilisée pour évaluer la réponse du modèle à la présence d'un vortex de tumble jusqu'à 600 rad/s. Les résultats de validation pour ce cas test sont tracés en Fig. C.3. Le modèle représente correctement l'effect du tumble sur l'évaporation et sur la propagation du spray dans le domaine.

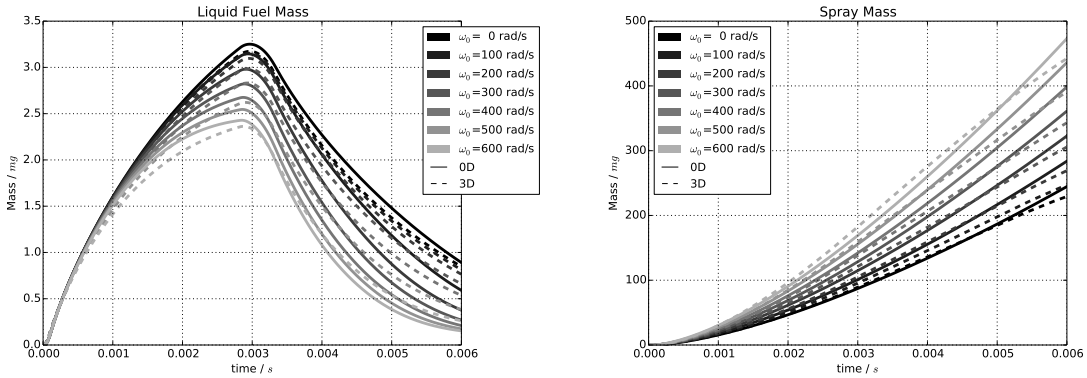

(a) Evaporation : masse de liquide en fonction du temps. **(b)** Entrainement d'air : masse de la zone de mélange en fonction du temps.)

Figure C.3: La bombe à volume constant avec tumble. Trait continu: 0D. Trait interrompu: 3D (reference).

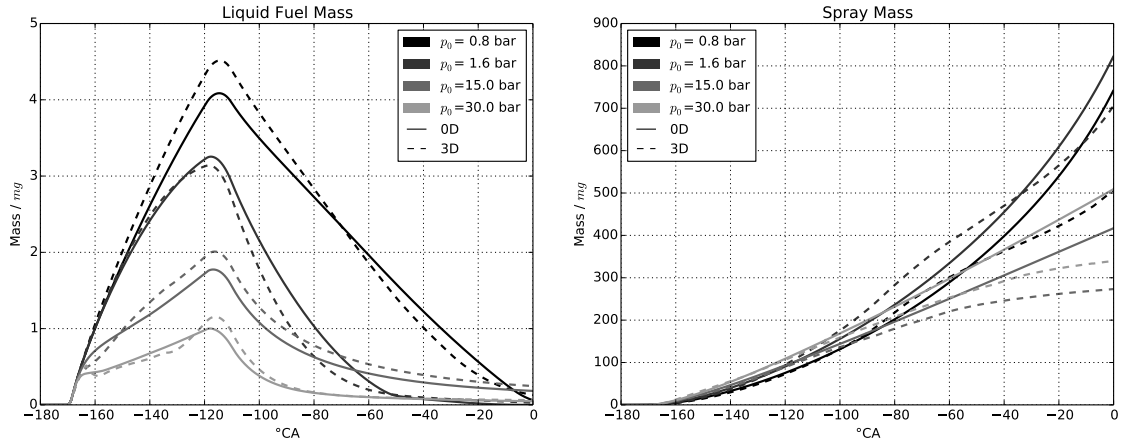

(a) Evaporation : masse de liquide en fonction du temps. **(b)** Entrainement d'air : masse de la zone de mélange en fonction du temps.)

Figure C.4: La bombe à volume variable. Trait continu: 0D. Trait interrompu: 3D (reference).

C.3.2 Bombe à volume variable

Ce cas test adresse la dynamique du spray et de la formation du mélange en conditions thermodinamiques variables. La géométrie consiste en un cylindre fermé, rempli d'air au repos, avec un injecteur mono-trou aligné avec l'axe du piston. Les résultats de validations pour ce cas sont montrés en Fig. C.4.

C.3.3 Moteur entraîné

En conclusion, la réponse du modéle à l'effet combiné des conditions thermodynamique variables et du tumble a été testé en simulant des injections d'iso-octane dans le moteur mono-cylinder ICAMDAC (de Francqueville, 2013). La Fig. C.5.

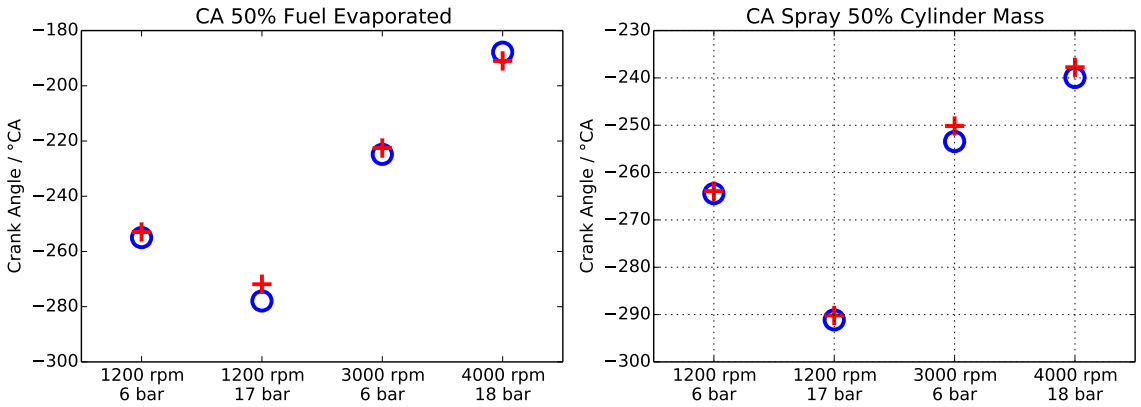

(a) Evaporation : masse de liquide en fonction du temps.

(b) Entrainement d'air : masse de la zone de mélange en fonction du temps.)

Figure C.5: Le moteur ICAMDAC : injections en entraîné. Croix: 0D. Cercles: 3D (reference).

C.4 Conclusion et Perspectives

Ce manuscrit présente le développement et la validation d'un modèle 0D de combustion dans les moteur à allumage commandé à injection directe. Le modèle proposé détaille les différents aspects de l'injection directe, de l'atomisation à l'évaporation et à la formation du mélange avec l'air. Les développements ont été validés à l'aide du calcul 3D (RANS) sur plusieur géometries et cas de référence.

Différentes perspectives s'ouvrent pour la continuation de ce travail :

- mise au point et validation du modèle de combustion ;
- l'extension de la PDF aux gas brûlés ;
- le développement d'un modéle de film liquide.

Bibliography

M. Abarham and I. Wichman. Mono-component fuel droplet evaporation in the presence of background fuel vapor. *International Journal of Heat and Mass Transfer*, 54(17-18): 4090–4098, 2011. doi: 10.1016/j.ijheatmasstransfer.2011.04.002. 11

B. Abramzon and W. Sirignano. Droplet vaporization model for spray combustion calculations. *International Journal of Heat and Mass Transfer*, 32(9):1605–1618, 1989. 13, 35, 68, 184

P. Anselmo-Filho, S. Hochgreb, R. Barlow, and R. Cant. Experimental measurements of geometric properties of turbulent stratified flames. *Proceedings of the Combustion Institute*, 32 II:1763–1770, 2009. doi: 10.1016/j.proci.2008.05.085. 26

C. Barba, C. Burkhardt, K. Boulouchos, and M. Bargende. A phenomenological combustion model for heat release rate prediction in high-speed di diesel engines with common rail injection. *SAE Technical Paper 2000-01-2933*, 10 2000. doi: 10.4271/2000-01-2933. 42

B. Belhassein, D. Chalet, P. Chesse, G. Alix, and R. Lebas. Calibration methodology in system simulation to predict heat transfer along the exhaust line of a diesel engine. *SAE Technical Paper 2014-01-1184*, 4 2014. 38

N. Bordet, C. Caillol, P. Higelin, and V. Talon. A physical 0d combustion model using tabulated chemistry with presumed probability density function approach for multi-injection diesel engines. *SAE Technical Paper 2010-01-1493*, 2010. doi: 10.4271/2010-01-1493. 42

S. Bougrine. *0-Dimensional Modeling of the Combustion of Alternative Fuels in Spark Ignition Engine*. PhD thesis, Ecole Centrale Paris, 2012. URL `http://theses.fr/2012ECAP0031`. 39

S. Bougrine, S. Richard, J.-B. Michel, and D. Veynante. Simulation of co and no emissions in a si engine using a 0d coherent flame model coupled with a tabulated chemistry approach. *Applied Energy*, 113:1199–1215, 2014. doi: 10.1016/j.apenergy.2013.08.038. 40

F. Bozza, A. Gimelli, and R. Tuccillo. The control of a VVA-equipped SI engine operation by means of 1d simulation and mathematical optimization. *SAE Technical Paper 2002-01-1107*, (2002-01-1107), 2002. doi: 10.4271/2002-01-1107. 41

F. Bozza, A. Gimelli, D. Siano, E. Torella, and G. Mastrangelo. A quasi-dimensional three-zone model for performance and combustion noise evaluation of a twin-spark high-egr engine. *SAE Technical Paper 2004-01-0619*, (2004-01-0619), 2004. doi: 10.4271/2004-01-0619. 41

F. Bozza, A. Gimelli, S. S. Merola, and B. M. Vaglieco. Validation of a fractal combustion model through flame imaging. *SAE Technical Paper 2005-01-1120*, (2005-01-1120), 2005. doi: 10.4271/2005-01-1120. 41

F. Charlette, C. Meneveau, and D. Veynante. A power-law flame wrinkling model for les of premixed turbulent combustion part i: Non-dynamic formulation and initial tests. *Combustion and Flame*, 131(1-2):159–180, 2002. doi: 10.1016/S0010-2180(02)00400-5. 40, 44

O. Colin and A. Benkenida. A new scalar fluctuation model to predict mixing in evaporating two-phase flows. *Combustion and Flame*, 134(3):207–227, 2003. doi: 10.1016/S0010-2180(03)00096-8. 24

O. Colin, A. Benkenida, and C. Angelberger. 3D modeling of mixing, ignition and combustion phenomena in highly stratified gasoline engines. *Oil and Gas Science and Technology*, 58 (1):47–62, 2003. doi: 10.2516/ogst:2003004. 24, 93

L. de Francqueville. Essais sur monocylindre opaque : Base de données moteur allumage commandé. Projet ICAMDAC – phase 4.2, IFPEN, 2013. 132, 133, 135, 153, 154, 155, 156, 157, 159, 160, 187

. Delphi Technologies. *Worldwide Emissions Standard: Passenger cars and light duty vehicles.* 2018. 2

S. Demesoukas. *0D/1D combustion modeling for the combustion systems optimization of spark ignition engines*. PhD thesis, Université d'Orléans, 2015. URL `http://www.theses.fr/2015ORLE2024`. 37, 41

F. Dos Santos and L. Le Moyne. Spray atomization models in engine applications, from correlations to direct numerical simulations. *Oil and Gas Science and Technology*, 66(5): 801–822, 2011. doi: 10.2516/ogst/2011116. 9

A. Dulbecco. *Modeling of Diesel HCCI combustion and its impact on pollutant emissions applied to global engine system simulation*. PhD thesis, INPT Toulouse, 2010. URL `http://theses.fr/2010INPT0015`. 42

A. Dulbecco, F. Lafossas, and T. Poinsot. A 0d phenomenological approach to model diesel hcci combustion with multi-injection strategies using probability density functions and detailed tabulated chemistry. *SAE International Journal of Engines*, 2(2009-01-0678):548–568, 2009. doi: 10.4271/2009-01-0678. 42

A. Dulbecco, S. Richard, and C. Angelberger. Investigation on the potential of quantitatively predicting ccv in di-si engines by using a one-dimensional cfd physical modeling approach: Focus on charge dilution and in-cylinder aerodynamics intensity. *SAE International Journal of Engines*, 8(2015-24-2401):2012–2028, 2015. doi: 10.4271/2015-24-2401. 38, 40

A. Dulbecco, S. Richard, O. Laget, and P. Aubret. Development of a quasi-dimensional kk turbulence model for direct injection spark ignition (disi) engines based on the formal reduction of a 3d cfd approach. *SAE Technical Paper 2016-01-2229*, 2016. doi: 10.4271/2016-01-2229. 41, 45

J. P. Dumas, L. Hermant, and J. Kashdan. Experimental characterisation of multi-hole injector spray behaviour in a high pressure/temperature chamber - database for gasoline direct injection. MAGIE project - tasks 3c & 4b, IFPEN, 2012. 87, 88, 89, 90, 186

M. M. Elkotb. Fuel atomization for spray modelling. *Progress in Energy and Combustion Science*, 8(1):61–91, 1982. 9

B. Galmiche, F. Halter, and F. Foucher. Effects of high pressure, high temperature and dilution on laminar burning velocities and markstein lengths of iso-octane/air mixtures. *Combustion and Flame*, 159(11):3286 – 3299, 2012. doi: 10.1016/j.combustflame.2012.06.008. 20, 28

D. Garrido-López and S. Sarkar. Effects of imperfect premixing coupled with hydrodynamic instability on flame propagation. *Proceedings of the Combustion Institute*, 30(1):621 – 628, 2005. ISSN 1540-7489. doi: 10.1016/j.proci.2004.07.014. 25, 26, 27

R. Grout, N. Swaminathan, and R. Cant. Effects of compositional fluctuations on premixed flames. *Combustion Theory and Modelling*, 13(5):823–852, 2009. doi: 10.1080/13647830903160291. 26, 27, 28

D. Haworth, R. Blint, B. Cuenot, and T. Poinsot. Numerical simulation of turbulent propane–air combustion with nonhomogeneous reactants. *Combustion and Flame*, 121 (3):395 – 417, 2000. doi: 10.1016/S0010-2180(99)00148-0. 24, 27

J. Hélie and A. Trouvé. Turbulent flame propagation in partially premixed combustion. *Proceedings of the Combustion Institute*, 27(1):891–898, 1998. doi: 10.1016/S0082-0784(98)80486-4. 23, 24, 26, 27

J. Hélie and A. Trouvé. A modified coherent flame model to describe turbulent flame propagation in mixtures with variable composition. *Proceedings of the Combustion Institute*, 28 (1):193–201, 2000. doi: 10.1016/S0082-0784(00)80211-8. 22, 23, 81

J. Hélie, J.-M. Duclos, T. Baritaud, T. Poinsot, and A. Trouvé. Influence of mixture fluctuations on combustion in direct injection spark ignition engines simulations. *SAE Technical Paper 2001-01-1226*, 2001. doi: 10.4271/2001-01-1226. 23

B. S. Higgins, C. J. Mueller, and D. L. Siebers. Measurements of Fuel Effects on Liquid-Phase Penetration in DI Sprays. *SAE Technical Paper 1999-01-0519*, 1999. doi: 10.4271/1999-01-0519. 17, 18

P. Hill and D. Zhang. The effects of swirl and tumble on combustion in spark-ignition engines. *Progress in Energy and Combustion Science*, 20(5):373 – 429, 1994. ISSN 0360-1285. doi: 10.1016/0360-1285(94)90010-8. 112

H. Hiroyasu, M. Arai, and M. Tabata. Empirical equations for the sauter mean diameter of a diesel spray. *SAE Technical Paper 890464*, 1989. 10

N. Iafrate. *Simulation aux grandes échelles diphasique dans les moteurs downsizés à allumage commandé*. PhD thesis, INPT Toulouse, 2016. URL `http://theses.fr/2016INPT0022`. 29, 36, 68, 133

K. Inagaki, M. Ueda, J. Mizuta, and K. Nakakita. Universal diesel engine simulator (UniDES): 1st report : Phenomenological multi-zone pdf model for predicting the transient behavior of diesel engine combustion. *SAE Technical Paper 2008-01-0843*, 04 2008. doi: 10.4271/2008-01-0843. 42, 71, 75

C. Jiménez, B. Cuénot, T. Poinsot, and D. Haworth. Numerical simulation and modeling for lean stratified propane-air flames. *Combustion and Flame*, 128(1–2):1 – 21, 2002. ISSN 0010-2180. doi: 10.1016/S0010-2180(01)00328-5. 21, 24, 27

W. Jones and B. E. Launder. The prediction of laminarization with a two-equation model of turbulence. *International journal of heat and mass transfer*, 15(2):301–314, 1972. 34

M. Kampa and E. Castanas. Human health effects of air pollution. *Environmental pollution*, 151(2):362–367, 2008. 2

L. Kaprielian. *Modélisation 0D pour la combustion dans les moteurs à allumage commandé : développements en proche paroi et dans le front de flamme.* PhD thesis, ENSAM Paris, 2015. URL `https://pastel.archives-ouvertes.fr/tel-01178792`. 37, 41

R. J. Kee, F. M. Rupley, and J. A. Miller. Chemkin-ii: A fortran chemical kinetics package for the analysis of gas-phase chemical kinetics. Technical report, Sandia National Labs., Livermore, CA (USA), 1989. 40

N. Keuth, G. Broustail, K. Mcaleer, M. Hollander, and S. Scheidel. Successful integration of a model based calibration methodology for non-standard corrections and protection functions. In *Simulation and Testing for Vehicle Technology*, pages 233–244. Springer, 2016. doi: 10.1007/978-3-319-32345-9_17. 37

M. M. Khan, J. Helie, M. Gorokhovski, A. Wood, G. Wigley, J. Kashdan, J. P. Dumas, M. Mojtabi, and P. Guibert. Numerical analysis of multihole gasoline direct injection sprays. In *12th International Conference on Liquid Atomization and Spray Systems, Heidelberg, Germany*. ICLASS, 2012. 8, 92

J. Kim, P. Moin, and R. Moser. Turbulence statistics in fully developed channel flow at low reynolds number. *Journal of Fluid Mechanics*, 177, 1987. 32

P. K. Kundu and I. M. Cohen. *Fluid Mechanics*. Cambridge University Press, 2000. 30, 31

F.-A. Lafossas, O. Colin, F. Le Berr, and P. Menegazzi. Application of a new 1d combustion model to gasoline transient engine operation. *SAE Technical Paper 2005-01-2107*, 2005. doi: 10.4271/2005-01-2107. 38, 41, 46

C. K. Law. Recent advances in droplet vaporization and combustion. *Progress in Energy and Combustion Science*, 8(3):171 – 201, 1982. doi: 10.1016/0360-1285(82)90011-9. 12, 13

H. Le Treut, R. Somerville, U. Cubash, Y. Ding, C. Mauritzen, A. Mokssit, T. Peterson, and M. Prather. Historical overview of climate change science. 2007. 2

P. Leduc, B. Dubar, A. Ranini, and G. Monnier. Downsizing of gasoline engine: an efficient way to reduce co2 emissions. *Oil & Gas Science and Technology - Rev. IFP*, 58(1):115–127, 2003. doi: 10.2516/ogst:2003008. 3

A. H. Lefebvre. *Atomization and Sprays*. Combustion: An International Series. Hemisphere Publishing Corporation (Taylor & Francis), 1989. ISBN 0-89116-603-3. 7, 8, 11, 12, 13

D. Maligne, J. Kashdan, and V. Ricordeau. Base de données ide : moteur optique. Projet ICAMDAC – phase 4.1, IFPEN, 2013. 132

G. Mauviot, A. Albrecht, and T. J. Poinsot. A new 0D approach for diesel combustion modeling coupling probability density function with complex chemistry. *SAE Technical Paper 2006-01-3332*, 2006. doi: 10.4271/2006-01-3332. 42

M. Metghalchi and J. C. Keck. Burning velocities of mixtures of air with methanol, isooctane, and indolene at high pressure and temperature. *Combustion and Flame*, 48:191 – 210, 1982. ISSN 0010-2180. doi: 10.1016/0010-2180(82)90127-4. 39, 46, 81

S. Mouriaux, O. Colin, and D. Veynante. Adaptation of a dynamic wrinkling model to an engine configuration. *Proceedings of the Combustion Institute*, 36(3):3415 – 3422, 2017. ISSN 1540-7489. doi: 10.1016/j.proci.2016.08.001. 36

J. D. Naber and D. L. Siebers. Effects of Gas Density and Vaporization on Penetration and Dispersion of Diesel Sprays. *SAE Technical Paper 960034*, 1996. 15, 16, 42, 69, 70, 125, 184

F. Pellegrino, A. Dulbecco, and D. Veynante. Development of a quasi-dimensional spray evaporation and mixture formation model for direct-injection spark-ignition engines. *SAE Technical Paper 2015-24-2471*, 2015-September, 2015. doi: 10.4271/2015-24-2471. 63

T. Poinsot and D. Veynante. *Theoretical and Numerical Combustion*. CNRS, 2011. 11, 20, 21, 31, 36

T. Poinsot, D. Veynante, A. Trouvé, and G. R. Ruetsch. Turbulent flame propagation in partially premixed flames. *Proceedings of the CRT Summer Program*, pages 111–141, 1996. 23, 27

E. Rehayem, A. de Kerautem, A. Dulbecco, O. Colin, and F. Le Berr. Towards a novel 0d gas turbine combustor modeling: Bridging the gap between dimensional and engine performance approaches. 2017. doi: 10.13009/EUCASS2017-249. 36

R. D. Reitz and F. Bracco. On the dependence of spray angle and other spray parameters on nozzle design and operating conditions. *SAE Technical Paper 790494*, 1979. 16

B. Renou, E. Samson, and A. Boukhalfa. An experimental study of freely propagating turbulent propane/air flames in stratified inhomogeneous mixtures. *Combustion Science and Technology*, 176(11):1867–1890, 2004. 24, 27, 28

S. Richard and D. Veynante. A 0-d flame wrinkling equation to describe the turbulent flame surface evolution in si engines. *Comptes Rendus - Mecanique*, 343(3):219–231, 2015. doi: 10.1016/j.crme.2014.09.003. 39

S. Richard, S. Bougrine, G. Font, F.-A. Lafossas, and F. le Berr. On the reduction of a 3d cfd combustion model to build a physical 0d model for simulating heat release, knock and pollutants in si engines. *Oil and Gas Science and Technology*, 64(3):223–242, 2009. doi: 10.2516/ogst/2008055. 38, 39, 41, 43, 44, 46, 47

S. Richard, A. Dulbecco, C. Angelberger, and K. Truffin. Development of a one-dimensional computational fluid dynamics modeling approach to predict cycle-to-cycle variability in spark-ignition engines based on physical understanding acquired from large-eddy simulation. *International Journal of Engine Research*, 16(3):379–404, 2015. doi: 10.1177/1468087414560592. 40

J. Rudloff, A. Dulbecco, and G. Font. The dual flame model (DFM) : A phenomenological 0d diesel combustion model to predict pollutant emissions. *SAE Technical Paper*, 09 2015. doi: 10.4271/2015-24-2388. 38

J. Sauter. Die grössenbestimmung der in gemischnebeln von verbrennungskraftmaschinen vorhandenen brennstoffteilchen. *VDI-Forschungsheft*, (279), 1926. 8

D. L. Siebers. Liquid-Phase Fuel Penetration in Diesel Sprays. *SAE Technical Paper 980809*, 1998. 17, 18, 19, 42, 97, 140

D. L. Siebers. Scaling Liquid-Phase Fuel Penetration in Diesel Sprays Based on Mixing-Limited Vaporization. *SAE Technical Paper 1999-01-0528*, 1999. doi: 10.4271/1999-01-0528. 16, 17, 18, 140

P. Souhaite and S. Mokhtari. Combustion system design of the new psa peugeot citroën eb turbo pure tech engine. In J. Liebl, editor, *Internationaler Motorenkongress 2014*, pages 49–72, Wiesbaden, 2014. Springer Fachmedien Wiesbaden. ISBN 978-3-658-05016-0. doi: 10.1007/978-3-658-05016-0_5. 4

D. Spalding. The combustion of liquid fuels. *Symposium (International) on Combustion*, 4 (1):847 – 864, 1953. 11, 12, 14

F. Steimle, A. Kulzer, H. Richter, D. Schwarzenthal, and C. Romberg. Systematic analysis and particle emission reduction of homogeneous direct injection si engines. *SAE Technical Paper 2013-01-0248*, 2, 04 2013. doi: 10.4271/2013-01-0248. 9

G. Stiesch. *Modeling Engine Spray and Combustion Processes*. Engineering online library. Springer, 2003. ISBN 3-540-00682-4. 9

J. Turner, A. Popplewell, R. Patel, T. Johnson, N. Darnton, S. Richardson, S. Bredda, R. Tudor, C. Bithell, R. Jackson, S. Remmert, R. Cracknell, J. Fernandes, A. Lewis, S. Akehurst, C. Brace, C. Copeland, R. Martinez-Botas, A. Romagnoli, and A. Burluka. Ultra boost for economy: Extending the limits of extreme engine downsizing. *SAE Int. J. Engines*, 7:387–417, 04 2014. doi: 10.4271/2014-01-1185. 5

K. Varde, D. Popa, and L. Varde. Spray angle and atomization in diesel sprays. *SAE Technical Paper 841055*, 1984. 9, 65, 184

A. Velghe, N. Gillet, and J. Bohbot. A high efficiency parallel unstructured solver dedicated to internal combustion engine simulation. *Computers & Fluids*, 45(1):116 – 121, 2011. doi: 10.1016/j.compfluid.2011.01.027. 22nd International Conference on Parallel Computational Fluid Dynamics (ParCFD 2010). 36, 87, 92, 124, 135

P. C. Vena, B. Deschamps, G. J. Smallwood, and M. R. Johnson. Equivalence ratio gradient effects on flame front topology in a stratified iso-octane/air turbulent V-flame. *Proceedings of the Combustion Institute*, 33(1):1551–1558, 2011. doi: 10.1016/j.proci.2010.06.041. 27

P. C. Vena, B. Deschamps, H. Guo, G. J. Smallwood, and M. R. Johnson. Heat release rate variations in a globally stoichiometric, stratified iso-octane/air turbulent V-flame. *Combustion and Flame*, 162(4):944 – 959, 2015. doi: 10.1016/j.combustflame.2014.09.019. 27

O. Vermorel, S. Richard, O. Colin, C. Angelberger, A. Benkenida, and D. Veynante. Towards the understanding of cyclic variability in a spark ignited engine using multi-cycle les. *Combustion and Flame*, 156(8):1525–1541, 2009. doi: 10.1016/j.combustflame.2009.04.007. 36

F. A. Williams. Combustion theory, (1985). *Cummings Publ. Co*, 1985. 31

G. Woschni. A universally applicable equation for the instantaneous heat transfer coefficient in the internal combustion engine. 1967. 51